

Reconstructing the Australasian monsoon over the last 40,000 years using speleothems and palaeoclimate modelling

Claire Elizabeth Krause

A thesis submitted for the degree of Doctor of Philosophy at
The Australian National University

Research School of Earth Sciences
August 2015



Australian
National
University

Declaration

The work presented in this thesis is an accurate account of original research performed during the academic program towards the degree of Doctor of Philosophy at The Australian National University. I certify that this thesis does not incorporate any material either previously submitted for a degree or diploma at any university, previously published or written by another person, except where due reference is made in the text.

Claire Krause

"If by some fiat I had to restrict all this writing to a single sentence, this is the one I would choose: The summit of Mt. Everest is marine limestone."

- John McPhee

Acknowledgements

A huge thank you needs to go firstly to my PhD supervisor, Mike Gagan. He set me off on my PhD journey in good stead, and was encouraging and supportive when my thesis evolved into new territory (for both of us!). Thank you for the incredible effort you put into refining and polishing my thesis into the document before you. I know my thesis would've been much less without your guidance. Thank you too to my co-supervisor Nerilie Abram who encouraged me to delve into the world of modelling (and brought me back when I got too excited). Your open door and willingness to help saw me through some rough patches, and I am truly grateful. Thank you to Andy Hogg and Mike Roderick for your words of wisdom and enthusiasm for my thesis. The support you both provided played a huge part in getting me to the end.

The thesis itself was not done in isolation, and there were many collaborators who contributed to this work. Firstly, thank you to the co-authors on my oxygen isotope work: Mike Gagan, Gavin Dunbar, John Hellstrom, Hai Cheng, Larry Edwards, Wahyoe Hantoro, Nerilie Abram and Hamdi Rifai. The paper has been a long and sometimes painful slog, and I appreciate all the help that you gave pulling the work together. Thanks also to the people who helped in this work behind the scenes; Heather Scott-Gagan, Joan Cowley, Daniel Becker and Joe Cali. Without you I would still be arguing with the MAT-251, trying to work out why it kept saying, "I am finished" when it had run only three samples. Your help in getting me through the lab work part of my thesis was invaluable. Thanks also to Linda McMorrow and Steven Eggins for their expertise in running the speleothem trace element analysis.

This research wouldn't have been possible without the help of our Indonesian colleagues, in particular Professor Wahyoe Hantoro, Dr Hamdi Rifai and the Indonesian Institute of Sciences. Thank you to Bambang Suwargadi, Gavin Dunbar, Neil Anderson, Dan Zwartz, Garry Smith, Djupriono, Engkos Kosasih, Linda Ayliffe and Nick Scroxtton for their assistance during fieldwork in Indonesia. Sincere thanks go to the staff of Bantimurung-Bulusaraung National Park (with special thanks to Saiful) for superb logistical support in the field during the 2009 and 2011 expeditions.

Thank you to Steven Phipps for the crash course in the CSIRO Mk3L model, and for your advice and support in producing some exciting results. Thank you too for helping me to troubleshoot my model runs, and for never looking down on me for

asking silly questions. Thank you to Peter Hopcroft for your enthusiasm in helping me delve into the world of vegetation modelling. Your patience and willingness to help are the reason I was able to complete that work at all. Thanks also to Paul Valdes, David Beerling and Joy Singarayer for making their model runs available for me to analyse.

I would also like to thank the Research School of Earth Sciences for their logistical support over the last four (and a bit) years. Thank you to the Australian government for providing me with an APA to keep me going, and to the ARC via Discovery grants DP0663274 and DP1095673 for funding the project. Thanks to the Mervyn and Katalin Paterson travel scholarship, as well as the ARC Centre of Excellence for Climate System Science for providing me with funding to travel to New York and work at NASA GISS. Thank you to the Australasian Quaternary Association for grants and travel awards, which allowed me to attend conferences in Australia and New Zealand. I am grateful for the friendships I have made within this organisation and I hope that they can continue into the future.

Thank you most of all to Nick Scropton, Ali Kimbrough and Jen Wurtzel for morning and afternoon teas, cookies and new food experiences. Your support and friendship throughout my thesis means more than I can express. I am immensely sad that my PhD journey is coming to an end because I will miss your support and council, but most of all, your friendship. Thank you to the whole student body at RSES for your friendship and cake. Thanks in particular to those special few who took the time to get to know me more closely.

Finally, I want to say a huge thank you to my family. Thank you Mum for always being interested in my work, and Dad for bragging about me to your footy mates. Thanks to Sarah for your care packages and Michael for your chats about climate change. I am so lucky to have such a caring and supportive family. Thanks to Pa for always being interested in my academic pursuits, and to Grandma for making sure getting married didn't get in the way of achieving.

John, thank you for agreeing to come along on my crazy thesis ride. Thank you for supporting me when I decided to go back to uni, and for "making the money" when I wasn't able to pitch in. I'm so glad that I chose to spend my life with you. You're my favourite.

Abstract

Deep atmospheric convection over the western equatorial Pacific occurs at the junction of the rising limbs of the meridional Hadley cells and the Pacific Walker circulation, making it one of the most atmospherically dynamic regions on Earth. Here, interactions between the Australasian monsoon and atmospheric convection result in highly variable regional precipitation patterns across different latitudes. The dynamics of the Australasian monsoon over the past ~40,000 years are relatively well understood at its northern limit (the East Asian Summer Monsoon), but less well known for its southern limit (the Indo-Australian Summer Monsoon). In the equatorial region however, even less is known about the past behaviour and dynamics of this major system.

Here we present a new, continuous, absolutely dated speleothem record from southwest Sulawesi, Indonesia that spans the past 40,000 years. Isotopic ratios of oxygen ($\delta^{18}\text{O}$) and carbon ($\delta^{13}\text{C}$) in the speleothem calcite were analysed at ~50-yr resolution to reconstruct rainfall amount and vegetation productivity. The records show that the strength of regional deep atmospheric convection is primarily controlled by sea level via the exposure and inundation of the Sunda Shelf. This sea-level control results in a relatively dry last glacial period that was terminated by the onset of deglaciation and the inundation of the Sunda Shelf, which abruptly increased the intensity of deep atmospheric convection.

The Sulawesi speleothem $\delta^{18}\text{O}$ record does not capture millennial-scale variability in response to North Atlantic Heinrich events, in contrast to nearby speleothem records from Borneo and Flores. To explore this observation, the climatic impact of Heinrich events in the western equatorial Pacific region was simulated using idealised North Atlantic freshwater hosing experiments performed with the HadCM3 and CSIRO Mk3L general circulation models. Precessional forcing is shown to influence the manifestation of Heinrich events, particularly across the Southern Hemisphere via the varying response of the Intertropical Convergence Zone. Additionally, high atmospheric carbon dioxide levels increase the duration of the Heinrich climate anomaly, compared to pre-industrial levels.

Sulawesi speleothem $\delta^{13}\text{C}$ is interpreted as a record of changing vegetation productivity. Comparison of the speleothem carbon isotopes with ice core atmospheric methane concentrations reveals a significant relationship during the glacial and early-

deglacial intervals. It is hypothesised that changing vegetation productivity as recorded by Sulawesi speleothems is indicative of broader tropical methane emissions, which are thought to dominate the glacial methane budget. This idea is explored using the Sheffield Dynamic Global Vegetation Model to simulate global climate and methane emissions over the past 40,000 years. The data-model comparisons confirm that temporal changes in the Sulawesi $\delta^{13}\text{C}$ record are in good agreement with modelled methane emissions over much of the tropics, lending weight to the likelihood that the tropics dominated total methane emissions during the glacial period when boreal sites were perennially frozen.

Together this work demonstrates the importance of the western equatorial Pacific in influencing regional climate and global climate signals. It is vital therefore, to continue to explore the past dynamics of this region as a potential driver of global climate changes.

Table of Contents

FRONT MATTER.....	I
<i>Declaration</i>	<i>iii</i>
<i>Acknowledgements</i>	<i>vii</i>
<i>Abstract</i>	<i>ix</i>
<i>Table of Contents</i>	<i>xi</i>
INTRODUCTION	1
BACKGROUND	1
<i>The Australasian monsoon domain</i>	2
KEY RESEARCH QUESTIONS.....	6
PROXY-MODEL COMPARISON STUDIES	8
MODERN CLIMATE OF SULAWESI.....	9
GEOLOGY AND VEGETATION OF SULAWESI.....	11
<i>Geological setting of Sulawesi</i>	11
<i>Vegetation history of Sulawesi</i>	13
THESIS STRUCTURE.....	15
<i>Chapter 1: Spatio-temporal evolution of Australasian monsoon hydroclimate over the last 40,000 years</i>	15
<i>Chapter 2: Sensitivity of modelled tropical climate to freshwater hosing of the North Atlantic</i>	15
<i>Chapter 3: A 40,000-year speleothem $\delta^{13}\text{C}$ record of environmental change in southwest Sulawesi</i>	16
<i>Chapter 4: Speleothem $\delta^{13}\text{C}$, vegetation modelling and the glacial methane budget</i>	16
REFERENCES	17
CHAPTER ONE: SPATIO-TEMPORAL EVOLUTION OF AUSTRALASIAN MONSOON HYDROCLIMATE OVER THE LAST 40,000 YEARS	31
1.1. INTRODUCTION	31

1.2. OXYGEN ISOTOPES IN SPELEOTHEMS	34
1.2.1. <i>Environmental controls on the $\delta^{18}O$ of rainfall</i>	35
1.3. MATERIALS AND METHODS	37
1.3.1. <i>Stalagmite collection and ^{230}Th dating</i>	37
1.3.2. <i>Stable isotope analysis and error reporting</i>	40
1.4. RESULTS AND DISCUSSION	43
1.4.1. <i>Interpretation of Sulawesi speleothem $\delta^{18}O$</i>	43
1.4.2. <i>Ice volume correction</i>	44
1.4.3. <i>Australasian monsoon speleothem synthesis</i>	45
1.4.4. <i>Palaeomonsoon map</i>	45
1.4.4.1. <i>Palaeomonsoon map interpretation</i>	48
1.4.5. <i>Millennial-scale variability</i>	52
1.4.6. <i>Heinrich events in HadCM3</i>	55
1.5. CONCLUSIONS.....	61
1.6. ACKNOWLEDGEMENTS.....	63
1.6.1. <i>Author contributions</i>	64
1.6.2. <i>Further acknowledgements</i>	64
1.7. REFERENCES.....	64

CHAPTER TWO: SENSITIVITY OF MODELLED TROPICAL CLIMATE TO FRESHWATER HOSING OF THE NORTH ATLANTIC	73
2.1. INTRODUCTION.....	73
2.2. HEINRICH EVENTS AND RATES OF FRESHWATER DISCHARGE.....	74
2.3. HOSING EXPERIMENTS	75
2.4. CSIRO Mk3L v1.2.....	80
2.4.1. <i>Model validation</i>	81
2.5. EXPERIMENT DESIGN.....	82
2.5.1. <i>Experiment one: Hosing sensitivity test</i>	82
2.5.2. <i>Experiment two: Hosing under changed orbital configuration</i>	83
2.5.3. <i>Experiment three: Hosing under changed atmospheric CO_2 concentrations</i>	83
2.5.4. <i>Target areas</i>	83

2.6. EXPERIMENT ONE: HOSING SENSITIVITY TEST	85
2.6.1. <i>Experiment design</i>	85
2.6.2. <i>AMOC overturning</i>	87
2.6.3. <i>SST response</i>	89
2.6.4. <i>Precipitation</i>	91
2.6.5. <i>Conclusions</i>	92
2.7. EXPERIMENT TWO: CHANGED ORBITAL CONFIGURATION.....	93
2.7.1. <i>Experiment design</i>	93
2.7.2. <i>Control boundary conditions</i>	94
2.7.3. <i>Hosing results</i>	96
2.7.3.1. <i>AMOC overturning</i>	96
2.7.3.2. <i>SST</i>	97
2.7.3.3. <i>Precipitation</i>	100
2.7.3.4. <i>Surface wind stress and MSLP</i>	100
2.7.4. <i>Discussion</i>	104
2.7.4.1. <i>Drivers of climatic response</i>	105
2.7.5. <i>Conclusions and implications</i>	106
2.8. EXPERIMENT THREE: CHANGED CO ₂ CONCENTRATION.....	107
2.8.1. <i>Experiment design</i>	107
2.8.2. <i>Control boundary conditions</i>	108
2.8.3. <i>Hosing results</i>	110
2.8.3.1. <i>AMOC overturning</i>	110
2.8.3.2. <i>SST</i>	110
2.8.3.3. <i>Precipitation</i>	114
2.8.3.4. <i>Surface wind stress and MSLP</i>	117
2.8.4. <i>Discussion</i>	117
2.8.5. <i>Conclusions and implications</i>	122
2.9. CONCLUSIONS.....	123
2.10. REFERENCES	124

CHAPTER THREE: A 40,000-YEAR SPELEOTHEM $\Delta^{13}\text{C}$ RECORD OF ENVIRONMENTAL CHANGE IN SOUTHWEST SULAWESI, INDONESIA	135
3.1. INTRODUCTION.....	135
3.2. MATERIALS AND METHODS	136
3.2.1. <i>Stalagmite collection and ^{230}Th dating</i>	<i>136</i>
3.2.2. <i>Stable isotope analysis and error reporting</i>	<i>139</i>
3.2.3. <i>Trace element analysis: Mg/Ca and Sr/Ca.....</i>	<i>141</i>
3.3. RESULTS.....	143
3.3.1. <i>Stable isotopes</i>	<i>143</i>
3.3.2. <i>Trace elements: Mg/Ca and Sr/Ca.....</i>	<i>144</i>
3.4. DISCUSSION.....	146
3.4.1. <i>Tropical rainfall: $\delta^{18}\text{O}$ and $\delta^{13}\text{C}$.....</i>	<i>146</i>
3.4.2. <i>Interpreting speleothem $\delta^{13}\text{C}$.....</i>	<i>147</i>
3.4.2.1. <i>C₃:C₄ vegetation changes</i>	<i>147</i>
3.4.2.2. <i>Inorganic processes</i>	<i>149</i>
3.4.2.3. <i>Testing for prior calcite precipitation (PCP)</i>	<i>150</i>
3.4.2.4. <i>Temperature and atmospheric CO₂: vegetation productivity</i>	<i>152</i>
3.4.3. <i>Comparison with regional $\delta^{13}\text{C}$ records</i>	<i>153</i>
3.4.4. <i>Comparison with SST, CO₂ and CH₄.....</i>	<i>155</i>
3.4.4.1. <i>IPWP SSTs and atmospheric CO₂.....</i>	<i>155</i>
3.4.4.2. <i>Atmospheric methane</i>	<i>156</i>
3.5. CONCLUSIONS.....	160
3.6. REFERENCES.....	160
CHAPTER FOUR: SPELEOTHEM $\delta^{13}\text{C}$, VEGETATION MODELLING AND THE GLACIAL METHANE BUDGET	169
4.1. INTRODUCTION.....	169
4.1.1. <i>A tropical driver of glacial atmospheric methane concentrations?.....</i>	<i>169</i>
4.1.2. <i>The global methane budget.....</i>	<i>170</i>
4.1.3. <i>Palaeo-records of atmospheric methane concentration.....</i>	<i>170</i>
4.2. POSSIBLE CONTRIBUTORS TO THE PAST ATMOSPHERIC METHANE SIGNAL.....	172
4.2.1. <i>Wetlands.....</i>	<i>173</i>

4.2.2. Shelf flooding hypothesis.....	175
4.2.3. Marine gas clathrates.....	175
4.3. MODELS AND METHODS.....	176
4.3.1. HadCM3 general circulation model.....	176
4.3.2. SDGVM vegetation and wetland model.....	177
4.3.2.1. Wetland module.....	180
4.3.2.2. Wetland module validation.....	180
4.3.3. Model simulations.....	183
4.4. RESULTS.....	183
4.4.1. Methane sources.....	183
4.4.2. Methane emissions from exposed Indonesian shelves.....	186
4.4.3. Seasonality of methane signal.....	188
4.4.4. Tropical drivers of glacial methane emissions.....	188
4.5. DISCUSSION.....	189
4.5.1. Speleothem $\delta^{13}\text{C}$ and the SDGVM.....	189
4.5.2. Drivers of speleothem $\delta^{13}\text{C}$	190
4.5.3. Is Indonesia representative of the tropics?.....	191
4.5.4. Does modelled methane match speleothem $\delta^{13}\text{C}$?.....	194
4.6. A TROPICAL DRIVER OF GLACIAL ATMOSPHERIC METHANE.....	196
4.7. ACKNOWLEDGEMENTS.....	197
4.8. REFERENCES.....	198
CONCLUSIONS.....	205
REVISITING THE KEY RESEARCH QUESTIONS.....	205
1. What are the key drivers of western equatorial Pacific hydroclimate, and how do they interact?.....	205
2. How did Heinrich events affect western equatorial Pacific hydroclimate?....	206
3. What role does the tropics play in driving global climate change?.....	208
3.a. How did Sulawesi vegetation respond to glacial-interglacial climate change?.....	208
3.b. Did the tropics play a role in driving the glacial atmospheric methane budget?.....	208

FUTURE WORK.....	209
APPENDIX	211
TABLE A1: SUMMARY OF ²³⁰ TH DATA FOR STALAGMITES GB09-3 AND GB11-9.....	212
TABLE A2: SUMMARY OF STALAGMITE GB09-3 ISOTOPE DATA.....	215
TABLE A3: SUMMARY OF STALAGMITE GB11-9 ISOTOPE DATA.....	236
TABLE A4: SUMMARY OF STALAGMITE GB09-3 TRACE ELEMENT DATA.....	245

INTRODUCTION

Background

Deep atmospheric convection over the western equatorial Pacific has been referred to as the global “heat engine” (e.g., Webster 1994; Rennó and Ingersoll 1996; Webster et al. 1998). Convection over the warm waters of the Indo-Pacific Warm Pool (IPWP; $>28^{\circ}\text{C}$) (Yan et al. 1992) forms the ascending branches of both a meridional Hadley cell, and the Pacific Walker circulations (Webster et al. 1998). The associated Intertropical Convergence Zone (ITCZ), identified by the convergence of surface trade winds, and the accompanying maximum in precipitation, follows the seasonal migration of the summer insolation maximum, bringing with it the monsoons of Australasia (Webster et al. 1998; Schneider et al. 2014). Strong land-sea temperature gradients between east Asia and Australia drive strong seasonal swings in the position of the ITCZ and the Australasian monsoon (Wu et al. 2012), which, on average, moves between 20°N (in boreal summer) and 8°S (in austral summer) (Schneider et al. 2014), making the western equatorial Pacific the most atmospherically dynamic region on Earth.

The Australasian monsoon is of vital importance to the billions of people living across the region who rely on monsoon rainfall for their livelihoods. While our understanding of the East Asian Summer Monsoon (EASM; the northern component of the Australasian monsoon) is relatively well developed, improving our knowledge of the nature and sensitivity of the Indo-Australian Summer Monsoon (IASM; the southern counterpart) is still an area of active investigation. Knowledge of the history of the Australasian monsoon may help to inform our understanding of possible future changes in rainfall across the region in the face of anthropogenic climate change. In this study,

we use geochemical records in speleothems from Sulawesi, Indonesia (the core of the Australasian monsoon system) and palaeoclimate modelling to explore the past hydroclimate dynamics of this critically important climate system.

The Australasian monsoon domain

On glacial-interglacial timescales, the Australasian monsoon is known to respond to both orbital and millennial-scale forcing, via changes in the mean position of the ITCZ, and the strength of deep atmospheric convection (e.g., Wang et al. 2001; Muller et al. 2008; Cheng et al. 2009; Griffiths et al. 2009; Meckler et al. 2012; Ayliffe et al. 2013; Carolin et al. 2013; Denniston et al. 2013b; Russell et al. 2014). Tropical monsoon systems display a prominent ~23-kyr (thousand years) cyclicity, driven by the precession of the earth's axial tilt. The precession cycle, one of the three so-called "Milankovitch cycles", refers to the cyclical change in the season of perihelion (the time when the distance between the earth and sun is smallest), which influences the difference in the amplitudes of the seasonal cycles of insolation in the northern versus southern hemispheres (Berger 1978; Berger 1988). The relative strength of local summer insolation between the northern and southern mid-latitudes drives an anti-phased monsoon response to precession forcing at the northern and southern ends of the monsoon system (e.g., Wang et al. 2006). The precession cycle dominates the low-frequency variability of the tropical monsoons, in contrast to the ~100-kyr cyclicity (driven by eccentricity – changes in the shape of the earth's orbit) which drives glacial-interglacial cycles as observed in the northern high latitudes (Hays et al. 1976; Chiang 2009; Abe-Ouchi et al. 2013).

In addition to the precession-scale monsoon variability, abrupt climate events lasting millennia, including Heinrich events, punctuate palaeoclimate variability. Heinrich events are caused by "armadas" of icebergs released from the land-based ice sheets surrounding the North Atlantic, which melt and introduce buoyant freshwater into the bottom-water formation region of the North Atlantic Ocean, temporarily disrupting the Atlantic Meridional Overturning Circulation (AMOC; Heinrich 1988; Bond et al. 1992; Broecker et al. 1992; Broecker 1994; Hemming 2004). Six Heinrich events, as well as the Younger Dryas (also known as H0), occurred over the past ~60

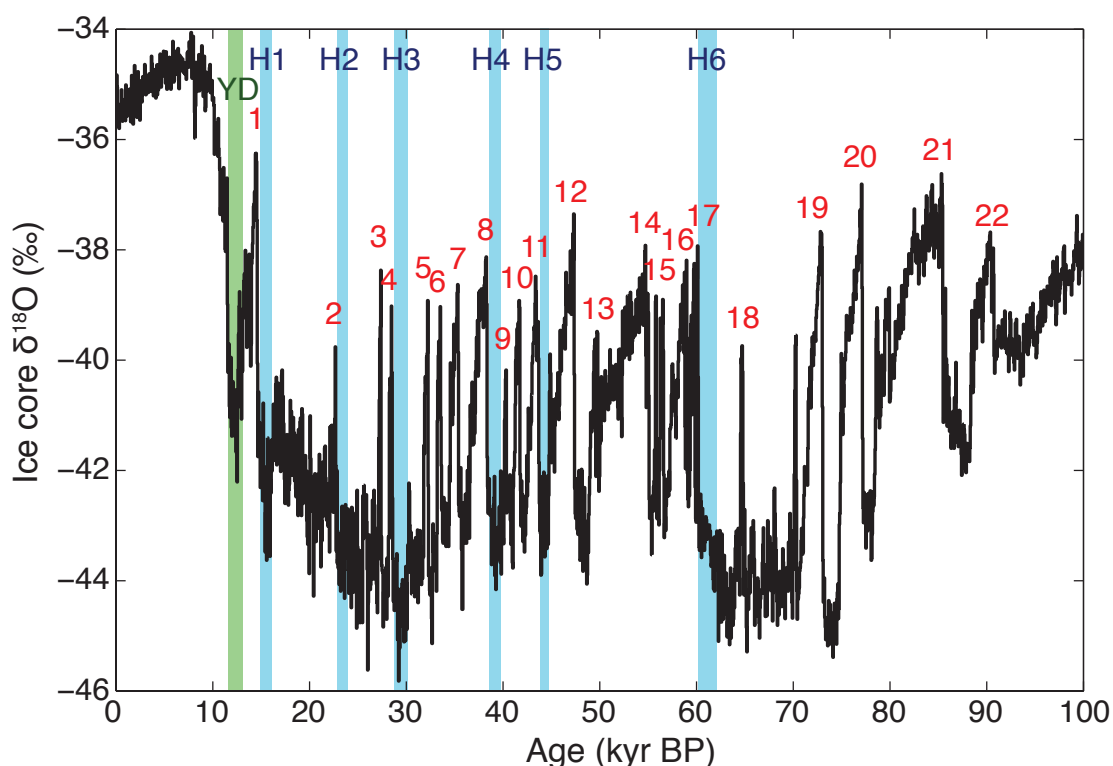


Figure 0.1: NGRIP ice core $\delta^{18}\text{O}$ for the last 100 kyr, showing the occurrence of D-O and Heinrich events. D-O events 1–22 are numbered in red. Heinrich events H1–H6 are indicated by blue shading. The Younger Dryas (also referred to as H0) is shown in green.

kyr and have been identified from ice-rafted debris found in sediment cores across the North Atlantic (Figure 0.1) (Heinrich 1988; Bond et al. 1992). Heinrich events influence global heat transport and hydroclimate, particularly within the Atlantic basin (e.g., Broecker 1991; Broecker 1998; Kanner et al. 2012), but have far-reaching influences via atmospheric and oceanic teleconnections (e.g., Wang et al. 2001; Shakun et al. 2007; Wu et al. 2008; Griffiths et al. 2009; Ayliffe et al. 2013; Denniston et al. 2013b).

The dynamics of the EASM are relatively well understood, with many studies of speleothems (e.g., Wang et al. 2001; Dykoski et al. 2005; Cheng et al. 2006; Johnson et al. 2006; Kelly et al. 2006; Zhou et al. 2008; Duan et al. 2014), loess profiles (e.g., Yu et al. 2010; Lu et al. 2013) and marine sediment cores (e.g., Kienast et al. 2003; Jiang et al. 2013) providing a coherent and long record of EASM variability (Figure 0.2).

Speleothem records, in particular, document the behaviour of the EASM from modern times (e.g., Hou et al. 2003; Wang et al. 2005; Zhang et al. 2008; Kuo et al. 2011; Li et al. 2011; Wan et al. 2011b), through the last four glacial terminations (e.g., Wang et al.

2001; Yuan et al. 2004; Cheng et al. 2006; Kelly et al. 2006; Wang et al. 2008; Cheng et al. 2009), building up an understanding of the EASM as a dynamic (e.g., Cosford et al. 2009; Wan et al. 2011a; Shi et al. 2012) and complex system (e.g., Cai et al. 2010; Clemens et al. 2010) (Figure 0.2 and Figure 0.3).

In contrast, our understanding of the IASM is relatively sparse, with relatively few palaeoclimate studies spanning the last glacial cycle in the large IASM domain (Figure 0.2). Speleothem (Griffiths et al. 2009; Lewis et al. 2011; Ayliffe et al. 2013; Denniston et al. 2013b; Denniston et al. 2013c; Griffiths et al. 2013), marine sediment (e.g., Spooner et al. 2005; van der Kaars et al. 2006; Mohtadi et al. 2011; Muller et al. 2012; Shiau et al. 2012; Kuhnt et al. 2015) and terrestrial proxy records (e.g., Wyrwoll and Miller 2001; Muller et al. 2008) record changes in IASM strength and position, documenting a general anti-phase relationship with the EASM on orbital and millennial time scales.

In the centre of the Australasian monsoon, speleothem, marine sediment and terrestrial proxies document a system that does not clearly follow either EASM or

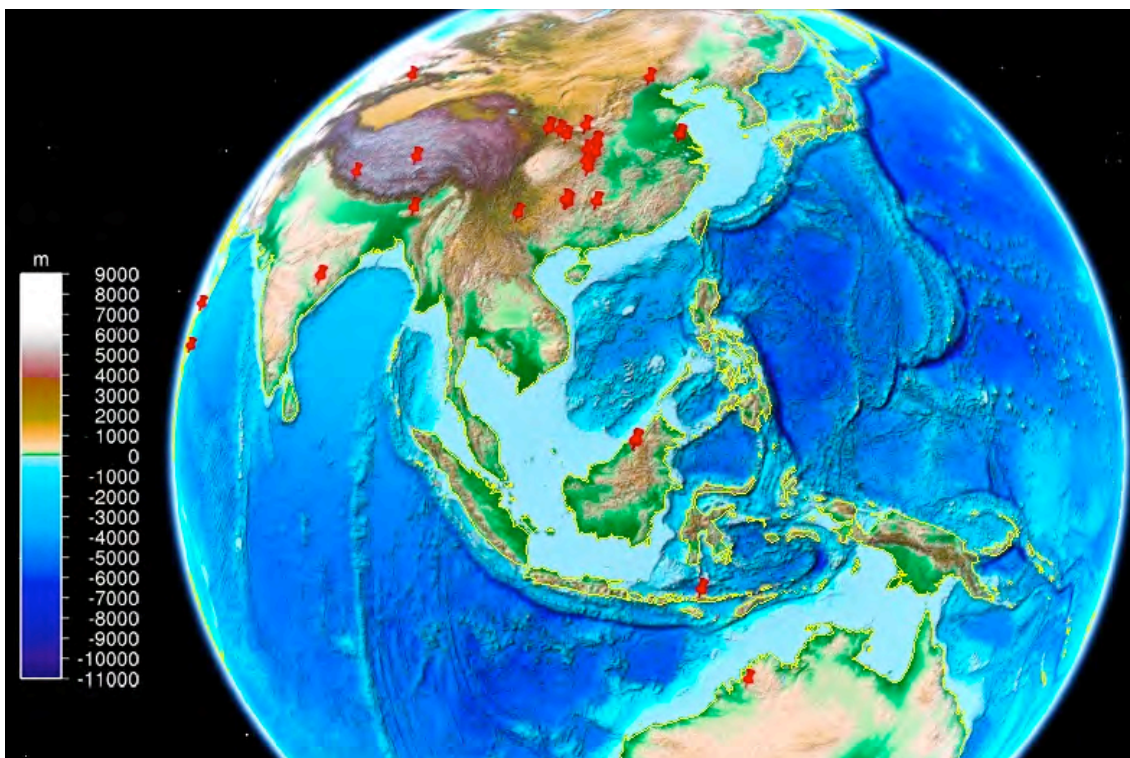


Figure 0.2: Locations of speleothem $\delta^{18}\text{O}$ records of the Australasian monsoon, as archived at NOAA's National Climatic Data Centre. Records for the EASM region outnumber those for the IASM and the core of the Australasian monsoon domain.

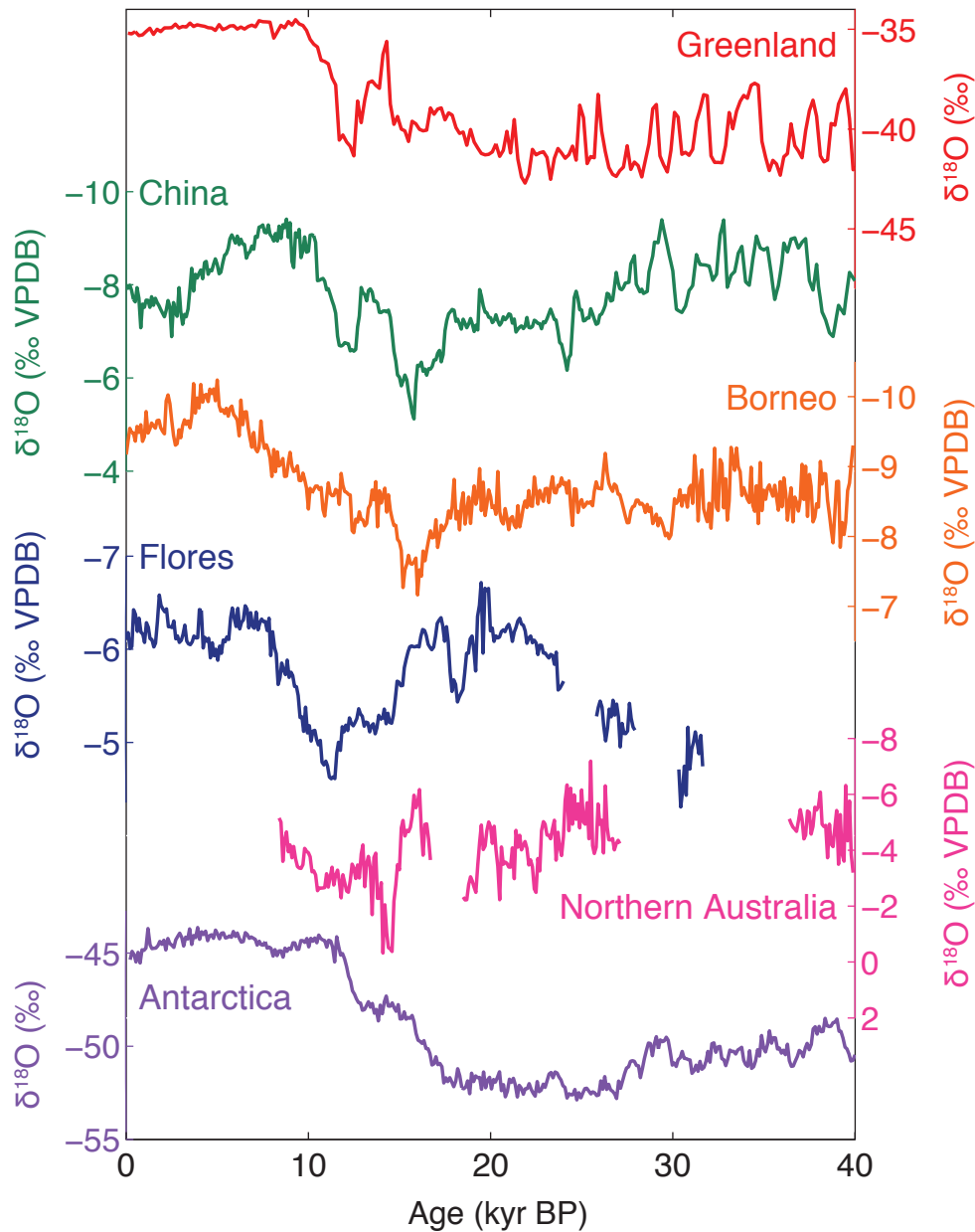


Figure 0.3: Key speleothem $\delta^{18}\text{O}$ records for the Australasian monsoon region (Wang et al. 2001; Dykoski et al. 2005; Partin et al. 2007; Griffiths et al. 2009; Lewis et al. 2011; Ayliffe et al. 2013; Carolin et al. 2013; Denniston et al. 2013a; Denniston et al. 2013b) plotted with ice core $\delta^{18}\text{O}$ records for Greenland (NGRIP 2004) and Antarctica (EPICA 2006).

IASM variability, and reveal the different climate responses across the Australasian monsoon domain. Speleothem $\delta^{18}\text{O}$ records from Malaysian Borneo have provided a continuous and highly resolved hydroclimate history spanning the last 100 kyr (Partin et al. 2007; Carolin et al. 2013) (Figure 0.3). These records show a high degree of

sensitivity to Heinrich events, with reduced rainfall at these times, in phase with speleothem $\delta^{18}\text{O}$ records from China (e.g., Wang et al. 2001; Wang et al. 2008). Meckler et al. (2012) extended the record for Borneo from 570 to 210 kyr BP, demonstrating the dominant role of insolation forcing during interglacials and sensitivity to high latitude climate change. Marine sediment and terrestrial proxy records from the western equatorial Pacific record coherent large-scale glacial-interglacial changes, but a more independent climate on millennial scales that does not clearly follow EASM or IASM variability (e.g., De Deckker et al. 2002; Tierney et al. 2012; Russell et al. 2014; Costa et al. 2015; Wicaksono et al. 2015).

Key research questions

The climatology of the western equatorial Pacific and the Australasian monsoon remains a key area of interest because of the interaction of large-scale atmospheric circulation systems over this region, and its potential influence on global climate. This region has also been identified as an important location for the development of early human culture (e.g., Aubert et al. 2014), highlighting the need to understand past environmental changes across Australasia. We identify three key research questions critical for understanding the role of the western equatorial Pacific in global climate change over the last glacial period:

1. What are the key drivers of western equatorial Pacific hydroclimate, and how do they interact?

Despite the large number of palaeo-studies examining Australasian monsoon hydroclimate, the role and interaction of the drivers of hydroclimate within this region – including deep atmospheric convection and the ITCZ – remains unresolved. Answering this question requires exploration of the sensitivity of western equatorial Pacific hydroclimate to local (e.g., sea level, temperature) and remote (e.g., orbital forcing, high-latitude ice sheets, Heinrich events, AMOC dynamics) climate forcings, as well as the ways in which these competing factors interact.

We use $\delta^{18}\text{O}$ records from speleothems in Sulawesi, Indonesia as a proxy for monsoon rainfall amount to explore the competing drivers of Australasian hydroclimate. This line of enquiry builds upon previous studies in the region to

better understand the spatial and temporal hydroclimate changes that occurred across Australasia over the past 40,000 years, and the ways in which the different components of the monsoon system responded to the range of climate drivers.

2. How did Heinrich events affect western equatorial Pacific hydroclimate?

Heinrich events are recorded in proxy records from the Australasian monsoon domain, however their strength and duration are not always consistent among events. While Heinrich events have been extensively explored within palaeoclimate models, the influence of changing boundary conditions on their global teleconnections and manifestation across the Australasian monsoon domain have not been extensively investigated.

Here we specifically focus on the potential influence of climate forcings from the North Atlantic, via rapid changes in the AMOC during Heinrich events, using the CSIRO Mk3L general circulation model. This study allows us to explore the strength and nature of teleconnections from the North Atlantic into the western equatorial Pacific under changing boundary conditions, building on previous studies that have explored the climatic impacts of Heinrich events in speleothem $\delta^{18}\text{O}$ records from this region.

3. What role does the tropics play in driving global climate change?

Here we will explore the role of tropical vegetation in driving the atmospheric methane budget of the last glacial period using two key lines of enquiry:

a. How did Sulawesi vegetation respond to glacial-interglacial climate change?

Exploration of the role of the tropics in driving the global atmospheric methane concentration first requires the establishment of a proxy capable of recording changes in tropical vegetation. While speleothem $\delta^{13}\text{C}$ has previously been interpreted as a record of vegetation productivity, it remains a contentious proxy due to the wide-range of factors influencing the $\delta^{13}\text{C}$ of speleothems.

We employ records of Sulawesi speleothem $\delta^{13}\text{C}$ as a proxy for tropical vegetation productivity, particularly during the last glacial period. The use of available published data, as well as trace element ratios within the speleothems themselves (Mg/Ca and Sr/Ca), allows us

to develop a robust and well-supported interpretation for speleothem $\delta^{13}\text{C}$. The establishment of a speleothem-based palaeo-vegetation proxy allows us to better constrain the timing of vegetation changes for comparison with well-resolved ice core records of atmospheric methane concentration.

b. Did the tropics play a role in driving the glacial atmospheric methane budget?

To date, studies of glacial atmospheric methane have relied on ice core records and palaeoclimate modelling, which do not allow for definitive attribution of the sources of atmospheric methane. Understanding the sources of glacial methane allows us to better understand the possible role of the tropics in driving global climate changes.

Here we combine vegetation proxy and palaeoclimate modelling methods to validate and upscale the results for Sulawesi to the wider tropics, and explore the role of the tropics in driving the glacial methane budget. The development of a tropical proxy for atmospheric methane concentrations facilitates a more definitive discussion of the role of different contributions to the global methane budget.

Proxy-model comparison studies

While palaeoclimate records provide vital reconstructions of palaeoenvironmental change, they are only able to provide information for locations where proxies have been identified and studied, and are thus limited by their spatial distribution. Palaeoclimate model simulations produce spatially complete palaeoenvironmental information that allows for exploration of spatial patterns and dynamics. However, climate models are only as good as the information used to constrain their output, and cannot be used to examine small-scale locations, because of limitations in model resolution (e.g., Butler 2003). Proxy-model comparison studies are therefore becoming more common, whereby proxy records are interpreted within the global framework of a palaeoclimate model, enabling the attribution of specific climate processes to the variability within proxy records, and conversely, ensuring the model simulations represent a good approximation of real palaeoclimates (e.g., Meissner 2007; Muller et al. 2008; Pausata

et al. 2011; Tierney et al. 2011; DiNezio and Tierney 2013; Phipps et al. 2013; Liu et al. 2014).

Palaeoclimate models produce gridded information for a large number of atmospheric (e.g., temperature, wind velocity, cloud height and cover, sea level pressure and precipitation) and oceanic (e.g., sea surface temperature, salinity, density, ocean currents and sea ice) climate variables, and when additional model components are added, can also provide information on biological (e.g., vegetation dynamics, oceanic productivity and soil processes) and chemical processes (e.g., nutrient cycling, methane emissions and the carbon cycle). To date, palaeoclimate models have been used to complement studies based on ice cores (e.g., Jouzel et al. 2003; Meissner 2007), marine sediment cores (e.g., Rohling et al. 2004; Oppo et al. 2007; Carlson 2009; LeGrande and Schmidt 2011; Tierney et al. 2012), terrestrial sediments (e.g., Muller et al. 2008; Uchikawa et al. 2010; Tierney et al. 2011; Sun et al. 2012), corals (e.g., An et al. 2004; Tindall et al. 2009; LeGrande and Schmidt 2011), speleothems (e.g., Lewis et al. 2010; Pausata et al. 2011; Tierney et al. 2012; Caley et al. 2014) as well as multiple proxies (e.g., Otto-Bliesner et al. 2003; LeGrande and Schmidt 2009; DiNezio and Tierney 2013; He et al. 2013; Phipps et al. 2013).

Modern climate of Sulawesi

Sulawesi is located in the western equatorial Pacific, within the warm waters of the IPWP. It straddles the equator, between $\sim 2^{\circ}\text{N}$ and $\sim 6^{\circ}\text{S}$, extending ~ 850 km from top to bottom. The climate of Sulawesi varies by latitude, from a strongly equatorial climate with no clear rainfall seasonality in the north, to the monsoonal climate of the south. The topography and peninsulas of Sulawesi result in markedly different mean annual rainfall patterns across the island. Makassar, on the western flank of the south-western peninsula, is strongly dominated by the IASM, which moves over the region from November to March (Figure 0.4). The dominant westerly flow of the IASM brings up to $\sim 80\%$ of Makassar's annual rainfall during this period (Baker et al. 1994). The dry season (during the austral winter) is amplified by the presence of a mountain range, which runs north/south down the southwest peninsula, blocking the easterly winter monsoon and minimising winter rainfall at Makassar (Figure 0.4). Sulawesi is located within a region of deep atmospheric convection, driven by evaporation over the IPWP

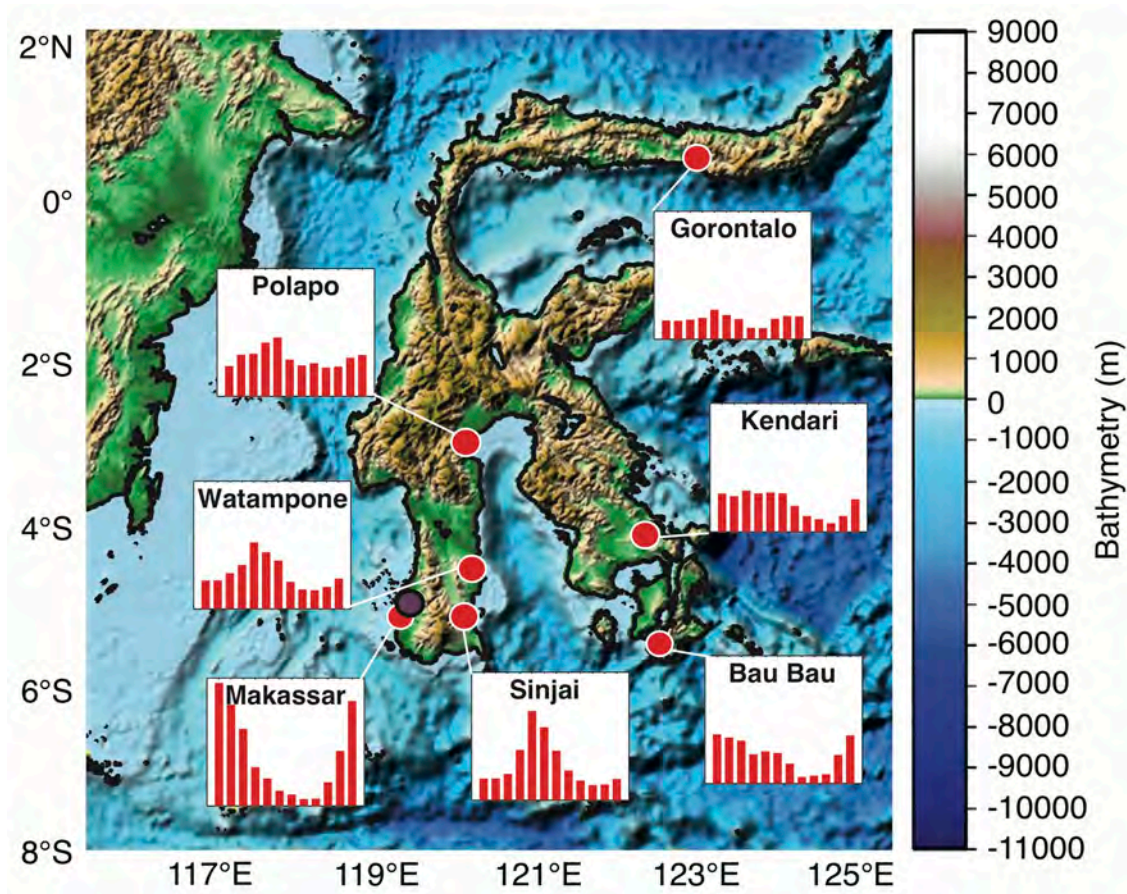


Figure 0.4: Bathymetry and topography of Sulawesi, Indonesia. Relief data are from the NOAA ETOPO1 1 arc-minute dataset (Amante and Eakins 2009). Rainfall data for each location are shown on the same y-axis (0-700 mm) (Baker et al. 1994). The location of Gempa Bumi cave is marked with a purple circle.

and strong convergence associated with the ITCZ. This strong atmospheric convection forms the rising limb of the meridional Hadley Cell, and the Pacific Walker circulation.

Sulawesi's climate is influenced by the El Niño Southern Oscillation (ENSO), a natural periodic fluctuation of the strength of the Pacific Walker circulation and sea surface temperatures (e.g., Walker 1923; Walker 1924; Berlage 1966; Rasmusson and Carpenter 1982). During an El Niño event, rainfall at Sulawesi falls below the annual average, with rainfall above average during La Niña events (Dai and Wigley 2000) (Figure 0.5).

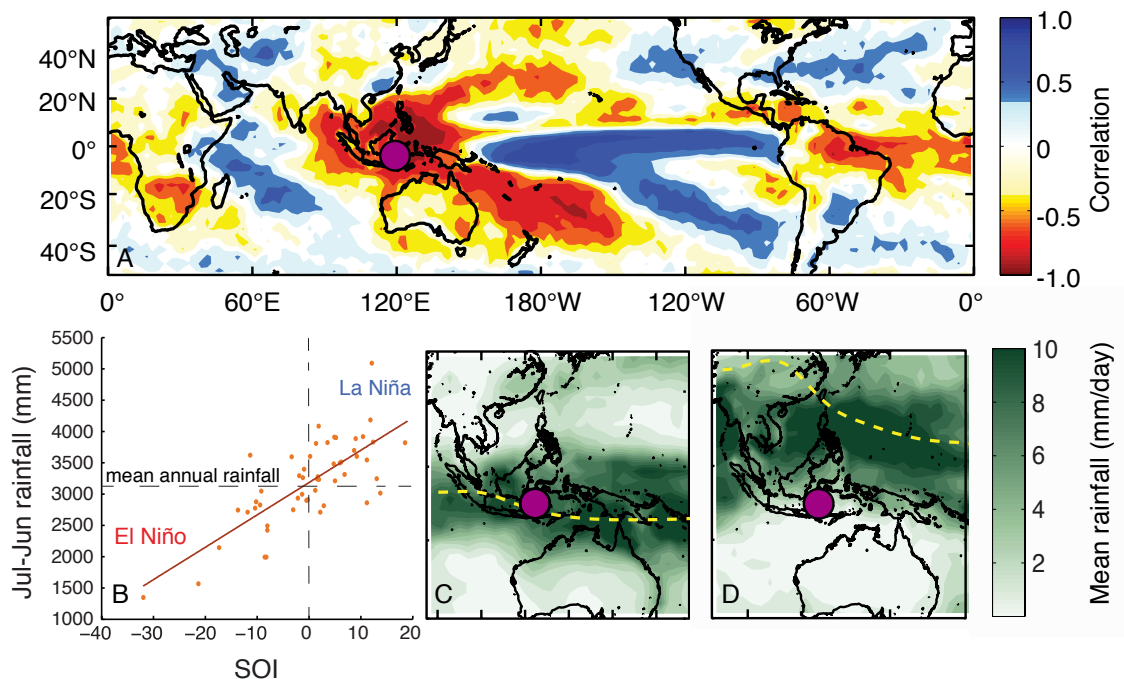


Figure 0.5: Influence of ENSO and the ITCZ on Australasian monsoon rainfall. (A) Correlation between NINO3.4 sea surface temperature (Kaplan et al. 1998) and CMAP reanalysis precipitation (Xie and Arkin 1997). (B) Relationship between total annual rainfall (July–June) at Makassar (IRI/LDEO) and the Southern Oscillation Index (SOI) (Australian Bureau of Meteorology). A strong positive relationship exists between rainfall amount and the SOI ($R=0.75$, $p\approx 0$). The mean annual rainfall for 1950–2002 is shown by a dashed horizontal line. (C) Mean DJF ITCZ position and rainfall for the period 1979–2004 (Janowiak and Xie 1999). (D) As in C, but for JJA. The location of Gempa Bumi cave, Sulawesi is marked with a purple circle.

Geology and vegetation of Sulawesi

Geological setting of Sulawesi

Sulawesi is located in the Indonesian archipelago to the east of Borneo, separated by the Makassar Strait. Tectonically, Sulawesi lies within the region of tectonic collision between the Indo-Australian, Philippine-Pacific and Asian plates (Wilson and Moss 1999). The island of Sulawesi is made up of four peninsulas, which are geologically diverse and broadly represent different lithotectonic units (Watkinson 2011), thought to

have been gradually accreted onto Sundaland during the Cretaceous and Tertiary (Wilson and Moss 1999) (Figure 0.6).

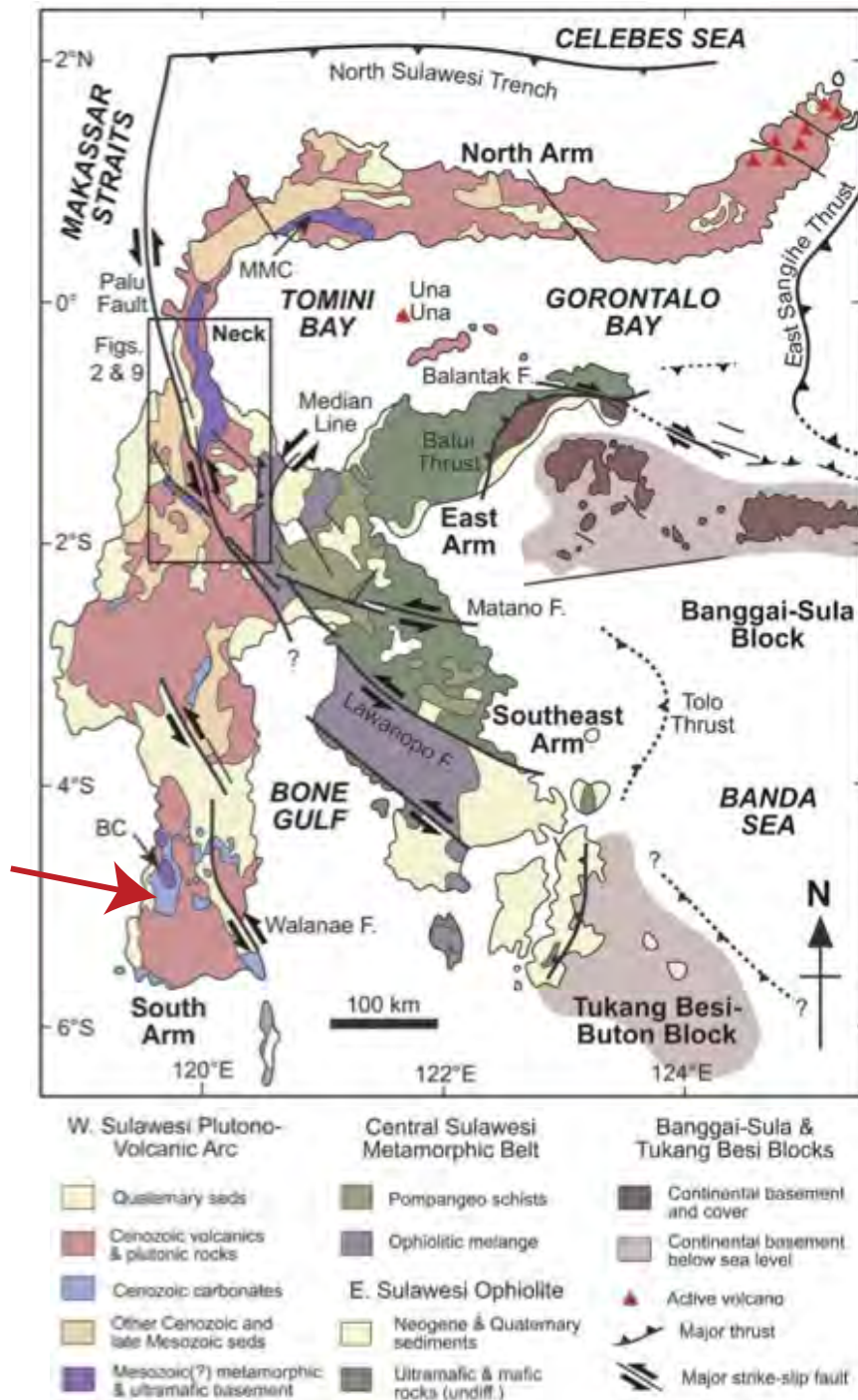


Figure 0.6: Summary of the geology of Sulawesi showing principal structures and geographical features. Red arrow shows the location of the Tonasa Limestone formation, and Gempa Bumi cave. Modified after figure 1 in Watkinson (2011).

The sediments forming the Tonasa Limestone Formation in south-western Sulawesi were originally deposited in a shallow marine environment during the mid-Eocene to mid-Miocene (Wilson and Bosence 1996; Wilson 2000). Gempa Bumi cave is located within the tower karst of the Tonasa formation at 5°S, 120°E and ~40 m above sea level, near Makassar on the southwest peninsula (Figure 0.7). Speleothem samples used for this study were collected from Gempa Bumi cave in 2009 and 2011.

Vegetation history of Sulawesi

Sulawesi has never been connected to a large land area (e.g., the Sunda Shelf), resulting

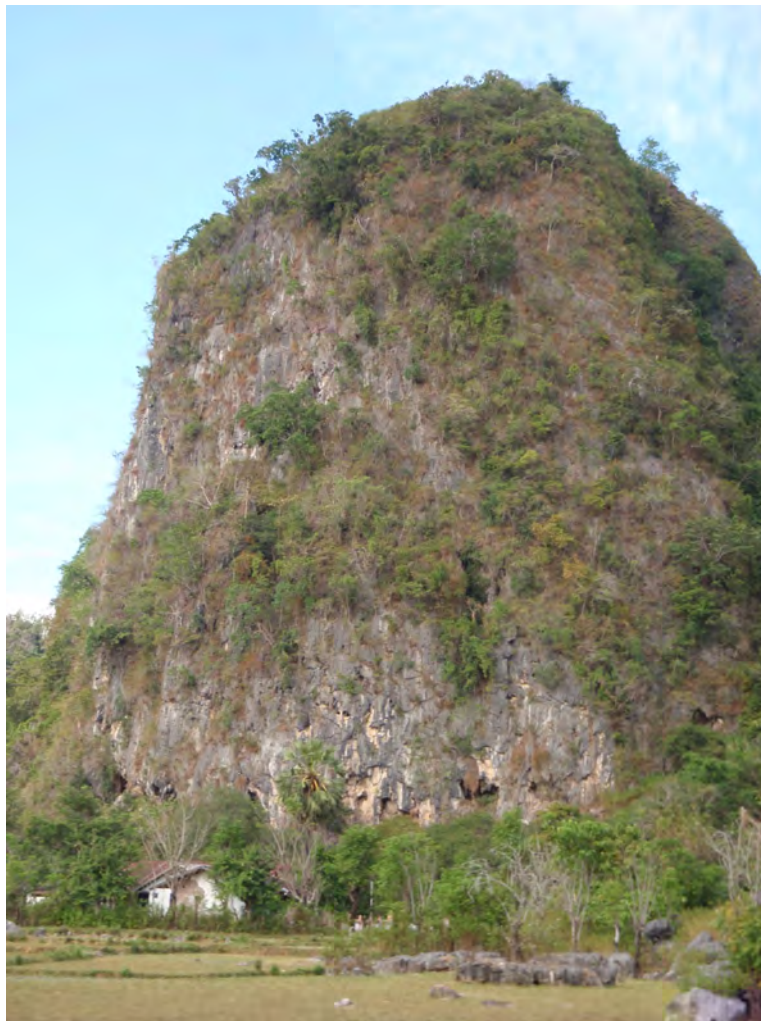


Figure 0.7: Tower karst of the Tonasa Limestone formation, southwest Sulawesi. Photo credit: Garry K. Smith.

in diverse flora and fauna often endemic to the island (Resosudarmo and Subiman 2003; Cannon et al. 2005). However, the nature and distribution of vegetation across Sulawesi is poorly understood, with few extensive vegetation surveys available (e.g., BAPPENAS 1991; Cannon et al. 2005). Sulawesi is largely covered by tropical rainforest, however the complex topography of the island, which extends to ~3500 m above sea level, means that the specific rainforest type varies from lowland through to montane (Cannon et al. 2005). The narrow nature of Sulawesi's peninsulas mean that no location is more than 100 km from the coast, and coastal mangroves and wetlands comprise 4% of the total land area of the island (Cannon et al. 2005).

Proxy records of the vegetation history of Sulawesi and Indonesia are based largely on pollen found in marine sediment cores (e.g., van der Kaars and Dam 1995; Sun et al. 2000; van der Kaars et al. 2001; Visser et al. 2004) and lake sediments (e.g., Hope 2001; Russell et al. 2014; Wicaksono et al. 2015). During the last glacial period, sea level was ~120 m lower than at present, exposing the large continental shelves of Indonesia between Sumatra and Borneo (Sunda Shelf) and between Papua New Guinea and Australia (Sahul Shelf). It has been suggested that grassland colonised the exposed Sunda Shelf, creating a "savannah corridor" across the sandy land-bridge connecting mainland Asia and western Indonesia (Bird et al. 2005). Changes in the vegetation distribution during the last glacial period are not well understood, and despite evidence for an increase of grassland and dry forest taxa (e.g., Hope 2001; Bird et al. 2005; Russell et al. 2014), some records point to the continued survival of tropical rainforest during this time (e.g., Sun et al. 2000; Visser et al. 2004).

In the modern day, ~60% of global methane emissions are from wetlands, of which ~60% are from tropical sources (Aselmann and Crutzen 1989; Cao et al. 1996; Guo et al. 2012). During the last glacial period, when much of the boreal wetlands were perennially frozen, tropical wetlands are believed to have become the dominant source of atmospheric methane emissions (e.g., Chappellaz et al. 1997; Dällenbach et al. 2000; Valdes et al. 2005; Kaplan et al. 2006; Fischer et al. 2008). It is therefore of interest to reconstruct the changes and behaviour of tropical vegetation, which acted as an important source for atmospheric trace gasses, including methane, and may have played a role in driving deglaciation to completion (Rhodes et al. 2015).

Thesis structure

This thesis aims to explore the dynamics of the Australasian monsoon and the western equatorial Pacific over the last 40 kyr. We address the three key research questions identified above using speleothems from Sulawesi, and supplement these records with palaeoclimate modelling. This thesis is divided into four chapters, centred on speleothem $\delta^{18}\text{O}$ and $\delta^{13}\text{C}$ records. Two modelling chapters accompany these research themes to test observations and hypotheses determined from the speleothem proxy records.

Chapter 1: Spatio-temporal evolution of Australasian monsoon hydroclimate over the last 40,000 years

This chapter presents the Sulawesi speleothem $\delta^{18}\text{O}$ record and discusses its climatic implications. Here we employ a novel new technique that synthesises previously published Australasian monsoon speleothem $\delta^{18}\text{O}$ records to produce a regional picture of hydroclimate over the past 40 kyr. We use this regional synthesis to deconvolve the relative roles of meridional movements of the ITCZ and changes in the strength of deep atmospheric convection in driving Australasian monsoon hydroclimate. Modelling results from HadCM3 supports our proxy synthesis through the exploration of the seasonality of simulated Heinrich events at Sulawesi. This chapter forms the basis of a manuscript currently in preparation for *Nature Geoscience*.

Chapter 2: Sensitivity of modelled tropical climate to freshwater hosing of the North Atlantic

Chapter two employs the CSIRO Mk3L general circulation palaeoclimate model to explore the nature of Heinrich events under changing boundary conditions. Three experiments are performed to determine:

- (1) the sensitivity of the CSIRO Mk3L to North Atlantic freshwater forcing of different magnitudes and durations;
- (2) the influence of changed orbital conditions (namely precession) on the model climate response to a simulated Heinrich event; and

(3) the influence of increased atmospheric CO₂ on the model climate response to a simulated Heinrich event.

These experiments are highly idealised, but shed light on the dynamics driving the model climate response to freshwater hosing of the North Atlantic and provide insights into the observed differences in the manifestation of Heinrich events as recorded in western equatorial Pacific speleothems.

Chapter 3: A 40,000-year speleothem $\delta^{13}\text{C}$ record of environmental change in southwest Sulawesi

This chapter explores the $\delta^{13}\text{C}$ record for Sulawesi, produced concurrently with the $\delta^{18}\text{O}$ record. We use trace element data (Mg/Ca and Sr/Ca) alongside published speleothem and palynological records from the region to develop a robust interpretation of Sulawesi speleothem $\delta^{13}\text{C}$ as a proxy for vegetation productivity. The Sulawesi $\delta^{13}\text{C}$ record is then used to explore the nature and dynamics of tropical vegetation over the past 40 kyr. We demonstrate a close association between Sulawesi speleothem $\delta^{13}\text{C}$ and ice core methane records and propose that tropical vegetation, as recorded in Sulawesi speleothems, is an important driver of the glacial atmospheric methane budget.

Chapter 4: Speleothem $\delta^{13}\text{C}$, vegetation modelling and the glacial methane budget

Chapter four explores the role of the tropics in the atmospheric methane budget using a coupled general circulation climate model. Here we use the Sheffield Dynamic Global Vegetation Model, coupled to HadCM3 to simulate the changing sources of methane emissions to the atmosphere over the last 40 kyr. We test the hypothesis that Sulawesi speleothem $\delta^{13}\text{C}$ records changes in vegetation productivity, and demonstrate that the speleothem $\delta^{13}\text{C}$ record closely follows modelled Sulawesi, Indonesian and tropical methane emissions. The use of a global model allows us to put the Sulawesi record into a broader context and explore the role of the tropics as a whole in driving the atmospheric methane budget since 40 kyr BP.

All data have been produced and analysed by the author, except where due reference is made.

References

- Abe-Ouchi, A., F. Saito, K. Kawamura, M. Raymo, J. i. Okuno, K. Takahashi and H. Blatter (2013). Insolation-driven 100,000-year glacial cycles and hysteresis of ice-sheet volume. *Nature* 500: 190–193.
- Amante, C. and B. W. Eakins (2009). ETOPO1 1 arc-minute global relief model: procedures, data sources and analysis. NOAA Technical Memorandum NESDIS NGDC-24, National Geophysical Data Center, NOAA.
- An, S.-I., A. Timmermann, L. Bejarano, F.-F. Jin, F. Justino, Z. Liu and A. W. Tudhope (2004). Modeling evidence for enhanced El Niño-Southern Oscillation amplitude during the Last Glacial Maximum. *Paleoceanography* 19: PA4009.
- Aselmann, I. and P. J. Crutzen (1989). Global distribution of natural freshwater wetlands and rice paddies, their net primary productivity, seasonality and possible methane emissions. *Journal of Atmospheric Chemistry* 8: 307–358.
- Aubert, M., A. Brumm, M. Ramli, T. Sutikna, E. W. Saptomo, B. Hakim, M. J. Morwood, G. D. van den Bergh, L. Kinsley and A. Dosseto (2014). Pleistocene cave art from Sulawesi, Indonesia. *Nature* 514: 223–227.
- Australian Bureau of Meteorology. from <http://www.bom.gov.au/climate/current/soi2.shtml>.
- Ayliffe, L. K., M. K. Gagan, J.-x. Zhao, R. N. Drysdale, J. C. Hellstrom, W. S. Hantoro, M. L. Griffiths, H. Scott-Gagan, E. St Pierre, J. A. Cowley and B. W. Suwargadi (2013). Rapid interhemispheric climate links via the Australasian monsoon during the last deglaciation. *Nature Communications* 4: 2908.
- Baker, C. B., J. K. Eischeid, T. R. Karl and H. F. Diaz (1994). The quality control of long-term climatological data using objective data analysis. *Preprints of AMS Ninth Conference on Applied Climatology*, Dallas, TX.
- BAPPENAS (1991). Biodiversity action plan for Indonesia. Jakarta, BAPPENAS.
- Berger, A. (1988). Milankovitch theory and climate. *Reviews of Geophysics* 26: 624–657.

- Berger, A. L. (1978). Long-term variations of daily insolation and Quaternary climatic changes. *Journal of the Atmospheric Sciences* 35: 2362–2367.
- Berlage, H. P. (1966). *The Southern Oscillation and World Weather*, Koninklijk Nederlands Meteorologisch Instituut, Mededelingen en Verhandelingen.
- Bird, M. I., D. Taylor and C. Hunt (2005). Palaeoenvironments of insular Southeast Asia during the Last Glacial Period: a savanna corridor in Sundaland? *Quaternary Science Reviews* 24: 2228–2242.
- Bond, G., H. Heinrich, W. Broecker, L. Labeyrie, J. McManus, J. Andrews, S. Huon, R. Jantschik, S. Clasen, C. Simet, K. Tedesco, M. Klas, G. Bonani and S. Ivy (1992). Evidence for massive discharges of icebergs into the North Atlantic ocean during the last glacial period. *Nature* 360: 245–249.
- Broecker, W., G. Bond, M. Klas, E. Clark and J. McManus (1992). Origin of the northern Atlantic's Heinrich events. *Climate Dynamics* 6: 265–273.
- Broecker, W. S. (1991). The great ocean conveyor. *Oceanography* 4: 79–89.
- Broecker, W. S. (1994). Massive iceberg discharges as triggers for global climate change. *Nature* 372: 421–424.
- Broecker, W. S. (1998). Paleocean circulation during the last deglaciation: A bipolar seesaw? *Paleoceanography* 13: 119–121.
- Butler, D. (2003). Heatwave underlines climate-model failures. *Nature* 424: 867.
- Cai, Y., L. Tan, H. Cheng, Z. An, R. L. Edwards, M. J. Kelly, X. Kong and X. Wang (2010). The variation of summer monsoon precipitation in central China since the last deglaciation. *Earth and Planetary Science Letters* 291: 21–31.
- Caley, T., D. M. Roche and H. Renssen (2014). Orbital Asian summer monsoon dynamics revealed using an isotope-enabled global climate model. *Nature Communications* 5: 5371.
- Cannon, C., J. Harting, A. Salim and M. Summers (2005). The Vegetation of Sulawesi: I. Coarse filter analysis. *Ecoregional Conservation Assessment*, The Nature Conservancy and Texas Tech University.
- Cao, M., S. Marshall and K. Gregson (1996). Global carbon exchange and methane emissions from natural wetlands: Application of a process-based model. *Journal of Geophysical Research* 101: 14399–14414.
- Carlson, A. E. (2009). Geochemical constraints on the Laurentide Ice Sheet contribution to Meltwater Pulse 1A. *Quaternary Science Reviews* 28: 1625–1630.

- Carolin, S. A., K. M. Cobb, J. F. Adkins, B. Clark, J. L. Conroy, S. Lejau, J. Malang and A. A. Tuen (2013). Varied response of Western Pacific hydrology to climate forcings over the Last Glacial period. *Science* 340: 1564–1566.
- Chappellaz, J., T. Blunier, S. Kints, A. Dällenbach, J.-M. Barnola, J. Schwander, D. Raynaud and B. Stauffer (1997). Changes in the atmospheric CH₄ gradient between Greenland and Antarctica during the Holocene. *Journal of Geophysical Research* 102: 15987–15997.
- Cheng, H., R. L. Edwards, W. S. Broecker, G. H. Denton, X. Kong, Y. Wang, R. Zhang and X. Wang (2009). Ice age terminations. *Science* 326: 248–252.
- Cheng, H., R. L. Edwards, Y. Wang, X. Kong, Y. Ming, M. J. Kelly, X. Wang, C. D. Gallup and W. Liu (2006). A penultimate glacial monsoon record from Hulu Cave and two-phase glacial terminations. *Geology* 34: 217–220.
- Chiang, J. C. H. (2009). The tropics in paleoclimate. *Annual Review of Earth and Planetary Sciences* 37: 263–297.
- Clemens, S. C., W. L. Prell and Y. Sun (2010). Orbital-scale timing and mechanisms driving Late Pleistocene Indo-Asian summer monsoons: Reinterpreting cave speleothem $\delta^{18}\text{O}$. *Paleoceanography* 25: PA4207.
- Cosford, J., H. Qing, D. Matthey, B. Eglington and M. Zhang (2009). Climatic and local effects on stalagmite $\delta^{13}\text{C}$ values at Lianhua Cave, China. *Palaeogeography, Palaeoclimatology, Palaeoecology* 280: 235–244.
- Costa, K. M., J. M. Russell, H. Vogel and S. Bijaksana (2015). Hydrological connectivity and mixing of Lake Towuti, Indonesia in response to paleoclimatic changes over the last 60,000 years. *Palaeogeography, Palaeoclimatology, Palaeoecology* 417: 467–475.
- Dai, A. and T. M. L. Wigley (2000). Global patterns of ENSO-induced precipitation. *Geophysical Research Letters* 27: 1283–1286.
- Dällenbach, A., T. Blunier, J. Flückiger, B. Stauffer, J. Chappellaz and D. Raynaud (2000). Changes in the atmospheric CH₄ gradient between Greenland and Antarctica during the Last Glacial and the transition to the Holocene. *Geophysical Research Letters* 27: 1005–1008.
- De Deckker, P., N. J. Tapper and S. van der Kaars (2002). The status of the Indo-Pacific Warm Pool and adjacent land at the Last Glacial Maximum. *Global and Planetary Change* 35: 25–35.

- Denniston, R. F., Y. Asmerom, M. Lachniet, V. J. Polyak, P. Hope, N. An, K. Rodzinyak and W. F. Humphreys (2013a). A Last Glacial Maximum through middle Holocene stalagmite record of coastal Western Australia climate. *Quaternary Science Reviews* 77: 101–112.
- Denniston, R. F., K.-H. Wyrwoll, Y. Asmerom, V. J. Polyak, W. F. Humphreys, J. Cugley, D. Woods, Z. LaPointe, J. Peota and E. Greaves (2013b). North Atlantic forcing of millennial-scale Indo-Australian monsoon dynamics during the Last Glacial period. *Quaternary Science Reviews* 72: 159–168.
- Denniston, R. F., K.-H. Wyrwoll, V. J. Polyak, J. R. Brown, Y. Asmerom, A. D. Wanamaker Jr, Z. LaPointe, R. Ellerbroek, M. Barthelmes, D. Cleary, J. Cugley, D. Woods and W. F. Humphreys (2013c). A stalagmite record of Holocene Indonesia-Australian summer monsoon variability from the Australian tropics. *Quaternary Science Reviews* 78: 155–168.
- DiNezio, P. N. and J. E. Tierney (2013). The effect of sea level on glacial Indo-Pacific climate. *Nature Geoscience* 6: 485–491.
- Duan, F., D. Liu, H. Cheng, X. Wang, Y. Wang, X. Kong and S. Chen (2014). A high-resolution monsoon record of millennial-scale oscillations during Late MIS 3 from Wulu Cave, south-west China. *Journal of Quaternary Science* 29: 83–90.
- Dykoski, C. A., R. L. Edwards, H. Cheng, D. Yuan, Y. Cai, M. Zhang, Y. Lin, J. Qing, Z. An and J. Revenaugh (2005). A high-resolution, absolute-dated Holocene and deglacial Asian monsoon record from Dongge Cave, China. *Earth and Planetary Science Letters* 233: 71–86.
- EPICA (2006). One-to-one coupling of glacial climate variability in Greenland and Antarctica. *Nature* 444: 195–198.
- Fischer, H., M. Behrens, M. Bock, U. Richter, J. Schmitt, L. Loulergue, J. Chappellaz, R. Spahni, T. Blunier, M. Leuenberger and T. F. Stocker (2008). Changing boreal methane sources and constant biomass burning during the last termination. *Nature* 452: 864–867.
- Griffiths, M. L., R. N. Drysdale, M. K. Gagan, J. C. Hellstrom, I. Couchoud, L. K. Ayliffe, H. B. Vonhof and W. S. Hantoro (2013). Australasian monsoon response to Dansgaard-Oeschger event 21 and teleconnections to higher latitudes *Earth and Planetary Science Letters* 369–370: 294–304.

- Griffiths, M. L., R. N. Drysdale, M. K. Gagan, J.-x. Zhao, L. K. Ayliffe, J. C. Hellstrom, W. S. Hantoro, S. Frisia, Y. Feng, I. Cartwright, E. St Pierre, M. J. Fischer and B. W. Suwargadi (2009). Increasing Australian-Indonesian monsoon rainfall linked to early Holocene sea-level rise. *Nature Geoscience* 2: 636–639.
- Guo, Z., X. Zhou and H. Wu (2012). Glacial-interglacial water cycle, global monsoon and atmospheric methane changes. *Climate Dynamics* 39: 1073–1092.
- Hays, J. D., J. Imbrie and N. J. Shackleton (1976). Variations in the Earth's orbit: Pacemaker of the ice ages. *Science* 194: 1121–1132.
- He, F., J. D. Shakun, P. U. Clark, A. E. Carlson, Z. Liu, B. L. Otto-Bliesner and J. E. Kutzbach (2013). Northern Hemisphere forcing of Southern Hemisphere climate during the last deglaciation. *Nature* 494: 81–85.
- Heinrich, H. (1988). Origin and consequences of cyclic ice rafting in the Northeast Atlantic Ocean during the past 130,000 years. *Quaternary Research* 29: 142–152.
- Hemming, S. R. (2004). Heinrich events: massive Late Pleistocene detritus layers of the North Atlantic and their global climate imprint. *Reviews of Geophysics* 42: RG1005.
- Hope, G. (2001). Environmental change in the Late Pleistocene and later Holocene at Wanda site, Soroako, South Sulawesi, Indonesia. *Palaeogeography, Palaeoclimatology, Palaeoecology* 171: 129–145.
- Hou, J. Z., M. Tan, H. Cheng and T. S. Liu (2003). Stable isotope records of plant cover change and monsoon variation in the past 2200 years: evidence from laminated stalagmites in Beijing, China. *Boreas* 32: 304–313.
- IRI/LDEO. from <http://iridl.ldeo.columbia.edu/SOURCES/.NOAA/.NCDC/.GCPS/.MONTHLY/.STATION/IWMO+9718000+VALUE/>.
- Janowiak, J. E. and P. Xie (1999). CAMS-OPI: A global satellite-rain gauge merged product for real-time precipitation monitoring applications. *Journal of Climate* 12: 3335–3342.
- Jiang, H., M. F. Knudsen, M.-S. Seidenkrantz, M. Zhao, L. Sha and L. Ran (2013). Diatom-based reconstruction of summer sea-surface salinity in the South China Sea over the last 15 000 years. *Boreas* 43: 208–219.

- Johnson, K. R., B. L. Ingram, W. D. Sharp and P. Zhang (2006). East Asian summer monsoon variability during Marine Isotope Stage 5 based on speleothem $\delta^{18}\text{O}$ records from Wanxiang Cave, central China. *Palaeogeography, Palaeoclimatology, Palaeoecology* 236: 5–19.
- Jouzel, J., F. Vimeux, N. Caillon, G. Delaygue, G. Hoffmann, V. Masson-Delmotte and F. Parrenin (2003). Magnitude of isotope/temperature scaling for interpretation of central Antarctic ice cores. *Journal of Geophysical Research* 108: 4361.
- Kanner, L. C., S. J. Burns, H. Cheng and R. L. Edwards (2012). High-latitude forcing of the South American Summer Monsoon during the last glacial. *Science* 335: 570–573.
- Kaplan, A., M. A. Cane, Y. Kushnir, A. C. Clement, M. B. Blumenthal and B. Rajagopalan (1998). Analysis of global sea surface temperature 1856–1991. *Journal of Geophysical Research* 103: 567–589.
- Kaplan, J. O., G. Folberth and D. A. Hauglustaine (2006). Role of methane and biogenic volatile organic compound sources in late glacial and Holocene fluctuations of atmospheric methane concentrations. *Global Biogeochemical Cycles* 20: GB2016.
- Kelly, M. J., R. L. Edwards, H. Cheng, D.-X. Yuan, Y. Cai, M. Zhang, Y. Lin and Z. An (2006). High resolution characterization of the Asian Monsoon between 146,000 and 99,000 years B.P. from Dongge Cave, China and global correlation of events surrounding Termination II. *Palaeogeography, Palaeoclimatology, Palaeoecology* 236: 20–38.
- Kienast, M., T. J. J. Hanebuth, C. Pelejero and S. Steinke (2003). Synchronicity of meltwater pulse 1a and the Bølling warming: New evidence from the South China Sea. *Geology* 31: 67–70.
- Kuhnt, W., A. Holbourn, J. Xu, B. Opdyke, P. De Deckker, U. Röhl and M. Mudelsee (2015). Southern Hemisphere control on Australian monsoon variability during the late deglaciation and Holocene. *Nature Communications* 6: 5916.
- Kuo, T.-S., Z.-Q. Liu, H.-C. Li, N.-J. Wan, C.-C. Shen and T.-L. Ku (2011). Climate and environmental changes during the past millennium in central western Guizhou, China as recorded by Stalagmite ZJD-21. *Journal of Asian Earth Sciences* 40: 1111–1120.

- LeGrande, A. N. and G. A. Schmidt (2009). Sources of Holocene variability of oxygen isotopes in paleoclimate archives. *Climate of the Past* 5: 441–455.
- LeGrande, A. N. and G. A. Schmidt (2011). Water isotopologues as a quantitative paleosalinity proxy. *Paleoceanography* 26: PA3225.
- Lewis, S. C., M. K. Gagan, L. K. Ayliffe, J.-x. Zhao, W. S. Hantoro, P. C. Treble, J. C. Hellstrom, A. N. LeGrande, M. Kelley, G. A. Schmidt and B. W. Suwargadi (2011). High-resolution stalagmite reconstructions of Australian-Indonesian monsoon rainfall variability during Heinrich stadial 3 and Greenland interstadial 4. *Earth and Planetary Science Letters* 303: 133–142.
- Lewis, S. C., A. N. LeGrande, M. Kelley and G. A. Schmidt (2010). Water vapour source impacts on oxygen isotope variability in tropical precipitation during Heinrich events. *Climate of the Past* 6: 325–343.
- Li, H.-C., Z.-H. Lee, N.-J. Wan, C.-C. Shen, T.-Y. Li, D.-X. Yuan and Y.-H. Chen (2011). The $\delta^{18}\text{O}$ and $\delta^{13}\text{C}$ records in an aragonite stalagmite from Furong Cave, Chongqing, China: A-2000-year record of monsoonal climate. *Journal of Asian Earth Sciences* 40: 1121–1130.
- Liu, Z., Z. Lu, X. Wen, B. L. Otto-Bliesner, A. Timmermann and K. M. Cobb (2014). Evolution and forcing mechanisms of El Niño over the past 21,000 years. *Nature* 515: 550 - 553.
- Lu, H., S. Yi, Z. Liu, J. A. Mason, D. Jiang, J. Cheng, T. Stevens, Z. Xu, E. Zhang, L. Jin, Z. Zhang, Z. Guo, Y. Wang and B. Otto-Bliesner (2013). Variation of East Asian monsoon precipitation during the past 21 k.y. and potential CO_2 forcing. *Geology* 41: 1023–1026.
- Meckler, A. N., M. O. Clarkson, K. M. Cobb, H. Sodemann and J. F. Adkins (2012). Interglacial hydroclimate in the tropical west Pacific through the late Pleistocene. *Science* 336: 1301–1304.
- Meissner, K. J. (2007). Younger Dryas: A data to model comparison to constrain the strength of the overturning circulation. *Geophysical Research Letters* 34: L21705.
- Mohtadi, M., D. W. Oppo, S. Steinke, J.-B. W. Stuut, R. De Pol-Holz, D. Hebbeln and A. Lückge (2011). Glacial to Holocene swings of the Australian-Indonesian monsoon. *Nature Geoscience* 4: 540–544.

- Muller, J., M. Kylander, R. A. J. Wüst, D. Weiss, A. Martinez-Cortizas, A. N. LeGrande, T. Jennerjahn, H. Behling, W. T. Anderson and G. Jacobson (2008). Possible evidence for wet Heinrich phases in tropical NE Australia: the Lynch's Crater deposit. *Quaternary Science Reviews* 27: 468–475.
- Muller, J., J. F. McManus, D. W. Oppo and R. Francois (2012). Strengthening of the Northeast Monsoon over the Flores Sea, Indonesia, at the time of Heinrich event 1. *Geology* 40: 635–638.
- NGRIP (2004). High-resolution record of Northern Hemisphere climate extending into the last interglacial period. *Nature* 431: 147–151.
- Oppo, D. W., G. A. Schmidt and A. N. LeGrande (2007). Seawater isotope constraints on tropical hydrology during the Holocene. *Geophysical Research Letters* 34: L13701.
- Otto-Bliesner, B. L., E. C. Brady, S.-I. Shin, Z. Liu and C. Shields (2003). Modeling El Niño and its tropical teleconnections during the last glacial-interglacial cycle. *Geophysical Research Letters* 30: 2198.
- Partin, J. W., K. M. Cobb, J. F. Adkins, B. Clark and D. P. Fernandez (2007). Millennial-scale trends in west Pacific warm pool hydrology since the Last Glacial Maximum. *Nature* 449: 452–455.
- Pausata, F. S. R., D. S. Battisti, K. H. Nisancioglu and C. M. Bitz (2011). Chinese stalagmite $\delta^{18}\text{O}$ controlled by changes in the Indian monsoon during a simulated Heinrich event. *Nature Geoscience* 4: 474–480.
- Phipps, S. J., H. V. McGregor, J. Gergis, A. J. E. Gallant, R. Neukom, S. Stevenson, D. Ackerley, J. R. Brown, M. J. Fischer and T. D. van Ommen (2013). Paleoclimate data-model comparison and the role of climate forcings over the past 1500 years. *Journal of Climate* 26: 6915–6936.
- Rasmusson, E. M. and T. H. Carpenter (1982). Variations in tropical sea surface temperature and surface wind fields associated with the Southern Oscillation/El Niño. *Monthly Weather Review* 110: 354–384.
- Rennó, N. O. and A. P. Ingersoll (1996). Natural convection as a heat engine: a theory for CAPE. *Journal of the Atmospheric Sciences* 53: 572–585.
- Resosudarmo, B. P. and N. I. L. Subiman (2003). The management of biodiversity in Indonesia at sustainable level. *The Indonesian Quarterly* XXXI: 73–87.

- Rhodes, R., H., E. J. Brook, J. C. H. Chiang, T. Blunier, O. Maselli, J., J. R. McConnell, D. Romanini and J. P. Severinghaus (2015). Enhanced tropical methane production in response to iceberg discharge in the North Atlantic. *Science* 348: 1016–1019.
- Rohling, E. J., R. Marsh, N. C. Wells, M. Siddall and N. R. Edwards (2004). Similar meltwater contributions to glacial sea level changes from Antarctic and northern ice sheets. *Nature* 430: 1016–1021.
- Russell, J. M., H. Vogel, B. L. Konecky, S. Bijaksana, Y. Huang, M. Melles, N. Wattrus, K. Costa and J. W. King (2014). Glacial forcing of central Indonesian hydroclimate since 60,000 y B.P. *Proceedings of the National Academy of Sciences* 111: 5100.
- Schneider, T., T. Bischoff and G. H. Haug (2014). Migrations and dynamics of the intertropical convergence zone. *Nature* 513: 45–53.
- Shakun, J. D., S. J. Burns, D. Fleitmann, J. Kramers, A. Matter and A. Al-Subary (2007). A high-resolution, absolute-dated deglacial speleothem record of Indian Ocean climate from Socotra Island, Yemen. *Earth and Planetary Science Letters* 259: 442–456.
- Shi, Z., X. Liu and X. Cheng (2012). Anti-phased response of northern and southern East Asian summer precipitation to ENSO modulation of orbital forcing. *Quaternary Science Reviews* 40: 30–38.
- Shiau, L.-J., M.-T. Chen, C.-A. Huh, M. Yamamoto and Y. Yokoyama (2012). Insolation and cross-hemispheric controls on Australian monsoon variability over the past 180 ka: new evidence from offshore southeastern Papua New Guinea. *Journal of Quaternary Science* 27: 911–920.
- Spooner, M. I., T. T. Barrows, P. De Deckker and M. Paterne (2005). Palaeoceanography of the Banda Sea, and Late Pleistocene initiation of the northwest monsoon. *Global and Planetary Change* 49: 28–46.
- Sun, X., X. Li, Y. Luo and X. Chen (2000). The vegetation and climate at the last deglaciation on the emerged continental shelf of the South China Sea. *Palaeogeography, Palaeoclimatology, Palaeoecology* 160: 301–316.
- Sun, Y., S. C. Clemens, C. Morrill, X. Lin, X. Wang and Z. An (2012). Influence of Atlantic meridional overturning circulation on the East Asian winter monsoon. *Nature Geoscience* 5: 46–49.

- Tierney, J. E., S. C. Lewis, B. I. Cook, A. N. LeGrande and G. A. Schmidt (2011). Model, proxy and isotopic perspectives on the East African Humid Period. *Earth and Planetary Science Letters* 307: 103–112.
- Tierney, J. E., D. W. Oppo, A. N. LeGrande, Y. Huang, Y. Rosenthal and B. K. Linsley (2012). The influence of Indian Ocean atmospheric circulation on Warm Pool hydroclimate during the Holocene epoch. *Journal of Geophysical Research* 117: D19108.
- Tindall, J. C., P. J. Valdes and L. C. Sime (2009). Stable water isotopes in HadCM3: Isotopic signature of El Niño-Southern Oscillation and the tropical amount effect. *Journal of Geophysical Research* 114: D04111.
- Uchikawa, J., B. N. Popp, J. E. Schoonmaker, A. Timmermann and S. J. Lorenz (2010). Geochemical and climate modeling evidence for Holocene aridification in Hawaii: dynamic response to a weakening equatorial cold tongue. *Quaternary Science Reviews* 29: 3057–3066.
- Valdes, P. J., D. J. Beerling and C. E. Johnson (2005). The ice age methane budget. *Geophysical Research Letters* 32: L02704.
- van der Kaars, S., P. De Deckker and F. X. Gingle (2006). A 100 000-year record of annual and seasonal rainfall and temperature for northwestern Australia based on a pollen record obtained offshore. *Journal of Quaternary Science* 21: 879–889.
- van der Kaars, S., D. Penny, J. Tibby, J. Fluin, R. A. C. Dam and P. Suparan (2001). Late Quaternary palaeoecology, palynology and palaeolimnology of a tropical lowland swamp: Rawa Danau, West-Java, Indonesia. *Palaeogeography, Palaeoclimatology, Palaeoecology* 171: 185–212.
- van der Kaars, W. A. and M. A. C. Dam (1995). A 135,000-year record of vegetational and climatic change from the Bandung area, West-Java, Indonesia. *Palaeogeography, Palaeoclimatology, Palaeoecology* 117: 55–72.
- Visser, K., R. Thunell and M. A. Gofñi (2004). Glacial-interglacial organic carbon record from the Makassar Strait, Indonesia: implications for regional changes in continental vegetation. *Quaternary Science Reviews* 23: 17–27.
- Walker, G. T. (1923). Correlation in seasonal variations of weather VIII. A preliminary study of world weather. *Memoirs of the India Meteorological Department* 24: 75–131.

- Walker, G. T. (1924). Correlation in seasonal variations of weather, IX. A further study of world weather. *Memoirs of the India Meteorological Department* 24: 275–333.
- Wan, N.-J., W. Chung, H.-C. Li, H. Lin, T.-L. Ku, C.-C. Shen, D.-X. Yuan, M. Zhang and Y. Lin (2011a). Comparison of speleothem $\delta^{18}\text{O}$ records from eastern China with solar insolation, ice core and marine records: Similarities and discrepancies on different time scales. *Journal of Asian Earth Sciences* 40: 1151–1163.
- Wan, N.-J., H.-C. Li, Z.-Q. Liu, H.-Y. Yang, D.-X. Yuan and Y.-H. Chen (2011b). Spatial variations of monsoonal rain in eastern China: Instrumental, historic and speleothem records. *Journal of Asian Earth Sciences* 40: 1139–1150.
- Wang, X., A. S. Auler, R. L. Edwards, H. Cheng, E. Ito and M. Solheid (2006). Interhemispheric anti-phasing of rainfall during the last glacial period. *Quaternary Science Reviews* 25: 3391–3403.
- Wang, Y., H. Cheng, R. L. Edwards, Y. He, X. Kong, Z. An, J. Wu, M. J. Kelley, C. A. Dykoski and X. Li (2005). The Holocene Asian Monsoon: links to solar changes and North Atlantic climate. *Science* 308: 854–857.
- Wang, Y., H. Cheng, R. L. Edwards, X. Kong, X. Shao, S. Chen, J. Wu, X. Jiang, X. Wang and Z. An (2008). Millennial- and orbital-scale changes in the East Asian monsoon over the past 224,000 years. *Nature* 451: 1090–1093.
- Wang, Y. J., H. Cheng, R. L. Edwards, Z. S. An, J. Y. Wu, C.-C. Shen and J. A. Dorale (2001). A high-resolution absolute-dated Late Pleistocene monsoon record from Hulu Cave, China. *Science* 294: 2345–2348.
- Watkinson, I. M. (2011). Ductile flow in the metamorphic rocks of central Sulawesi. *Geological Society, London, Special Publications* 355: 157–176.
- Webster, P. J. (1994). The role of hydrological processes in ocean-atmosphere interactions. *Reviews of Geophysics* 32: 427–476.
- Webster, P. J., V. O. Magaña, T. N. Palmer, J. Shukla, R. A. Tomas, M. Yanai and T. Yasunari (1998). Monsoons: Processes, predictability, and the prospects for prediction. *Journal of Geophysical Research* 103: 14451–14510.
- Wicaksono, S. A., J. M. Russell and S. Bijaksana (2015). Compound-specific carbon isotope records of vegetation and hydrologic change in central Sulawesi, Indonesia, since 53,000 yr BP. *Palaeogeography, Palaeoclimatology, Palaeoecology* 430: 47–56.

- Wilson, M. E. J. (2000). Tectonic and volcanic influences on the development and diachronous termination of a tertiary tropical carbonate platform. *Journal of Sedimentary Research* 70: 310–324.
- Wilson, M. E. J. and D. W. J. Bosence (1996). The Tertiary evolution of South Sulawesi: a record in redeposited carbonates of the Tonasa Limestone Formation. *Tectonic Evolution of Southeast Asia*. R. Hall and D. Blundell, Geological Society Special Publication. 106: 365–389.
- Wilson, M. E. J. and S. J. Moss (1999). Cenozoic palaeogeographic evolution of Sulawesi and Borneo. *Palaeogeography, Palaeoclimatology, Palaeoecology* 145: 303–337.
- Wu, G., Y. Liu, B. He, Q. Bao, A. Duan and F.-F. Jin (2012). Thermal controls on the Asian Summer Monsoon. *Scientific Reports* 2: 404.
- Wu, L., C. Li, C. Yang and S.-P. Xie (2008). Global teleconnections in response to a shutdown of the Atlantic Meridional Overturning Circulation. *Journal of Climate* 21: 3002–3019.
- Wyrwoll, K.-H. and G. H. Miller (2001). Initiation of the Australian summer monsoon 14,000 years ago. *Quaternary International* 83-85: 119–128.
- Xie, P. and P. A. Arkin (1997). Global precipitation: a 17-year monthly analysis based on gauge observations, satellite estimates, and numerical model outputs. *Bulletin of the American Meteorological Society* 78: 2539–2558.
- Yan, X.-H., C.-R. Ho, Q. Zheng and V. Klemas (1992). Temperature and size variabilities of the Western Pacific Warm Pool. *Science* 258: 1643–1645.
- Yu, G. Q., P. B. Tian, L. Na, L. Qiong, Z. Jundi, G. Hongshan and L. Jia (2010). Pattern of abrupt climatic fluctuation in the East Asian Monsoon during the Last Glacial: Evidence from Chinese loess records. *Comptes Rendus Geoscience* 342: 189–196.
- Yuan, D., H. Cheng, R. L. Edwards, C. A. Dykoski, M. J. Kelley, M. Zhang, J. Qing, Y. Lin, Y. Wang, J. Wu, J. A. Dorale, Z. An and Y. Cai (2004). Timing, duration and transitions of the last interglacial Asian Monsoon. *Science* 304: 575–578.
- Zhang, P., H. Cheng, R. L. Edwards, F. Chen, Y. Wang, X. Yang, J. Liu, M. Tan, X. Wang, J. Liu, C. An, Z. Dai, J. Zhou, D. Zhang, J. Jia, L. Jin and K. R. Johnson (2008). A test of climate, sun and culture relationships from an 1810-year Chinese cave record. *Science* 322: 940–942.

Zhou, H., J.-x. Zhao, Y. Feng, M. K. Gagan, G. Zhou and J. Yan (2008). Distinct climate change synchronous with Heinrich event one, recorded by stable oxygen and carbon isotopic compositions in stalagmites from China. *Quaternary Research* 69: 306–315.

CHAPTER ONE

Spatio-temporal evolution of Australasian monsoon hydroclimate over the last 40,000 years^{*}

1.1. Introduction

Deep atmospheric convection over the western equatorial Pacific is critical for the redistribution of energy and moisture within Earth's climate system (e.g., Webster 1994). This convection is driven by evaporation of the warm waters of the Indo-Pacific Warm Pool (>28°C), and is vital for the global heat transport from the equator to the poles (Schneider et al. 2014). Western equatorial Pacific convection drives zonal and meridional climate modes, including the dynamic Australasian monsoon system (e.g., Chiang 2009). Latitudinal movements of the region of maximum convective rainfall over the western equatorial Pacific form part of the global Intertropical Convergence Zone (ITCZ), which acts as Earth's meteorological equator. The seasonal migration of the ITCZ, and associated seasonal reversals of the Australasian monsoon (incorporating the East Asian summer monsoon (EASM) and Indo-Australian summer monsoon

^{*} This chapter forms the basis of a manuscript currently submitted to *Nature Communications*.

(IASM)) determine the distribution and timing of rainfall throughout the tropics and subtropics of Australasia (Webster et al. 1998) (Figure 1.1). The combined effect of

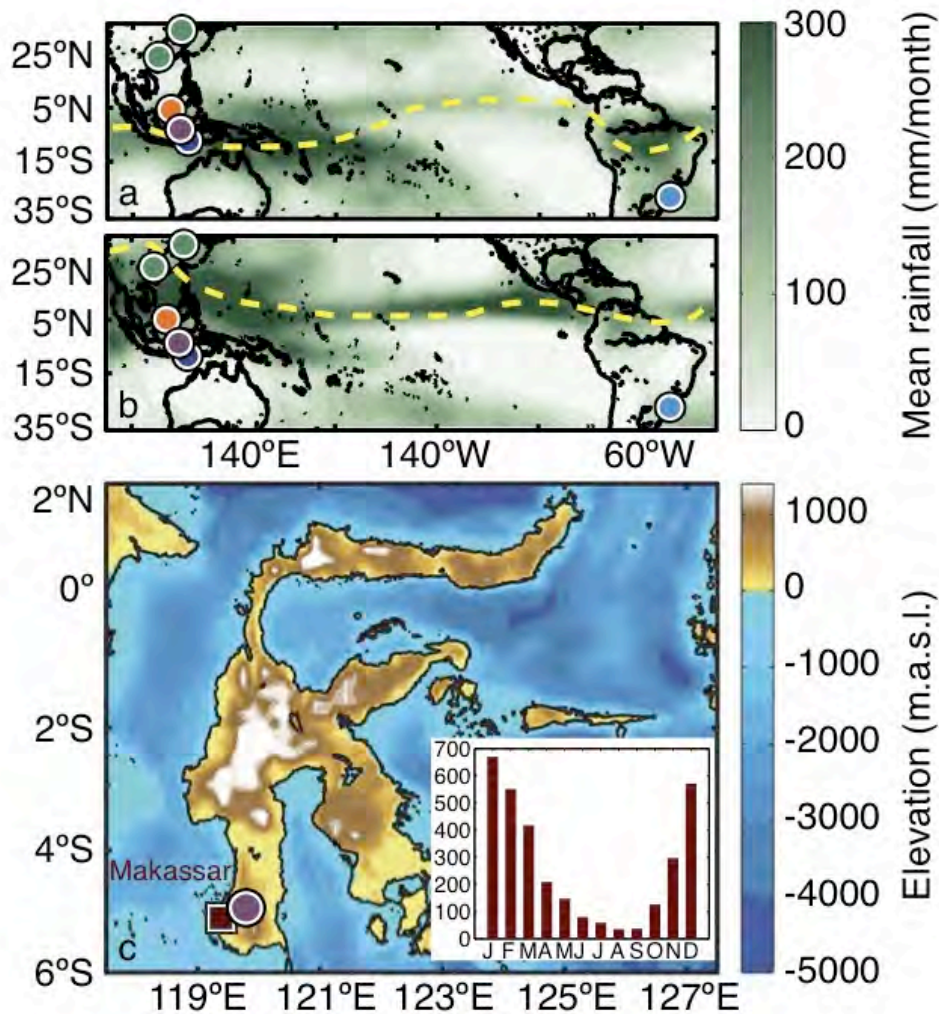


Figure 1.1: Location map showing tropical Pacific hydroclimate. Mean January (a) and July (b) rainfall for the period 1979–2014. Dashed yellow lines show the approximate location of the ITCZ. Circles in a-b indicate the locations of speleothem records for Hulu and Dongge caves, China (green) (Wang et al. 2001; Dykoski et al. 2005); Gunung Buda, Borneo (orange) (Partin et al. 2007; Carolin et al. 2013); Liang Luar Cave, Flores (dark blue) (Griffiths et al. 2009; Lewis et al. 2011; Ayliffe et al. 2013); Botuverá Cave, Brazil (light blue) (Wang et al. 2007) and Gempa Bumi Cave, Sulawesi (purple; this study). (c) Topography of Sulawesi with the locations of Gempa Bumi Cave (purple circle), the nearest major town (Makassar; maroon square), and monthly mean rainfall (mm/month) recorded at Makassar (inset).

deep atmospheric convection and the large latitudinal sweep of the ITCZ make the Australasian monsoon domain the most atmospherically dynamic region on Earth.

Speleothem records from the northern and southern regions of the Australasian monsoon document anti-phased rainfall responses to precessional forcing and millennial-scale climate events, interpreted as latitudinal shifts in the mean location of the ITCZ (Wang et al. 2001; Griffiths et al. 2009; Lewis et al. 2011; Ayliffe et al. 2013; Denniston et al. 2013) (Figure 1.2). Records from the core of the western equatorial Pacific, however, suggest that reduced rainfall coeval with Heinrich events may indicate

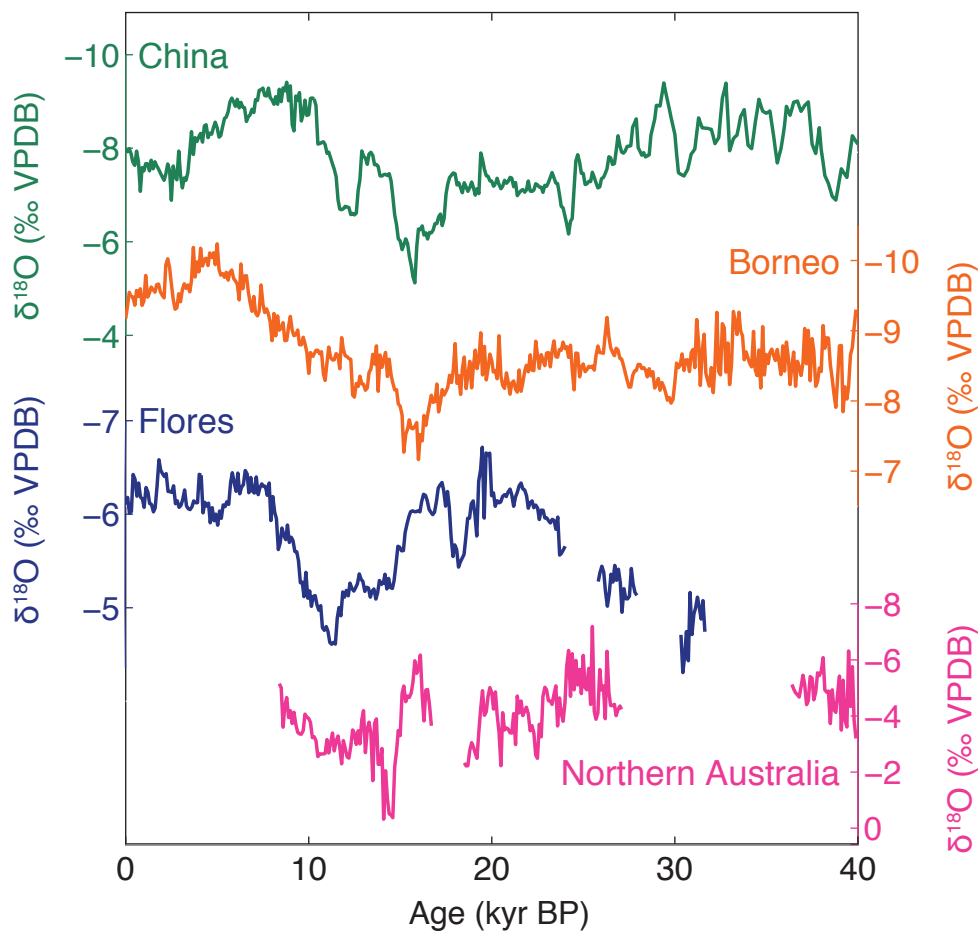


Figure 1.2: Key published speleothem $\delta^{18}\text{O}$ records for the western equatorial Pacific covering the last 40 kyr. Hulu and Dongge caves, China (green; Wang et al. 2001; Dykoski et al. 2005), Gunung Buda, Borneo (orange; Partin et al. 2007; Carolin et al. 2013), Liang Luar Cave, Flores (blue; Griffiths et al. 2009; Lewis et al. 2011; Ayliffe et al. 2013), and Ball Gown Cave, northern Australia (pink; Denniston et al. 2013).

reduced convective activity over the western equatorial Pacific (Partin et al. 2007; Carolin et al. 2013; Russell et al. 2014). Changes in the strength of deep atmospheric convection have implications for total rainfall received, whereas shifts in the ITCZ influence rainfall distribution; therefore, it is of critical importance to document the interaction of these processes in the past to fully understand the role of the Australasian monsoon in global climate.

The lack of continuous, highly resolved climate records from the IASM domain prevents the development of a regional picture of the behaviour of this monsoon system. Our understanding of the relationship between North Atlantic climate events and the western equatorial Pacific, as well as the relative behaviour of the EASM and IASM, will be explored in more detail using a well-dated climate record from Sulawesi, Indonesia. The location of Gempa Bumi Cave at 5°S, 119°E in Sulawesi allows us to study changes in IASM strength, ITCZ location and Indo-Pacific Warm Pool (IPWP) dynamics. It is well placed geographically between published speleothem records from Borneo and Flores (Figure 1.2) to further develop our understanding of the migration of the monsoon and its response to North Atlantic climate forcings.

1.2. Oxygen isotopes in speleothems

Speleothems have been used as palaeoclimate proxies since the 1960s, when they were recognised as a valuable source of palaeoclimate information (Broecker et al. 1960; Hendy and Wilson 1968; Duplessy et al. 1970; Hendy 1971). The popularity of speleothems as a palaeoclimate archive has increased greatly now they can be precisely dated using refined multi-collector inductively coupled mass spectrometer (MC-ICP-MS) ^{230}Th measurement techniques, which produce well-constrained and high quality records (Hellstrom 2003; Cheng et al. 2013a). Recently, oxygen isotope ratios ($^{18}\text{O}/^{16}\text{O}$) in speleothems from the tropics have been used to reconstruct past changes in monsoon rainfall and circulation (e.g., Partin et al. 2007; Griffiths et al. 2009; Lewis et al. 2011; Kanner et al. 2012; Ayliffe et al. 2013; Carolin et al. 2013; Cheng et al. 2013b; Denniston et al. 2013). However, the interpretation of speleothem $\delta^{18}\text{O}$ variability is not universal, and must be interpreted within the understanding of local and regional hydrology and climatology (e.g., Lachniet 2009; Fairchild and Baker 2012).

1.2.1. Environmental controls on the $\delta^{18}\text{O}$ of rainfall

Under equilibrium growth conditions, speleothem $\delta^{18}\text{O}$ is dependent on two factors: the $\delta^{18}\text{O}$ of the drip water and the carbonate-water temperature-dependent fractionation of $\delta^{18}\text{O}$ controlled by cave temperature (e.g., Hendy 1971; Lachniet 2009). Kim and O'Neil (1997) experimentally determined the temperature dependent fractionation relationship of synthetic calcite:

$$1000\ln\alpha_{(\text{calcite-water})} = 18.03(10^3\text{T}^{-1}) - 32.42$$

At $\sim 29^\circ\text{C}$, the mean annual temperature near sea level at Sulawesi, this fractionation factor would result in a $\delta^{18}\text{O}$ /temperature relationship between calcite and water of $-0.23\text{‰}/^\circ\text{C}$. Therefore, in the Indo-Pacific Warm Pool, where reconstructed sea surface temperatures for the Last Glacial Maximum (LGM) are $3\text{--}4^\circ\text{C}$ cooler than at present (Lea et al. 2000; Stott et al. 2002), the effect of the LGM-Holocene change in temperature alone would result in a ~ -0.7 to -0.9‰ shift in the $\delta^{18}\text{O}$ of speleothem calcite. However, the slope of the positive correlation between tropical rainfall $\delta^{18}\text{O}$ and mean annual temperature (e.g., Dansgaard 1964; Rozanski et al. 1993), is such that it largely counteracts the influence of changing temperature on the $\delta^{18}\text{O}$ of tropical speleothems.

The $\delta^{18}\text{O}$ of rainfall is therefore the primary determinant of speleothem $\delta^{18}\text{O}$ in the tropics. In addition to the temperature effect, the $\delta^{18}\text{O}$ of rainfall can be influenced by factors including continentality, rainfall amount, vapour source and ice volume, which result from the progressive rain-out of moisture from an air mass (Dansgaard 1964; Rozanski et al. 1993). Continentality refers to the decrease in the $\delta^{18}\text{O}$ of precipitation with distance from the ocean (Dansgaard 1964). This is caused by the Rayleigh distillation of an inland moving parcel of air, which progressively rains out the heavy isotope ^{18}O , resulting in increasingly depleted precipitation (Figure 1.3). The effect of continentality can be countered somewhat by the contribution of ^{18}O -enriched inland moisture sources such as lakes, rivers and soil moisture (Koster et al. 1993). The continentality of a site is not stationary through time, with changes in sea level resulting in an increase in the continentality of sites as continental shelves are exposed at low sea levels.

The amount effect refers to the negative correlation between $\delta^{18}\text{O}$ and precipitation amount (Dansgaard 1964; Rozanski et al. 1993). The amount effect occurs

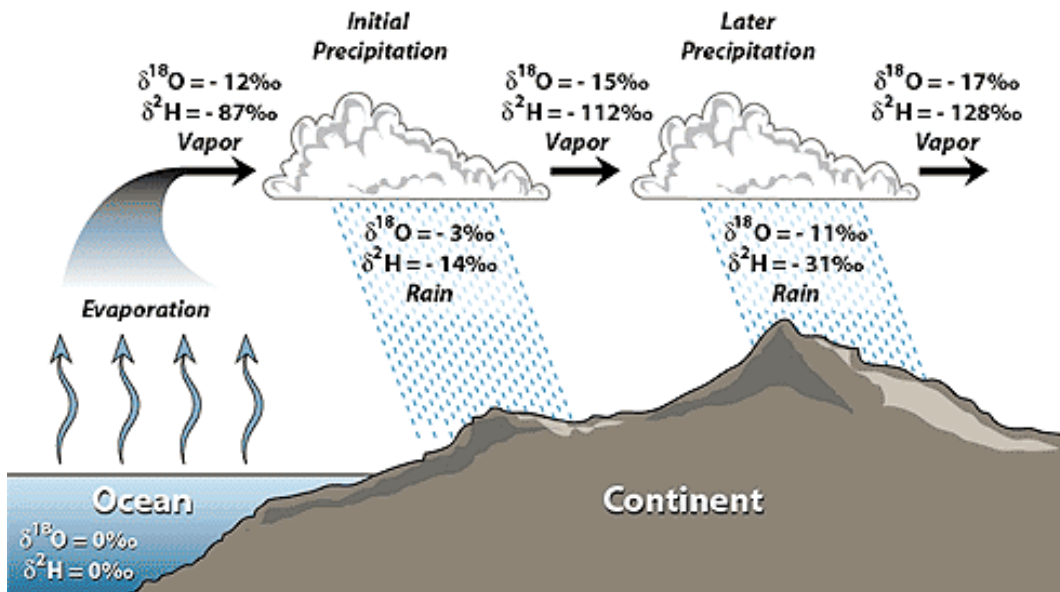


Figure 1.3: Rayleigh distillation of an air mass. The $\delta^{18}\text{O}$ of precipitation becomes more negative following the progressive rain-out of the heavier ^{18}O isotope (SAHRA 2005)

as a result of the preferential rainout of isotopically heavier water molecules from a precipitating cloud, leaving the remaining moisture relatively depleted in ^{18}O (Dansgaard 1964; Vuille et al. 2003). This process is most prevalent where deep atmospheric convection is common, as strong convective events lead to higher total precipitation, and a more pronounced amount effect (Vuille et al. 2003). The amount effect is best observed at intraseasonal or longer timescales (Risi et al. 2008), and is the dominant control on speleothem $\delta^{18}\text{O}$ values in the low latitudes (Cobb et al. 2007; Moerman et al. 2013).

The source effect refers to the observation that air masses derived from different geographical regions have a different $\delta^{18}\text{O}$ signature (Rozanski et al. 1993; Cole et al. 1999). These differences arise from the source moisture itself, as well as the transport distance to rainout (Cole et al. 1999), as well as differing $\delta^{18}\text{O}$ of seawater at different locations (LeGrande and Schmidt 2006). Source moisture in the tropics is most likely derived locally compared to source moisture in the high latitudes (Cole et al. 1999).

Over glacial-interglacial scales, changes in the volume of ice stored on land alter the $\delta^{18}\text{O}$ of seawater (Schrag et al. 1996; Waelbroeck et al. 2002; Bintanja et al. 2005). Evaporation preferentially removes oxygen ^{16}O from the ocean, leaving it relatively enriched in ^{18}O (Dansgaard 1964). At the Last Glacial Maximum, when sea level was

~130 m lower than at present, the build-up of isotopically light ice on high-latitude landmasses resulted in a ~ 1‰ ^{18}O -enrichment of the global ocean (Schrag et al. 1996). This, in turn, affects the $\delta^{18}\text{O}$ of water evaporated from the surface ocean, and the $\delta^{18}\text{O}$ of the resulting precipitation. Since the “ice volume effect” influences the average $\delta^{18}\text{O}$ of the world’s ocean, this underlying bias in rainfall $\delta^{18}\text{O}$ can be corrected for, allowing qualitative comparisons of rainfall amount between glacial and interglacial periods. The ice volume effect can be accounted for reasonably well using established relationships between eustatic sea level and the $\delta^{18}\text{O}$ of seawater over the last glacial-interglacial period (e.g., Waelbroeck et al. 2002; Bintanja et al. 2005), as has been done recently in published speleothem studies (Ayliffe et al. 2013; Carolin et al. 2013).

1.3. Materials and methods

1.3.1. Stalagmite collection and ^{230}Th dating

Stalagmite GB09-3 was collected in 2009 from Gempa Bumi cave in southwest Sulawesi (5°S, 120°E, 140 m above sea level; Figure 1.1). GB09-3 has a length of ~700 mm and an average diameter of ~50 mm (Figure 1.4). Stalagmite GB11-9 was collected in 2011 from Gempa Bumi Cave to demonstrate replication of the isotope record across its interval of overlap with the older glacial section of GB09-03. Stalagmite GB11-9 has a length of ~615 mm and an average diameter of ~80 mm (Figure 1.5). Both samples were not actively growing at the time of collection.

A key advantage of speleothems as palaeoclimate recorders is their ability to be precisely dated using uranium-thorium techniques, allowing long, continuous and high resolution speleothem records to be underpinned by well constrained chronologies (Edwards et al. 1987; Fairchild and Baker 2012). The high solubility of uranium in ground waters and the comparatively low solubility of thorium results in very large uranium/thorium ratios in newly deposited speleothems (Hellstrom 2003). Over time, ^{234}U decays into its daughter isotope ^{230}Th , with the ratio of measured $^{230}\text{Th}/^{234}\text{U}$ in speleothem calcite indicating the age of deposition of the speleothem (Edwards et al. 1987).

A total of 36 samples were analysed for uranium and thorium isotopes to develop the chronology for GB09-3 (Appendix Table A1). Six samples were analysed at

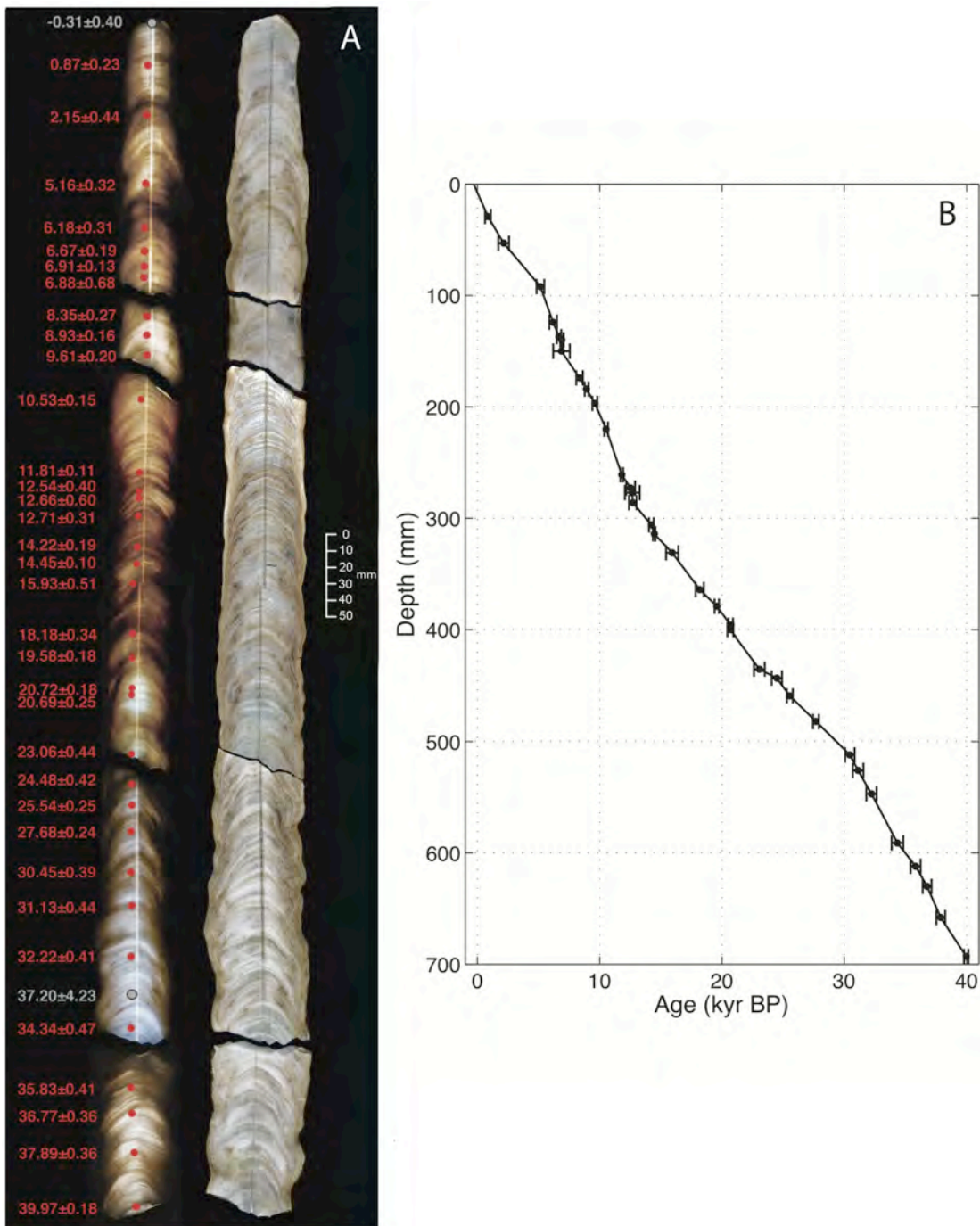


Figure 1.4: Photographs of stalagmite GB09-3 with age model. (A) Back-lit (left) and reflected light (right) photograph of stalagmite. The sampling track used for stable isotope analysis is visible down the centre of the stalagmite. Red dots show the locations of ^{230}Th dates, expressed as kyr BP (where present is defined as AD1950). Two dates shown in grey were not used in the final age model. Details of the ^{230}Th age data are given in Appendix Table A1. (B) Age-depth plot for GB09-3. All ages are in stratigraphic sequence, within error. The mean growth rate for GB09-3 is 0.9 mm per 50 years, with no determinable hiatuses.

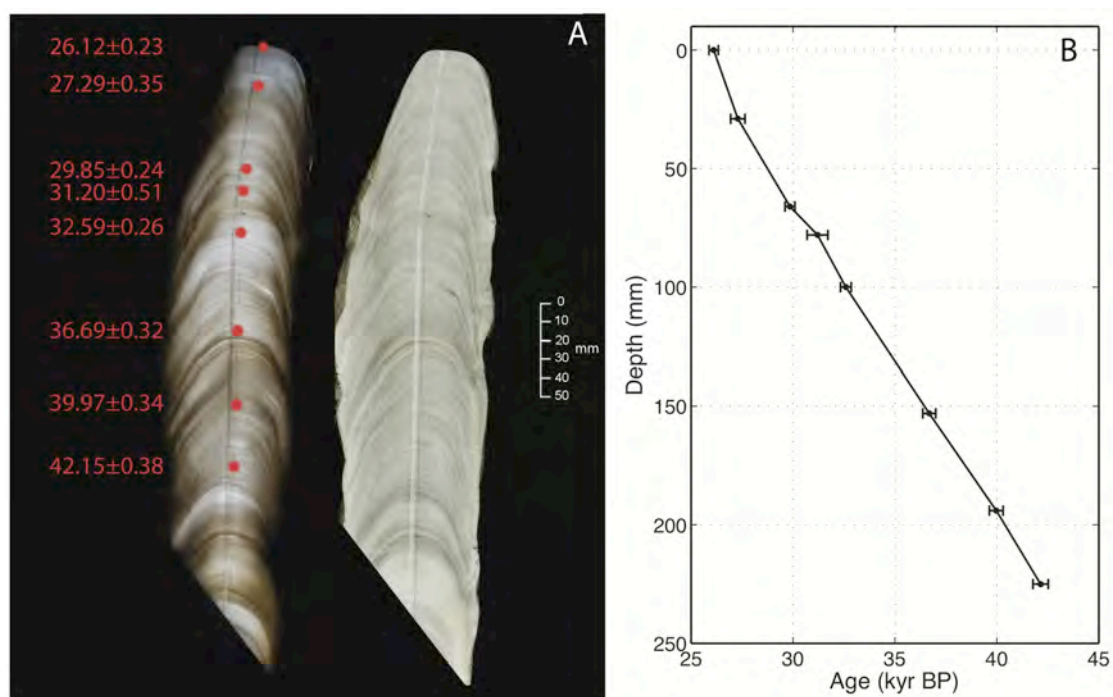


Figure 1.5: Photographs of stalagmite GB11-9 with age model. (A) Back-lit (left) and reflected light (right) photograph of stalagmite. Sampling track used for stable isotope analysis is visible down the centre of the stalagmite. Red dots show the locations of ^{230}Th dates, expressed as kyr BP (where present is defined as AD1950). Details of the U-series analysis are given in Appendix Table A1. (B) Age-depth plot for GB11-9. All ages are in stratigraphic sequence, within error. The mean growth rate for GB11-9 over the period 40–26 kyr BP is 0.7 mm per 50 years, with no determinable hiatuses. Data from the lower section of GB11-9 are not included in this study.

the University of Minnesota (by Hai Cheng and R. Lawrence Edwards), with the remaining 30 samples analysed at the University of Melbourne (by John Hellstrom). Eight ^{230}Th dates for GB11-9 were analysed at the University of Melbourne (by John Hellstrom). Dates were taken adjacent to the stable isotope sampling track, with an average sample size of 65 mg. Samples were analysed using multi-collector coupled plasma mass spectrometry (MC-ICP-MS), following the methods of Hellstrom et al. (2003).

While speleothems can be considered a closed system for the purpose of uranium-thorium dating, detrital thorium brought into the system during speleothem deposition (and not the result of radioactive decay within the speleothem), needs to be accounted for to ensure that calculated ages do not incorrectly overestimate the age of the sample (Hellstrom 2006). The ratio of $^{230}\text{Th}/^{232}\text{Th}$ acts as an indicator of the degree

of detrital contamination, as ^{232}Th is not a product of the ^{234}U decay chain, and therefore must have been deposited within the speleothem during deposition.

All samples were corrected for detrital thorium using an initial [$^{230}\text{Th}/^{232}\text{Th}$] ratio of 3.0 ± 0.75 . This value was determined using a Monte Carlo analysis on stratigraphic constraints on measured ages, (Hellstrom 2006) and represents the most likely initial thorium value for Sulawesi, based on the available ages of GB09-3. This value resulted in an average age correction of GB09-3 of 3% for ages older than 10 kyr BP, and 9% for all ages (note that the correction has the largest effect on younger dates, where the ratio of $^{230}\text{Th}/^{232}\text{Th}$ is smaller). Dating samples of GB11-9 were much cleaner, with the detrital correction only resulting in an average age correction of 0.1%.

Age models were created using the Monte Carlo technique of Hellstrom (2006), which aligns ^{230}Th dates (corrected for detrital thorium) within their errors to ensure that they are in stratigraphic order. Two ^{230}Th ages were excluded from the age model of GB09-3: GB09-3-2 and GB09-3-uD6. Both of these samples had very large relative errors due to high detrital thorium (130% and 11% respectively. N.B. GB09-3-2 was the stalagmite top date) and were inconsistent with surrounding dates. When these two ages were excluded, the remaining age model had all dates in stratigraphic sequence, with no determinable hiatuses (Figure 1.4). The mean growth rate for GB09-3 over the period 40–0 kyr BP was 0.9 mm per 50 years.

The age model for GB11-9 comprises eight ^{230}Th ages, all in stratigraphic order, within error. All eight dates were used in the final age model, which was produced using the same Monte Carlo method as for GB09-3. The mean growth rate for GB11-9 over the period 40–23 kyr BP was 0.7 mm per 50 years (Figure 1.5).

1.3.2. Stable isotope analysis and error reporting

GB09-3 was continuously sampled for stable isotope analysis at an average interval of 0.9 mm (~50 year resolution) along the central growth axis. Sampling was performed using a Sheridan GCM micromill and a 1 mm diameter mill bit. Stable isotope analysis was conducted on 755 samples (Appendix Table A1), with an average sample size of 200 μg . Measurements of $\delta^{18}\text{O}$ and $\delta^{13}\text{C}$ were made at The Australian National University using a Finnigan MAT-251 mass spectrometer coupled to an automated Kiel carbonate device. GB11-9 was slabbed about the central growth axis and micromilled

along the central axis using a 1-mm diameter drill bit at an interval of 0.7 mm, equating at an average sampling interval of ~50 years. Analysis of $\delta^{18}\text{O}$ and $\delta^{13}\text{C}$ was conducted on a total of 323 samples (Appendix Table A1).

For the isotope analysis, one NBS-19 standard was analysed for every 5–8 samples to ensure consistency among runs. Results are reported relative to Vienna Pee Dee Belemnite (VPDB) following adjustment using the in-run measurements of NBS-19 ($\delta^{18}\text{O} = -2.20\text{‰}$) and less frequent measurements of NBS-18 ($\delta^{18}\text{O} = -23.0\text{‰}$). The analytical error for measurements of NBS-19 was calculated by finding the standard deviation of NBS-19 across all runs. Using this method, the analytical error for NBS-19 $\delta^{18}\text{O}$ was 0.05‰ ($n = 187, 1\sigma$) for GB09-3, and 0.04‰ ($n = 83, 1\sigma$) for GB11-9.

The reproducibility of $\delta^{18}\text{O}$ for the stalagmite samples themselves was determined by running duplicate and triplicate measurements. Samples with a run standard deviation greater than 0.05‰ (in $\delta^{18}\text{O}$) were re-run, in order to minimise error related to analysis methods. Additionally, $\delta^{18}\text{O}$ values that deviated largely from adjacent values in the time series were duplicated to ensure that abrupt peaks and troughs in the data set reflect real changes in speleothem $\delta^{18}\text{O}$. Triplicates were run where duplicate measurements differed by more than 0.1‰ in $\delta^{18}\text{O}$. The mean standard error for duplicate/triplicate analyses of $\delta^{18}\text{O}$ was 0.05‰ ($n=126$) for GB09-3 and 0.03‰ ($n=46$) for GB11-9 (Figure 1.6).

Quantification of the sample errors for GB09-3 allows a comparison of the signal: error ratio. This relationship is important, as it clarifies whether observed variability is due to errors associated with the $\delta^{18}\text{O}$ measurements, or real $\delta^{18}\text{O}$ signal. Analysis of the standard error of the mean $\delta^{18}\text{O}$ values for individual samples suggests that small-scale variability within the $\delta^{18}\text{O}$ record is detectable (Figure 1.6A). The same technique was applied to GB11-9, which also shows good reproducibility of $\delta^{18}\text{O}$ (Figure 1.6B).

Signal replication of overlapping growth intervals in the two stalagmites provides a valuable test for calcite deposition in isotopic equilibrium because it is unlikely that different stalagmites could record similarly fractionated signals (Dorale and Liu 2009). Agreement between the $\delta^{18}\text{O}$ records from GB09-3 and GB11-9 is good, both in terms of their mean $\delta^{18}\text{O}$ values and the amplitudes of shorter-term oscillations (Figure 1.7). The average $\delta^{18}\text{O}$ values over the period of overlap (40–26 kyr BP) are -

5.88‰ for GB09-3 and -5.57‰ for GB11-9. Furthermore, the degree of $\delta^{18}\text{O}$ variability in GB09-3 (0.20‰, 1σ) is mirrored in GB11-9 (0.20‰, 1σ). This supports our interpretation that Sulawesi speleothem $\delta^{18}\text{O}$ is deposited in isotopic equilibrium.

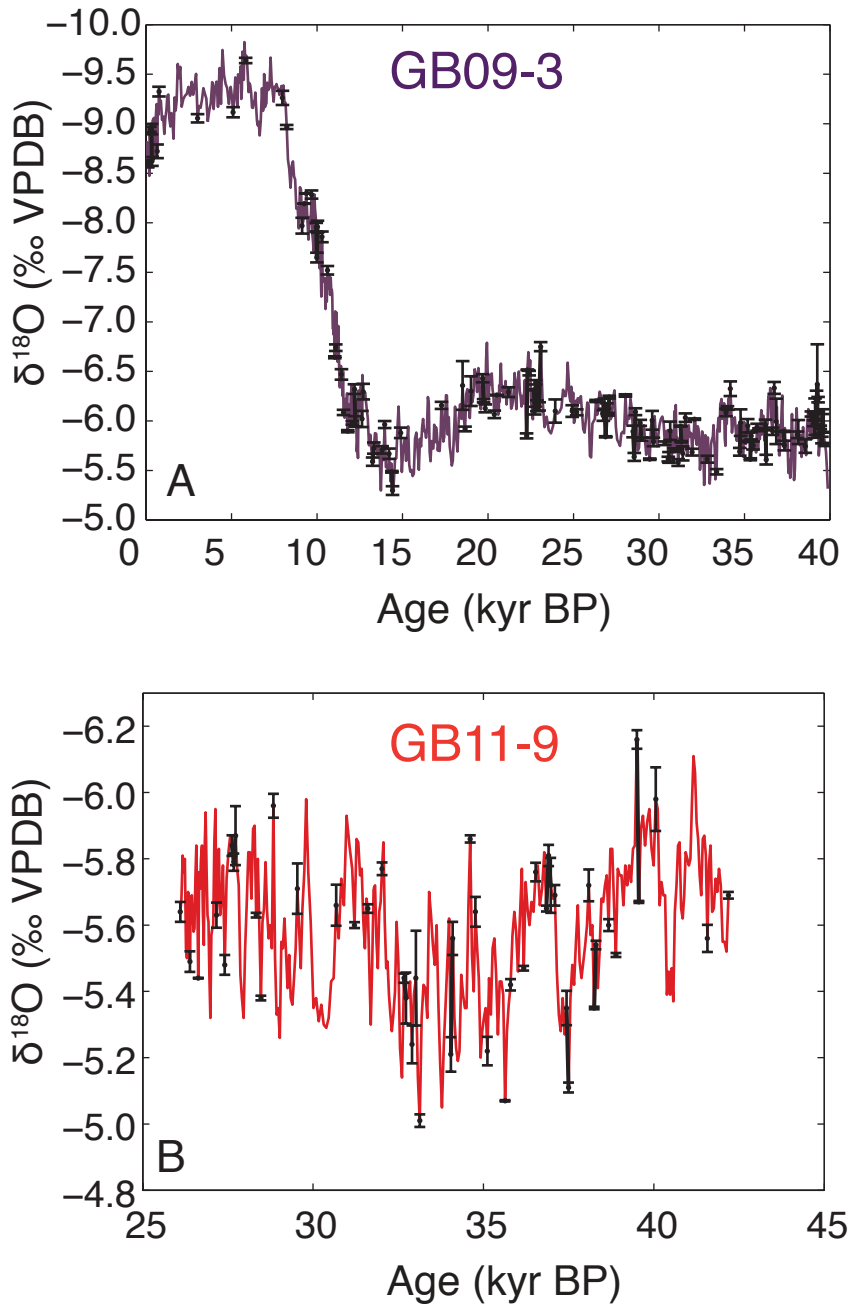


Figure 1.6: Analytical uncertainties for measurements of $\delta^{18}\text{O}$ in (a) GB09-3 and (b) GB11-9. Error bars equal to one standard error are shown for samples where duplicate or triplicate measurements were run. The analytical uncertainties for $\delta^{18}\text{O}$ are much smaller than the size of the signal being interpreted, both for long-term changes and short-term millennial features.

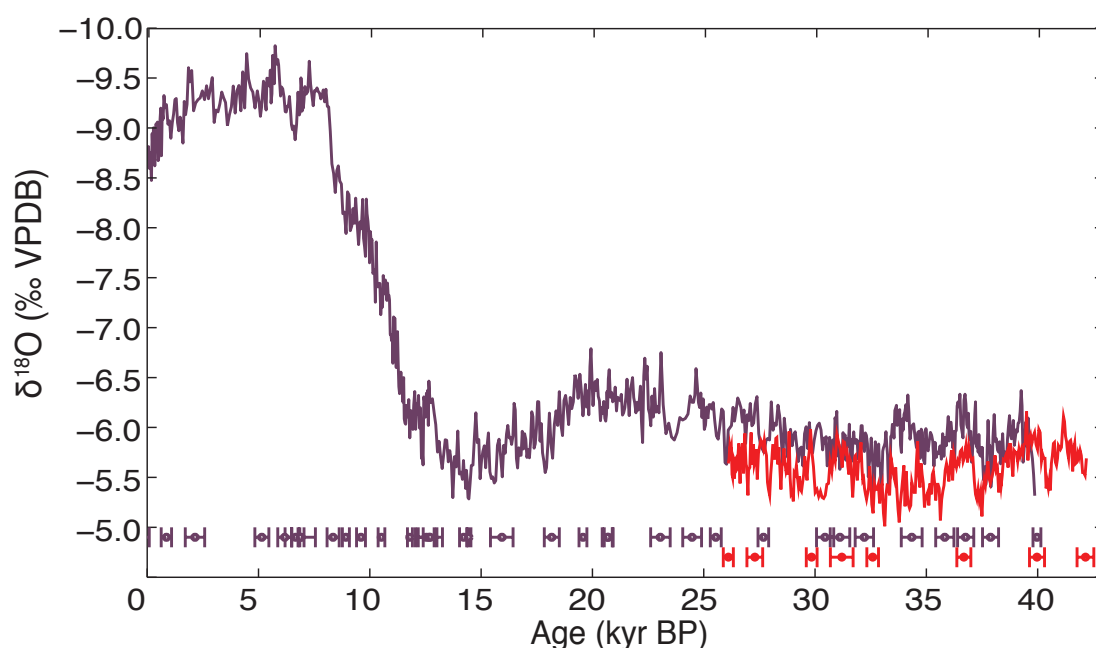


Figure 1.7: Gempa Bumi Cave $\delta^{18}\text{O}$ record for the period 40 kyr BP to present (GB09-3; purple) shown with the replicate record from the same cave (GB11-9; red).

1.4. Results and discussion

1.4.1. Interpretation of Sulawesi speleothem $\delta^{18}\text{O}$

We interpret changes in Sulawesi speleothem $\delta^{18}\text{O}$ as a proxy for relative changes in rainfall amount. In the modern tropical climatological setting of the western equatorial Pacific, the $\delta^{18}\text{O}$ of precipitation decreases as precipitation amount increases (Cobb et al. 2007; Moerman et al. 2013). This “amount effect” (Dansgaard 1964) forms the basis for past monsoon rainfall reconstructions from speleothem $\delta^{18}\text{O}$ records across the region (Partin et al. 2007; Griffiths et al. 2009; Lewis et al. 2011; Ayliffe et al. 2013; Carolin et al. 2013). Temperature effects on the fractionation of oxygen isotopes in tropical precipitation are small (Dansgaard 1964) and approximately negated by the opposing temperature-dependent fractionation of oxygen isotopes in cave calcite (Hendy and Wilson 1968).

1.4.2. Ice volume correction

Over glacial-interglacial time scales, changes in the volume of ice stored on land alter the $\delta^{18}\text{O}$ of seawater and resulting precipitation (Schrag et al. 1996; Waelbroeck et al. 2002; Bintanja et al. 2005). This means that an ice volume correction is necessary to examine relative changes in monsoon strength between the LGM and Holocene, along the lines of recent speleothem $\delta^{18}\text{O}$ studies (Ayliffe et al. 2013; Carolin et al. 2013). An ice volume correction was applied to all of the speleothem $\delta^{18}\text{O}$ records used in this study to account for the effects of changes in the $\delta^{18}\text{O}$ of seawater (Figure 1.8 and Figure 1.9).

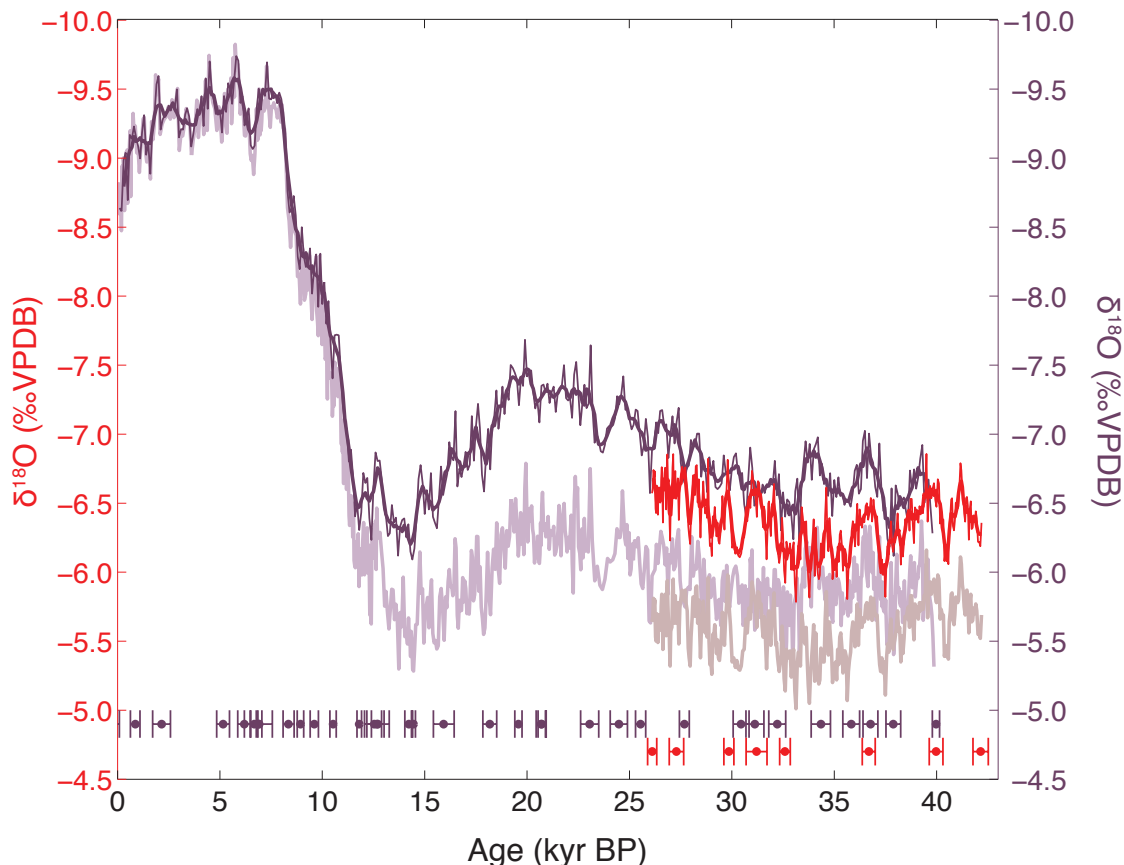


Figure 1.8: Ice volume corrected Gempa Bumi Cave $\delta^{18}\text{O}$ record for the period 40 kyr BP to present (GB09-3; purple) shown with the replicate record from the same cave (GB11-9; red). Uncorrected time series are shown in the lighter colours. Corrected data are shown with a 5-point moving average (approximately 250 years) for each record. The positions and one standard error uncertainties of ^{230}Th dates for both stalagmites are shown below the $\delta^{18}\text{O}$ profiles.

To perform the ice volume correction, the speleothem $\delta^{18}\text{O}$ time series were binned at 100-yr average resolution to ensure that the corrections were applied in the same way to all datasets. We use the record of Bintanja et al. (2005) for global seawater $\delta^{18}\text{O}$ change (relative to the present day). This global seawater $\delta^{18}\text{O}$ record is routinely used to correct for the effects of ice volume changes on ice core temperature reconstructions (Jouzel et al. 2003; Stenni et al. 2010). We use a simple subtraction of the global ocean $\delta^{18}\text{O}$ change to correct the speleothem records for ice volume effects (Ayliffe et al. 2013; Carolin et al. 2013), because of the expected retention of ocean $\delta^{18}\text{O}$ changes in tropical rainfall (Jouzel et al. 2003).

1.4.3. Australasian monsoon speleothem synthesis

In this study, we use speleothem records from China (Dongge and Hulu caves) (Wang et al. 2001; Dykoski et al. 2005), Borneo (Partin et al. 2007; Carolin et al. 2013), Sulawesi (this study) and Flores (Griffiths et al. 2009; Lewis et al. 2011; Ayliffe et al. 2013) to examine the spatial and temporal evolution of changes in monsoon rainfall across the Australasian monsoon domain (Figure 1.9). The narrow monsoon belt of northern Australia is likely to be very sensitive to exposure of the adjacent continental shelf during glacial times, affecting the monsoon signal recorded in this region. With this in mind, and in lieu of a continuous 40-kyr speleothem record for northern Australia, we use a speleothem record for South America as a southern anchor point for the monsoon system. This is consistent with other studies that have made north-south monsoon comparisons using records from China and South America (Wang 2009; Cheng et al. 2012).

1.4.4. Palaeomonsoon map

To qualitatively visualise broad-scale changes in Australasian monsoon hydroclimate over the last 40 kyr, we combine filtered speleothem $\delta^{18}\text{O}$ records across a latitudinal transect (Figure 1.1 and Figure 1.9) to construct a palaeomonsoon map (Figure 1.10). To isolate the precession-forced component of $\delta^{18}\text{O}$ variability across the Australasian speleothem transect, a 25-kyr low-pass Butterworth filter was applied to each record to

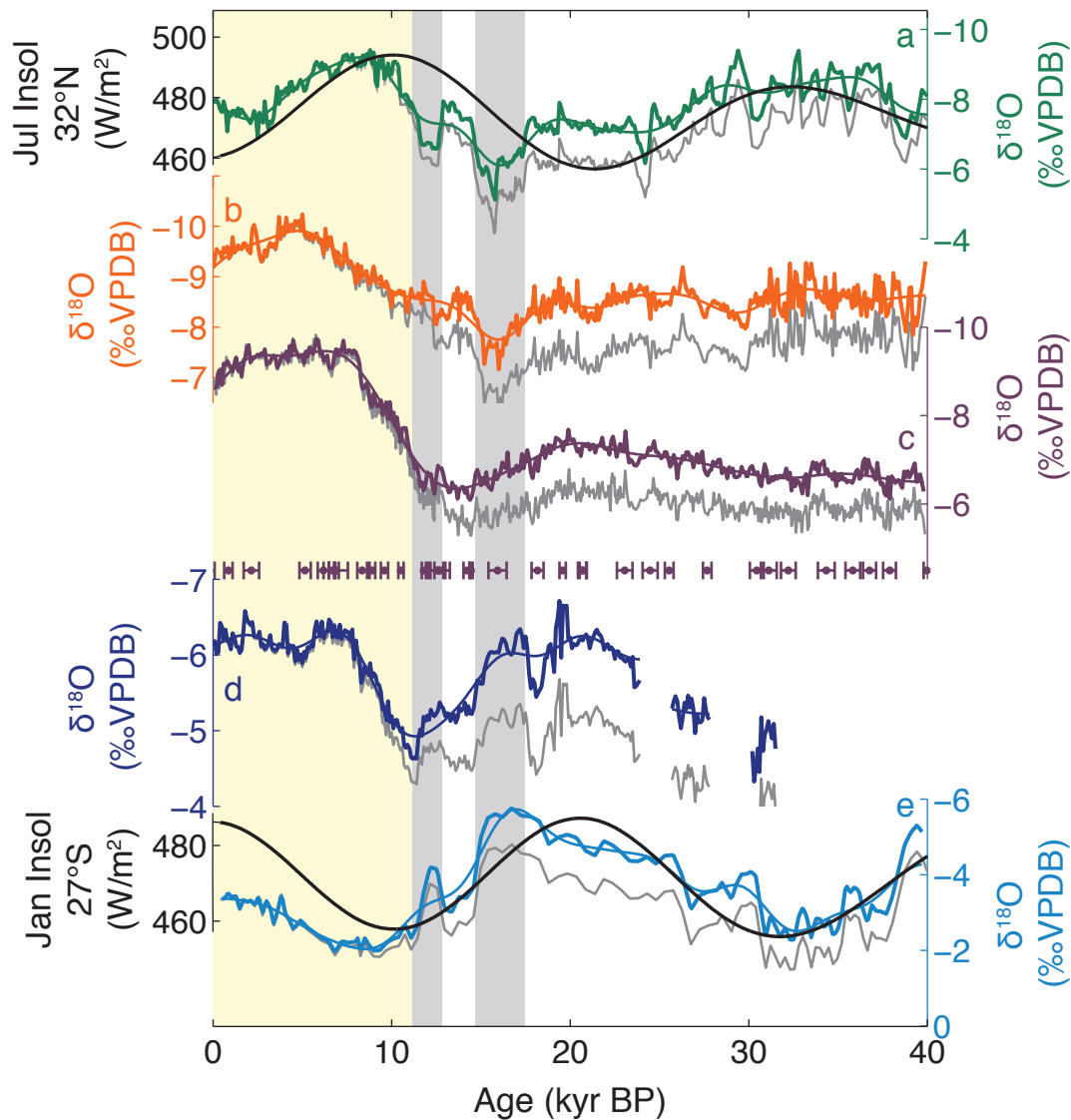


Figure 1.9: Speleothem $\delta^{18}\text{O}$ records. (a) Hulu and Dongge caves, China (Wang et al. 2001; Dykoski et al. 2005) and July insolation at 32°N ; (b) Gunung Buda National Park, Borneo (Partin et al. 2007; Carolin et al. 2013); (c) Sulawesi (this study); (d) Liang Luar Cave, Flores (Griffiths et al. 2009; Lewis et al. 2011; Ayliffe et al. 2013); (e) Botuverá Cave, Brazil (Wang et al. 2007) and January insolation at 27°S . All $\delta^{18}\text{O}$ records have been corrected for ice-volume effects, with uncorrected data shown in grey. Thin coloured lines show the 25-kyr low-pass filtered records used in Fig. 3a. The ^{230}Th dates (with ± 2 s.e. of mean) for Sulawesi are shown in purple (d). Grey shading highlights prominent weak monsoon intervals in China (Cheng et al. 2009) related to Heinrich Stadial 1 and the Younger Dryas. Yellow shading denotes the strong atmospheric convection interval in the western equatorial Pacific.

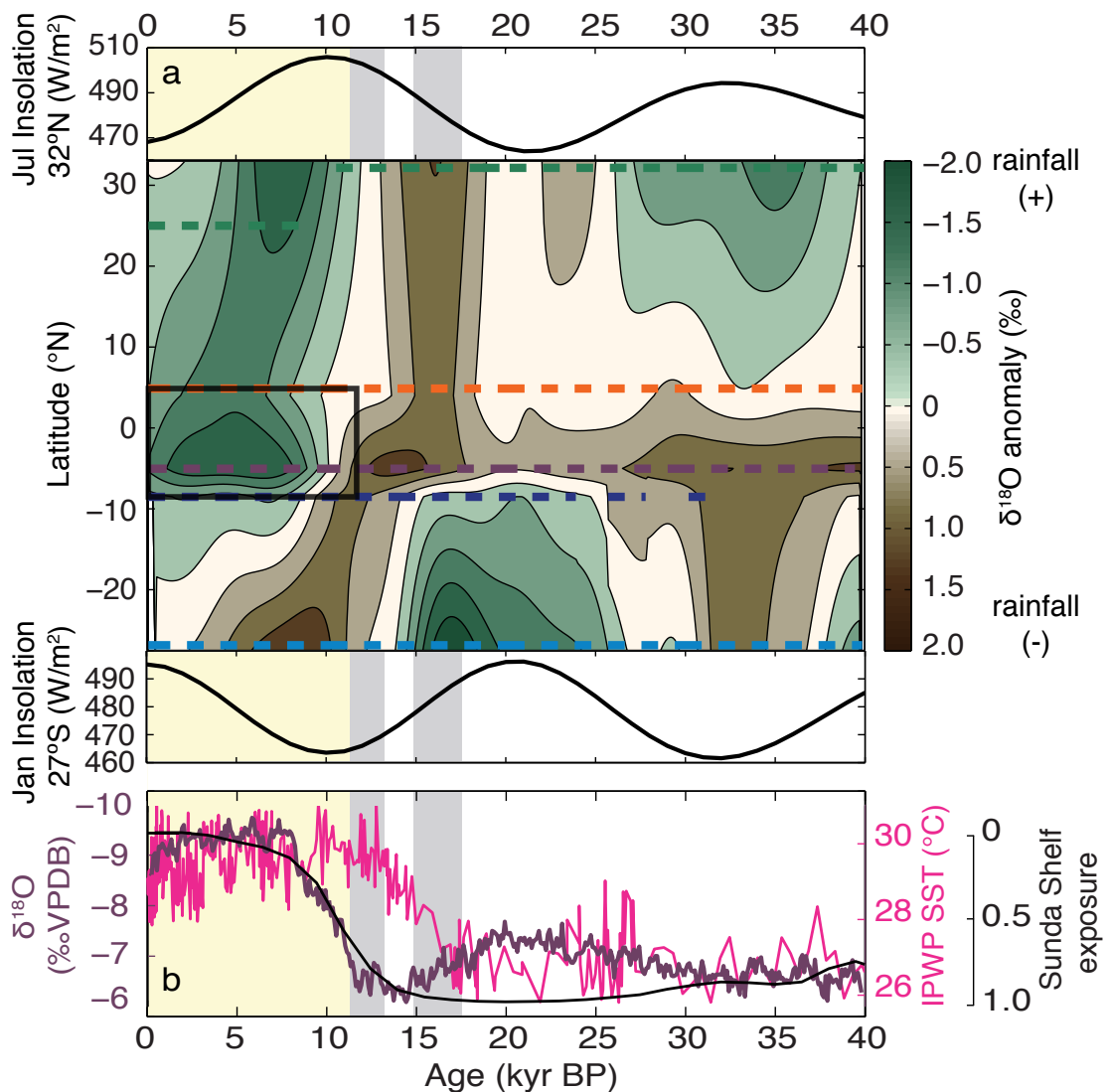


Figure 1.10: Orbital-scale palaeomonsoon changes over the last 40 kyr. (a) Qualitative palaeomonsoon spatio-temporal reconstruction with summer insolation curves for 32°N (top) and 27°S (bottom). Dashed lines indicate the latitude and timespan of speleothem $\delta^{18}\text{O}$ records used to construct the map (colours as for Figure 1.9). Black box highlights post-glacial increase in deep atmospheric convection over the western equatorial Pacific. (b) $\delta^{18}\text{O}$ record for Sulawesi shown with January insolation at 27°S (grey). SST for the Indo-Pacific Warm Pool (Stott et al. 2002) and fraction of Sunda Shelf exposed above sea level (bounded by 95°E-120°E and 10°S-10°N) (Carolin et al. 2013). Grey and yellow shading as in Figure 1.9.

remove high-frequency variability (Figure 1.9). Oxygen isotope anomalies for each filtered record were calculated by subtracting the mean isotope value for the 23–0 kyr BP interval. This timeframe includes one complete precession cycle, ensuring that the

normalisation includes both maximum and minimum local insolation values. It also represents the period of common data coverage for the records; ensuring anomalies are comparable among different records. The oxygen-isotope anomaly time-series were then plotted according to latitude and linearly interpolated to fill between the spatio-temporal transects of speleothem data (Figure 1.10).

There are a number of speleothem $\delta^{18}\text{O}$ records for South America (Wang et al. 2004; Cruz et al. 2005; Wang et al. 2006; Wang et al. 2007; Cruz et al. 2009; Kanner et al. 2012) that could be used as the southern anchor for our study. Insolation-driven signals dominate the palaeomonsoon map, therefore we excluded records where insolation does not appear to have a strong influence on the record (Kanner et al. 2012). We also exclude discontinuous records (Wang et al. 2004; Wang et al. 2006) and records that do not span the entire period from 40 kyr BP to the present (Cruz et al. 2009). Based on these criteria, two records from Botuverá Cave in Brazil meet our data requirements (Cruz et al. 2005; Wang et al. 2007). Both records broadly agree on low-frequency features, but we selected the record of Wang et al. (2007) for the analysis because it has stronger chronological control over the last 40 kyr compared to the record of Cruz et al. (2005).

1.4.4.1. Palaeomonsoon map interpretation

This new spatio-temporal perspective reveals a striking disconnect between rainfall changes in the subtropical and equatorial regions of the Australasian monsoon domain. Anti-phased rainfall anomalies that follow precessional changes in mid-latitude summer insolation dominate the broad-scale patterns of northern and southern monsoon rainfall in the subtropics over the last 40 kyr (Figure 1.10). In contrast, a dry background climate state dominates the core of the Australasian monsoon region prior to ~12 kyr BP.

Sulawesi, at 5°S, appears to lie near the centre of sustained, dry anomalies, with the low $\delta^{18}\text{O}$ values (high rainfall) of the Holocene never achieved over the dry late glacial interval (~12–40 kyr BP) in this record. Pervasive dry conditions at this time are a feature of other rainfall indicators from Sulawesi (Tierney et al. 2012; Russell et al. 2014) (Figure 1.11) and the wider western equatorial Pacific region (DiNezio and Tierney 2013; Dubois et al. 2014), and demonstrate that deep atmospheric convection over the western equatorial Pacific was suppressed during the late glacial interval.

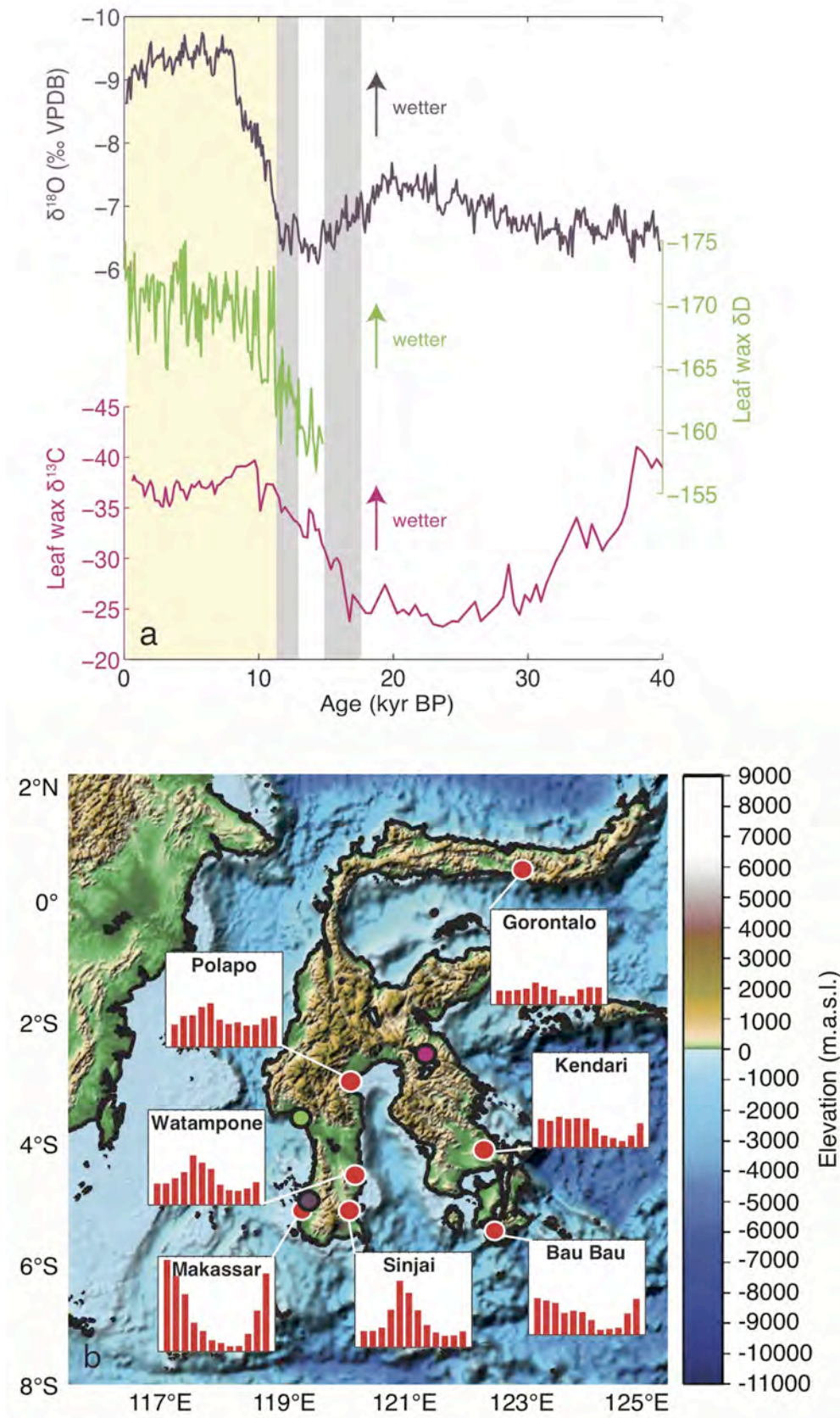


Figure 1.11

Figure 1.11: Comparison of rainfall proxy records from Sulawesi. (a) Sulawesi speleothem $\delta^{18}\text{O}$ (purple), sediment core leaf wax δD from the Makassar Strait (Tierney et al. 2012)(green), leaf wax $\delta^{13}\text{C}$ from Lake Towuti, Sulawesi (Russell et al. 2014) (pink). (b) Topographic map of Sulawesi (Amante and Eakins 2009) with modern mean monthly rainfall from station data (Baker et al. 1994) (all plotted with the same y-scale of 0–700 mm/month). Yellow dots show the locations of rainfall stations, and purple, green and pink dots show the location of records from (a). The topography of Sulawesi makes seasonal rainfall variability at some sites highly localised. It is likely that these regional differences in rainfall seasonality can account for the apparent rainfall anti-phasing between different locations across Sulawesi.

The palaeomonsoon reconstruction provides a temporal context for previous spatial examinations (DiNezio and Tierney 2013) of western equatorial Pacific hydroclimate at the Last Glacial Maximum (LGM). We find that the suppressed atmospheric convection over the western equatorial Pacific during the late glacial period ended abruptly with a step-wise increase in western equatorial Pacific rainfall into the Holocene. The rapid decrease in speleothem $\delta^{18}\text{O}$ began at ~ 12 kyr BP in Sulawesi, and is recorded to a lesser extent in speleothems from Borneo and Flores (Figure 1.9 and Figure 1.10). Importantly, the main strengthening of deep convection over the western equatorial Pacific occurred too late to be triggered entirely by rising sea surface temperatures (Stott et al. 2002), which would have increased atmospheric moisture fluxes over the region (Figure 1.10b). Instead, the two largest $\delta^{18}\text{O}$ decreases in the Sulawesi record coincide with rapid flooding of the Sahul (~ 12 – 11 kyr BP) and Sunda (~ 8.5 kyr BP) shelves (Figure 1.12). Flooding event 1 occurs from 12–11 kyr BP during the flooding of the Sahul Shelf across the Gulf of Carpentaria (De Deckker et al. 2002; Reeves et al. 2008). Flooding event 2 occurs at around 8.5 kyr BP during the flooding of the Sunda Shelf. The timing of the flooding of the Sunda Shelf has been previously placed at approximately 9.5 kyr BP (Linsley et al. 2010; Griffiths et al. 2013). However, examination of these records reveals that the transition spans ~ 1 kyr, suggesting that the 8.5 kyr BP signal in the Sulawesi speleothem record is the same event (Figure 1.12). These rapid changes in speleothem $\delta^{18}\text{O}$ likely represent a combination of the reorganisation of local water masses, changes in source moisture pathways (Linsley et al. 2010) and intensification of the Walker circulation caused by enhanced convection

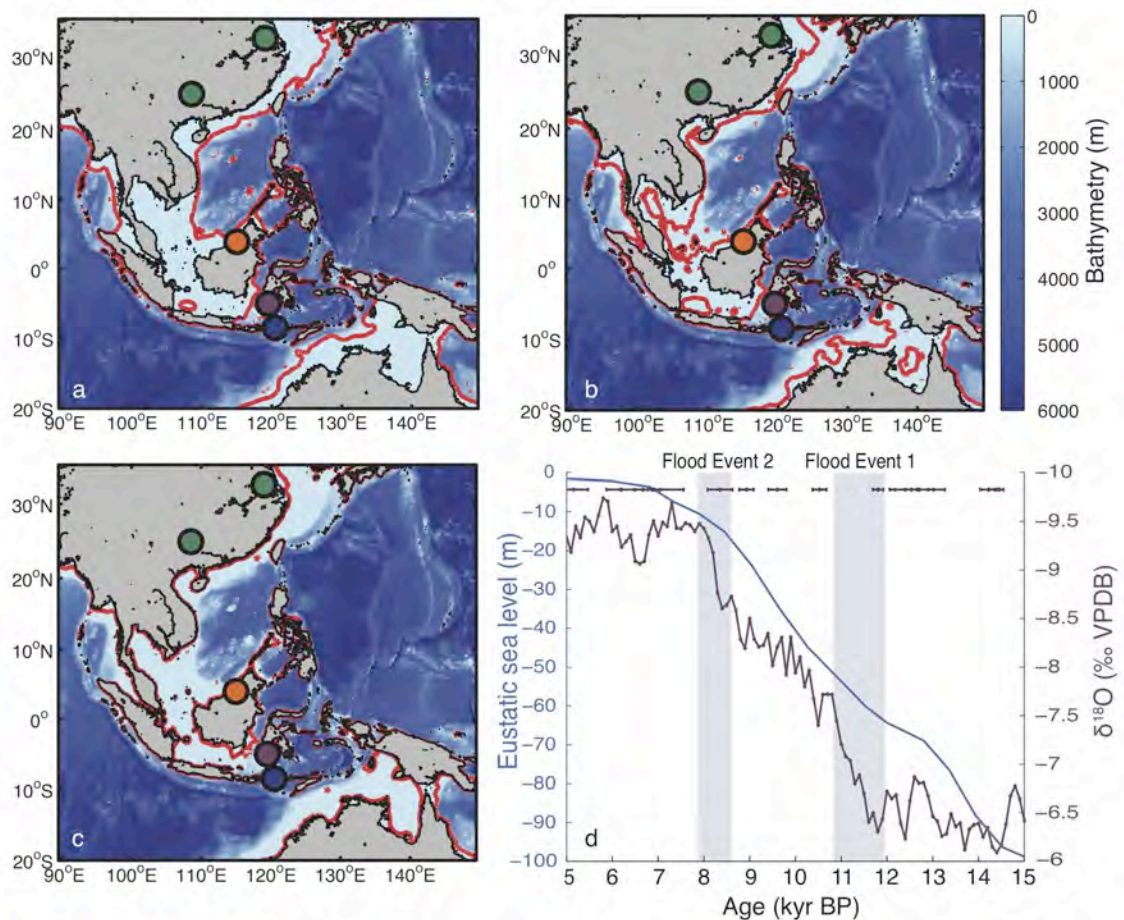


Figure 1.12: Bathymetry of the IPWP and timing of continental shelf flooding events. (a) Bathymetry of the IPWP, with the -125 m contour in red, highlighting the sea level low stand during the LGM. (b) As for (a), but with the -60 m contour highlighting the approximate depth of the Sahul Shelf flooding. (c) As for (a) but with the -15 m contour highlighting the approximate depth of the Sunda Shelf flooding. Speleothem locations marked by coloured circles (colours as for Figure 1.9). (d) Sulawesi flood events, plotted against regional eustatic sea level (Reeves et al. 2013).

over newly formed seas in the western equatorial Pacific region (Griffiths et al. 2009; Tierney et al. 2012; DiNezio and Tierney 2013).

Consistent with our observations of suppressed atmospheric convection over the western equatorial Pacific during the late glacial period, an earlier spatial assessment of Indo-Pacific hydroclimate at the LGM found that its structure was best captured by simulations of the HadCM3 model, where exposure of the Sunda Shelf displaced the ascending branch of the Pacific Walker circulation to the east of Papua New Guinea (DiNezio and Tierney 2013). The new Sulawesi record and palaeomonsoon map

support the hypothesis that pervasive late-glacial dry conditions in the western equatorial Pacific were only terminated when deep atmospheric convection strengthened in response to rising sea levels and the inundation of shallow continental shelves in the region, well after the onset of deglaciation (DiNezio and Tierney 2013; Griffiths et al. 2013).

A second prominent feature of the palaeomonsoon reconstruction is the interplay between orbital and millennial-scale climate forcing during deglaciation. The most southerly excursion of the ITCZ over the last 40 kyr occurred between ~18 and 15 kyr BP (Figure 1.10). This period corresponds with Heinrich Stadial 1 (H1), which led to a weak monsoon interval in China (Cheng et al. 2009), enhanced monsoon rainfall in Flores (Ayliffe et al. 2013) (Figure 1.9) and an extreme wet phase across northern Australia (Muller et al. 2008; Denniston et al. 2013). H1 occurred ~4 kyr after a Southern Hemisphere summer insolation maximum and during a time of near maximum Northern Hemisphere ice sheet extent. Together, these conditions cooled the Northern Hemisphere relative to the Southern Hemisphere and displaced the Australasian monsoon to an extreme southerly position. A southward shift of latitudinal climate belts during H1 has been proposed as a key mechanism in the sequence of events leading to the release of carbon dioxide from the Southern Ocean during the onset of deglaciation (Anderson et al. 2009; Denton et al. 2010). The anomalous position of the Australasian monsoon during H1 documented here supports the hypothesis that a southward shift in the mean location of the ITCZ was critical for propagating Northern Hemisphere climate changes into the Southern Hemisphere during deglaciation.

1.4.5. Millennial-scale variability

To examine high-frequency variability across the Australasian monsoon domain, we subtracted the 25-kyr low-pass filtered records from the ice volume corrected speleothem $\delta^{18}\text{O}$ records (Figure 1.13). To compare variability between speleothem and ice core records, we subtracted the 25-kyr low-pass filtered records from published ice core $\delta^{18}\text{O}$ records to produce a millennial-scale variability record for NGRIP. We examine glacial-interglacial changes in millennial-scale $\delta^{18}\text{O}$ variability by determining the standard deviation of each filtered record in the 11–0 kyr BP interval and for the interval prior to 11 kyr BP (Figure 1.13).

Strong latitudinal gradients are evident in the magnitude of millennial-scale hydroclimate variability across the Australasian monsoon domain (Figure 1.13), with

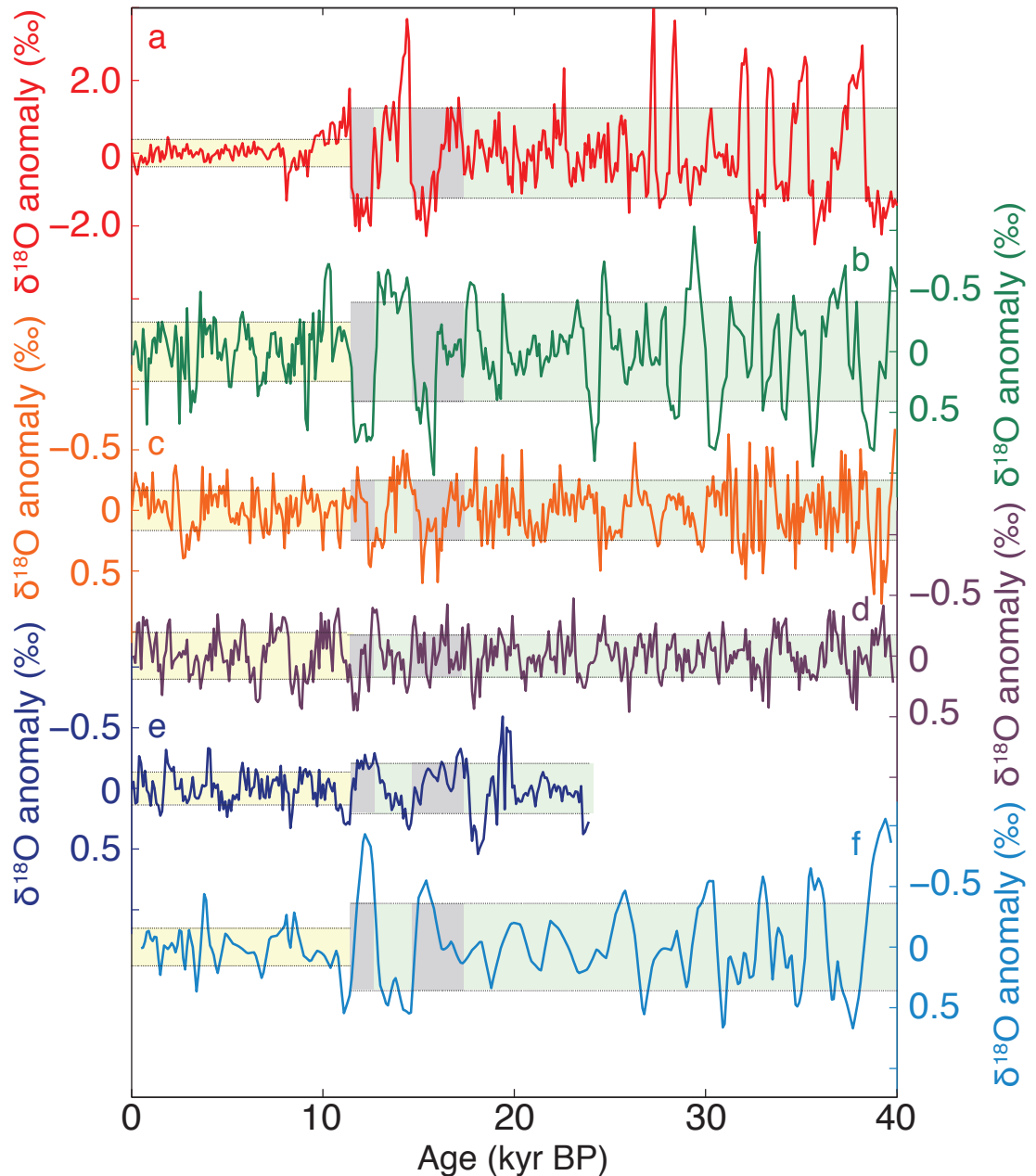


Figure 1.13: Millennial-scale palaeomonsoon variability over the last 40 kyr. (a) NGRIP ice core (NGRIP 2004), (b) China, (c) Borneo, (d) Sulawesi, (e) Flores and (f) Brazil $\delta^{18}\text{O}$ anomalies after removing 25-kyr low-pass filter. Dotted lines and shading represent the $\pm 1\sigma$ range in variability for the glacial (40–11 kyr BP; apart from (e) 24–11 kyr; green) and interglacial (11 kyr BP–present; yellow). Grey shading as in Figure 1.9. Note that the $\delta^{18}\text{O}$ scales are the same, except for NGRIP.

the largest changes in $\delta^{18}\text{O}$ occurring at the northern and southern peripheries of the monsoon system. Here, latitudinal shifts in the mean location of the ITCZ in response to North Atlantic Heinrich and Dansgaard-Oeschger (D-O) climate events (NGRIP 2004) influence the amount of rainfall received. Consequently, markedly increased millennial-scale variability is observed in China (and Brazil) during the late glacial period when North Atlantic climate was highly variable compared to the more stable Holocene epoch (Wang et al. 2001; Dykoski et al. 2005; Wang et al. 2007) (Figure 1.13). Across Australasia, the amplitude of millennial-scale $\delta^{18}\text{O}$ excursions decreases toward the equator. Speleothems from Borneo (Partin et al. 2007; Carolin et al. 2013) and Flores (Griffiths et al. 2009; Lewis et al. 2011; Ayliffe et al. 2013) show an anti-phased rainfall response to Heinrich events, but weaker D-O events are not reliably observed. Neither Heinrich nor D-O events are evident in Sulawesi, and the millennial-scale $\delta^{18}\text{O}$ variability was similarly suppressed during the late glacial interval and the Holocene (Figure 1.13). Together, these latitudinal gradients show that while North Atlantic Heinrich and D-O events caused marked shifts in the ITCZ and an associated rainfall seesaw at the peripheries of the Australasian monsoon, the strength of atmospheric convection and rainfall over the central western equatorial Pacific was less responsive to millennial-scale climate shifts.

Sulawesi at 5°S appears to lie at a fulcrum between hemispherically opposed rainfall anomalies experienced at the northern and southern limits of the Australasian monsoon. The millennial-scale climate stability in the core of the Australasian monsoon could be the outcome of the dry late glacial climate of the western equatorial Pacific, which may have reduced the capacity of millennial events to cause a measureable rainfall response (Figure 1.10 and Figure 1.13). The stability of western equatorial Pacific convection to millennial-scale forcing may also be a consequence of the broad latitudinal sweep of the ITCZ over the western equatorial Pacific region, with shifts in the position of the ITCZ influencing rainfall at its margins without affecting convective rainfall over the core western equatorial Pacific region. Alternatively, southward displacements of the ITCZ during millennial climate events may have caused Sulawesi to transition to a climate regime influenced by the Northern Hemisphere side of the Australasian monsoon. If so, any accompanying change in precipitation seasonality may not be recorded by the Sulawesi speleothems because the nearby mountainous barrier restricts rainfall reaching the cave site during boreal summer (Figure 1.11b).

1.4.6. Heinrich events in HadCM3

We explored the muted sensitivity of western equatorial Pacific rainfall to millennial-scale events by simulating the seasonal pattern of rainfall anomalies for the three most recent Heinrich events using the HadCM3 general circulation model (Singarayer and Valdes 2010; Singarayer et al. 2011). Heinrich events one (H1; 17 kyr BP), two (H2; 24 kyr BP) and three (H3; 32 kyr BP) were simulated using idealised hosing experiments in HadCM3. These were initialised from pre-industrial conditions, and forced with time appropriate orbital, greenhouse gas and ice sheet (including sea level) conditions. A model/proxy study of the LGM demonstrated the skill of HadCM3 in modelling conditions across the IPWP during the LGM compared to other models participating in the Paleoclimate Modelling Intercomparison Project, supporting the use of this model to examine past climate conditions over the IPWP (DiNezio and Tierney 2013). The ensemble control simulation (mean of 17, 24 and 32 kyr BP control runs; i.e. without hosing applied) shows a 6°C global average cooling, with the largest cooling over the North American Laurentide Ice Sheet (Figure 1.14). There is a small reduction in the global rate of precipitation, centred over the IPWP because of a weakening of the Australasian monsoon, in agreement with proxy records (DiNezio and Tierney 2013) and the palaeomonsoon map (Figure 1.10 and Figure 1.15).

The equilibrium time slice runs for 17, 24 and 32 kyr BP were hosed to simulate a Heinrich event. The experimental design follows the PMIP protocol established in Stouffer et al. (2006), with one Sverdrup ($1 \text{ Sv} = 1 \times 10^6 \text{ m}^3 \text{ s}^{-1}$) of freshwater continuously added to the surface of the North Atlantic between 50°N and 70°N latitude for 200 model years. Recently, the validity of hosing experiments in simulating Heinrich events have been called into question (Barker et al. 2015); however, intrinsic model stability requires the application of a forcing to initiate the shutdown of the AMOC, and hosing experiments remain a valid method for simulating the modelled climate response to Heinrich events within the current suite of climate models. HadCM3 has been found to be a relatively stable model, only displaying small anomalies in response to the more realistic freshwater forcing of 0.1 Sv, also used within PMIP (Stouffer et al. 2006; Kageyama et al. 2013). For this reason, we use the 1 Sv experiment for our analysis, as this forcing scenario best replicates the conditions recorded in proxy records during a Heinrich event; however, we recognise that this

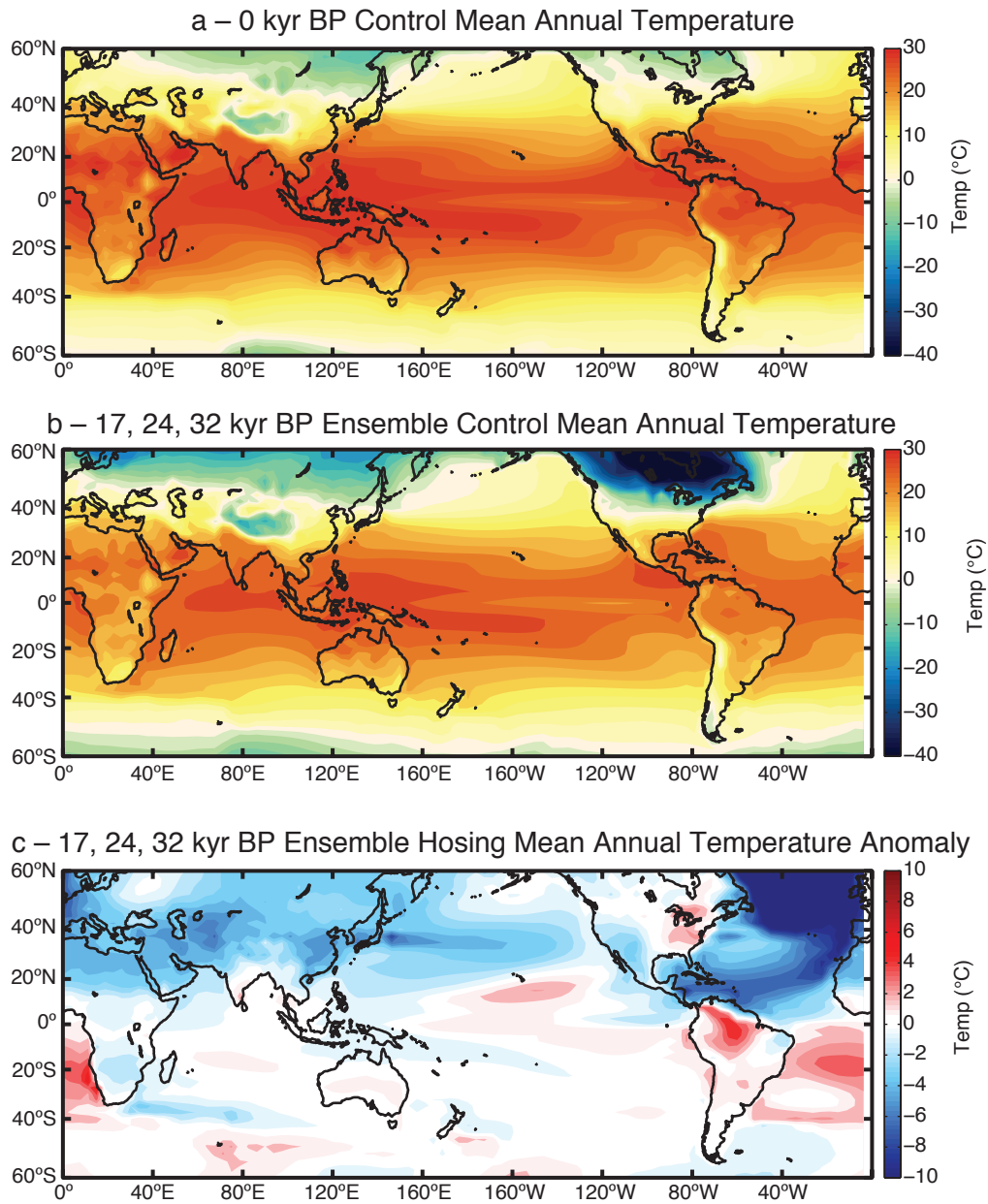


Figure 1.14: Modelled mean temperature. (a) 0 kyr BP (pre-industrial control) mean annual surface air temperature. (b) 17, 24 and 32 kyr BP ensemble control mean annual surface air temperature. (c) Hosing minus control ensemble mean annual surface air temperature anomalies. Anomalies are calculated using the ensemble mean hosing and control values.

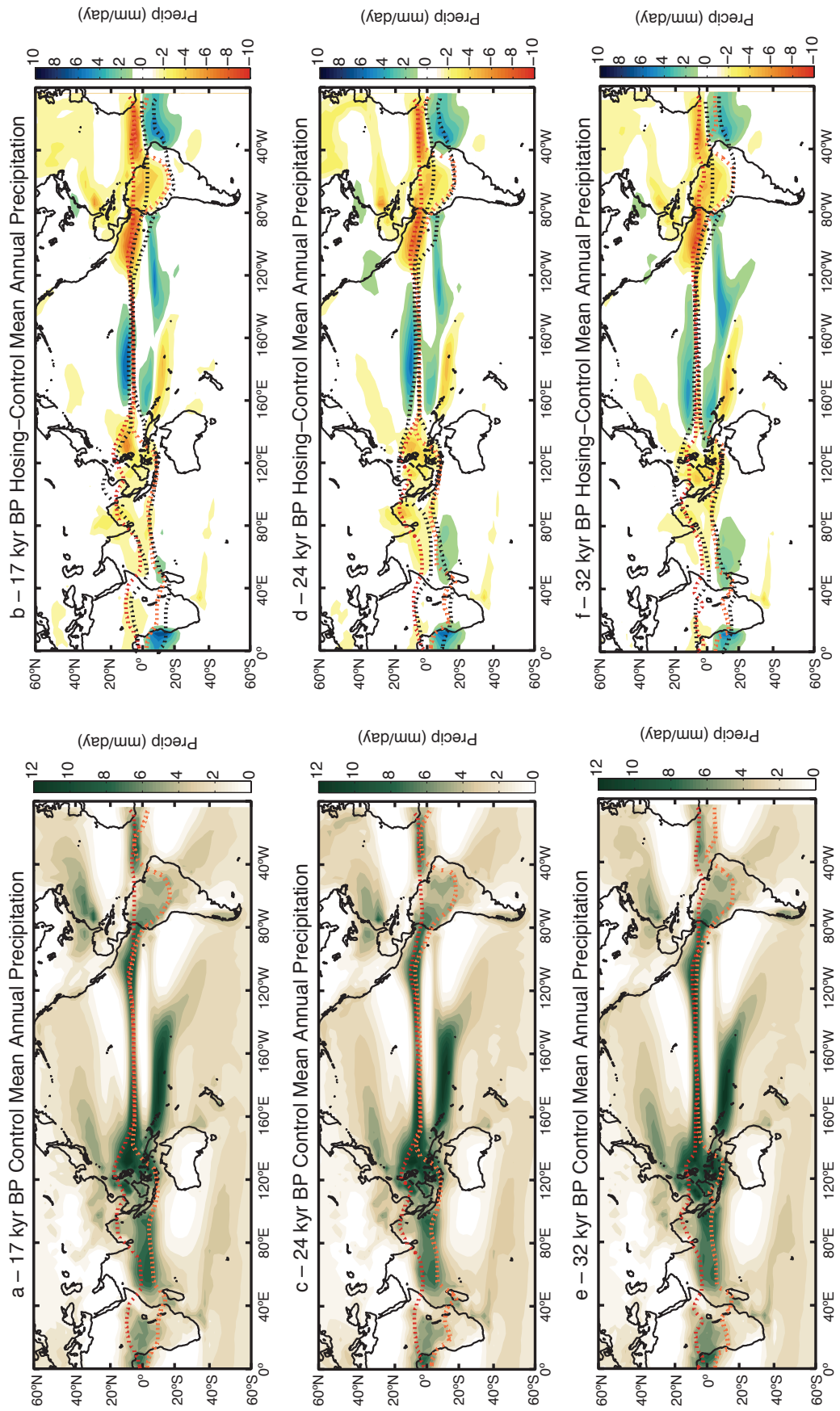


Figure 1.15

Figure 1.15: Modelled precipitation and ITCZ location. Control mean annual precipitation for (a) 17 kyr BP, (c) 24 kyr BP and (e) 32 kyr BP. Mean January and July ITCZ positions are shown with red dashed lines. Hosing minus control mean annual precipitation for (b) 17 kyr BP, (d) 24 kyr BP and (f) 32 kyr BP. Red dashed lines show the control ITCZ locations (as in left column). Black dashed lines show mean January and July ITCZ location in the hosing simulations.

experiment is idealised and not reflective of realistic Heinrich forcing (Fairbanks 1989; Deschamps et al. 2012). One Sv of freshwater added to the North Atlantic causes a large perturbation of the model AMOC (Singarayer and Valdes 2010) and a southward shift of the model ITCZ, in line with proxy data. The model was allowed to equilibrate, and the results presented represent a climatology for the last 30 years of each simulation.

Full details of the experimental set up can be found in Singarayer et al. (2010).

Hosing of the North Atlantic Ocean results in a marked cool anomaly over the North Atlantic, because of the dramatic reduction of the strength of the AMOC (Figure 1.14c). Subsequently, the South Atlantic warms because of the establishment of a bipolar seesaw, and the ITCZ over the Atlantic shifts south. Anomalies in the North Atlantic are propagated into the eastern Pacific Ocean by anomalous easterly winds, moving across the Isthmus of Panama (Figure 1.16c). A temperature dipole is established in the eastern Pacific, with cool temperature anomalies north of the equator, and warm anomalies south of the equator, causing a southward shift of the ITCZ in this region (Figure 1.14 and Figure 1.15). The north Pacific trade winds weakened, with anomalous westerly winds over the western Pacific, and a net drying over the IPWP.

Hosing results from HadCM3 compare well with those from CCSM3, with the spatial patterns of temperature and precipitation anomalies very similar between models (Mohtadi et al. 2014). CCSM3 shows a clear southward shift of the ITCZ over the Indian Ocean, resulting from a weakening of the southern Indian Ocean Hadley circulation. This result is mirrored in HadCM3, demonstrated by northerly wind anomalies across the equatorial Indian Ocean (Figure 1.15 and Figure 1.16). The comparable results for Heinrich events across the Indian Ocean achieved by the HadCM3 and CCSM3 simulations gives confidence to the skill of the HadCM3 model in simulating a reproducible response to a simulated Heinrich event.

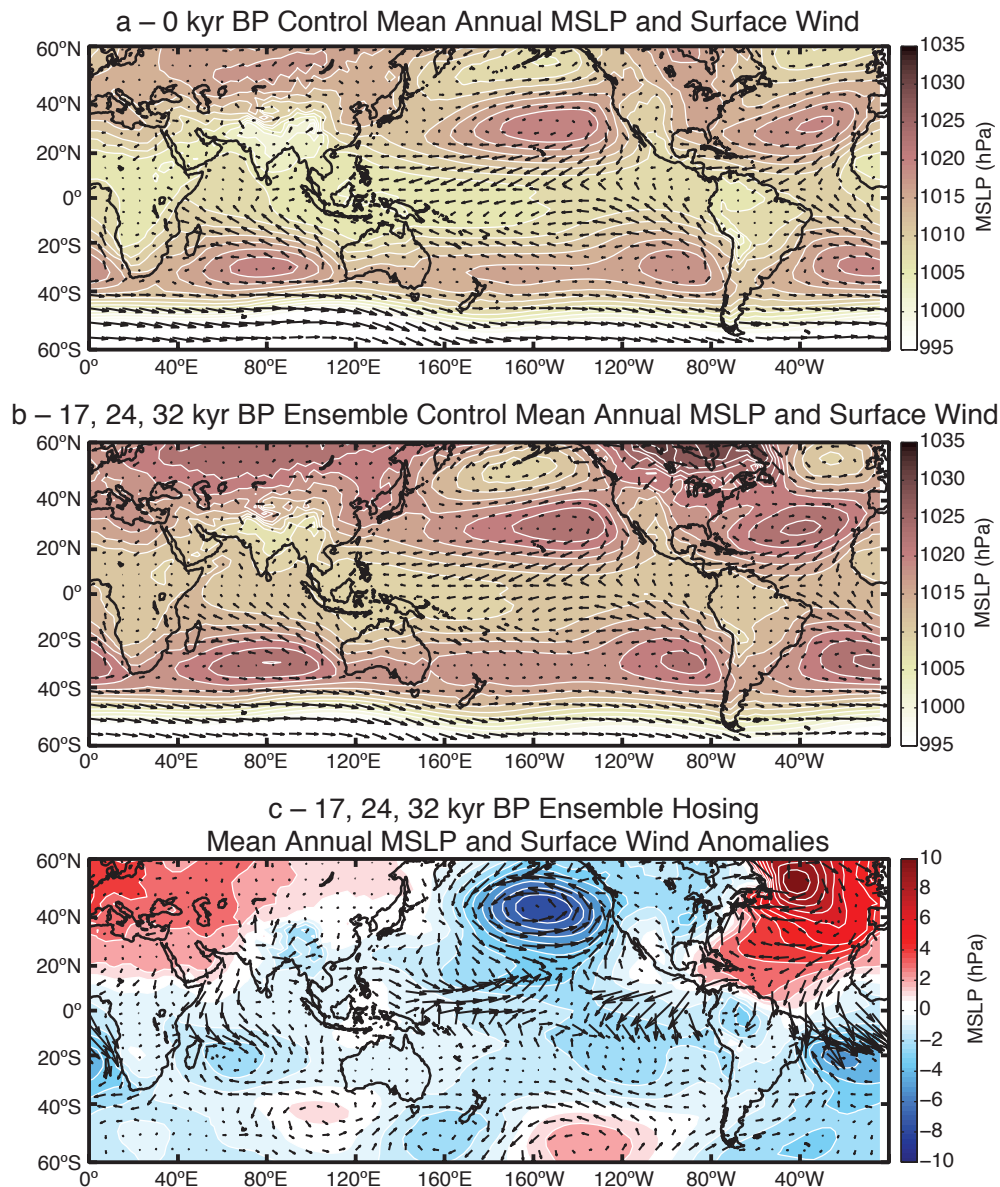


Figure 1.16: Modelled mean annual MSLP and surface wind. (a) 0 kyr BP (pre-industrial control) mean annual MSLP and surface wind. (b) 17, 24 and 32 kyr BP ensemble control mean annual MSLP and surface wind. (c) Hosing minus control ensemble mean annual MSLP and surface wind anomalies. Anomalies are calculated using the ensemble mean hosing and control values.

The seasonality of precipitation across a latitudinal transect of the western equatorial Pacific was examined through the production of spatio-temporal precipitation anomaly maps. A longitudinally averaged, latitudinal transect of the western equatorial Pacific (35°N to 20°S, 112–120°E) was calculated for each month to produce a spatial map of the seasonally evolving precipitation distribution across the western equatorial

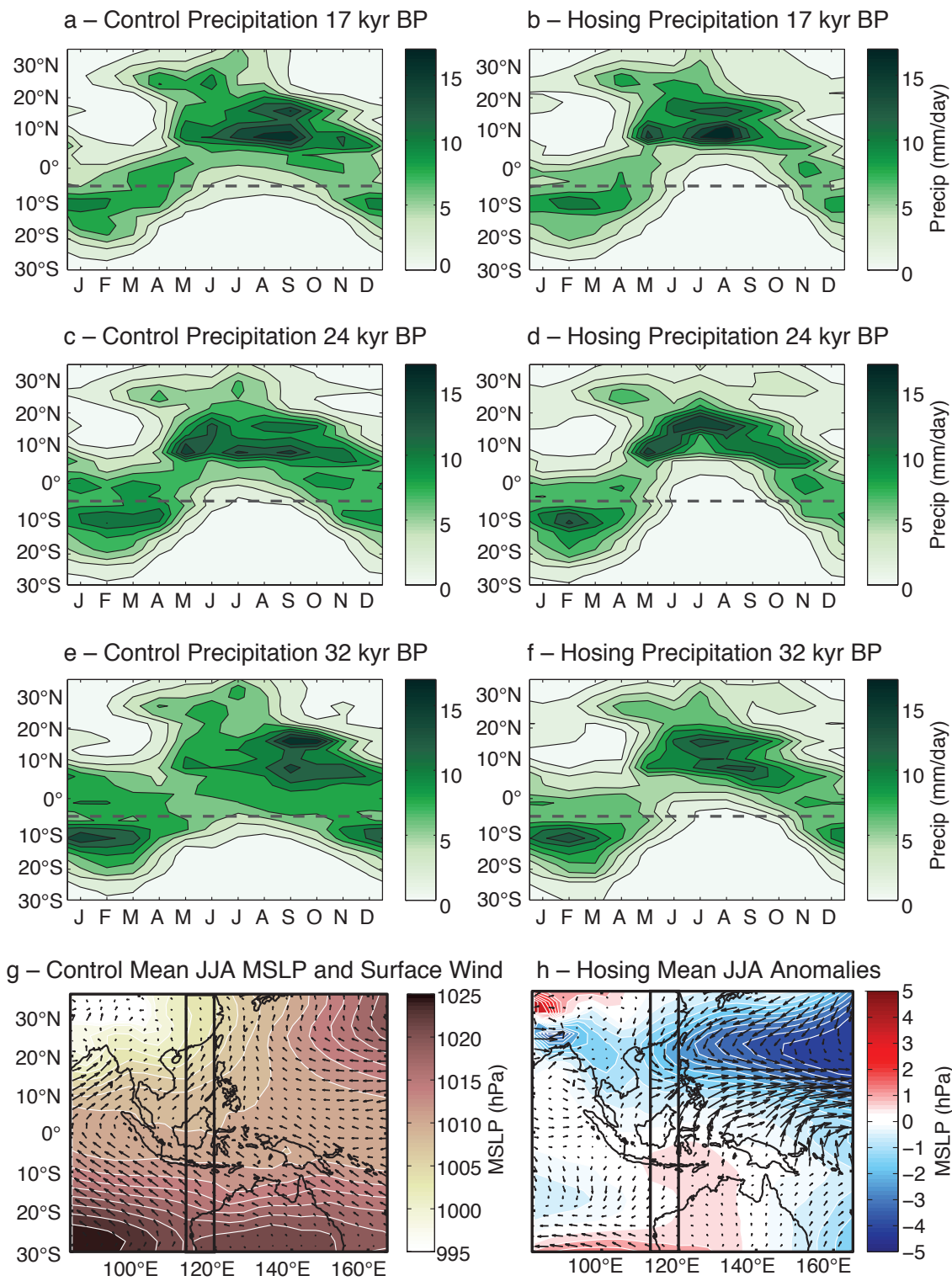


Figure 1.17

Figure 1.17: Modelled rainfall seasonality transect over the IPWP. (a–f) Rainfall seasonality averaged longitudinally over a latitudinal transect (116–120°E; shown in panels g and h). Mean rainfall for each month was calculated for the transect and plotted to produce a spatio-temporal map of rainfall seasonality across the IPWP. The latitude of Sulawesi is given by a dashed line. The total rainfall anomaly (hosing-control) averaged across the latitudinal transect plotted by month is shown in the far right column. (g) Mean June, July and August MSLP and surface winds averaged for the 17, 24 and 32 kyr BP control runs. (h) Mean June, July and August MSLP and surface wind anomalies (hosing-control) averaged for the 17, 24 and 32 kyr BP runs.

Pacific (Figure 1.17). When forced with freshwater hosing of the North Atlantic, rainfall seasonality at Sulawesi is enhanced for all three simulated Heinrich events (Figure 1.17 and Figure 1.18). The larger seasonal range at Sulawesi is the result of a decline in rainfall during ~June–September (the local dry season), with no accompanying change in austral summer monsoon rainfall. This asymmetry of the seasonal pattern is caused by a simulated narrowing of the width of the ITCZ over the western equatorial Pacific during boreal summer, a result of southerly winds pushing northwards over the western equatorial Pacific toward an anomalous low-pressure cell in the North Pacific (Figure 1.16 and Figure 1.17). Sulawesi, at 5°S receives greatly reduced JJA rainfall, beyond that associated with the local dry season. The dominance of austral summer rainfall at this site, however, results in only a small net change in annual precipitation, and no discernible Heinrich events. The simulated decline in ~June–September rainfall in the HadCM3 experiments suggests that, on average, the Northern Hemisphere drying during Heinrich events might have extended south to Sulawesi, in-phase with the rainfall response in Borneo. Future research targeting palaeoclimate records from southern locations that are sensitive to the austral winter monsoon (Figure 1.11) would be valuable in assessing the changes in ITCZ positioning produced in model hosing experiments.

1.5. Conclusions

Our palaeomonsoon reconstruction highlights the different processes that drive spatial

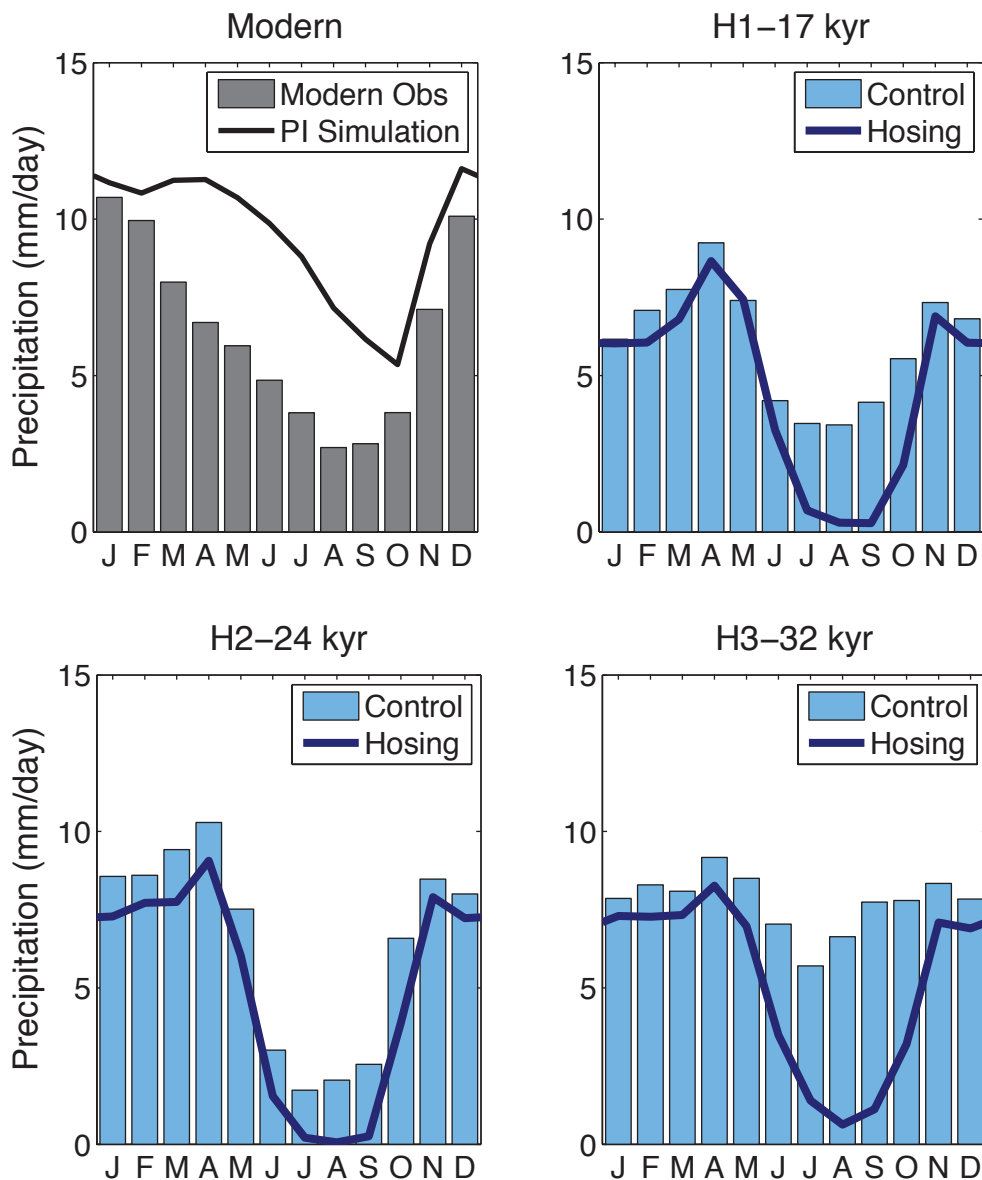


Figure 1.18: Seasonality of modelled rainfall at Sulawesi. Modelled rainfall averaged over the four grid boxes surrounding Sulawesi ($116\text{--}120^{\circ}\text{E}$, $2.5\text{--}5^{\circ}\text{S}$) for each month, for the three simulated Heinrich events. The hosing and control runs are given for each simulation.

and temporal rainfall variability across the Australasian monsoon domain. In Australasia, glacial-interglacial variations in western equatorial Pacific continental shelf exposure influence the intensity of deep atmospheric convection over the centre of the western equatorial Pacific (Meckler et al. 2012). In contrast, precession-dominated modulation of rainfall is largely restricted to the northern and southern peripheries of

the Australasian monsoon domain. On millennial scales, the latitudinal response of the Australasian monsoon decreases toward the core of the western equatorial Pacific region, culminating in a lack of expression in the Sulawesi record. The stability of core western equatorial Pacific convection to millennial-scale forcing may also be matched by a similar gradient in millennial-scale rainfall impacts in a zonal direction across the western equatorial Pacific. For example, a marine sediment record from the equatorial eastern Indian Ocean indicates that North Atlantic millennial-scale climate forcing dominated over orbital-scale climate changes at this location (Mohtadi et al. 2014). Taken together, our findings demonstrate that glacial-interglacial changes in northern ice sheets drive the intensity of deep atmospheric convection over the western equatorial Pacific, whereas North Atlantic millennial-scale climate change serves to redistribute monsoon rainfall latitudinally across Australasia. While intertropical rainfall patterns clearly respond to remote climate drivers, it appears that changes in deep convection over the core of the western equatorial Pacific are too subtle to initiate millennial-scale climate change.

1.6. Acknowledgements

This thesis chapter forms the basis of a first-author manuscript currently submitted to *Nature Communications*. The manuscript titled “Spatio-temporal evolution of Australasian monsoon hydroclimate over the last 40,000 years” was co-authored by:

- Michael K. Gagan – The Australian National University
- Gavin B. Dunbar – Victoria University of Wellington
- John C. Hellstrom – The University of Melbourne
- Hai Cheng – Xi’an Jiatong University and University of Minnesota
- R. Lawrence Edwards – University of Minnesota
- Wahyoe S. Hantoro – Indonesian Institute of Sciences
- Nerilie J. Abram – The Australian National University
- Hamdi Rifai – State University of Padang

1.6.1. Author contributions

M.K.G. designed the study. G.B.D., M.K.G., W.S.H. and H.R. carried out the fieldwork. C.E.K. performed the speleothem sampling and isotope analysis. J.C.H., H.C., R.L.E. and C.E.K carried out the ^{230}Th analyses and J.C.H. constructed the age model. C.E.K analysed the HadCM3 model simulations (which had been previously run and published). C.E.K., M.K.G., N.J.A. and G.B.D. interpreted the data and wrote the paper.

1.6.2. Further acknowledgements

The project was carried out under Kementerian Negara Riset dan Teknologi (RISTEK) research permit numbers 04/TKPIPA/FRP/SM/IV/2009 and 1b/TKPIPA/FRP/SM/I/2011. We are indebted to Bambang Suwargadi, Neil Anderson, Dan Zwartz and the staff of Bantimurung-Bulusaraung National Park for their invaluable assistance in the field. We also thank Heather Scott-Gagan, Joan Cowley, Joe Cali and Daniel Becker for laboratory assistance, and Paul Valdes, Joy Singarayer and Peter Hopcroft for providing the HadCM3 simulations for analysis.

1.7. References

- Amante, C. and B. W. Eakins (2009). ETOPO1 1 arc-minute global relief model: procedures, data sources and analysis. NOAA Technical Memorandum NESDIS NGDC-24, National Geophysical Data Center, NOAA.
- Anderson, R. F., S. Ali, L. I. Bradtmiller, S. H. H. Nielsen, M. Q. Fleisher, B. E. Anderson and L. H. Burckle (2009). Wind-driven upwelling in the Southern Ocean and the deglacial rise in atmospheric CO_2 . *Science* 323: 1443–1448.
- Ayliffe, L. K., M. K. Gagan, J.-x. Zhao, R. N. Drysdale, J. C. Hellstrom, W. S. Hantoro, M. L. Griffiths, H. Scott-Gagan, E. St Pierre, J. A. Cowley and B. W. Suwargadi (2013). Rapid interhemispheric climate links via the Australasian monsoon during the last deglaciation. *Nature Communications* 4: 2908.

- Baker, C. B., J. K. Eischeid, T. R. Karl and H. F. Diaz (1994). The quality control of long-term climatological data using objective data analysis. *Preprints of AMS Ninth Conference on Applied Climatology*, Dallas, TX.
- Barker, S., J. Chen, X. Gong, L. Jonkers, G. Knorr and D. Thornalley (2015). Icebergs not the trigger for North Atlantic cold events. *Nature* 520: 333–336.
- Bintanja, R., R. S. W. van de Wal and J. Oerlemans (2005). Modelled atmospheric temperatures and global sea levels over the past million years. *Nature* 437: 125–128.
- Broecker, W. S., E. A. Olson and P. C. Orr (1960). Radiocarbon measurements and annual rings in cave formations. *Nature* 185: 93–94.
- Carolin, S. A., K. M. Cobb, J. F. Adkins, B. Clark, J. L. Conroy, S. Lejau, J. Malang and A. A. Tuen (2013). Varied response of Western Pacific hydrology to climate forcings over the Last Glacial period. *Science* 340: 1564–1566.
- Cheng, H., R. L. Edwards, W. S. Broecker, G. H. Denton, X. Kong, Y. Wang, R. Zhang and X. Wang (2009). Ice age terminations. *Science* 326: 248–252.
- Cheng, H., R. L. Edwards, C.-C. Shen, V. J. Polyak, Y. Asmerom, J. Woodhead, J. Hellstrom, Y. Wang, X. Kong, C. Spötl, X. Wang and E. C. Alexander Jr (2013a). Improvements in ^{230}Th dating, ^{230}Th and ^{234}U half-life values, and U-Th isotopic measurements by multi-collector inductively coupled plasma mass spectrometry. *Earth and Planetary Science Letters* 371–372: 82–91.
- Cheng, H., A. Sinha, F. W. Cruz, X. Wang, R. L. Edwards, F. M. d'Horta, C. C. Ribas, M. Vuille, L. D. Stott and A. S. Auler (2013b). Climate change patterns in Amazonia and biodiversity. *Nature Communications* 4: 1411.
- Cheng, H., A. Sinha, X. Wang, F. W. Cruz and R. L. Edwards (2012). The global paleomonsoon as seen through speleothem records from Asia and the Americas. *Climate Dynamics* 39: 1045–1062.
- Chiang, J. C. H. (2009). The tropics in paleoclimate. *Annual Review of Earth and Planetary Sciences* 37: 263–297.
- Cobb, K. M., J. F. Adkins, J. W. Partin and B. Clark (2007). Regional-scale climate influences on temporal variations of rainwater and cave dripwater oxygen isotopes in northern Borneo. *Earth and Planetary Science Letters* 263: 207–220.
- Cole, J. E., D. Rind, R. Webb, S., J. Jouzel and R. Healy (1999). Climatic controls on interannual variability of precipitation $\delta^{18}\text{O}$: Simulated influence of temperature,

precipitation amount, and vapor source region. *Journal of Geophysical Research* 104: 14223–14235.

- Cruz, F. W., S. J. Burns, I. Karmann, W. D. Sharp, M. Vuille, A. O. Cardoso, J. A. Ferrari, P. L. Silva Dias and O. Viana Jr (2005). Insolation-driven changes in atmospheric circulation over the past 116,000 years in subtropical Brazil. *Nature* 434: 63–66.
- Cruz, F. W., M. Vuille, S. J. Burns, X. Wang, H. Cheng, M. Werner, R. L. Edwards, I. Karmann, A. S. Auler and H. Nguyen (2009). Orbitally driven east-west antiphasing of South American precipitation. *Nature Geoscience* 2: 210–214.
- Dansgaard, W. (1964). Stable isotopes in precipitation. *Tellus* 16: 436–468.
- De Deckker, P., N. J. Tapper and S. van der Kaars (2002). The status of the Indo-Pacific Warm Pool and adjacent land at the Last Glacial Maximum. *Global and Planetary Change* 35: 25–35.
- Denniston, R. F., K.-H. Wyrwoll, Y. Asmerom, V. J. Polyak, W. F. Humphreys, J. Cugley, D. Woods, Z. LaPointe, J. Peota and E. Greaves (2013). North Atlantic forcing of millennial-scale Indo-Australian monsoon dynamics during the Last Glacial period. *Quaternary Science Reviews* 72: 159–168.
- Denton, G. H., R. F. Anderson, J. R. Toggweiler, R. L. Edwards, J. M. Schaefer and A. E. Putnam (2010). The Last Glacial Termination. *Science* 328: 1652–1656.
- Deschamps, P., N. Durand, E. Bard, B. Hamelin, G. Camoin, A. L. Thomas, G. M. Henderson, J. i. Okuno and Y. Yokoyama (2012). Ice-sheet collapse and sea-level rise at the Bølling warming 14,600 years ago. *Nature* 483: 559–564.
- DiNezio, P. N. and J. E. Tierney (2013). The effect of sea level on glacial Indo-Pacific climate. *Nature Geoscience* 6: 485–491.
- Dorale, J. A. and Z. Liu (2009). Limitations of Hendy Test criteria in judging the paleoclimate suitability of speleothems and the need for replication. *Journal of Cave and Karst Studies* 71: 73–80.
- Dubois, N., D. W. Oppo, V. V. Galy, M. Mohtadi, S. van der Kaars, J. E. Tierney, Y. Rosenthal, T. I. Eglinton, A. Lückge and B. K. Linsley (2014). Indonesian vegetation response to changes in rainfall seasonality over the past 25,000 years. *Nature Geoscience* 7: 513–517.
- Duplessy, J. C., J. Labeyrie, C. Lalou and H. V. Nguyen (1970). Continental climatic variations between 130,000 and 90,000 years BP. *Nature* 226: 631–633.

- Dykoski, C. A., R. L. Edwards, H. Cheng, D. Yuan, Y. Cai, M. Zhang, Y. Lin, J. Qing, Z. An and J. Revenaugh (2005). A high-resolution, absolute-dated Holocene and deglacial Asian monsoon record from Dongge Cave, China. *Earth and Planetary Science Letters* 233: 71–86.
- Edwards, R. L., J. H. Chen and G. J. Wasserburg (1987). ^{238}U - ^{234}U - ^{230}Th - ^{232}Th systematics and the precise measurement of time over the past 500,000 years. *Earth and Planetary Science Letters* 81: 175–192.
- Fairbanks, R. G. (1989). A 17,000-year glacio-eustatic sea level record: influence of glacial melting rates on the Younger Dryas event and deep-ocean circulation. *Nature* 342: 637–642.
- Fairchild, I. J. and A. Baker (2012). *Speleothem science: From process to past environments*. West Sussex, UK, John Wiley & Sons Ltd.
- Griffiths, M. L., R. N. Drysdale, M. K. Gagan, J.-x. Zhao, L. K. Ayliffe, J. C. Hellstrom, W. S. Hantoro, S. Frisia, Y. Feng, I. Cartwright, E. St Pierre, M. J. Fischer and B. W. Suwargadi (2009). Increasing Australian-Indonesian monsoon rainfall linked to early Holocene sea-level rise. *Nature Geoscience* 2: 636–639.
- Griffiths, M. L., R. N. Drysdale, M. K. Gagan, J.-x. Zhao, J. C. Hellstrom, L. K. Ayliffe and W. S. Hantoro (2013). Abrupt increase in east Indonesian rainfall from flooding of the Sunda Shelf ~9500 years ago. *Quaternary Science Reviews* 74: 273–279.
- Hellstrom, J. C. (2003). Rapid and accurate U/Th dating using parallel ion-counting multi-collector ICP-MS. *Journal of Analytical Atomic Spectrometry* 18: 1346–1351.
- Hellstrom, J. C. (2006). U-Th dating of speleothems with high initial ^{230}Th using stratigraphical constraint. *Quaternary Geochronology* 1: 289–295.
- Hendy, C. H. (1971). The isotopic geochemistry of speleothems-I. The calculation of the effects of different modes of formation on the isotopic composition of speleothems and their applicability as palaeoclimatic indicators. *Geochimica et Cosmochimica Acta* 35: 801–824.
- Hendy, C. H. and A. T. Wilson (1968). Palaeoclimatic data from speleothems. *Nature* 219: 48–51.

- Jouzel, J., F. Vimeux, N. Caillon, G. Delaygue, G. Hoffmann, V. Masson-Delmotte and F. Parrenin (2003). Magnitude of isotope/temperature scaling for interpretation of central Antarctic ice cores. *Journal of Geophysical Research* 108: 4361.
- Kageyama, M., U. Merkel, B. Otto-Bliesner, M. Prange, A. Abe-Ouchi, G. Lohmann, R. Ohgaito, D. M. Roche, J. Singarayer, D. Swingedouw and X. Zhang (2013). Climatic impacts of fresh water hosing under Last Glacial Maximum conditions: a multi-model study. *Climate of the Past* 9: 935–953.
- Kanner, L. C., S. J. Burns, H. Cheng and R. L. Edwards (2012). High-latitude forcing of the South American Summer Monsoon during the last glacial. *Science* 335: 570–573.
- Kim, S.-T. and J. R. O'Neil (1997). Equilibrium and nonequilibrium oxygen isotope effects in synthetic carbonates. *Geochimica et Cosmochimica Acta* 61: 3461–3475.
- Koster, R. D., D. P. de Valpine and J. Jouzel (1993). Continental water recycling and H₂¹⁸O concentrations. *Geophysical Research Letters* 20: 2215–2218.
- Lachniet, M. S. (2009). Climatic and environmental controls on speleothem oxygen-isotope values. *Quaternary Science Reviews* 28: 412–432.
- Lea, D. W., D. K. Pak and H. J. Spero (2000). Climate impact of Late Quaternary equatorial Pacific sea surface temperature variations. *Science* 289: 1719–1724.
- LeGrande, A. N. and G. A. Schmidt (2006). Global gridded data set of the oxygen isotopic composition in seawater. *Geophysical Research Letters* 33: L12604.
- Lewis, S. C., M. K. Gagan, L. K. Ayliffe, J.-x. Zhao, W. S. Hantoro, P. C. Treble, J. C. Hellstrom, A. N. LeGrande, M. Kelley, G. A. Schmidt and B. W. Suwargadi (2011). High-resolution stalagmite reconstructions of Australian-Indonesian monsoon rainfall variability during Heinrich stadial 3 and Greenland interstadial 4. *Earth and Planetary Science Letters* 303: 133–142.
- Linsley, B. K., Y. Rosenthal and D. W. Oppo (2010). Holocene evolution of the Indonesian throughflow and the western Pacific warm pool. *Nature Geoscience* 3: 578–583.
- Meckler, A. N., M. O. Clarkson, K. M. Cobb, H. Sodemann and J. F. Adkins (2012). Interglacial hydroclimate in the tropical west Pacific through the late Pleistocene. *Science* 336: 1301–1304.

- Moerman, J. W., K. M. Cobb, J. F. Adkins, H. Sodemann, B. Clark and A. A. Tuen (2013). Diurnal to interannual rainfall $\delta^{18}\text{O}$ variations in northern Borneo driven by regional hydrology. *Earth and Planetary Science Letters* 369–370: 108–119.
- Mohtadi, M., M. Prange, D. W. Oppo, R. De Pol-Holz, U. Merkel, X. Zhang, S. Steinke and A. Lückge (2014). North Atlantic forcing of tropical Indian Ocean climate. *Nature* 509: 76–80.
- Muller, J., M. Kylander, R. A. J. Wüst, D. Weiss, A. Martinez-Cortizas, A. N. LeGrande, T. Jennerjahn, H. Behling, W. T. Anderson and G. Jacobson (2008). Possible evidence for wet Heinrich phases in tropical NE Australia: the Lynch's Crater deposit. *Quaternary Science Reviews* 27: 468–475.
- NGRIP (2004). High-resolution record of Northern Hemisphere climate extending into the last interglacial period. *Nature* 431: 147–151.
- Partin, J. W., K. M. Cobb, J. F. Adkins, B. Clark and D. P. Fernandez (2007). Millennial-scale trends in west Pacific warm pool hydrology since the Last Glacial Maximum. *Nature* 449: 452–455.
- Reeves, J. M., H. C. Bostock, L. K. Ayliffe, T. T. Barrows, P. De Deckker, L. S. Devriendt, G. B. Dunbar, R. N. Drysdale, K. E. Fitzsimmons, M. K. Gagan, M. L. Griffiths, S. G. Haberle, J. D. Jansen, C. Krause, S. Lewis, H. V. McGregor, S. D. Mooney, P. Moss, G. C. Nanson, A. Purcell and S. van der Kaars (2013). Palaeoenvironmental change in tropical Australasia over the last 30,000 years – a synthesis by the OZ-INTIMATE group. *Quaternary Science Reviews* 74: 97–114.
- Reeves, J. M., A. R. Chivas, A. García, S. Holt, M. J. J. Couapel, B. G. Jones, D. I. Cendón and D. Fink (2008). The sedimentary record of palaeoenvironments and sea-level change in the Gulf of Carpentaria, Australia, through the last glacial cycle. *Quaternary International* 183: 3–22.
- Risi, C., S. Bony and F. Vimeux (2008). Influence of convective processes on the isotopic composition ($\delta^{18}\text{O}$ and δD) of precipitation and water vapor in the tropics: 2. Physical interpretation of the amount effect. *Journal of Geophysical Research* 113: D19306.
- Rozanski, K., L. Araguás-Araguás and R. Gonfiantini (1993). Isotopic patterns in modern global precipitation. *Climate Change in Continental Isotopic Records*.

P. K. Swart, K. C. Lohmann, J. Mckenzie and S. Savin. Washington, D.C., American Geophysical Union.

Russell, J. M., H. Vogel, B. L. Konecky, S. Bijaksana, Y. Huang, M. Melles, N.

Wattrus, K. Costa and J. W. King (2014). Glacial forcing of central Indonesian hydroclimate since 60,000 y B.P. *Proceedings of the National Academy of Sciences* 111: 5100.

SAHRA. (2005). Retrieved 4/2/2015, 2015, from

<http://web.sahra.arizona.edu/programs/isotopes/oxygen.html>.

Schneider, T., T. Bischoff and G. H. Haug (2014). Migrations and dynamics of the intertropical convergence zone. *Nature* 513: 45–53.

Schrag, D. P., G. Hampt and D. W. Murray (1996). Pore fluid constraints on the temperature and oxygen isotopic composition of the glacial ocean. *Science* 272: 1930–1932.

Singarayer, J. S. and P. J. Valdes (2010). High-latitude climate sensitivity to ice-sheet forcing over the last 120 kyr. *Quaternary Science Reviews* 29: 43–55.

Singarayer, J. S., P. J. Valdes, P. Friedlingstein, S. Nelson and D. J. Beerling (2011). Late Holocene methane rise caused by orbitally controlled increase in tropical sources. *Nature* 470: 82–86.

Stenni, B., V. Masson-Delmotte, E. Selmo, H. Oerter, H. Meyer, R. Röthlisberger, J. Jouzel, O. Cattani, S. Falourd, H. Fischer, G. Hoffmann, P. Iacumin, S. J. Johnsen, B. Minster and R. Udisti (2010). The deuterium excess records of EPICA Dome C and Dronning Maud Land ice cores (East Antarctica). *Quaternary Science Reviews* 29: 146–159.

Stott, L., C. Poulsen, S. Lund and R. Thunell (2002). Super ENSO and global climate oscillations at millennial time scales. *Science* 297: 222–226.

Stouffer, R. J., J. Yin, J. M. Gregory, K. W. Dixon, M. J. Spelman, W. Hurlin, A. J. Weaver, M. Eby, G. M. Flato, H. Hasumi, A. Hu, J. H. Jungclaus, I. V. Kamenkovich, A. Levermann, M. Montoya, S. Murakami, S. Nawrath, A. Oka, W. R. Peltier, D. Y. Robitaille, A. Sokolov, G. Vettoretti and S. L. Weber (2006). Investigating the causes of the response of the thermohaline circulation to past and future climate changes. *Journal of Climate* 19: 1365–1387.

Tierney, J. E., D. W. Oppo, A. N. LeGrande, Y. Huang, Y. Rosenthal and B. K. Linsley (2012). The influence of Indian Ocean atmospheric circulation on Warm Pool

- hydroclimate during the Holocene epoch. *Journal of Geophysical Research* 117: D19108.
- Vuille, M., R. S. Bradley, M. Werner, R. Healy and F. Keimig (2003). Modeling $\delta^{18}\text{O}$ in precipitation over the tropical Americas: 1. Interannual variability and climatic controls. *Journal of Geophysical Research* 108: 4174.
- Waelbroeck, C., L. Labeyrie, E. Michel, J. C. Duplessy, J. F. McManus, K. Lambeck, E. Balbon and M. Labracherie (2002). Sea-level and deep water temperature changes derived from benthic foraminifera isotopic records. *Quaternary Science Reviews* 21: 295–305.
- Wang, P. (2009). Global monsoon in a geological perspective. *Chinese Science Bulletin* 54: 1113–1136.
- Wang, X., A. S. Auler, R. L. Edwards, H. Cheng, P. S. Cristalli, P. L. Smart, D. A. Richards and C.-C. Shen (2004). Wet periods in northeastern Brazil over the past 210 kyr linked to distant climate anomalies. *Nature* 432: 740–743.
- Wang, X., A. S. Auler, R. L. Edwards, H. Cheng, E. Ito and M. Solheid (2006). Interhemispheric anti-phasing of rainfall during the last glacial period. *Quaternary Science Reviews* 25: 3391–3403.
- Wang, X., A. S. Auler, R. L. Edwards, H. Cheng, E. Ito, Y. Wang, X. Kong and M. Solheid (2007). Millennial-scale precipitation changes in southern Brazil over the past 90,000 years. *Geophysical Research Letters* 34: L23701.
- Wang, Y. J., H. Cheng, R. L. Edwards, Z. S. An, J. Y. Wu, C.-C. Shen and J. A. Dorale (2001). A high-resolution absolute-dated Late Pleistocene monsoon record from Hulu Cave, China. *Science* 294: 2345–2348.
- Webster, P. J. (1994). The role of hydrological processes in ocean-atmosphere interactions. *Reviews of Geophysics* 32: 427–476.
- Webster, P. J., V. O. Magaña, T. N. Palmer, J. Shukla, R. A. Tomas, M. Yanai and T. Yasunari (1998). Monsoons: Processes, predictability, and the prospects for prediction. *Journal of Geophysical Research* 103: 14451–14510.

CHAPTER TWO

Sensitivity of modelled tropical climate to freshwater hosing of the North Atlantic

2.1. Introduction

Climate models have been used since the late sixties to simulate the physical processes driving the earth's climate system (Manabe and Bryan 1969). Hosing experiments, where fresh water is added to the surface of the North Atlantic Ocean to represent Heinrich-like events, are relatively simple perturbation experiments that provide information on the sensitivity of the climate system to abrupt forcing. Hosing experiments attempt to replicate the effects of a Heinrich event by adding freshwater to the North Atlantic Ocean in the downwelling region of the Atlantic Meridional Overturning Circulation (AMOC), reducing the density of surface water and slowing down the rate of bottom-water formation.

We use the CSIRO Mk3L general circulation model (GCM) to investigate the dynamics of the AMOC in response to freshwater forcing (i.e. hosing) of various magnitudes and durations to determine the conditions required to severely perturb the AMOC. We then examine the modelled response of the AMOC under two different boundary conditions:

1. with 10-kyr orbital forcing, which represents a time of northern summer insolation maxima (as opposed to the PI, where the summer insolation maximum is in the south), and
2. with atmospheric CO₂ increased to 400 ppmv – the current atmospheric CO₂ concentration due to continued anthropogenic CO₂ emissions.

These two boundary condition changes are equilibrated and hosed, in order to test the effect of orbital and CO₂ changes on the climate response to a simulated Heinrich event.

2.2. Heinrich events and rates of freshwater discharge

The last glacial period was punctuated by a series of iceberg calving events from the large ice sheets of North America, into the North Atlantic Ocean. These events released large volumes of freshwater into the surface waters of the North Atlantic where dense bottom-waters form, in most cases altering the strength of the global ocean's thermohaline circulation. These freshwater influx events are known as “Heinrich events” and are identified from ice rafted debris layers in sediment cores from the North Atlantic (Heinrich 1988; Bond et al. 1992; Broecker et al. 1992). Seven such Heinrich events (including the Younger Dryas) have been identified over the last 100 kyr (Table 2.1). These events coincide with decreases in Greenland temperature (Johnsen et al. 1992; Bond et al. 1993), weakening of the Atlantic Meridional Overturning Circulation (AMOC) (Broecker 1994; McManus et al. 2004), southward shifts of the Intertropical Convergence Zone (ITCZ) (Wang et al. 2001; Griffiths et al. 2009; Kanner et al. 2012; Muller et al. 2012; Ayliffe et al. 2013; Denniston et al. 2013) and the strengthening of a thermal “bipolar seesaw” (Broecker 1998; Barker et al. 2009; Pedro et al. 2011).

Proxy reconstructions and ice sheet models have been used to estimate the volume and rate of freshwater discharge into the North Atlantic during large outburst events, including Heinrich events and Meltwater Pulse 1A (MWP1A). Proxy reconstructions of past sea levels from corals provide estimates of the rate and magnitude of rapid sea level rises. Early estimates of deglacial sea level rise were from corals from Barbados, and suggested rates of sea level rise up to 40 mm yr⁻¹ during

Table 2.1: Heinrich event ages and sources. Age data compiled by Hemming (2004).

Event	Approx. age (kyr BP)	Likely source	Reference
H0 (YD)	~12.9	Freshwater outburst from Lake Agassiz	(Broecker 2006) (Carlson et al. 2007)
H1	16.8	Hudson Strait / Laurentide Ice Sheet	(Bond et al. 1992) (Bond et al. 1993)
H2	24.0	Hudson Strait / Laurentide Ice Sheet	(Bond et al. 1992) (Bond et al. 1993)
H3	~ 31.0	Fennoscandian Ice Sheet?	(Meese et al. 1997)
H4	38	Hudson Strait / Laurentide Ice Sheet	(Meese et al. 1997)
H5	45	Hudson Strait / Laurentide Ice Sheet	(Meese et al. 1997)
H6	~ 60	Fennoscandian Ice Sheet?	(Meese et al. 1997)

MWP1A at ~14.6 kyr BP, equating to a freshwater influx of 0.45 Sv ($1 \text{ Sv} = 10^6 \text{ m}^3\text{s}^{-1}$) (Fairbanks 1989). Corals from Tahiti with very strong chronological constraints similarly suggest that rates of freshwater discharge during MWP1A could have been as high as $\sim 46 \text{ mm yr}^{-1}$ (0.52 Sv) (Deschamps et al. 2012). Estimates based on the volume of ice rafted debris deposited across the North Atlantic suggest short-lived bursts of iceberg rafting could have released up to 1 Sv of freshwater during a single year, with a long-term flux over 300–500 years of 0.15–0.3 Sv (Hemming 2004). Modelling by Clarke (2003) suggests that outbursts from Lake Agassiz as large as 5–10 Sv could have occurred during the 8.2 ka event, however, these were short lived, most likely occurring over less than one year.

2.3. Hosing experiments

A range of “Heinrich-like” hosing experimental designs can be found within the published literature. These experiments are commonly carried out using palaeoclimate general circulation models (Table 2.2). The different rates and volumes of freshwater hosing used by each experiment attempt to replicate different aspects of Heinrich events, based on what the authors are attempting to test.

The Palaeoclimate Model Intercomparison Project (PMIP) was established in order to coordinate the systematic study of General Circulation Models (GCMs), and to

Table 2.2: Selection of published hosing experimental designs. This list is not exhaustive.

Rate	Duration	Region of the North Atlantic	Boundary Conditions	Model	References
0.1 Sv	500 years	50°–70°N	PI	Manabe 91	(Manabe and Stouffer 2000)
0.1 Sv	100 years	50°–70°N	PI PI PI	PMIP ensemble PMIP ensemble HadCM3	(Stouffer et al. 2006) (Timmermann et al. 2007b) (Dong and Sutton 2007)
0.5 Sv	100 years	various	PI	FAMOUS	(Smith and Gregory 2009)
0.6 Sv	60 years	55°–75°N	PI PI	GFDL CM2.0 GFDL CM2.0 and CCSM3	(Zhang and Delworth 2005) (Wan et al. 2011)
1 Sv	100 years	50°–70°N	PI PI PI PI PI 17, 24, 32, 38, 46, 60 kyr BP	PMIP ensemble PMIP ensemble HadCM3 FAMOUS GISS ModelE-R HadCM3	(Stouffer et al. 2006) (Timmermann et al. 2007b) (Dong and Sutton 2007; Lu et al. 2008) (Smith and Gregory 2009) (Lewis et al. 2010) (Singarayer and Valdes 2010)
8 Sv	1 year	55°–85°N	PI	HadCM3	(Dong and Sutton 2002)
16 Sv	1 year	upper 970 m Nth Atl Ocean	LGM (21 kyr)	CCSM3	(Pausata et al. 2011)

assess their ability to simulate large climate changes, such as those that occurred during the Last Glacial Maximum (LGM) (Joussaume and Taylor 2000). Initially, experiments included an LGM and 6-kyr BP boundary condition spin up only. A water hosing experiment was added to the second phase of the project (PMIP2), with 0.1 Sv of freshwater added to the North Atlantic Ocean between 50°–70°N, for 100 years. After this time, the water forcing is switched off, and the model is allowed to re-equilibrate (Stouffer et al. 2006). The broad application of freshwater across the North Atlantic was chosen to ensure that the bottom-water forming region was affected in each model and to minimise numerical complexities associated with advecting this water away from the input location. A second, more idealised hosing experiment was also proposed, where the freshwater input was increased to 1 Sv for 100 years. While 0.1 Sv represents a more realistic freshwater flux for simulating a Heinrich event (Fairbanks 1989; Deschamps et al. 2012), the inherent stability of many climate models only results in localised climate responses within the Atlantic Ocean basin in response to the perturbation (Stouffer et al. 2006; Kageyama et al. 2013), missing the long-range

teleconnections identified from proxy records (e.g. Ayliffe et al. 2013; Carolin et al. 2013; Denniston et al. 2013). A 1-Sv experiment was therefore also added to ensure that the model AMOC was severely perturbed, resulting in stronger climate anomalies that can be compared with proxy records (Stouffer et al. 2006).

A total of 14 models participated in the PMIP2 hosing simulations (Stouffer et al. 2006), and a number of additional models have since performed these prescribed experiments (incl. HadCM3 (Lu and Dong 2008), FAMOUS (Smith and Gregory 2009) and GISS ModelE-R (Lewis et al. 2010)). This not only provided an extensive study on the dynamics of the AMOC, but also allowed the performance of the models themselves to be evaluated against an ensemble.

While hosing experiments are relatively common, the response of these experiments to changing boundary conditions remains poorly understood and tested. Most hosing experiments use pre-industrial (PI) boundary conditions, which represent climate prior to the onset of anthropogenic climate change, with CO₂ concentrations held at ~280 ppmv (Table 2.3). This is the easiest and most robust model set up, as the

Table 2.3: Pre-industrial boundary conditions as defined for the PMIP2 experiments. Notes: 1: vegetation provided. 2: Insolation as at 1950 AD. 3: Spin up as per each model group’s usual protocol. OA refers to ocean-atmosphere models, while OAV includes OA models with an interactive vegetation scheme. Table from the PMIP2 website <https://pmip2.lsce.ipsl.fr/>.

Boundary conditions	Value				
Vegetation	OA		OAV		
	Fixed (1)		Interactive		
Ice sheets	Modern				
Topography, coastlines	Modern				
Greenhouse gases	CO ₂	CH ₄	N ₂ O	CFC	O ₃
	Pre-industrial (around 1750)				
	280 ppm	760 ppb	270 ppb	0	Modern - 10 DU
Insolation (2)	Solar constant = 1365 W/m ²				
	Eccentricity		Obliquity		Angular precession
	0.016724		23.446 °		102.04 °
Initial ocean state	Modern Initialize 3-D ocean temperature and salinity from the Levitus 1998 datasets				
Model spinup	See note 3 below				

model is initiated from observed conditions and is easily validated against observational datasets. This provides a means of testing the behaviour of the model in simulating a known scenario, and gives more confidence in its ability to simulate unknown conditions. The PMIP hosing experiments suggest the use of PI boundary conditions, making PI hosing simulations the most common within the literature (e.g. Dong and Sutton 2002; Zhang and Delworth 2005; Stouffer et al. 2006; Smith and Gregory 2009; Lewis et al. 2010).

The effect of boundary conditions on the modelled climate response to hosing events has not been explored extensively, with only a small number of published studies available that explicitly examine a systematic change in boundary conditions (Bitz et al. 2007; Hu et al. 2008; Swingedouw et al. 2009; Kageyama et al. 2013). Bitz et al. (2007) use three different boundary conditions – PI, LGM and 4xCO₂ simulations – to examine the possible role of background climates on the response to freshwater forcing. The authors find that the boundary conditions play an important role in determining the rate of AMOC recovery following the shutdown induced by freshwater forcing, with the PI simulation recovering within ~40 years, the 4xCO₂ recovering within ~70 years, and the LGM simulation not recovering during the 235-year experiment.

Other studies have examined the role of boundary conditions on the climate effects of a simulated Heinrich event by applying freshwater hosing to different background climate states such as the LGM (Hu et al. 2008) or specific Heinrich events (Singarayer and Valdes 2010; Mohtadi et al. 2014). Swingedouw et al (2009), for example, tested the sensitivity of last interglacial, LGM, 6 kyr BP, PI and 2xCO₂ simulations to freshwater forcing. The collapse and recovery of the AMOC is found to be similar between experiments, despite the use of differing boundary conditions, with the exception of the LGM simulation, which shows a much higher sensitivity and slower rate of AMOC recovery.

Understanding the influence of boundary conditions on the modelled climate response to simulated Heinrich events is useful both for understanding the variability observed in proxy records between Heinrich events, and for understanding the sensitivity of palaeoclimate models. Heinrich events 1–6 occurred over a period of ~50 kyr, during which time changes in insolation parameters and greenhouse gas concentrations led to a range of climate states, which inevitably affected the global manifestation of Heinrich events. In the western equatorial Pacific, for example,

speleothems from Borneo record the presence of H1–6 as dry precipitation anomalies, however the magnitude and nature of these signals varies between events, from short-lived and somewhat unclear excursions during H2–4, to larger excursions during H1 and 5, and a prominent dry anomaly during H6 (Figure 2.1) (Carolin et al. 2013).

Examining the role of boundary conditions on modelled climate also provides an opportunity to explore the sensitivity and internal dynamics of the model used. The magnitude and nature of any observed differences between boundary condition runs assists in developing our understanding of the model sensitivities and physical

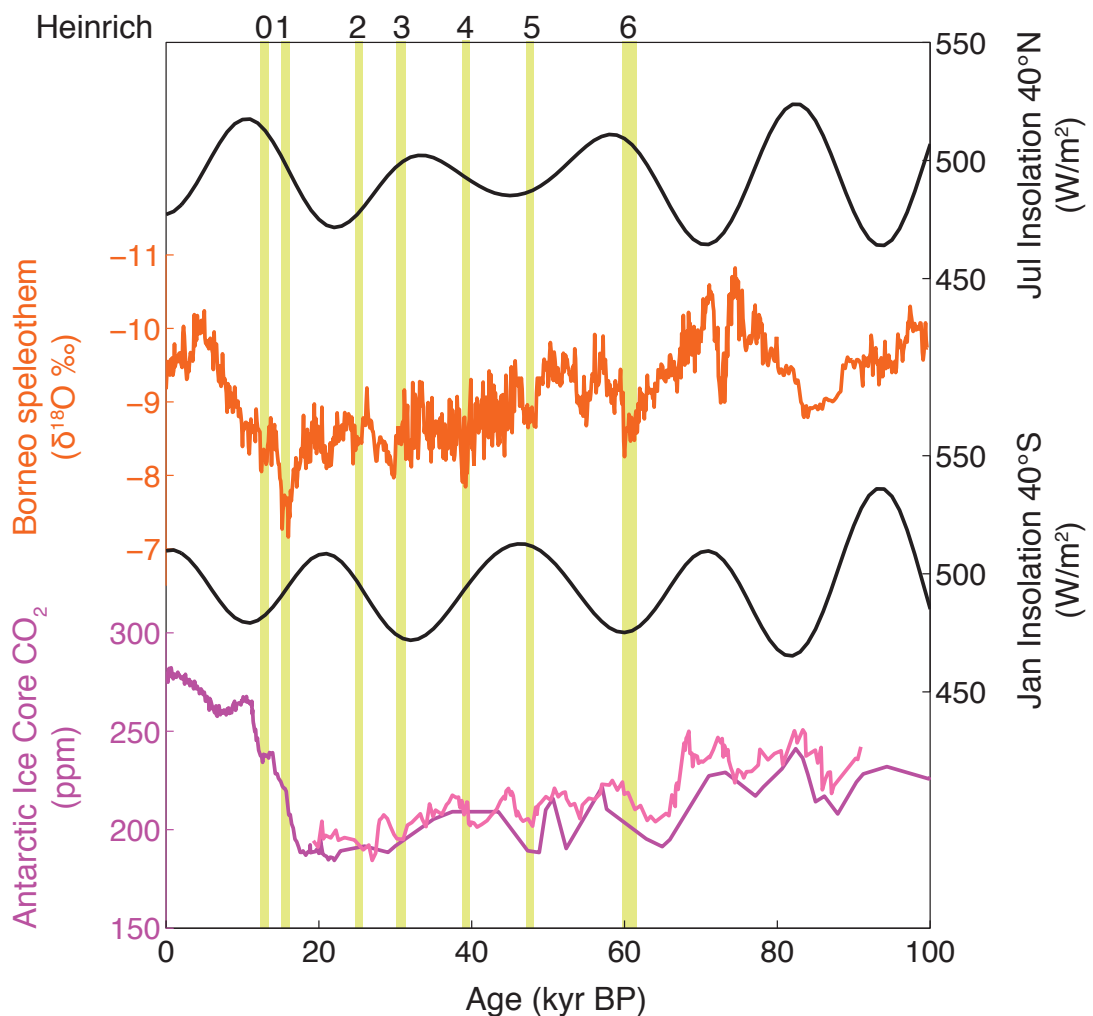


Figure 2.1: Heinrich events as seen in speleothems from Borneo. Top black: July insolation at 40°N, Orange: Borneo speleothem $\delta^{18}\text{O}$ (Carolin et al. 2013), Bottom black: January insolation at 40°S, Pink/purple: Antarctic CO_2 from EPICA Dome C and (purple; Monnin et al. 2001) the Byrd ice core (pink; Ahn and Brook 2007; Ahn and Brook 2008). Heinrich events 1–6 are shaded in yellow. Note that the Heinrich events occur during a range of insolation and CO_2 conditions.

mechanisms associated with abrupt climate shifts. This potentially allows for the study of threshold effects if the climate is moved closer to a tipping point under a certain background climate state. For example, a hosing simulation run under both northern and southern insolation maxima provides information on the reproducibility of the model's response to freshwater forcing, as well as the model's sensitivity to insolation parameters.

2.4. CSIRO Mk3L v1.2

We have chosen to use the CSIRO Mk3L palaeoclimate model for our hosing experiments, as it has the advantages of a fully coupled GCM (realistic model physics, dynamic model components), combined with a resolution that is coarse enough to make it computationally efficient. The time taken for a model to run is heavily dependent on the model resolution, with a doubling of resolution adding approximately ten times the computing time required to complete a run (UCAR 2011). The resolution of the CSIRO Mk3L is both fine enough that it contains a realistic representation of global geography and physics, but coarse enough that one model year can be run in 40 minutes, using only 4 CPUs. This makes the CSIRO Mk3L ideal for running multiple millennial-scale simulations to test the influence of various forcing parameters.

The CSIRO Mk3L climate model is a fully coupled atmosphere-land-sea ice-ocean GCM, capable of modelling the dynamic response of the climate system to imposed forcing events on millennial timescales (Phipps et al. 2011). It includes atmospheric, land surface, sea ice and ocean model components, which are coupled every hour, in order to simulate diurnal cycles in sea surface temperature (SST) and salinity. This rate of coupling allows the model to better represent the tropical climate, including processes such as the El Niño Southern Oscillation (ENSO). Flux adjustments are not required, as the model is stable on millennial time scales; however, they are applied in order to maintain a more stable climatology. We use version 1.2 of this model, which includes an enhanced spatial resolution within the ocean module (Phipps et al. 2013). A full description of the CSIRO Mk3L GCM climate model can be found in Phipps (2010) and Phipps et al. (2011).

Three key modules comprise the atmospheric, land and sea ice components of the CSIRO Mk3L model: the atmospheric model, the land surface model and the sea ice

model. Each of these components has a resolution of 5.6° lat x 3.2° lon. The atmospheric model has 18 vertical levels, and simulates a variety of variables including temperature, precipitation, cloud properties, wind and evaporation. The land surface model includes 13 land surface/vegetation types and nine soil types, as well as six soil thickness layers. A snow model calculates the temperature, density, thickness and albedo of snow packs. Ice sheets are not dynamically represented; however, there are land surface and soil types that represent the presence of persistent ice cover. The sea ice model simulates dynamic sea ice, which is influenced by wind, ocean temperatures and currents. When the ocean temperature within a given grid box falls below -1.85°C , it is converted to sea ice.

The ocean model has a resolution of 2.8° lat x 1.6° lon x 21 vertical levels. The higher resolution of the ocean model is possible due to the computationally efficient nature of the ocean module, which allows for increased resolution without greatly increasing the total time taken to run the model. Bottom topography is derived from the ETOPO2v2 bathymetry data set (U.S. Department of Commerce et al. 2006). Fields for SST, sea surface salinity (SSS) and the zonal and meridional components of the surface velocity are passed to the atmospheric module every hour and are used to drive the remaining model modules.

2.4.1. Model validation

The CSIRO Mk3L climate model has been extensively validated against modern climate observations, demonstrating the model's ability to realistically simulate a known climate state. Surface air temperature and precipitation are well represented within CSIRO Mk3L, with a realistic representation of the ITCZ and the model surface air temperature matching reanalysis data within 1°K over 56% of the Earth's surface, and within 2°K over 85% (Figure 2.2)(Phipps et al. 2011). The rate of North Atlantic Deep Water (NADW) formation is slightly too weak within the model: 14.7 Sv compared to an observed rate of 15–20 Sv. However, it is comparable to other models with similar physics and spatial resolutions (Phipps et al. 2011).

The CSIRO Mk3L has been used previously to simulate tropical Pacific palaeoclimates, including ENSO, (Phipps and Brown 2010; Santos et al. 2011; Santos et al. 2012; Borlace et al. 2013), supporting our use of this model over this region. The

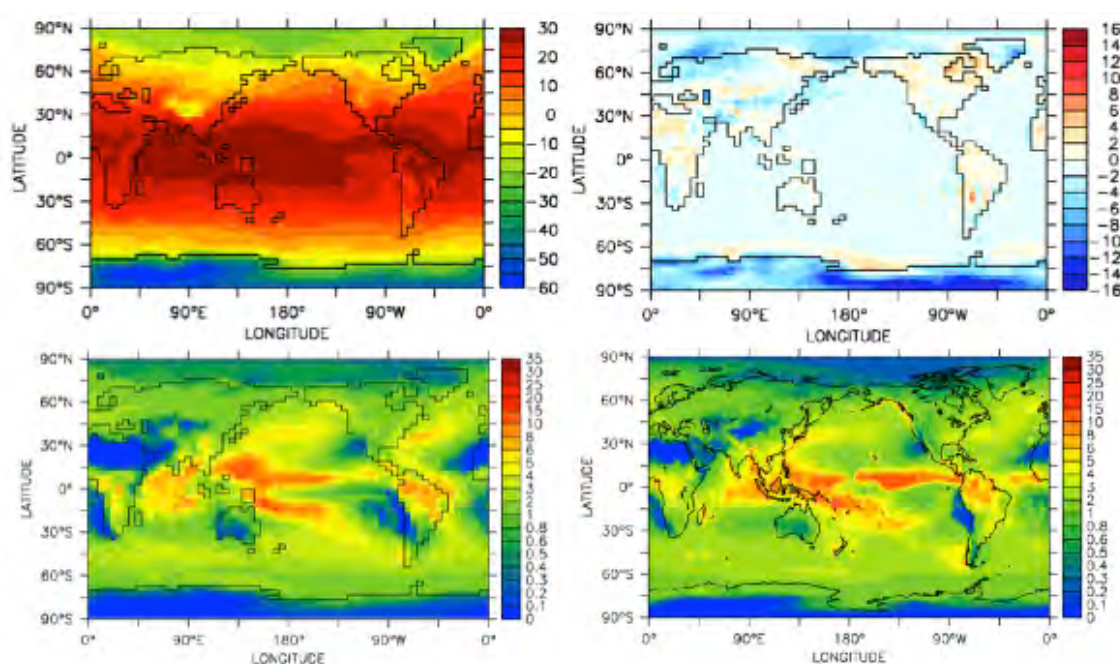


Figure 2.2: Validation of CSIRO Mk3L control climatology. Top: Annual mean temperature ($^{\circ}\text{C}$) for CSIRO Mk3L (left) and CSIRO Mk3L minus NCEP2 reanalysis for 1979–2003 (right). Bottom: Annual mean precipitation (mm/day) for CSIRO Mk3L (left) and the Legates and Willmott observational climatology v2.01 (1990; right). Figures from Phipps et al. (2011).

variability of ENSO within the CSIRO Mk3L was validated over the Holocene, and shown to compare well to coral proxy records from the central Pacific (Phipps et al. 2013). Additionally, simulations from the CSIRO Mk3L model have contributed to the PMIP and CMIP (Climate Model Intercomparison Project) and have been analysed as a member of a multi-model ensemble of monsoon rainfall dynamics (Tao et al. 2010; Jiang et al. 2013; Zheng and Braconnot 2013; Zheng et al. 2013; Li et al. 2014; Perez-Sanz et al. 2014).

2.5. Experiment design

2.5.1. Experiment one: Hosing sensitivity test

A hosing sensitivity test was carried out with the CSIRO Mk3L model in order to examine the influence of different hosing experimental designs on the modelled climate sensitivity. Hosing experiments had not previously been performed with the CSIRO

Mk3L model so sensitivity experiments were required to assess the model's response to forced changes in the AMOC.

2.5.2. Experiment two: Hosing under changed orbital configuration

The influence of precession on the modelled climate response to a simulated Heinrich event is examined. We test the model's response to hosing under both a northern hemisphere and southern hemisphere summer insolation maximum to see what effect, if any, this has on the climate.

2.5.3. Experiment three: Hosing under changed atmospheric CO₂ concentrations

Here we investigate the influence of 400 ppmv CO₂ concentrations on the climate's response to a simulated Heinrich event. This experiment represents an idealised scenario, where the climate has been allowed to equilibrate to the changed CO₂ concentration before applying the hosing – a scenario that is unlikely under anthropogenic climate change due to the high rate of change in CO₂ forcing. The volume of freshwater added to the North Atlantic in this experiment (a total of ~8.8 metres sea level equivalent (msle)) is greater than the total volume locked up within the Greenland ice sheet (~6 msle). We therefore use this experiment to examine the dynamical climate response to a perturbation of the AMOC, rather than as a realistic indicator of possible future climate change.

2.5.4. Target areas

In order to determine the strength and nature of the modelled climate response to the outlined experiments, we will focus our analysis on four key target areas (Figure 2.3):

1. North equatorial Atlantic
2. South equatorial Atlantic
3. NINO 3.4 region

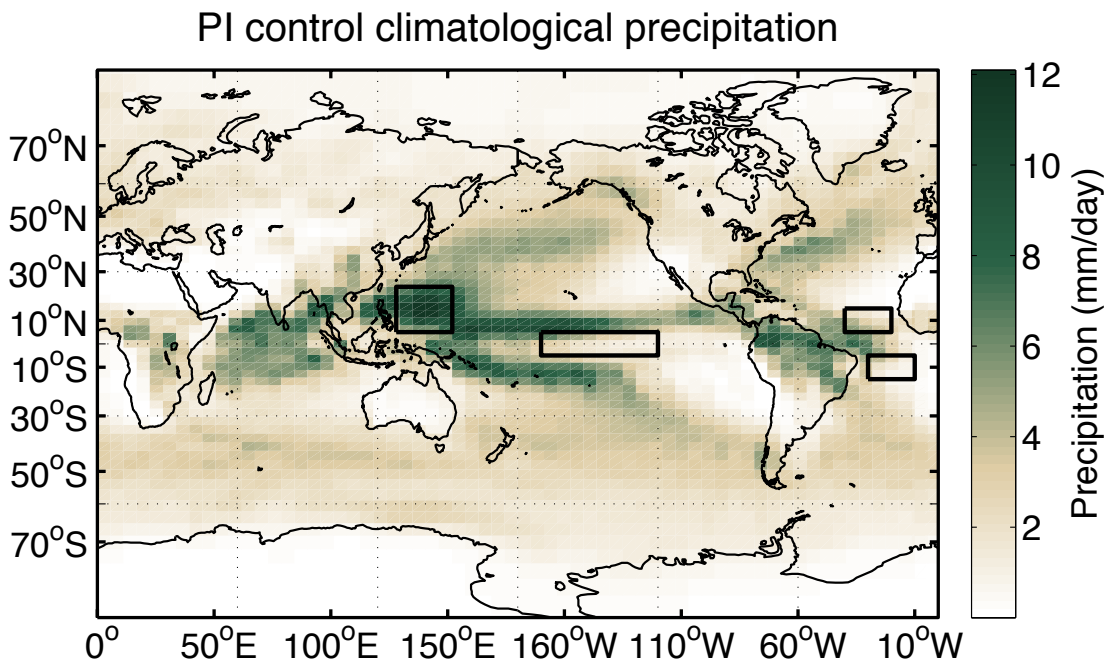


Figure 2.3: Mean annual precipitation (mm/day) for the pre-industrial (PI) control experiment. Four target areas used in this study are outlined in black (left to right): WPWP, NINO 3.4 region, north equatorial Atlantic and the south equatorial Atlantic. Note that the region representing the WPWP is located to the northeast of the centre of the actual warm pool, in a homogenous region outside of the influence of model land/sea boundaries, which may skew the results.

4. Western Pacific Warm Pool (WPWP)

Examination of the climatic response of the north and south equatorial Atlantic provides a diagnostic of the magnitude and nature of the response of the AMOC to the model forcing. The size of anomalies in this region also determines the strength of teleconnections into the Pacific, influencing the strength of the anomalous easterlies across the Isthmus of Panama, providing information on the ability of the forced North Atlantic anomaly to move into the Pacific via atmospheric pathways across the Americas (e.g. Zhang and Delworth 2005; Dong and Sutton 2007; Timmermann et al. 2007b). Relative changes in the strength of the NINO 3.4 region and the WPWP could also provide evidence of the nature of the teleconnection into the western Pacific. This could suggest whether anomalies are propagated across the Pacific Ocean or via the strength and position of the westerly jet across the Eurasian landmass into the northern Australasian monsoon domain (e.g. Sun et al. 2012).

Teleconnections into the tropical Pacific via the Isthmus of Panama will generate anomalies in the NINO 3.4 region, allowing us to track the progress of climate anomalies across the Pacific. This region is also intimately connected to the western equatorial Pacific via the mechanisms of ENSO, providing information on the behaviour of the tropical Pacific.

The western equatorial Pacific is the key focus of our study, as we hope to dynamically understand the nature of Heinrich events within this region. We will be comparing model results with proxy records from this region in order to better understand the drivers of Heinrich events and the influence of boundary conditions on their manifestation across the western equatorial Pacific. It is important to note that we will be using a target area just to the northeast of the central WPWP in the CSIRO Mk3L to represent the behaviour of the warm pool itself (Figure 2.3). This is done to avoid model artefacts caused by land/sea boundaries within the model warm pool, which may skew the results in this region.

We will also be examining the response of large-scale climate features including the ITCZ and the Southern Ocean westerly winds. Changes in the behaviour of these features have important influences on the organisation and behaviour of atmospheric circulation, which can feed back and affect the climate response to the applied freshwater perturbations in locations outside of the Atlantic Ocean basin. These features can influence the strength and behaviour of teleconnections from the North Atlantic, and will be important in understanding the drivers of observed changes.

2.6. Experiment one: Hosing sensitivity test

2.6.1. Experiment design

The sensitivity of the CSIRO Mk3L GCM to abrupt climate forcing was tested using three hosing experiments of different magnitudes. The three sensitivity experimental designs were:

- 0.1 Sv for 100 years (hereafter S0.1/100)
 - = 0.88 metres sea level equivalent (m.s.l.e.)

- Following the PMIP2 protocol (Stouffer et al. 2006)
- 1 Sv for 100 years (hereafter S1/100)
 - = 8.8 m.s.l.e.
 - Following the PMIP2 protocol (Stouffer et al. 2006)
- 2 Sv for 50 years (hereafter S2/50)
 - = 8.8 m.s.l.e.

The three experiments were designed to examine the influence of magnitude (S1/100 and S2/50 both were hosed with the same volume of water, but over different time periods); versus duration of hosing on the modelled climate response (S0.1/100 and S1/100 were both hosed over the same period, but with different volumes of water).

The freshwater was applied uniformly across the North Atlantic Ocean, from 50°–70°N, following the established PMIP protocol (Stouffer et al. 2006). Pre-industrial boundary conditions were used (present-day orbital configuration, 280 ppmv CO₂) and following the period of hosing, the model was allowed to re-equilibrate. A control experiment was run using the same preindustrial boundary conditions; however, no perturbation was applied.

Three key parameters will be discussed in the subsequent results sections (with a fourth parameter – surface wind stress and MSLP – discussed for the boundary condition experiments):

1. AMOC overturning (determined by finding the maximum meridional overturning streamfunction value in the North Atlantic (30°–50°N))
2. SST
3. Precipitation.

These parameters represent the majority of the climate model responses, with other variables mirroring changes in these parameters. For example, changes in surface air temperature and MSLP closely mirror changes in SST, precipitation and meridional and zonal wind fields.

2.6.2. AMOC overturning

In all three experiments, the rate of AMOC overturning was reduced during the period of freshwater hosing, before recovering following the cessation of forcing and overshooting the initial control AMOC strength, and finally returning to the strength seen in the control run (Figure 2.4). Experiment S0.1/100 recorded the smallest perturbation to the AMOC, because of the relatively small freshwater forcing applied. The rate of AMOC overturning halved by year 95 of the experiment, reaching 6.4 Sv, from an initial rate of 12.8 Sv (50% reduction). Following the cessation of hosing, the AMOC quickly recovered, overshooting to a maximum strength of 19.3 Sv ~140 years after the forcing stopped, before returning to the control strength approximately 100 years later (Figure 2.4).

The AMOC response in experiments S1/100 and S2/50 was similar, despite the fact that the same volume of freshwater was applied over different periods for each experiment. The same amount of freshwater was applied in each experiment (8.8 msle); however, the period of application was halved in experiment S2/50, compared to S1/100. Despite this, the behaviour and timing of recovery was similar between experiments (Figure 2.4). In S1/100, the AMOC completely shut down by year 90, with the AMOC in S2/50 essentially shutting down by year 46 (1.9 Sv). The recovery of both experiments took approximately the same time, with experiment S1/100 reaching its maximum AMOC strength ~310 years after the forcing was switched off, compared to S2/50, at year ~330. Both experiments then returned to similar AMOC strengths at the end of the experiment.

Experiments of equal forcing size (S1/100 and S2/50) behaved similarly when compared to experiments forced over the same period but at different rates (S0.1/100 and S1/100), which show large differences in AMOC behaviour. Experiment S1/100 and S2/50 both show a similar rate of AMOC collapse and recovery, despite the fact that the freshwater was applied twice as fast in S2/50. Experiment S0.1/100, which was perturbed over the same period as S1/100, but with a smaller forcing, showed a smaller reduction in AMOC strength, and a faster recovery (Figure 2.4).

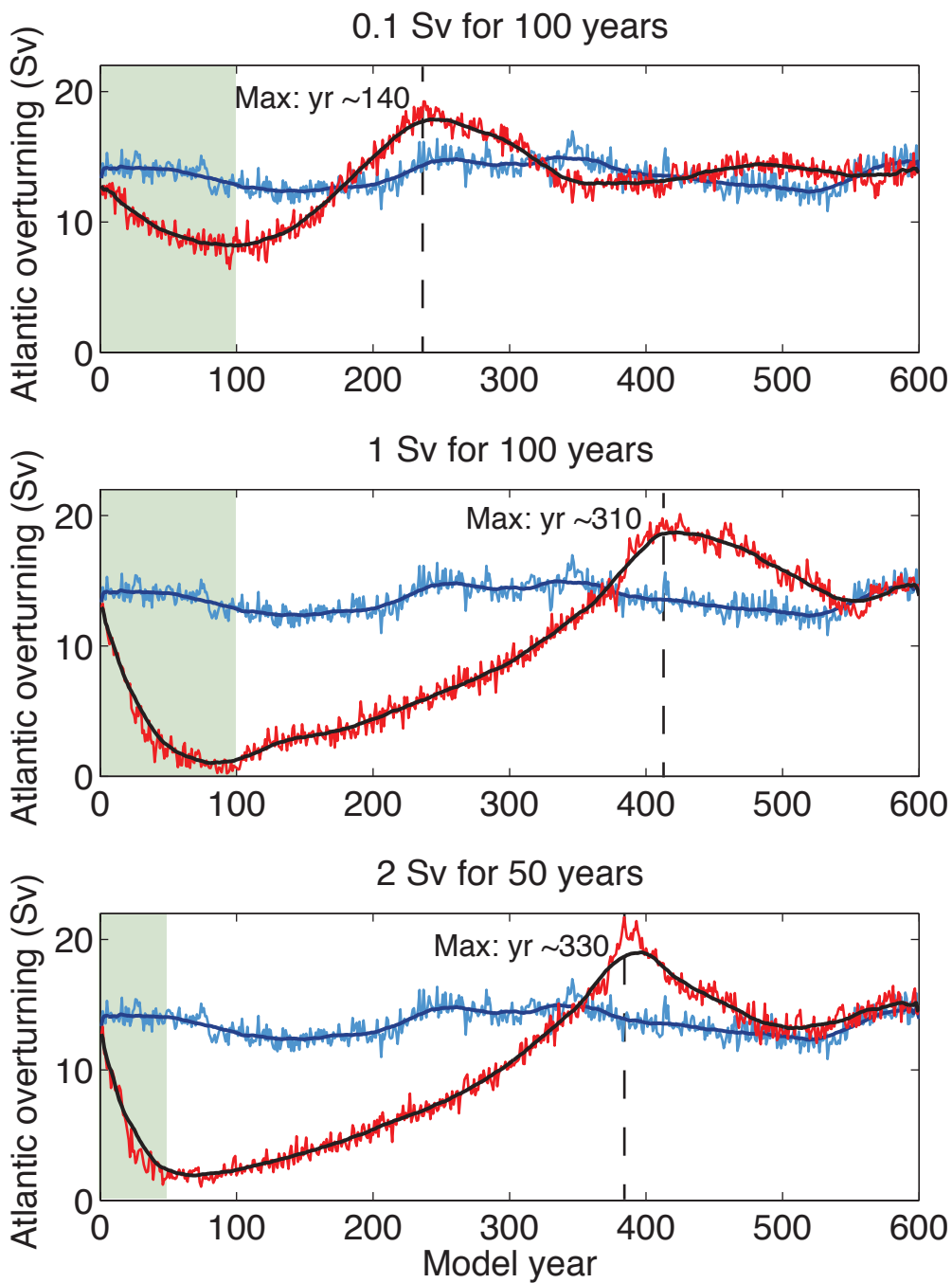


Figure 2.4: Atlantic meridional overturning strength in each of the three sensitivity experiments (red), with a 10-year moving average (black). The control runs are shown in blue, with a 10-year moving average in dark blue. The periods of freshwater hosing are shaded in green. The vertical dashed line in each plot shows the timing of the maximum in AMOC strength. Maximum years are given in years since the cessation of freshwater forcing.

2.6.3. SST response

A bipolar SST anomaly developed in the tropical Atlantic in all three hosing experiments; however, the size of the anomaly was strongest in experiments S1/100 and S2/50, with S0.1/100 showing anomalies only slightly greater than the natural/control variability (Figure 2.5 and Figure 2.6). S1/100 and S2/50 both show a cooling anomaly in the northern equatorial Atlantic and a warming anomaly in the southern equatorial Atlantic, indicative of a reduction in northward heat transport caused by the slowdown

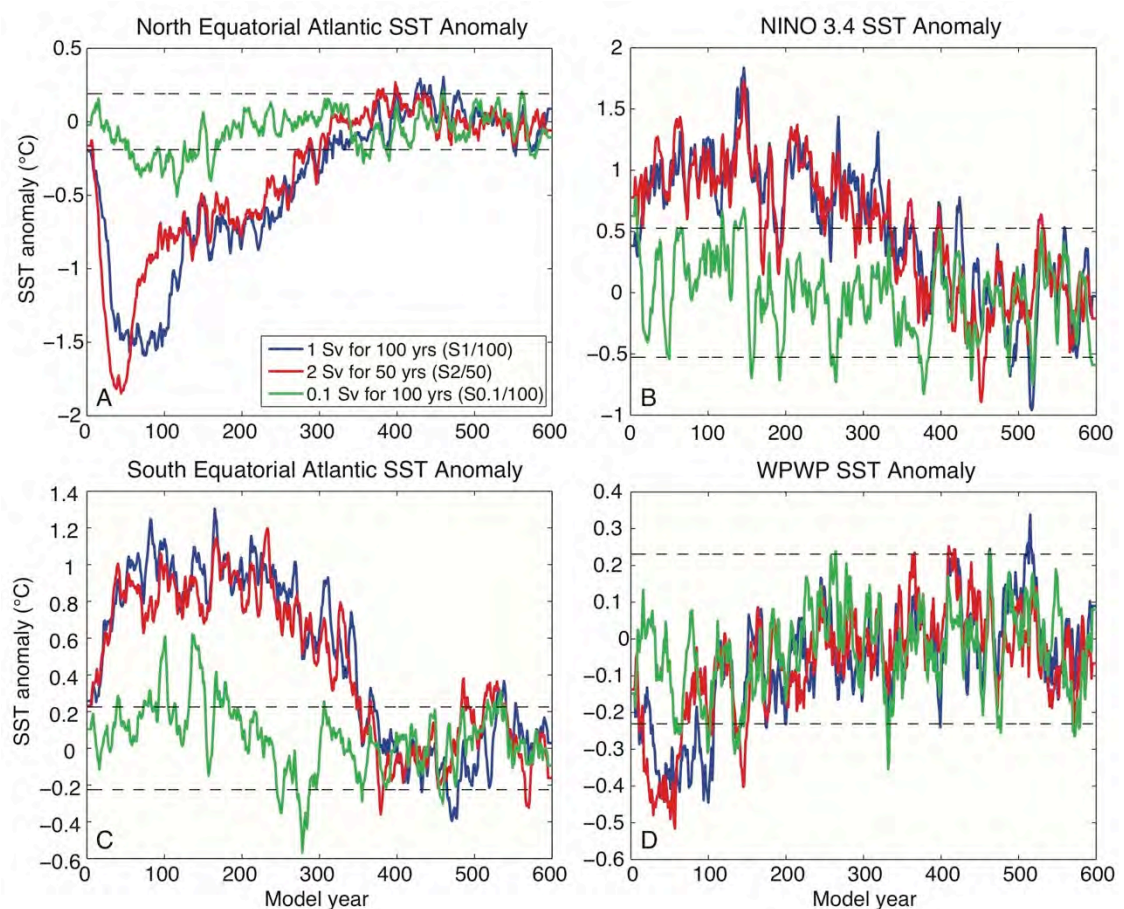


Figure 2.5: SST anomalies for the three sensitivity experiments. (A) Modelled SST anomalies for the north equatorial Atlantic for the three sensitivity experiments. (B) As in (A) but for the NINO 3.4 region of the central Pacific. (C) As in (A) but for the south equatorial Atlantic. (D) As in (A) but for the Western Pacific Warm Pool. Dashed lines depict 1-sigma variability within the control run for each region. See Figure 2.3 for an explanation of the regions examined. Note that experiment S2/50 (red) was hosed for half as long as S1/100 and S0.1/100 (see Figure 2.4).

of the AMOC. S0.1/100 shows a much weaker bipolar SST anomaly, which peaked in the 50 years after hosing ceased (model year 100–150; Figure 2.5).

The SST anomalies in the NINO 3.4 region of the central Pacific vary according to magnitude of hosing, but not the rate of hosing. Experiment S0.1/100, which applied only 0.88 m.s.l.e. of freshwater to the North Atlantic, shows no discernible SST anomalies in the central Pacific, with values varying within the range of the control experiment. Both S1/100 and S2/50, which applied freshwater forcing one order of

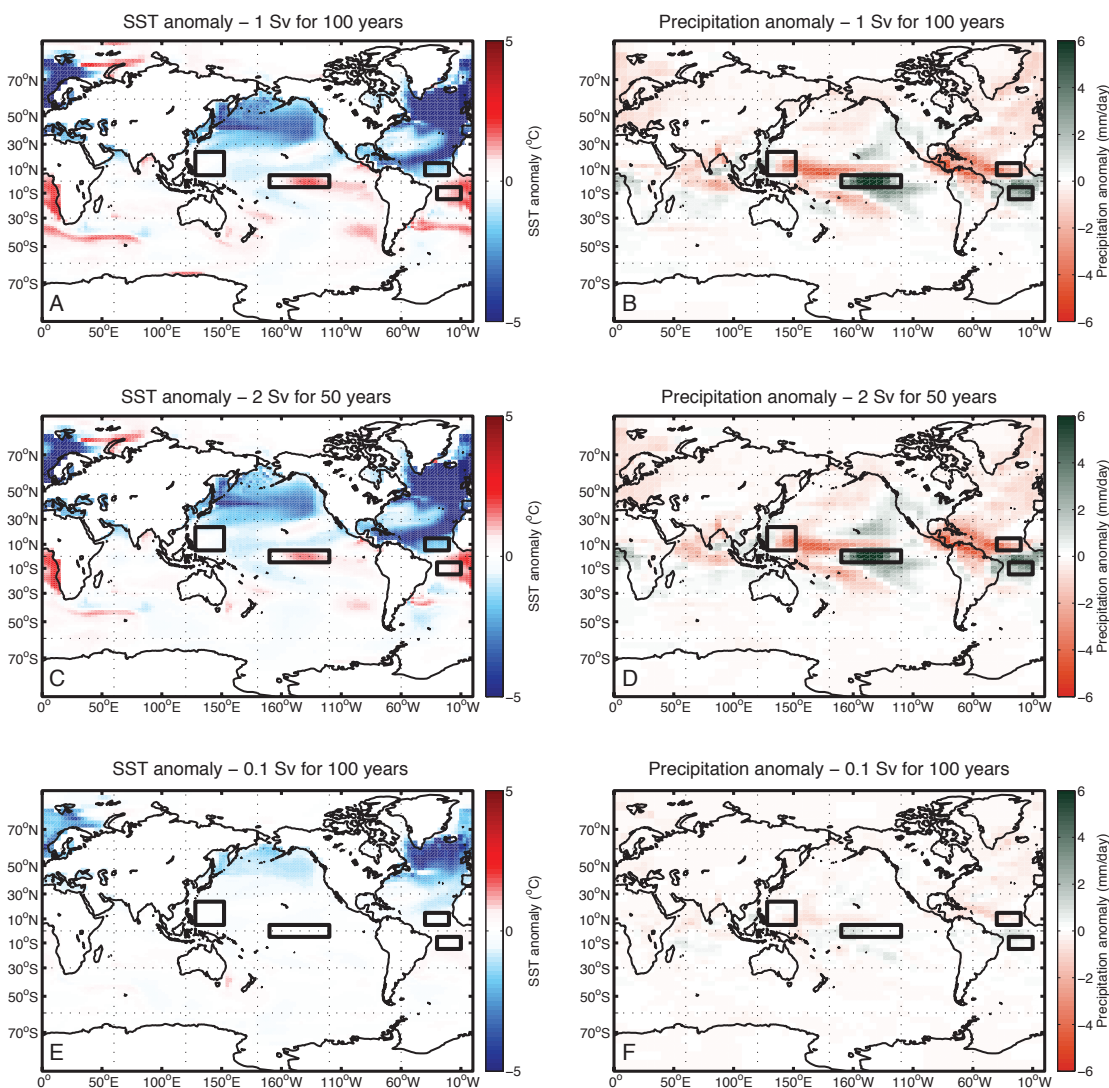


Figure 2.6: SST and precipitation anomalies for the three sensitivity experiments. The mean climate of the last 20 years of the hosing period is shown for each plot (years 80–100 for S1/100 and S0.1/100, and years 30–50 for S2/50).

magnitude larger than S0.1/100 (8.8 m.s.l.e.), show a warming anomaly in the NINO 3.4 region. The spatial pattern of this warming anomaly shows characteristics similar to the typical El Niño pattern, with relatively cool SSTs in the western Pacific (Figure 2.6). SST anomalies in the WPWP are evident, although short-lived, for experiments S1/100 and S2/50; however, experiment S0.1/100 does not record anomalies in this region outside that seen in the model control run (Figure 2.5).

While all three experiments developed a bipolar seesaw in the equatorial Atlantic in response to freshwater forcing of the North Atlantic, this anomaly was only strongly significant in experiments S1/100 and S2/50. These two experiments also propagated climate anomalies into the tropical Pacific Ocean, with SST anomalies seen in both the NINO 3.4 region and the WPWP.

2.6.4. Precipitation

Precipitation anomalies mirror SST anomalies, with experiments S1/100 and S2/50 recording strong regional precipitation anomalies, and S0.1/100 recording weak, or no precipitation anomalies, particularly outside of the Atlantic Ocean basin (Figure 2.6). The bipolar SST anomalies within the Atlantic Ocean are mirrored in a southward shift of the ITCZ, bringing strong wet precipitation anomalies to the south equatorial Atlantic, and dry precipitation anomalies to the north equatorial Atlantic in S1/100 and S2/50 (Figure 2.7). Experiment S0.1/100 shows a weak southward shift of the ITCZ, again peaking in the 50 years after hosing ceased.

Precipitation anomalies in the NINO 3.4 region of the central Pacific, and in the Western Pacific Warm Pool (WPWP) show clear anomalies for the large hosing experiments, and no discernable anomalies beyond the control run variability for the weak hosing experiment (Figure 2.7). A strong increase in precipitation occurs in the NINO 3.4 region in experiments S1/100 and S2/50, mirroring the El Niño-like pattern in the ocean (Figure 2.6). Reduced precipitation is evident in the WPWP region; however, this anomaly only weakly exceeds the model variability in this region (Figure 2.7B and D). No precipitation anomalies are evident in either the NINO 3.4 region or the WPWP for experiment S0.1/100.

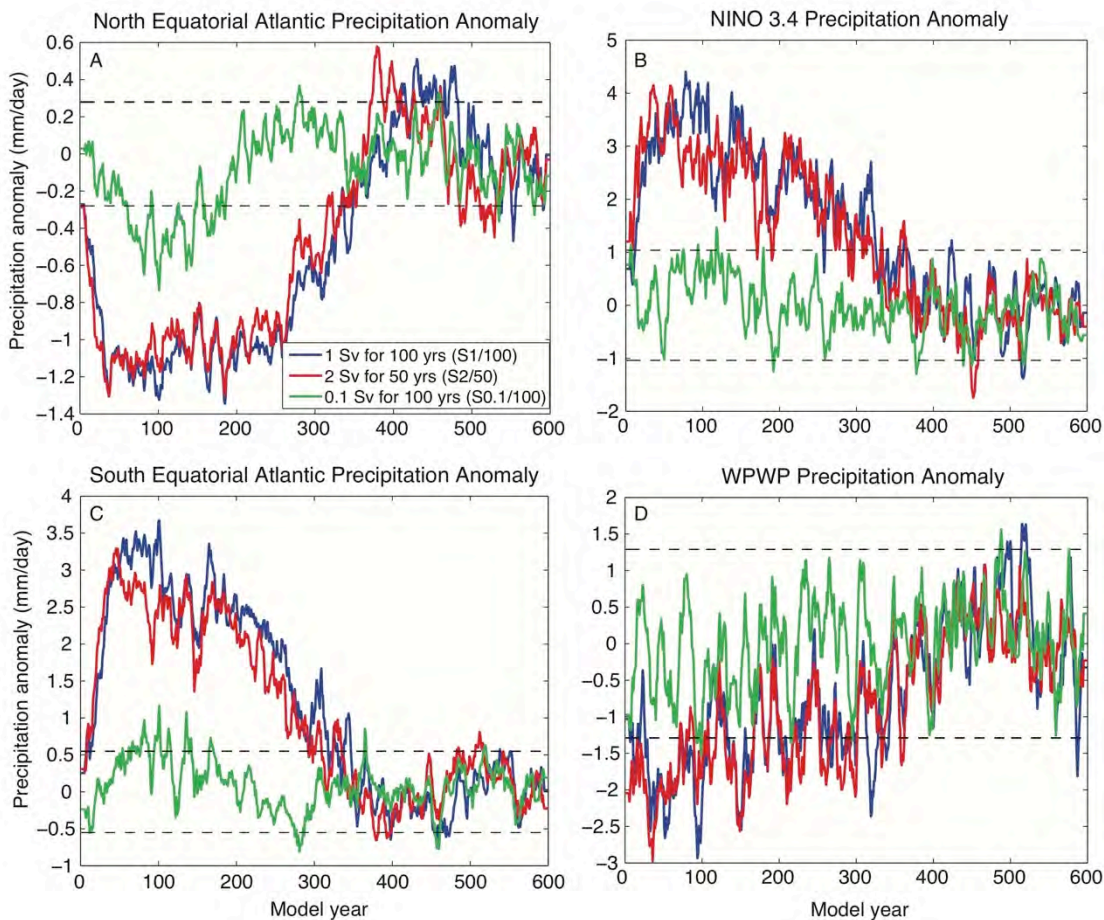


Figure 2.7: Precipitation anomalies for the three sensitivity experiments. (A) Modelled precipitation anomalies for the north equatorial Atlantic. (B) As in (A) but for the NINO 3.4 region of the central Pacific. (C) As in (A) but for the south equatorial Atlantic. (D) As in (A) but for the Western Pacific Warm Pool (WPWP). Dashed lines depict 1-sigma variability within the control run for each region. See Figure 2.3 for an explanation of the regions examined. Note that experiment S2/50 (red) was hosed for half as long as S1/100 and S0.1/100 (see Figure 2.4).

2.6.5. Conclusions

The hosing sensitivity tests carried out using the CSIRO Mk3L model demonstrate that the magnitude, rather than the duration of freshwater forcing determines the climatological response. Experiment S0.1/100, which added the smallest amount of freshwater to the North Atlantic shows weak climatological anomalies within the Atlantic Ocean basin and little to no signal outside of this region (Figure 2.6).

The two experiments with larger freshwater forcing – S1/100 and S2/50 both show strong climate anomalies within the Atlantic Ocean and display teleconnections

into the eastern Pacific and, to a lesser extent, the western Pacific. Proxy records of Heinrich events record climatological responses to freshwater forcing as far away as the WPWP (e.g., Partin et al. 2007; Griffiths et al. 2009; Ayliffe et al. 2013; Carolin et al. 2013), suggesting that a larger freshwater forcing is required to more accurately model the proxy records. The S1/100 experimental design was used as part of the PMIP2 suite of experiments, and we therefore use this freshwater forcing scenario for the remainder of the hosing experiments.

2.7. Experiment two: Changed orbital configuration

2.7.1. Experiment design

The response of the climate system to a freshwater perturbation under two orbital configurations was tested. In the modern day, the ~23 kyr precession cycle is in its southern summer maximum phase, with an insolation maximum over the southern hemisphere during austral summer and an insolation minimum over the northern hemisphere during boreal summer (Figure 2.1). A pre-industrial experiment was carried out, using 280 ppmv of CO₂, and modern orbital configuration (hereafter experiment OSH – orbital southern hemisphere maxima). We tested the influence of the orbital configuration on the climate response to a freshwater perturbation by simulating a 10 kyr BP orbital configuration, which represents a precessional phase change, with a northern hemisphere summer insolation maximum (hereafter experiment ONH – orbital northern hemisphere maxima). All other variables, including CO₂, were held constant.

Both simulations were equilibrated prior to the application of 1 Sv of freshwater forcing to the North Atlantic for 100 years (the same hosing design as experiment S1/100). Two control experiments were run, using the OSH and ONH orbital boundary conditions; however, no freshwater perturbation was applied. A model ensemble was constructed for both ONH and OSH hosing experiments, whereby three simulations were carried out using the same model parameters, but were started from different years of the control experiment. This was done to ensure that any variability in the control run did not affect or skew our results. Anomalies were calculated for each individual

experiment by subtracting the forced run from the respective control run. An ensemble mean for each set of simulations (ONH and OSH) was produced by calculating the average anomaly for each set of three experiments to ensure that results were reproducible and reflected a forced response rather than internal variability. The difference between experiments OSH and ONH is taken to reflect the influence of orbital configuration on the modelled climate response to a simulated Heinrich event.

2.7.2. Control boundary conditions

In order to assess the impact that changed orbital configuration has on the modelled climate response to North Atlantic freshwater forcing; we first need to examine the nature of the climate response to changed boundary conditions. To do this, climatologies were created for each control run by averaging model parameters over the entire run length. The difference between the northern hemisphere and southern hemisphere summer insolation maxima control climatologies was examined by subtracting the 0 kyr control (experiment OSH) from the 10-kyr control (experiment ONH) (Figure 2.8). The difference between these two experiments reflects the influence of changed orbital parameters on the model boundary conditions. The model response to a change in orbital parameters is consistent with other studies, increasing our confidence in the model's ability to accurately simulate orbitally-forced climate changes (e.g. Liu et al. 2003; Lorenz et al. 2006; Timmermann et al. 2007a; Li and Harrison 2008).

Surface air temperatures and SSTs show similar patterns of difference, with warm anomalies in the high latitudes in experiment ONH, compared to OSH (Figure 2.8A and B). The movement of the summer insolation maximum into the northern hemisphere can likely account for the warmer temperatures across much of the northern latitudes. Relatively warmer temperatures across the Southern Ocean in ONH are caused by weaker westerly winds over this region, which diminish upwelling of cool, deep waters (Figure 2.8B and G). Relatively strong reductions in sea ice in the Arctic Ocean (Figure 2.8F) and an accompanying sea surface freshening (Figure 2.8D) in this region in ONH follow an increase in temperatures across the Arctic. The tropics are generally cooler in ONH, compared to OSH, because of a reduction in the strength of the Walker circulation, and a northward shift and narrowing of the ITCZ (Figure 2.8C and G).

ONH control – OSH control

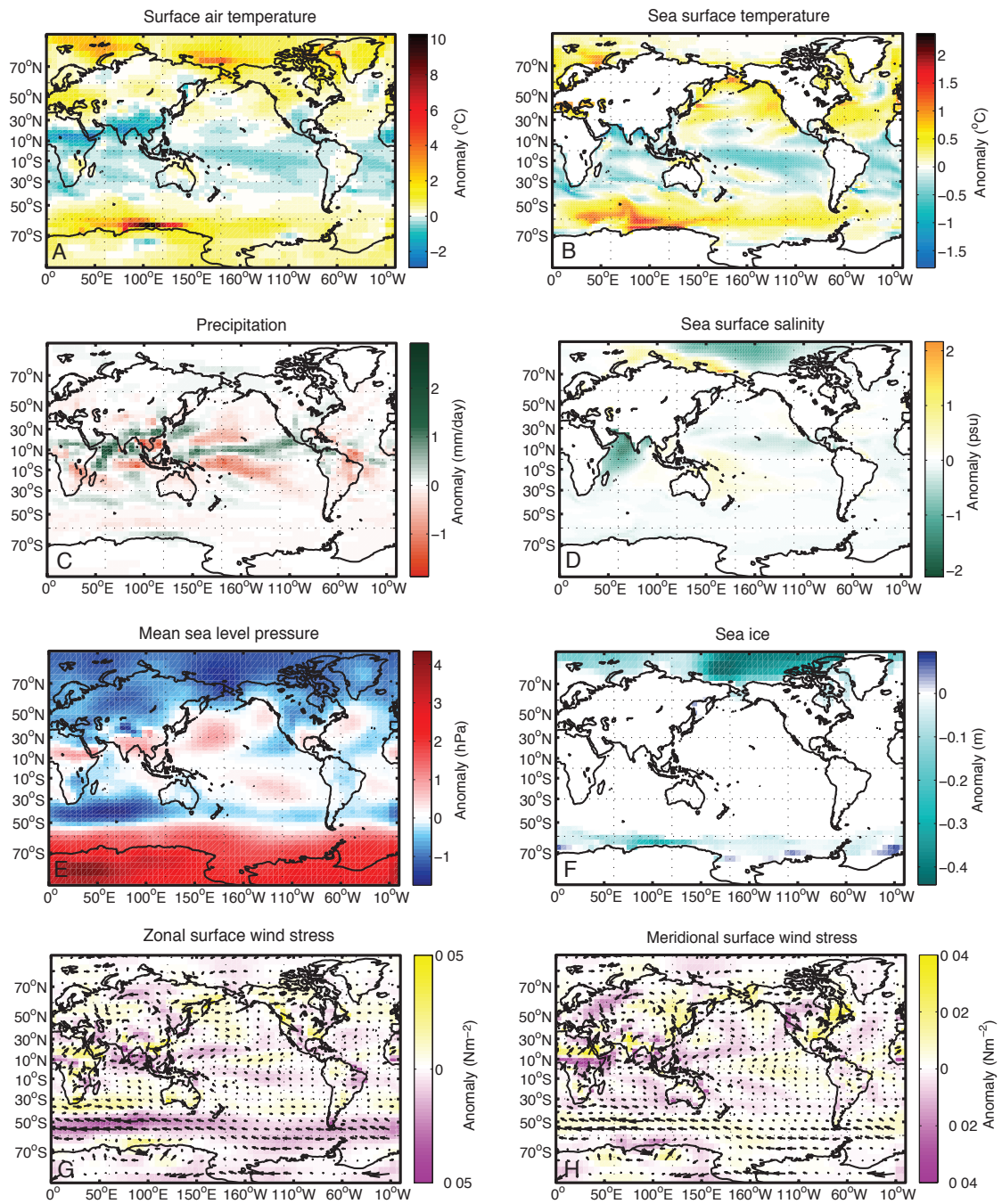


Figure 2.8: Influence of changed orbital parameters on model boundary conditions. Anomalies for each variable were calculated by subtracting the run climatologies from each control (ONH–OSH). Wind vector anomalies (arrows) are shown overlying shaded (G) zonal and (H) meridional surface wind stress anomalies.

Precipitation changes are strongest throughout the tropics in both experiments, with the ITCZ moving to the north in ONH (Figure 2.8C). The movement of the summer insolation maximum into the northern hemisphere leads to a northward shift of the ITCZ, most notably over the Indian Ocean and Africa. A weaker shift is evident over central America and the Atlantic Ocean. A narrowing of the ITCZ occurs in the central Pacific Ocean, with negative rainfall anomalies from 10°S–5°N and 15°N–30°N, suggesting a reduction in the width of the ITCZ across this region. Stronger reductions in rainfall to the south, however, suggest a northward shift in the ITCZ in this location as well as in ONH.

Strong zonal changes in mean sea level pressure (MSLP), zonal wind stress and temperature across the Southern Ocean are related to the relaxing of thermal gradients in this region in ONH relative to OSH, caused by the northward movement of the ITCZ (Figure 2.8C) and its attendant convective cells. A reduction in the thermal gradient between the mid and high southern latitudes results in a decrease in the temperature (Figure 2.8A and B) and MSLP gradient (Figure 2.8E) between the Southern mid-latitudes and Antarctica, a weakening of the Southern Ocean westerlies (Figure 2.8G), and a reduction in Ekman upwelling, which in turn results in further warming of Southern Ocean surface temperatures (Figure 2.8B).

2.7.3. Hosing results

2.7.3.1. AMOC overturning

Freshwater forcing applied to the North Atlantic results in the shutdown of the AMOC by year 100 in both OSH and ONH, before it recovers after freshwater forcing ceases (Figure 2.9). The rate of AMOC overturning is reduced by ~94% in both OSH and ONH, relative to its starting strength, indicating similar sensitivities to the applied freshwater forcing under both orbital configurations.

The rate of recovery of the AMOC is similar in both OSH and ONH, with the ensembles reaching their maximum values in model years 423 and 434, respectively (Figure 2.9). Statistical testing using a paired sample t-test of the timing of the maximum AMOC strength of the two ensemble means indicates that the rate of recovery is not statistically different between experiments ($p=0.12$), suggesting that orbital configuration is not influencing the rate of AMOC recovery. The AMOC

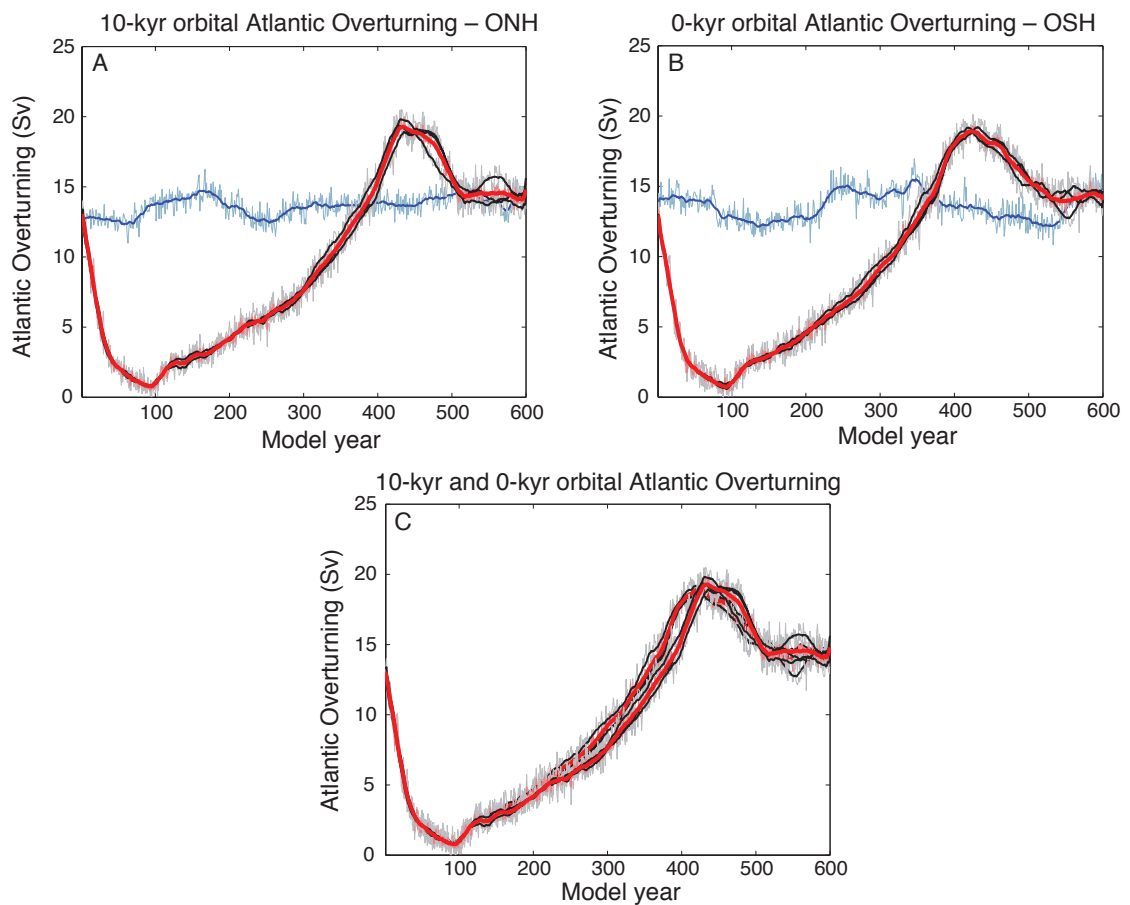


Figure 2.9: Atlantic meridional overturning in (A) 10-kyr BP orbital experiment; ONH and (B) 0-kyr BP orbital experiment; OSH. Grey lines show results from the three individual ensemble members, with a 20-year running mean for each member in black. The ensemble mean of the three runs, with a 20-year running mean is given in red. Control run variability is shown in light blue, with a 20-year running mean in dark blue. Note that ensemble members were initiated from different years of the control experiment. (C) ONH and OSH plotted together to highlight the relative timing of AMOC recovery between experiments. The difference in the AMOC recovery between experiments is not statistically significant.

strength overshoots the initial control strength in both simulations, before returning to the strength seen in the control run by the end of the experiment.

2.7.3.2. SST

Regional variability in SST is similar for the two experiments, with no discernable difference in SST behaviour because of the changed orbital forcing. A bipolar SST

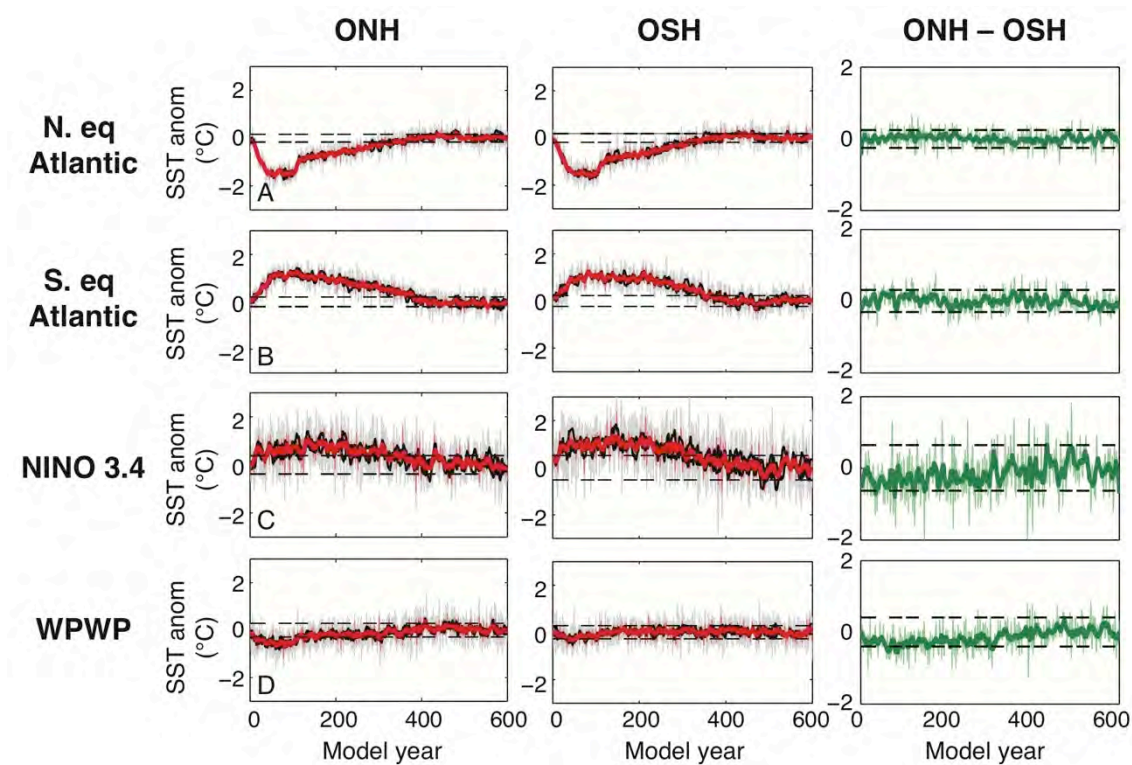


Figure 2.10: Regional SST anomalies for the four target areas. See Figure 2.3 for an explanation of the regions examined. (A) North equatorial Atlantic, (B) South equatorial Atlantic, (C) NINO 3.4, (D) Western Pacific Warm Pool. Individual run results for ONH and OSH are shown in grey, with a 10-year moving average in black. The ensemble results are shown in red with a 10-year moving average. ONH–OSH (right-hand column) shows the difference between the ONH and OSH ensembles (red lines). Dashed lines show 1-sigma variability in the control runs in columns one and two, and 1-sigma variability in the control difference in column three. Note that the ensemble mean differences are negligible for the four target areas.

anomaly is present within the equatorial Atlantic in both experiments, with the strength of the anomaly not differing between simulations (Figure 2.10A and B).

The strength of the teleconnected SST anomaly in the Pacific is slightly stronger in experiment ONH; however, the difference between the experiments is small, and not reproduced by all ensemble members (Figure 2.11). The SST anomaly in the NINO 3.4 region of the Pacific is similar between experiments, with both simulations showing a warm temperature anomaly, above that expected by modelled natural variability (Figure 2.10C). However, the nature of the anomaly within the NINO 3.4 region is not well represented within either the ONH or OSH model runs, with ensemble members of each run not agreeing on the magnitude, or sign of the anomaly (Figure 2.11).

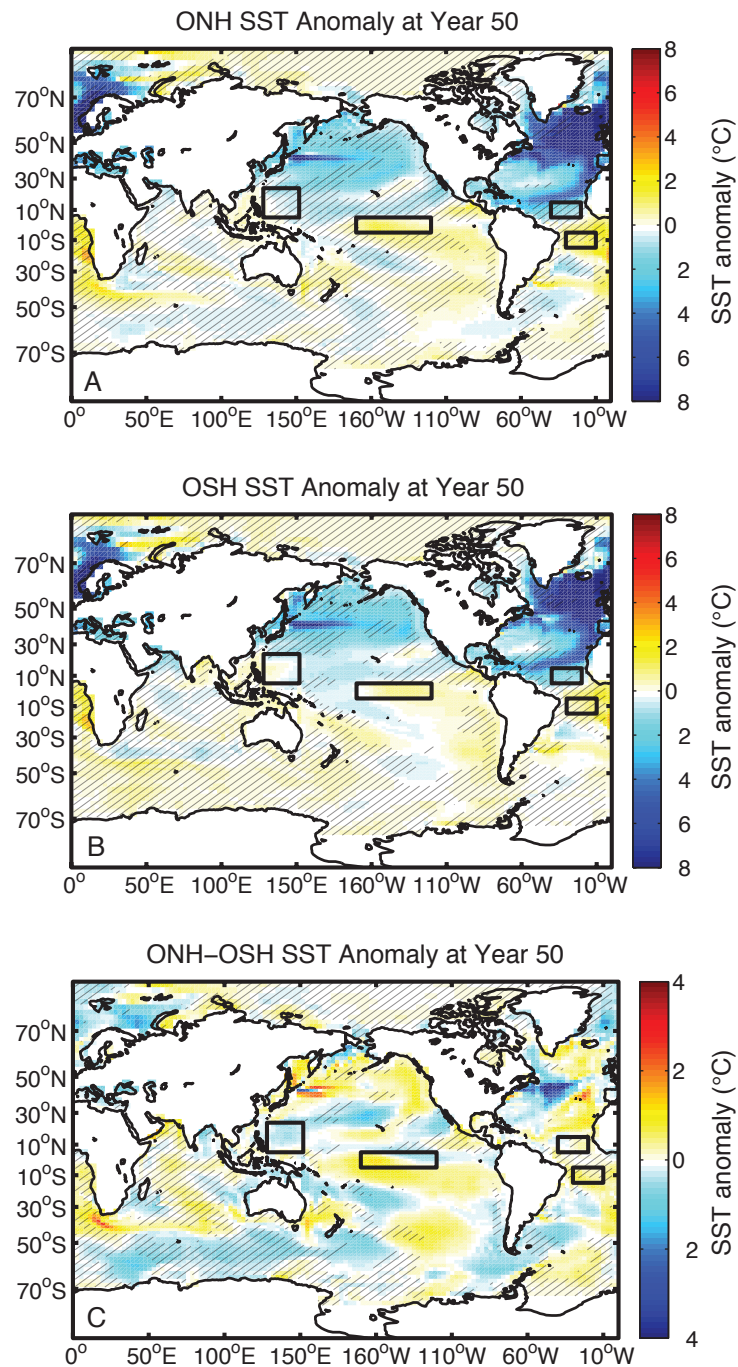


Figure 2.11: Spatial pattern of mean ensemble SST anomalies in (A) ONH, (B) OSH, and (C) ONH-OSH at year 50 (halfway through the hosing perturbation). Anomalies in (A) and (B) are calculated relative to their respective control runs. The difference between the ONH and OSH anomalies is shown in (C). Hatching in (A) and (B) denotes agreement between the three ensemble members within $\pm 0.5^\circ\text{C}$ of the ensemble mean. Hatching in (C) denotes agreement between at least 6/9 ensemble member differences within $\pm 0.5^\circ\text{C}$ of the ensemble mean difference. Note that the ensemble mean differences are negligible for the four target areas.

ONH shows a weak, cool SST anomaly in the WPWP until year 100, above the modelled natural variability, with experiment OSH not recording an abnormal anomaly in SST in this region (Figure 2.10D). Although the anomaly is weak in ONH, it is present across ensemble members (Figure 2.11), and together with the positive anomaly across parts of the central Pacific, suggests a weak El-Niño-like state of the Pacific in response to North Atlantic freshwater hosing (Figure 2.11). The lack of consistent anomalies in the central and western Pacific in OSH, suggest a weaker long-range teleconnection in this experiment. Additional simulations would improve the certainty of this conclusion.

2.7.3.3. Precipitation

Regional precipitation anomalies are very similar for the experiments, with both ONH and OSH exhibiting a southward shift of the Atlantic ITCZ, and a weak El-Niño-like pattern across the tropical Pacific. A clear southward shift of the Atlantic ITCZ is evident in precipitation anomalies in both ONH and OSH (Figure 2.12A and B). The strength of this shift is similar in both experiments, with no discernable difference in the size and timing of precipitation patterns in this region (Figure 2.13).

The precipitation response in the Pacific is similar between experiments. The strong meridional precipitation anomalies across the equatorial Pacific in both experiments suggest a southward shift of the ITCZ in this region. The strength of the teleconnection is possibly slightly stronger in OSH, compared to ONH (Figure 2.12C and D and Figure 2.13). It is difficult to detect this change in the regionally averaged precipitation anomalies; however, the spatial pattern of the precipitation response shows a stronger penetration of the signal into the western Pacific in ONH (Figure 2.13). However, this result is not seen within all ensemble members and requires additional simulations to detect with more certainty.

2.7.3.4. Surface wind stress and MSLP

The surface wind fields show a strong meridional response to North Atlantic climate forcing in ONH, compared to OSH, which shows more zonal asymmetry (Figure 2.14). The strength of the Southern Ocean westerly winds is increased in ONH, in response to the freshwater forcing of the North Atlantic. Interestingly, the wind field in OSH is much more regionally diverse, with small-scale centres of high and low-pressure

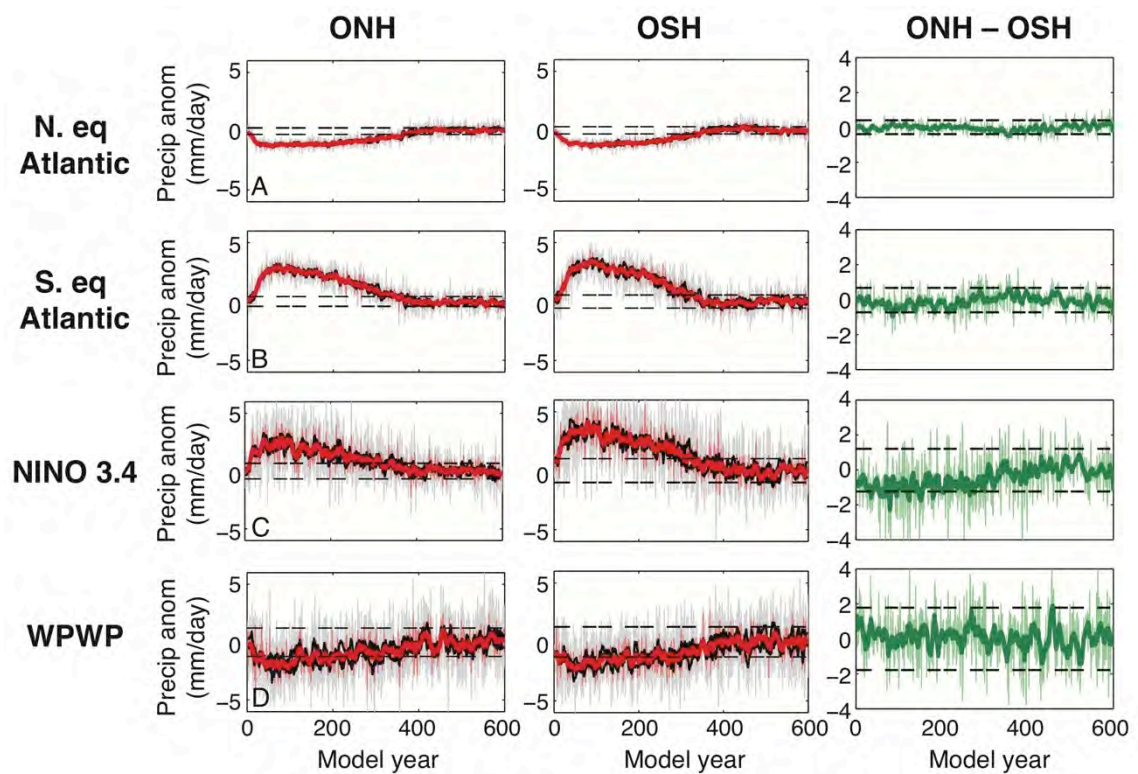


Figure 2.12: Regional precipitation anomalies for the four target areas. See Figure 2.3 for an explanation of the regions examined. (A) North equatorial Atlantic, (B) South equatorial Atlantic, (C) NINO 3.4, (D) Western Pacific Warm Pool. Individual run results for ONH and OSH are shown in grey, with a 10-year moving average in black. The ensemble results are shown in red with a 10-year moving average. ONH–OSH (right-hand column) shows the difference between the ONH and OSH ensembles (red lines). Dashed lines show 1-sigma variability in the control runs in columns one and two, and 1-sigma variability in the control difference in column three. Note that the ensemble mean differences are small for the four target areas.

anomalies resulting in a much more asymmetrical response, and no clear uniform shift in the strength of the large atmospheric circulation cells.

The response of the Southern Ocean and Antarctica varies between experiments, with ONH showing an ocean-wide low-pressure anomaly across this region, as opposed to experiment OSH, which sees much more zonal asymmetry (Figure 2.14). The response of OSH is reminiscent of a negative state of the Southern Annular Mode, with a high pressure cell centred across the Antarctic continent, and a series of low pressure centres across the southern mid-latitudes (Figure 2.14B).

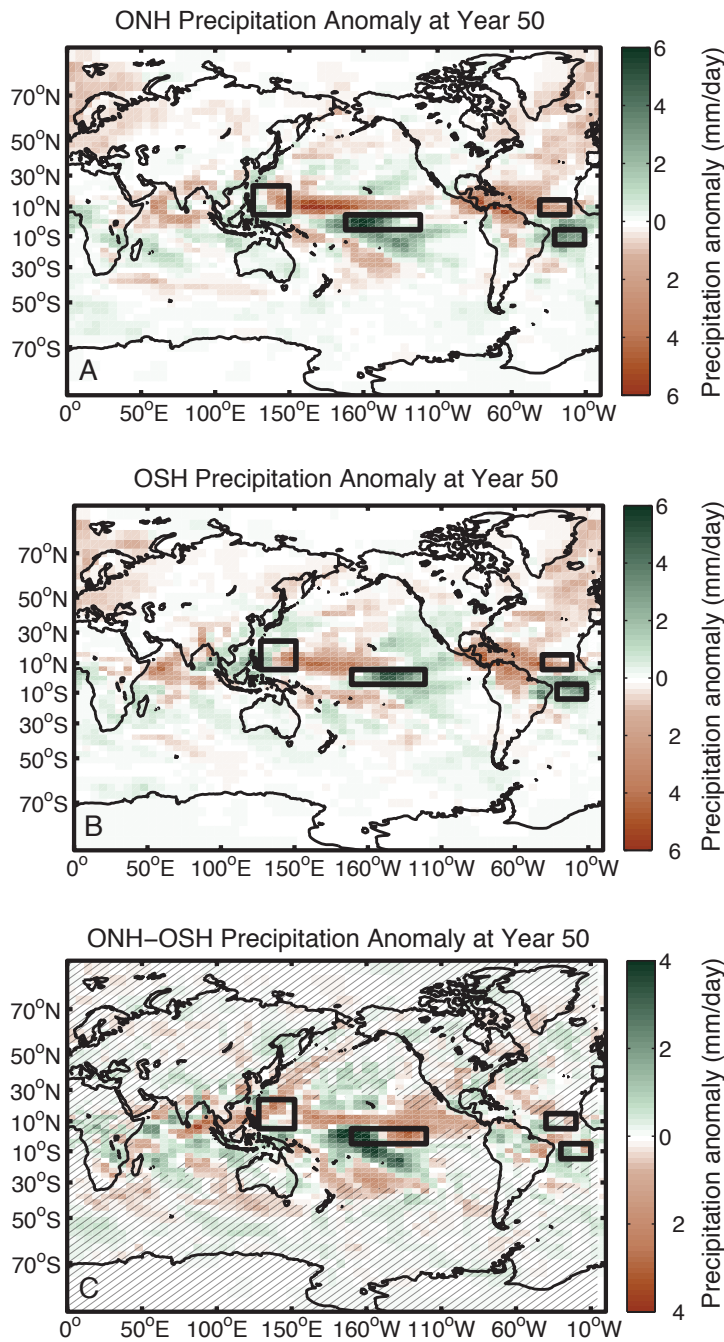


Figure 2.13: Spatial pattern of mean ensemble precipitation anomalies in (A) ONH, (B) OSH, and (C) ONH-OSH at year 50 (halfway through the hosing perturbation). Anomalies in (A) and (B) are calculated relative to their respective control runs. The difference between the ONH and OSH anomalies is shown in (C). Hatching is not shown in (A) and (B) as ensemble members agree within ± 1 mm/day everywhere. Hatching in (C) denotes agreement between at least 6/9 ensemble member differences within ± 1 mm/day of the ensemble mean plotted. Note the increased strength of the precipitation anomalies across the Pacific in ONH, relative to OSH.

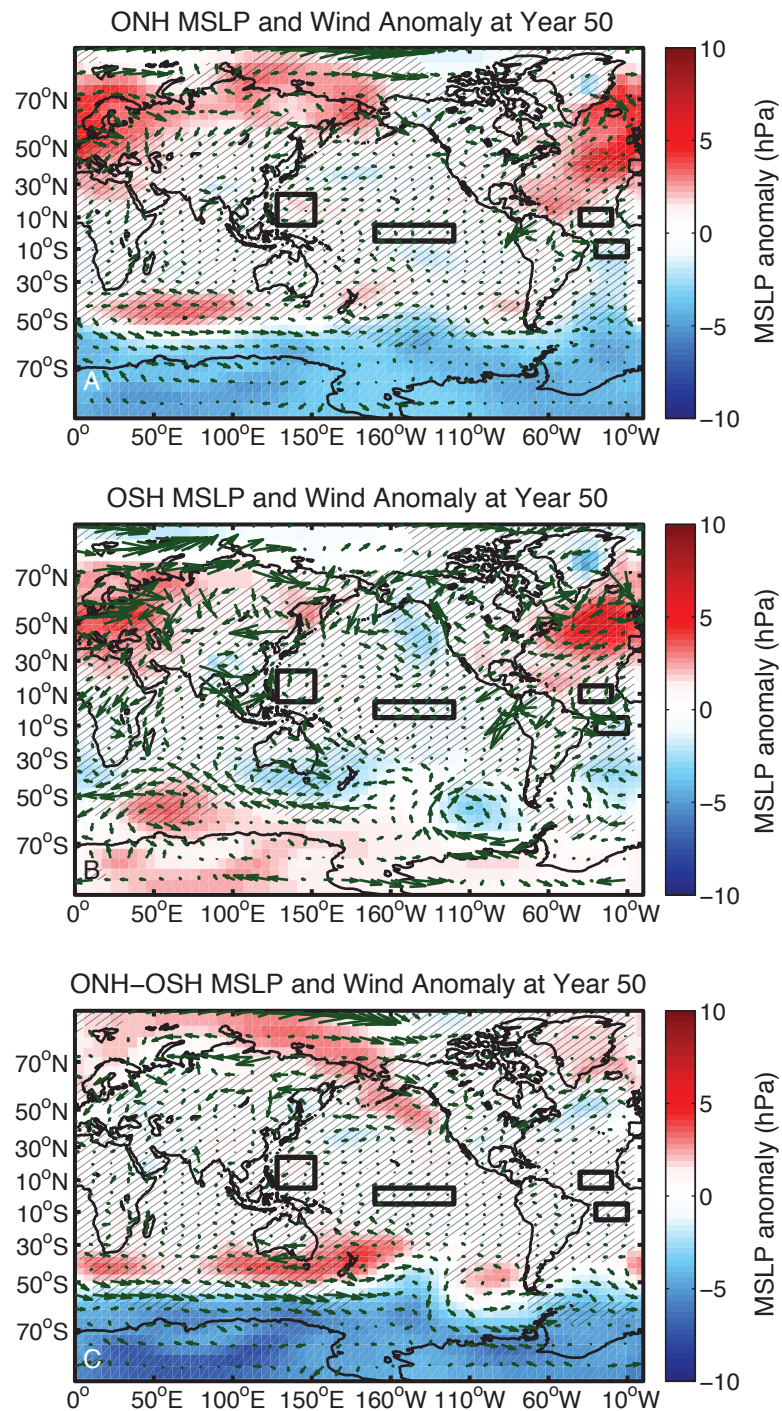


Figure 2.14: MSLP (shaded) and surface wind stress (arrows) anomalies at year 50. Anomalies calculated as in Figure 2.11. Hatching in (A) and (B) denotes agreement between the MSLP of the three ensemble members within ± 2 hPa of the ensemble mean plotted. Hatching in (C) denotes agreement between the MSLP of at least 6/9 ensemble member differences within ± 2 hPa of the ensemble mean plotted. Note that the largest differences between the two experiments occur across the Southern Ocean.

2.7.4. Discussion

The influence of precessional forcing on the modelled climate response to North Atlantic freshwater forcing is strongest in the Pacific and Southern Oceans, with the response within the Atlantic almost identical between simulations. The impact of freshwater forcing in ONH led to a pronounced strengthening of the southern hemisphere westerlies over the Southern Ocean (Figure 2.14). The more northerly mean ITCZ position within the control experiment resulted in weaker Southern Ocean westerlies, because of the northern hemisphere southern insolation maximum, (Figure 2.8G), and a reduction of the equator-pole pressure and temperature gradient across the whole of the southern hemisphere. This initial orbitally forced state may have primed the climate for a strong southward shift of the ITCZ once the model was forced by a freshwater flux into the North Atlantic. It has, however, been suggested that models may overestimate the precessional influence on the Southern Ocean westerlies, with the signal less apparent in available proxy records (Shulmeister et al. 2004). Despite this, precession signals have been found (although not always explicitly discussed or clear) in a number of Southern Ocean wind proxies (Lamy et al. 1998; Shulmeister et al. 2004; Martínez-García et al. 2011; Ledru and Stevenson 2012), supporting the idea of a common precession driver between the tropics and the high latitudes.

The responses of the Pacific and Southern Oceans to the same forcing in the OSH experiment were surprisingly different, with a far less annular response and a more asymmetrical pattern of variability evident, particularly within the MSLP field (Figure 2.14). A negative SAM-like state was initiated across the southern high latitudes in response to freshwater forcing of the North Atlantic.

A weak El-Niño-like state resulted from the hosing of the North Atlantic in both experiments. The warming of the eastern Pacific SSTs and cooling of the western Pacific, mirrored by a wet eastern Pacific anomaly and a dry western Pacific anomaly together suggest a more El-Niño-like state of the Pacific in response to North Atlantic freshwater forcing (Figure 2.11 and Figure 2.13). This response has been observed in other modelling studies where freshwater has been applied in the same manner as this study to a PI control run (Timmermann et al. 2007b; Lu and Dong 2008; Wu et al. 2008). It is important to note, however, that the patterns of SST and precipitation anomalies across the tropical Pacific Ocean are not identical between all ensemble

members (in both OSH and ONH) and should therefore be replicated to improve the robustness of this result.

The climatic response to freshwater forcing under different precession boundary conditions has not, to this author's knowledge, been tested before. While a strong southward shift of the ITCZ and a strong meridional response of the Southern Ocean as in ONH (Stouffer et al. 2006; Lewis et al. 2010), and an El-Niño-like state of the equatorial Pacific seen in both ONH and OSH (Dong and Sutton 2002; Zhang and Delworth 2005; Timmermann et al. 2007b; Lu and Dong 2008) have both been observed in other models in response to a simulated Heinrich event, these two responses have not been observed within the same model (Figure 2.14).

2.7.4.1. Drivers of climatic response

The largest difference between the ONH and OSH experiments is evident across the Southern Ocean. Surface wind stress fields for the ONH and OSH experiments demonstrate the influence of boreal vs. austral summer insolation maxima on the response of the modelled climate. Strong meridional gradients in wind stress in the Southern Ocean in ONH suggest the strengthening of the westerly wind field in response to North Atlantic hosing (Figure 2.14A and 16), a response that stems from the perturbation of the more northerly mean position of the ITCZ in the control simulation. A larger reduction in sea ice thickness in ONH may also help to force a southward shift of the Southern Ocean westerlies by shifting the effective coastline further south. In experiment OSH, the southern summer insolation maximum causes relatively stronger westerlies prior to the application of freshwater forcing to the North Atlantic, resulting in a less pronounced influence on the Southern Ocean wind field in OSH (Figure 2.14C and D). The presence of easterly anomalies across parts of the Southern Ocean suggests a weakening of the westerlies – or of their annular structure – in response to North Atlantic forcing; the opposite response to that in ONH (Figure 2.14).

Despite the difference in precessional forcing, the spatial response of the equatorial Pacific Ocean to simulated Heinrich events was similar between the two experiments, with ONH possibly exhibiting stronger anomalies compared to OSH. This result supports the work of previous studies, which have demonstrated the importance of the teleconnection across the Isthmus of Panama in transmitting anomalies from the Atlantic into the Pacific Ocean (e.g., Dong and Sutton 2007; Lu and Dong 2008).

2.7.5. Conclusions and implications

We have explored the influence of precessional forcing on the modelled climate response to a simulated Heinrich event using the CSIRO Mk3L GCM. We have shown that boundary conditions under a northern summer insolation maximum move the mean position of the ITCZ to the north, allowing a strong southward shift of the atmospheric circulation cells following hosing of the North Atlantic. A southern hemisphere summer insolation maximum, however, results in a southward shift of the mean ITCZ position prior to the application of North Atlantic hosing, and a much more muted and asymmetrical climate response to North Atlantic freshwater forcing. In both experiments, a weak El-Niño-like state is established during the period of hosing, however the strength of these anomalies appear to be slightly stronger in ONH, compared to OSH.

From our idealised experiments, it can be suggested that the strength of the response of the Pacific to a Heinrich event may change under varying precessional forcings, which may in turn be evident within proxy records. The amplitude of precessional forcing in the northern hemisphere was relatively weak from ~45–25 kyr BP across Heinrich events 3–5, however Heinrich event 6, which occurred at ~60 kyr BP, occurred just prior to a strong northern maximum (Figure 2.1). This event is seen clearly in Borneo, with two stalagmites recording significant drying at this time (Carolin et al. 2013), and in Flores with a similarly significant event (Scroxton 2014). Available proxy evidence does not necessarily support the opposite conclusion, with Heinrich event 5 at ~45 kyr BP, during a time of relatively strong southern summer insolation recorded as an abrupt event within the Borneo record (Partin et al. 2007; Carolin et al. 2013), and as an ambiguous wet anomaly within the Flores speleothem record (Scroxton 2014). Additional proxy and modelling evidence is required to further explore this hypothesis.

Although the experiment is highly idealised, there is some support from proxy records within the WPWP that the strength of the long-range teleconnection from a near shutdown of the AMOC into the western Pacific could be dependent on the precessional configuration. The results also suggest that the impacts of different orbital configurations could be strongest in the southern hemisphere extratropics, which warrants further investigation.

2.8. Experiment three: Changed CO₂ concentration

The daily concentration of atmospheric CO₂ reached 400 ppmv for the first time on 10 May 2013, with April 2014 the first month to record an average CO₂ concentration above 400 ppmv (Tans and Keeling 2014). While a lot of research has been done on the likely climate response to increased atmospheric CO₂ concentrations (see IPCC 2013 for a summary), the possibility of changed sensitivity of the climate to perturbations under these conditions remains an area of investigation (e.g. Bitz et al. 2007; Swingedouw et al. 2009; Swingedouw et al. 2015).

2.8.1. Experiment design

The response of the climate system to a freshwater perturbation under two atmospheric CO₂ concentrations was tested. The pre-industrial model experiment used in experiment two (OSH) is used again here to isolate the influence of CO₂ on the climate's response to hosing. Here, we focus on the CO₂ concentration of this experiment, and will refer to this run as “CO₂-280” in this section. A second hosing run was carried out using a CO₂ concentration of 400 ppmv (hereafter “CO₂-400”). All model parameters were the same as in CO₂-280, except for the CO₂ concentration. The hosing was carried out using 1 Sv of freshwater applied to the North Atlantic for 100 model years, as in experiment two. Both of these experiments were run as ensembles, with the mean of the ensemble members used to compare the runs. Three ensemble members were run for each experiment – starting from different years of the control experiment to account for any internal model variability – alongside their respective control runs (i.e. three perturbed runs and three control runs for each configuration). Anomalies were calculated for each experiment by subtracting the forced run from the respective control run. An ensemble mean was produced by calculating the average anomaly for each experiment. The difference between the ensemble mean anomaly of CO₂-280 and CO₂-400 is compared to examine the influence of CO₂ concentration on the climate response to North Atlantic freshwater forcing.

A second ensemble of CO₂ experiments were attempted to reproduce CO₂ conditions at the LGM, with CO₂ concentrations set to 160 ppmv. These experiments proved to be highly unstable within the CSIRO Mk3L model and were unable to be completed within the constraints of this project. LGM CO₂ experiments remain a key target for future work following on from this thesis.

2.8.2. Control boundary conditions

The control run of CO₂-400 represents a warmer world compared to CO₂-280 (previously called OSH), with almost uniform increases in temperature across the earth. Surface air temperature in CO₂-400 is on average 1.8°C warmer than in CO₂-280 (Figure 2.15A). This warming is stronger in the Arctic and along the Indian Ocean portion of the Antarctic coastline, where temperatures are up to 12°C warmer. SSTs are also warmer, with average SSTs 1°C warmer in CO₂-400 (Figure 2.15B). There are noticeable regions of comparably cooler SSTs in the Arctic, and around parts of the Antarctic coastline, likely caused by a decrease in sea ice in these regions (Figure 2.15F).

Precipitation is similar between CO₂-400 and CO₂-280, except for the equatorial Pacific and Atlantic. The Pacific ITCZ is narrower in CO₂-400, with strong rainfall along the equator, and relatively less rainfall at 10°N and 10°S, compared to CO₂-280 (Figure 2.15C). In the Atlantic, a reduction in rainfall is also seen at 10°S. The orbital configuration of both experiments is for a precessional summer insolation maximum in the Southern Hemisphere. The control simulation suggests that despite this, the ITCZ is shifted slightly to the north in CO₂-400, back towards the equator. In CO₂-280, the ITCZ generally sits to the south of the equator, as would be expected with a southern insolation maximum.

Surface wind stress fields are similar between CO₂-400 and CO₂-280, with only small differences evident between runs. The strength of the Southern Ocean westerlies is slightly reduced in CO₂-400, likely caused by the more northerly position of the ITCZ in this run, compared to CO₂-280 (Figure 2.15G). There are weakly anomalous easterly winds across North America in CO₂-400, which may become significant once the freshwater forcing is applied, as this region is where the atmospheric teleconnection

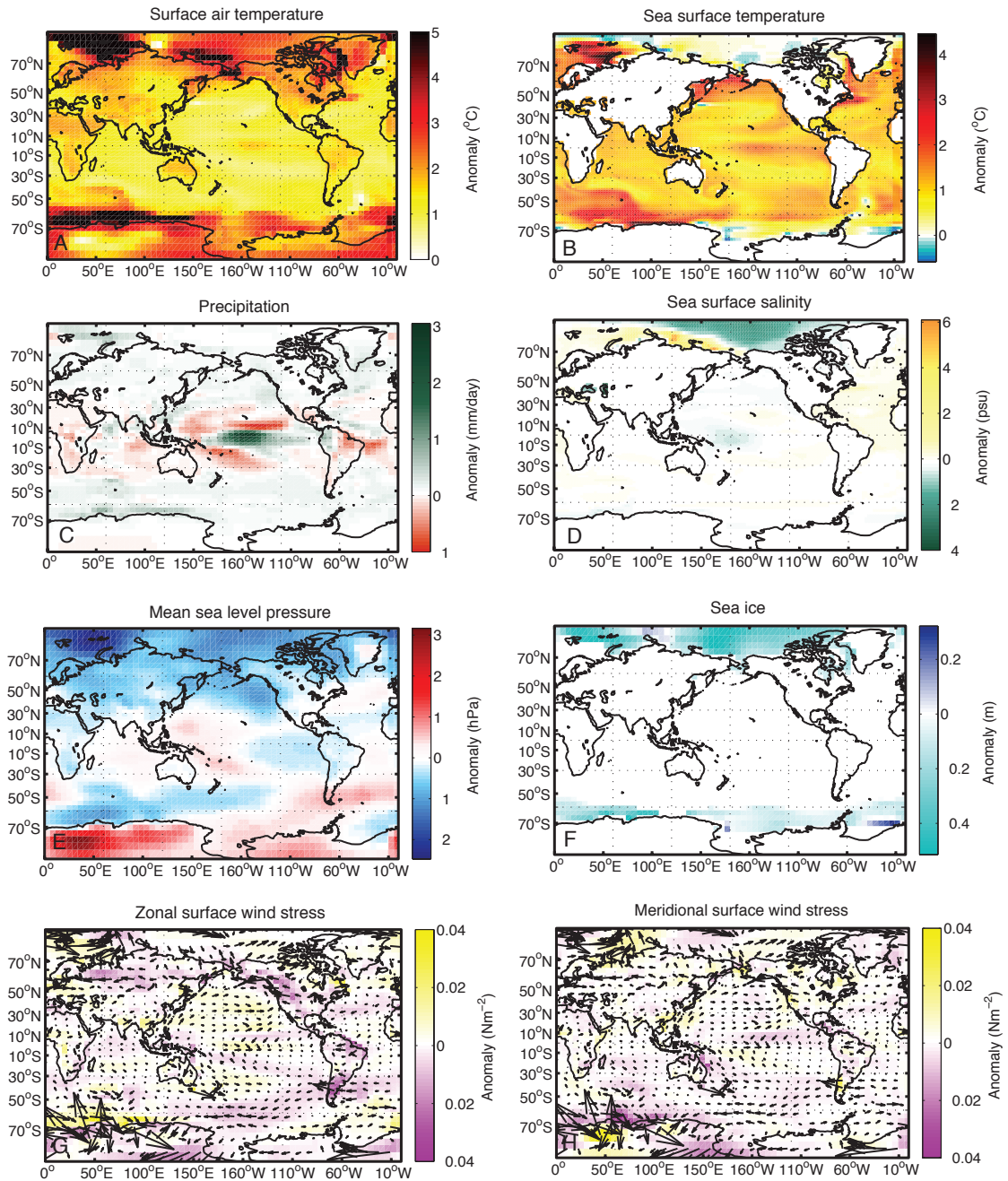
CO₂-400 control – CO₂-280 control

Figure 2.15: Influence of higher atmospheric CO₂ concentration on model boundary conditions. Anomalies for each variable were calculated by subtracting the climatologies from each control (CO₂-400 – CO₂-280). Wind vector anomalies are drawn with arrows, overlying shaded (G) zonal and (H) meridional surface wind stress anomalies.

from the North Atlantic forces the eastern Pacific. Meridional surface wind stress is similar between experiments, except for the Indian Ocean sector of the Antarctic (East Antarctica), where the localised temperature differences in CO₂-400 have created an offshore wind gradient (Figure 2.15H).

2.8.3. Hosing results

2.8.3.1. AMOC overturning

The recovery rate of the AMOC is markedly different between experiments, occurring approximately 100 years later in CO₂-400, despite the forcing being applied in the same way to both experiments. The pattern of AMOC collapse and recovery is similar between CO₂-400 and CO₂-280; however, it takes the CO₂-400 experiment approximately 100 years longer to recover from the perturbation (Figure 2.16). The two experiments begin to diverge significantly from model year ~100, with CO₂-280 reaching its maximum strength in model year ~420, compared to CO₂-400, which reaches its maximum strength in model year ~530.

The control AMOC strength in CO₂-400 is more stable compared to CO₂-280, which displays a higher degree of variability, and some possible cyclicity (Figure 2.16A and B). AMOC strength in the CO₂-400 control is, on average, stronger than CO₂-280, varying around 14.5 Sv, compared to CO₂-280, which moves between ~15 Sv and ~13 Sv. The stability of the AMOC in CO₂-400 may play a part in the longer time taken to return to control conditions, with the higher level of internal forcing possibly pushing the AMOC back to control conditions more quickly in the CO₂-280 experiment.

2.8.3.2. SST

Regional SST anomalies are similar between experiments; however, these anomalies persist for longer in CO₂-400, compared to CO₂-280. SST anomalies in both experiments show an Atlantic equatorial bipolar SST anomaly, with warm anomalies in the south equatorial region, and cool anomalies in the north (Figure 2.17). The magnitude of these anomalies is similar between the two experiments; however, the anomalies persist for longer in CO₂-400, in line with the slower recovery of the AMOC in this experiment.

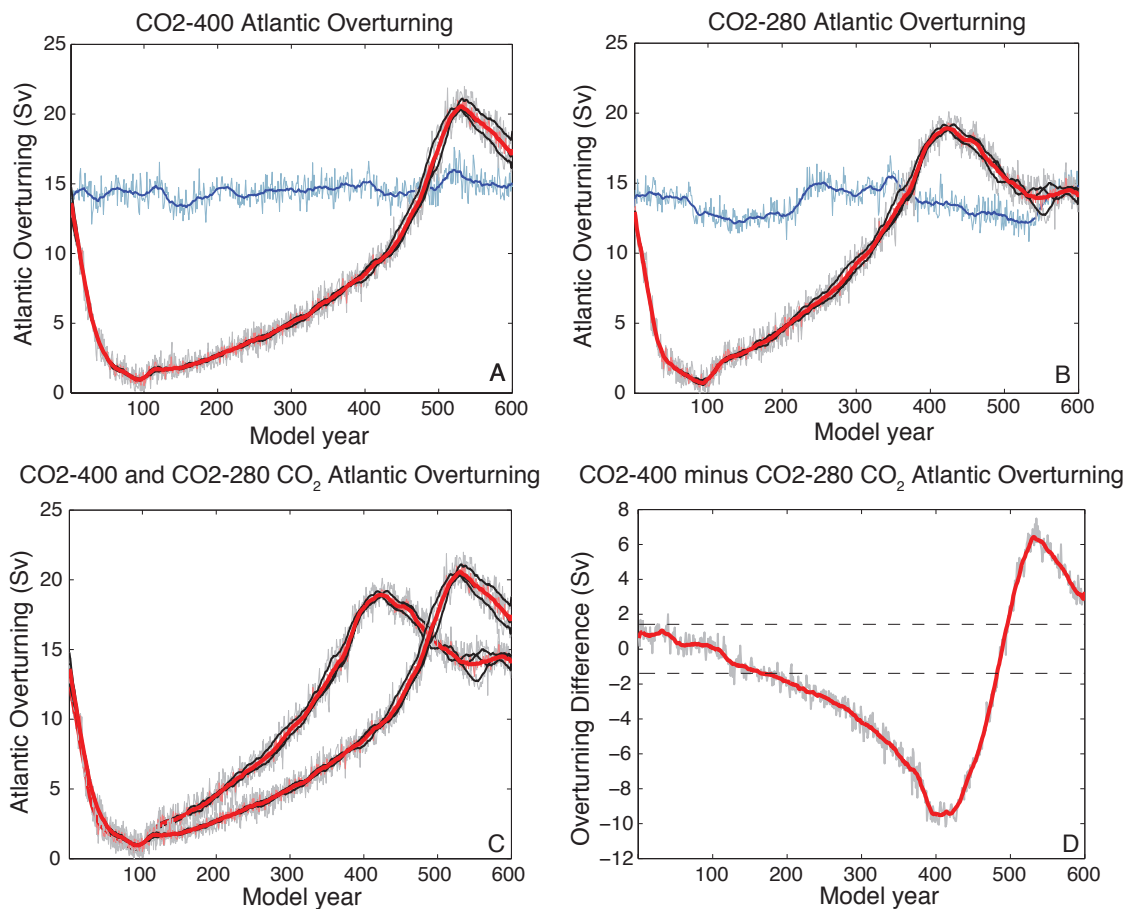


Figure 2.16: Atlantic meridional overturning in (A) CO₂-400 CO₂ experiment and (B) CO₂-280 CO₂ experiment. Grey lines show results from the three individual ensemble members, with a 20-year running mean for each run in black. The ensemble mean of the three runs, with a 20-year running mean is given in red. Control run variability is shown in light blue, with a 20-year running mean in dark blue. (C) CO₂-400 and CO₂-280 plotted together to highlight the difference in timing. (D) AMOC ensemble anomaly (CO₂-400 ensemble–CO₂-280 ensemble; grey), with a 20-year running mean in red. Dashed lines denote the 1-sigma variability of the difference between control runs.

NINO 3.4 SST anomalies are also similar between experiments; however, the magnitude of the anomaly is slightly smaller in CO₂-400, and lasts longer than in CO₂-280. The eastern Pacific SST anomaly only just moves outside of the range of modelled natural variability in CO₂-400, sitting at the very edge of a naturally occurring warm anomaly (Figure 2.17). The warm anomaly in CO₂-280 is marginally stronger; however, clearly moves outside of the range of natural modelled variability for this run. The anomaly persists longer in CO₂-400, compared to CO₂-280.

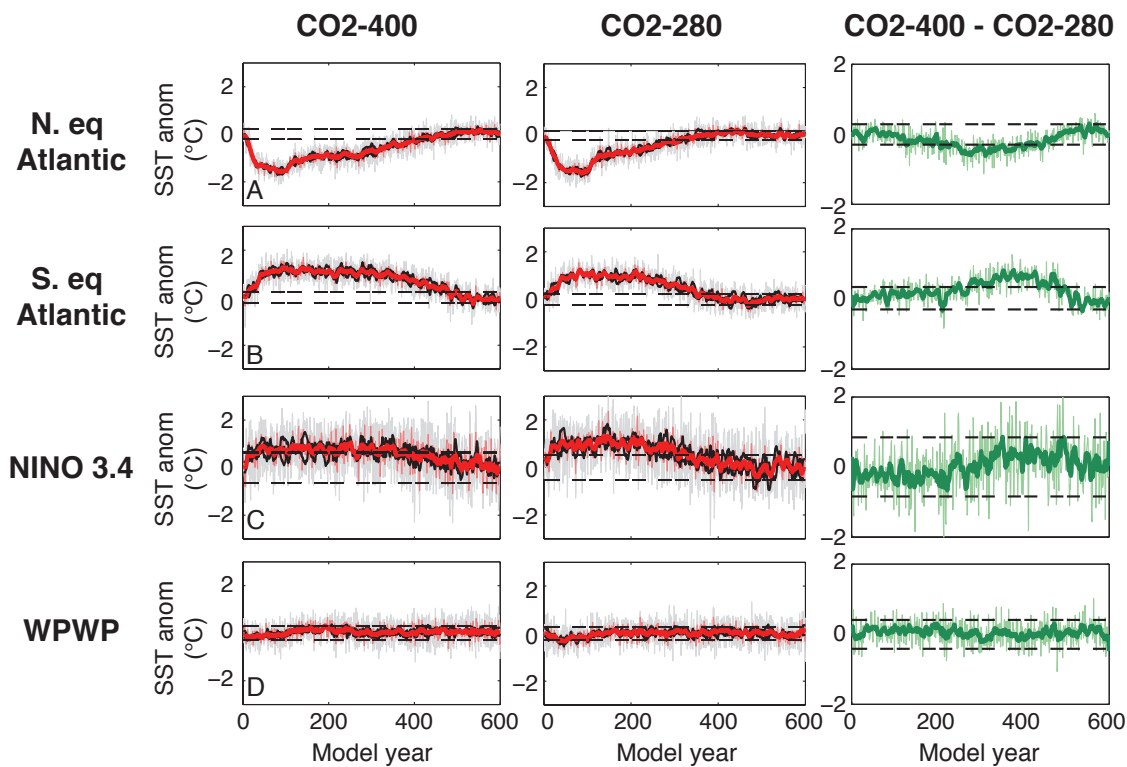


Figure 2.17: Regional SST anomalies for the four target areas. (A) North equatorial Atlantic, (B) South equatorial Atlantic, (C) NINO 3.4, (D) Western Pacific Warm Pool. CO2-400 (column one) shows the single run results in grey, with a 20-year moving average for each run in black, and the ensemble mean in red. CO2-280 (column two) as in column one. CO2-400-CO2-280 (column three) shows the difference between CO2-400 and CO2-280. Dashed lines show 1-sigma variability in the control runs in columns one and two, and 1-sigma variability in the control difference in column three.

No significant SST anomaly is evident in the western Pacific in either experiment, suggesting that the strength of the long-range teleconnection is damped in both experiments. The SST anomalies recorded in the WPWP are similar for both experiments, with neither moving significantly beyond the range of natural model variability (Figure 2.17).

The pattern of SST variability across the Pacific is very similar in both experiments, with both simulations showing a warm eastern Pacific and cool western Pacific SST anomaly. A zonal asymmetry in the Pacific Ocean is seen in both experiments, with the anomalies not strongly extending into the western Pacific in either run (Figure 2.18).

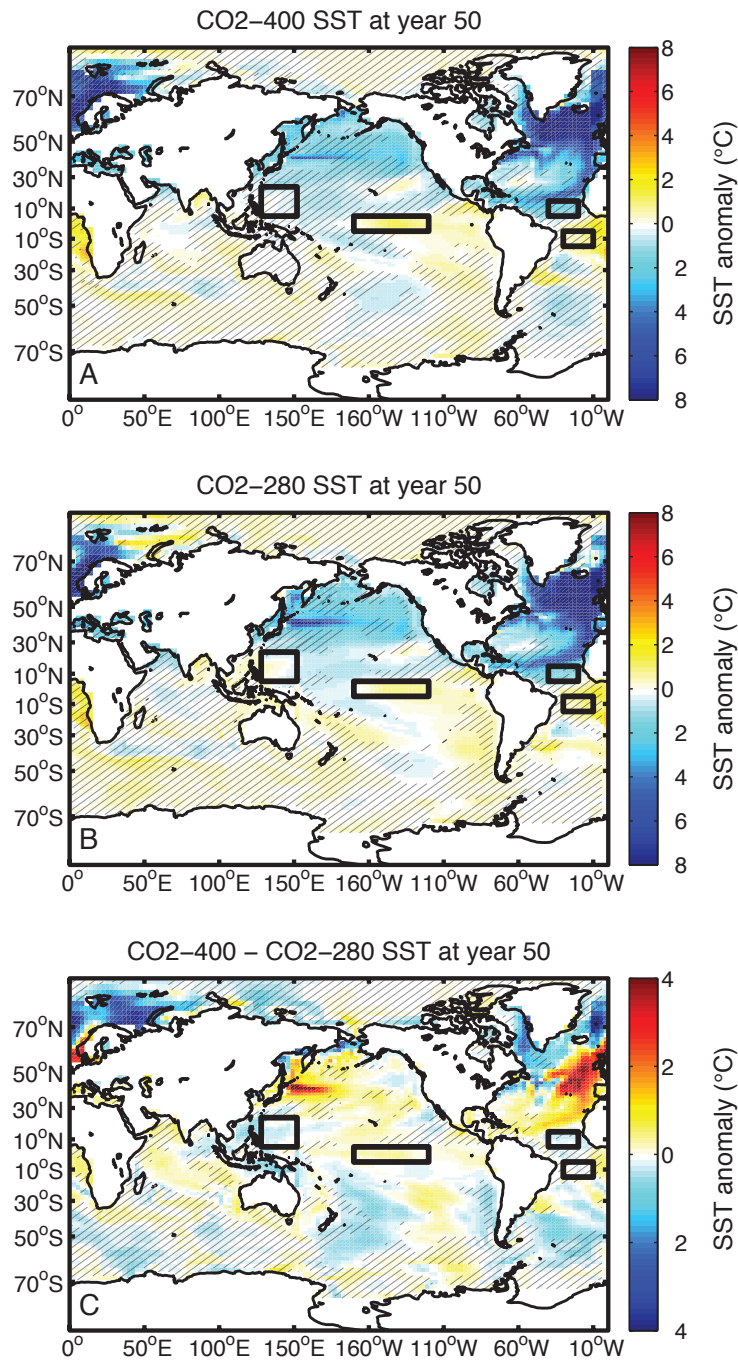


Figure 2.18: Spatial pattern of SST anomalies in (A) CO2-400, (B) CO2-280, and (C) CO2-400-CO2-280 at year 50 (half-way through hosing perturbation). Anomalies in (A) and (B) are calculated relative to their respective control runs. The difference plotted in (C) is the difference in these anomalies. Hatching in (A) and (B) denotes agreement between the three ensemble members within $\pm 0.5^\circ\text{C}$ of the ensemble mean plotted. Hatching in (C) denotes agreement between at least 6/9 ensemble member differences within $\pm 0.5^\circ\text{C}$ of the ensemble mean plotted.

The notable difference between the experiments is a weaker cooling anomaly in the eastern North Atlantic in CO₂-400 compared to CO₂-280. Despite this warmer anomaly in CO₂-400, the magnitude of AMOC shut down is similar in both experiments, suggesting that the NADW formation region is being similarly affected in both experiments.

2.8.3.3. Precipitation

Patterns of precipitation are similar in both CO₂-400 and CO₂-280, with the main point of difference the duration of these anomalies. A clear southward shift of the Atlantic ITCZ is evident with strong positive rainfall anomalies seen in the southern equatorial Atlantic in both experiments (Figure 2.19B), accompanied by a dry anomaly in the north (Figure 2.19A). The magnitude of this shift is the same in both the CO₂-400 and CO₂-280 experiments, with the anomaly persisting longer in CO₂-400.

The NINO 3.4 region experienced wet precipitation anomalies in both experiments, in contrast to the western Pacific, which saw dry anomalies. The NINO 3.4 region experienced a strong wet anomaly in both experiments, of approximately the same magnitude as that seen in the southern equatorial Atlantic (Figure 2.19C). The time evolution of this anomaly varied slightly between experiments, with CO₂-280 seeing a maximum in rainfall occurring during the first 100 years of the experiment (during the forcing), before returning to pre-perturbation levels by model year ~300. Experiment CO₂-400 however, experienced sustained maximum rainfall beyond the perturbation period, before slowly returning to pre-perturbation levels by model year ~400. The WPWP saw a dry anomaly during the hosing period in both experiments; however, this anomaly persisted longer in CO₂-280, compared to CO₂-400, the opposite result to all our variables thus far (Figure 2.19D). It is possible that the duration of the WPWP anomaly in CO₂-400 was influenced by the starting conditions of this experiment, with the anomaly at year zero more positive in CO₂-400, compared to CO₂-280 (Figure 2.19D).

The spatial pattern of precipitation is very similar in both experiments, with only small differences evident between CO₂-400 and CO₂-280. A clear southward shift of the Atlantic ITCZ is evident in both experiments (Figure 2.20), supporting our regionally averaged results. There is a clear asymmetry in precipitation anomalies across the Pacific in both experiments; however, the pattern is slightly stronger in CO₂-

400 (Figure 2.20C). The central Pacific experienced a stronger positive rainfall anomaly in CO₂-400, compared to CO₂-280, with the South Pacific Convergence Zone (SPCZ) clearly drying during the perturbation period in CO₂-400. The precipitation anomalies appear to differ across the WPWP, with this region largely drying in CO₂-400, but wetting in CO₂-280. The broad region of WPWP drying seen in CO₂-400 suggests that there is not a clear ITCZ shift in this region, as a wetter band does not accompany it to the south (Figure 2.20C). Instead, this result suggests an El-Niño-like state in the Pacific, with wetter conditions in the eastern Pacific, and dryer conditions in the western Pacific. This result was previously found for experiment OSH (now called CO₂-280;

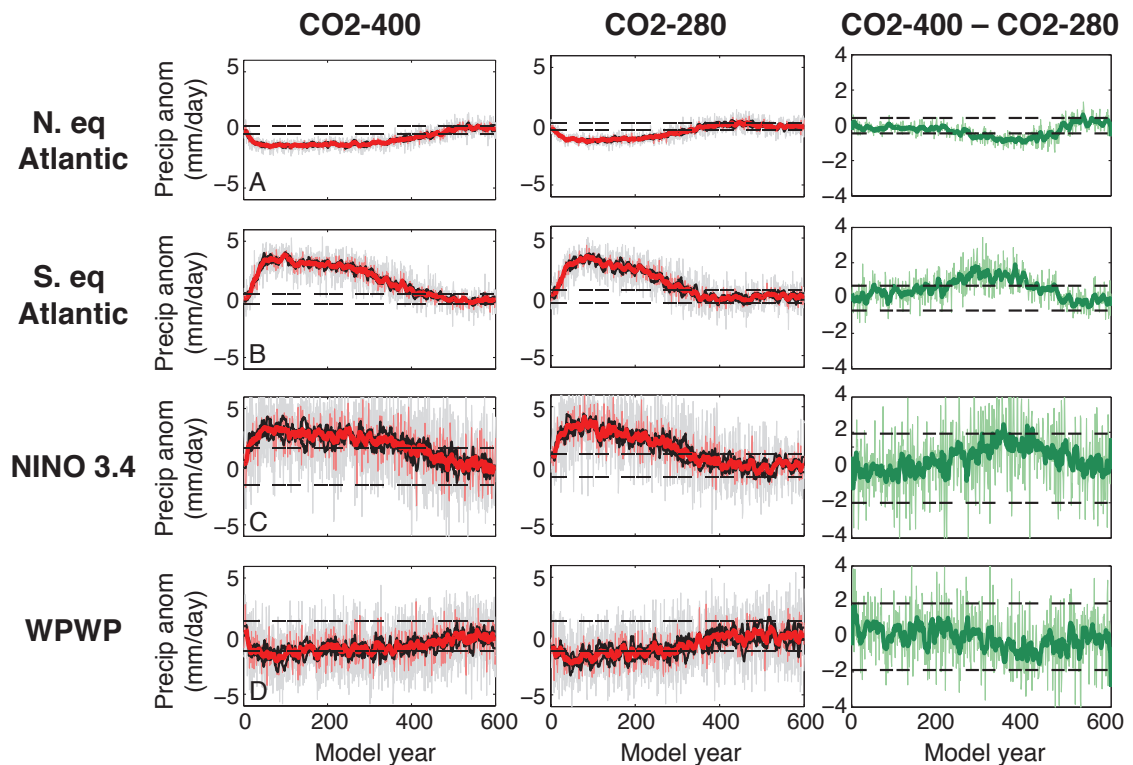


Figure 2.19: Regional precipitation anomalies for the four target areas. (A) North equatorial Atlantic, (B) South equatorial Atlantic, (C) NINO 3.4, (D) Western Pacific Warm Pool. CO₂-400 (column one) shows the single run results in grey, with a 20-year moving average for each run in black, and the ensemble mean in red. CO₂-280 (column two) as in column one. CO₂-400-CO₂-280 (column three) shows the difference between CO₂-400 and CO₂-280. Dashed lines show 1-sigma variability in the control runs in columns one and two, and 1-sigma variability in the control difference in column three.

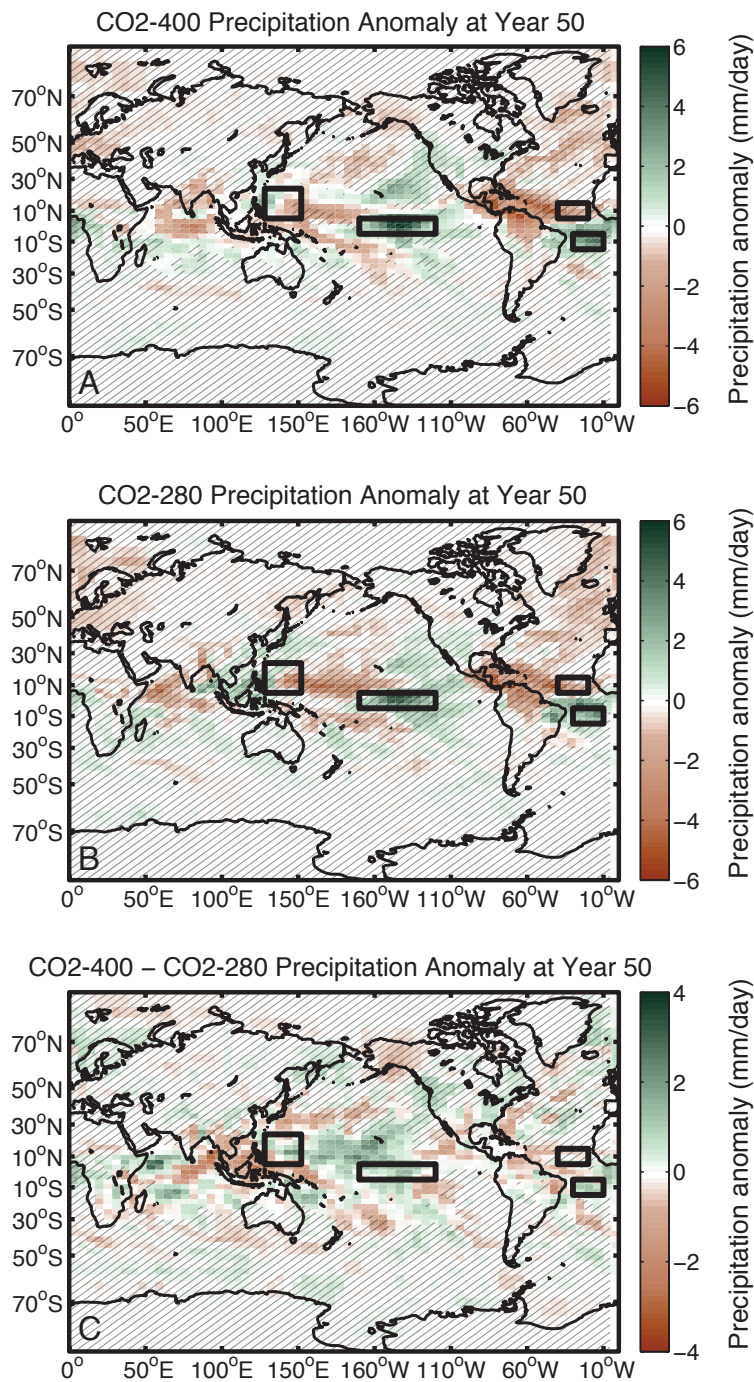


Figure 2.20: Spatial pattern of precipitation anomalies in (A) CO2-400, (B) CO2-280, and (C) CO2-400–CO2-280 at year 50 (half-way through hosing perturbation). Anomalies in (A) and (B) are calculated relative to their respective control runs. The difference plotted in (C) is the difference in these anomalies. Hatching in (A) and (B) denotes agreement between the three ensemble members within ± 1 mm/day of the ensemble mean plotted. Hatching in (C) denotes agreement between at least 6/9 ensemble member differences within ± 1 mm/day of the ensemble mean plotted.

see section 2.7.4); however, compared to CO₂-280, this pattern appears stronger in CO₂-400.

2.8.3.4. Surface wind stress and MSLP

The strength of the atmospheric teleconnection from the North Atlantic, across the Isthmus of Panama and into the eastern Pacific is similar in both experiments, explaining the agreement in the nature of climate anomalies seen in this region (Figure 2.21). A weak northeasterly wind stress anomaly is evident along the equator in CO₂-280, extending from the North Atlantic Ocean, across the central Pacific and into the western Pacific region (Figure 2.21B). This anomaly is also evident in CO₂-400, but it does not extend into the western Pacific, instead, reaching only to ~180°W (Figure 2.21A).

A strong meridional wind response is evident in the Southern Ocean in CO₂-400, with CO₂-280 showing more asymmetrical zonal anomalies (Figure 2.21). The Southern Ocean westerlies strengthen in CO₂-400, likely due to the weaker state of these winds prior to the application of freshwater forcing.

MSLP anomalies across the Southern Ocean differ between CO₂ experiments, with CO₂-400 recording generally low pressures in this region, compared to CO₂-280, which experiences generally high-pressure anomalies. Low-pressure anomalies in CO₂-400 over Antarctica support the idea of a southward shift in the Southern Ocean westerlies in this experiment (Figure 2.21).

2.8.4. Discussion

Atmospheric CO₂ concentration influences the recovery rate of the AMOC to freshwater forcing of the North Atlantic in the CSIRO Mk3L (Figure 2.16), mirroring the results of a previous study (Bitz et al. 2007). The spatial patterns of climate anomalies are similar for the two experiments, with only localised regional differences. The key difference between the experiments relates to the persistence of the AMOC and associated climate anomalies, which last ~100 years longer in CO₂-400, compared to CO₂-280 (Figure 2.16, Figure 2.17 and Figure 2.19). These differences appear to be related to the character of the AMOC circulation in each experiment.

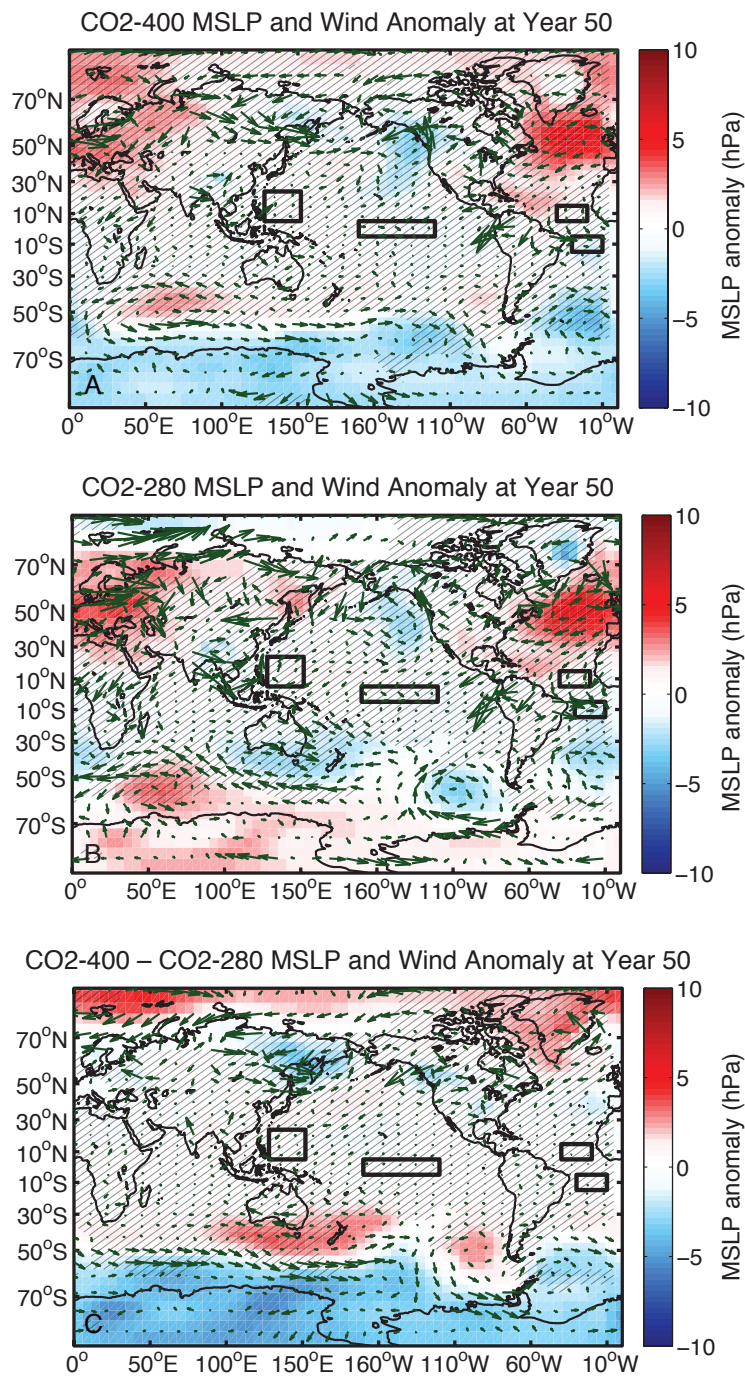


Figure 2.21: MSLP (shaded) and surface wind stress (arrows) anomalies at year 50. Anomalies in (A) and (B) are calculated relative to their respective control runs. The difference plotted in (C) is the difference in these anomalies. Hatching in (A) and (B) denotes agreement between the MSLP of the three ensemble members within ± 2 hPa of the ensemble mean plotted. Hatching in (C) denotes agreement between the MSLP of at least 6/9 ensemble member differences within ± 2 hPa of the ensemble mean plotted.

The AMOC circulation is driven by a combination of temperature and salinity induced density differences, whereby cool, salty water sinks within the North Atlantic, pulling warmer and fresher surface water northward into the North Atlantic Ocean, which in turn cools, becomes more saline and sinks, driving the overturning circulation. In a 400-ppmv CO₂ world, warmer surface waters resulting from an intensification of Earth's greenhouse effect reduce the thermal-driven density of surface waters in the NADW formation region of the North Atlantic. The salinity of these waters must therefore increase in order for them to become sufficiently dense and sink (Thorpe et al. 2001; IPCC 2007).

Following the application of freshwater to the surface of the North Atlantic Ocean, surface density reduces (Figure 2.22A), shutting off the NADW formation, and consequently, the AMOC (Figure 2.16). This in turn leads to a build-up of saline waters in the northern subtropical Atlantic (Figure 2.23). The stronger dependence of the AMOC circulation on salinity in the 400 ppmv CO₂ experiment causes the high surface density to recover more slowly in CO₂-400 (years 401–500; Figure 2.22E), than in CO₂-280. (years 301–400; Figure 2.22D). In CO₂-400, the “off” state of the AMOC is a positive feedback on the continued suppression of deep-water formation. The shutdown of the Gulf Stream removes a source of salt water to the NADW formation region, acting as a positive feedback to reinforce the shut down (Bitz et al. 2007). As a result, the AMOC takes longer to recover in CO₂-400, since it must overcome this feedback in order to build up salinity in the surface waters of the North Atlantic, and reinitiate bottom water formation (Yin and Stouffer 2007) (Figure 2.22 and 26).

The other key difference between the two CO₂ hosing experiments is the strength of the long-range teleconnection into the western Pacific. The weaker equatorial easterly winds in CO₂-400, versus CO₂-280 account for the weaker long-range teleconnection, with the atmospheric anomalies from the North Atlantic not able to penetrate into the WPWP (Figure 2.21). The weaker wind anomalies in CO₂-400 are related to the warmer surface waters in the north-eastern Atlantic Ocean in CO₂-400, which create a weaker meridional temperature gradient within the Atlantic, reducing the strength of the easterly winds (Figure 2.18). This has implications for the IPWP region, which would likely experience a weaker or more asymmetrical response to a shut down of the AMOC circulation than locations closer to the North Atlantic.

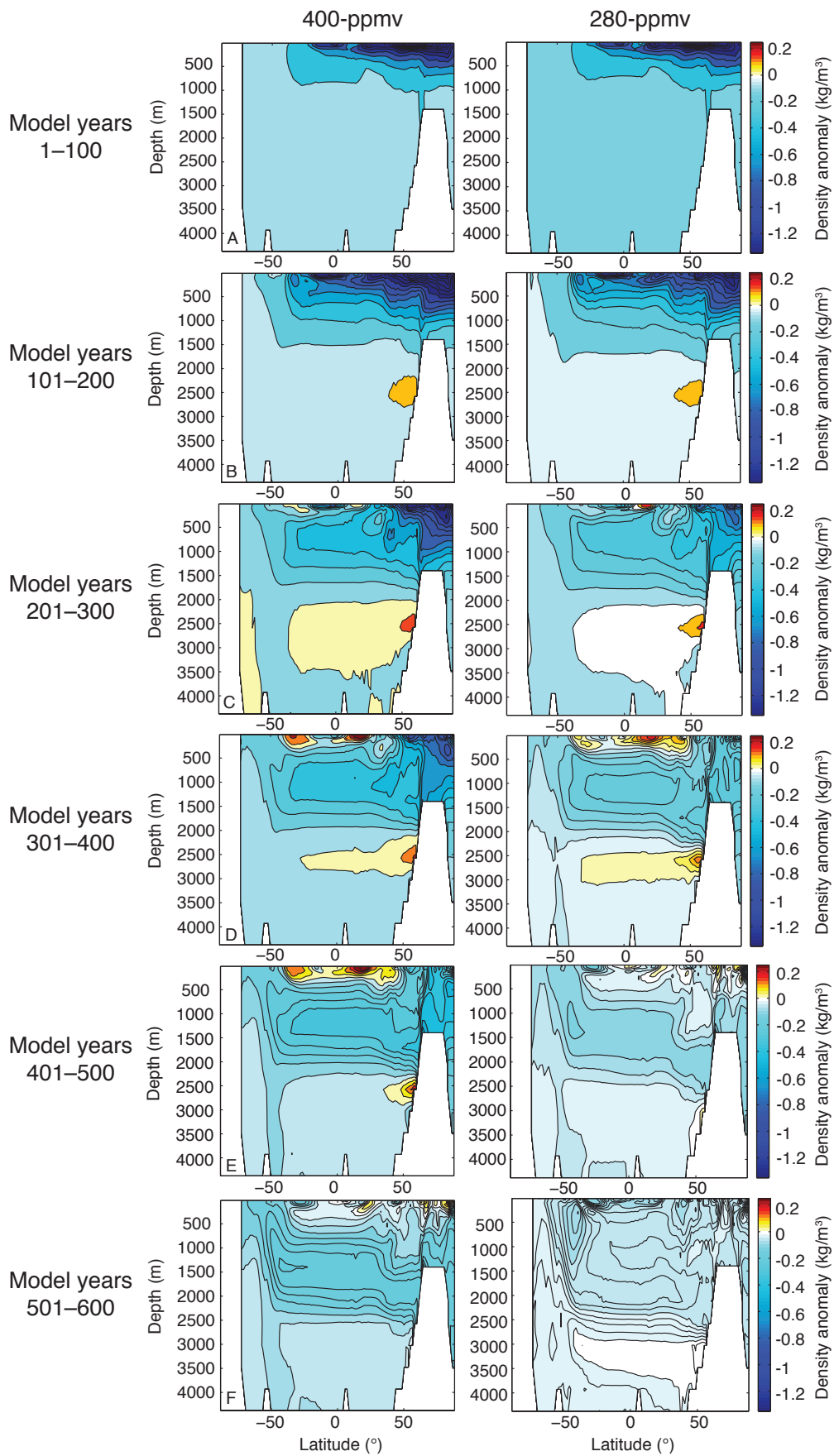


Figure 2.22:

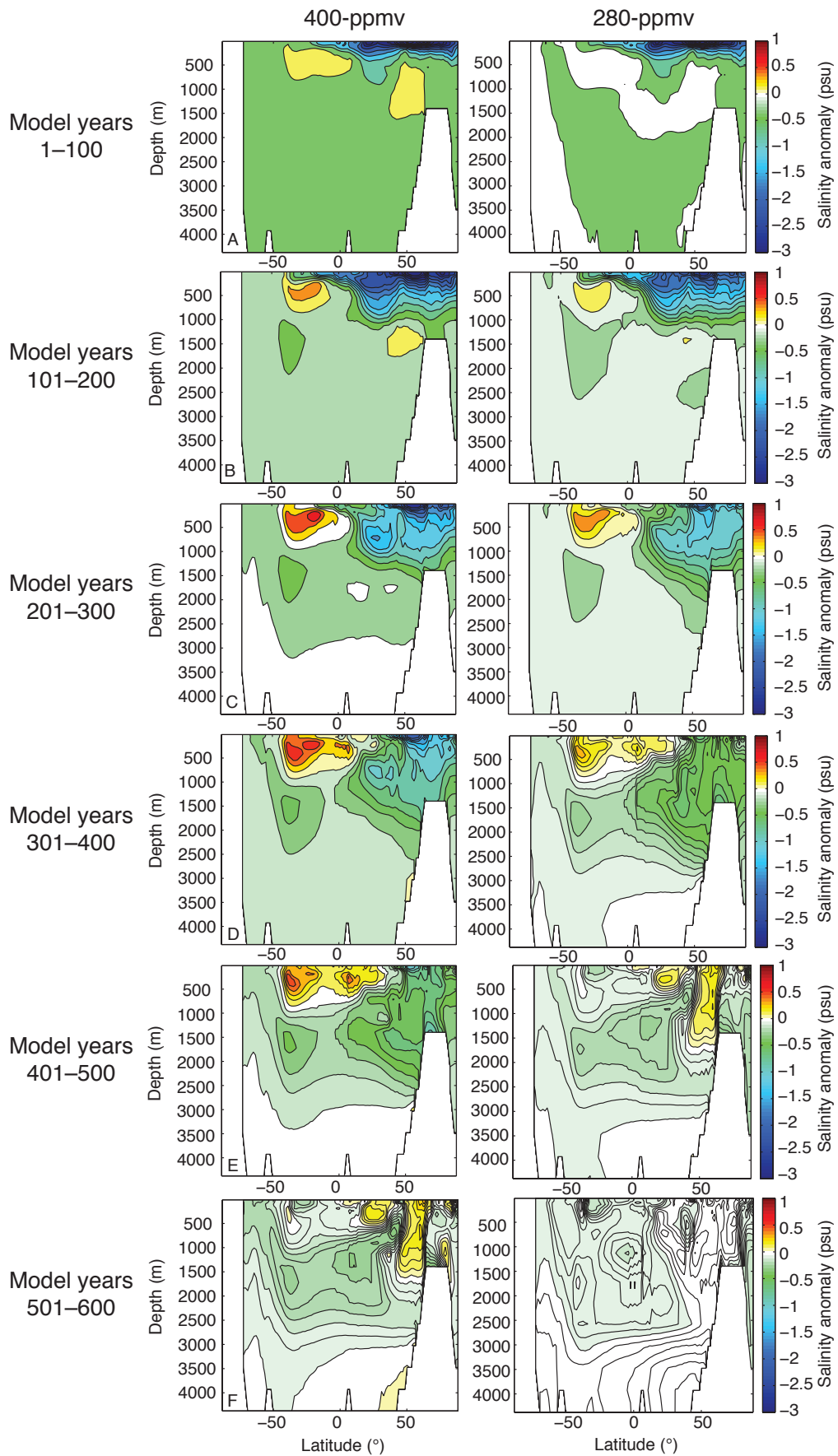


Figure 2.23:

Figure 2.22: Zonally integrated density (calculated from temperature and salinity) anomalies for the Atlantic Ocean. Each panel represents the mean of the 100-year period displayed on the left. The two columns show the results from CO₂-400 (left column) and CO₂-280 (right column). Positive anomalies indicate more dense water in the hosing run, compared to the control; negative anomalies are less dense.

Figure 2.23: As in Figure 2.22, but for salinity. Positive anomalies indicate more saline waters in the hosing run, compared to the control; negative anomalies more fresh waters.

2.8.5. Conclusions and implications

We have simulated the effect of North Atlantic freshwater hosing on the climate, equilibrated to 400 ppmv atmospheric CO₂ concentrations and compared the results with those for pre-industrial boundary conditions (280 ppmv) to explore the influence of an increase in CO₂ on climate sensitivity to North Atlantic freshwater forcing within the CSIRO Mk3L climate model. Our key finding is that the recovery time of the AMOC circulation is significantly slower in a 400-ppmv world, compared to a 280-ppmv world. As such, the resulting climate anomalies stemming from the AMOC shutdown persist for longer in the 400-ppmv experiment. The different rates of AMOC recovery relate to the influence of higher SSTs and lower salinity on NADW formation. Higher SSTs in CO₂-400, brought about by global warming, cause salinity to become a more important driver of deep-water formation in CO₂-400, compared to CO₂-280. The recovery of the AMOC is faster in CO₂-280 because the higher surface ocean density (as determined by temperature and salinity) required to initiate bottom water formation recovers more quickly (Figure 2.22). In the 400-ppmv experiment, greater salinity is required to offset the effect of higher SSTs, to reinitiate bottom water formation, thus taking longer to recover and advect into the North Atlantic (Figure 2.23).

While a complete shutdown of the AMOC in response to future climate change is unlikely (Rahmstorf 2006; Driesschaert et al. 2007; Kriegler et al. 2009), a slow-down of the AMOC is predicted in models (Schmittner et al. 2005; Srokosz et al. 2012; Cheng et al. 2013), and has already been observed across the North Atlantic (Rahmstorf et al. 2015). Our results suggest that a future slow-down of the AMOC could persist for

many centuries, because of a build up of freshwater in the bottom-water formation region of the North Atlantic (Figure 2.23). Current estimates of the rate of Greenland melting suggest freshwater fluxes as high as ~ 0.54 mm/yr (Chen et al. 2006) which, while significant, are an order of magnitude smaller than the rates estimated for past Heinrich events (see section 2.1). Therefore, it is unlikely that this magnitude of freshwater forcing will be large enough to initiate a significant change in the AMOC. Any slowdown will likely result in localised climate effects, although the influence of warmer initial SSTs as well as the nature of the sensitivity of the AMOC in a warmer world may change the volume of freshwater required to initiate an AMOC shutdown and should be investigated further. We have shown that the strength of the teleconnection of Heinrich climate perturbations into the tropical Pacific is related to the strength of the meridional temperature gradient within the North Atlantic Ocean. The weaker perturbation of the AMOC would likely result in muted SST anomalies in the eastern Pacific, resulting in a weak and likely minimal teleconnection into the western Pacific Ocean.

2.9. Conclusions

We have demonstrated the relative influence of the magnitude and duration of freshwater forcing in the North Atlantic on the modelled climate response within the CSIRO Mk3L GCM. The magnitude of forcing, rather than the duration, appears to be the key factor in determining the modelled climate response to a simulated Heinrich event. A freshwater hosing magnitude of 1 Sv across the North Atlantic is required to shut down the AMOC in the CSIRO Mk3L model, as has been demonstrated for other models (Stouffer et al. 2006).

The response of the modelled climate to changes in the model boundary conditions was explored. We ran two experiments where the orbital configuration and CO₂ concentrations were changed prior to the application of hosing and found that the boundary conditions played a key role in determining the climate's response to freshwater hosing. When the ITCZ was shifted to the north, as in the ONH experiment, the model's response to a North Atlantic forcing was to shift the ITCZ south, causing a strengthening of the Southern Ocean westerlies. When the ITCZ was already shifted to the south, as in OSH/CO₂-280, the response was much less latitudinally homogenous,

with a negative SAM-like state established across the southern high latitudes. An El Niño-like state, with warm anomalies in the eastern Pacific and cool anomalies in the west, was established in both experiments, highlighting the importance of the atmospheric teleconnection across the Isthmus of Panama in propagating climate anomalies into the Pacific Ocean. Increased atmospheric CO₂ concentrations, as in the CO₂-400 experiment, increased the duration of the AMOC shutdown and associated climate perturbation by changing the relative importance of temperature and salinity drivers of surface water density in the NADW formation region.

The influence of boundary conditions on the modelled climate response to a simulated Heinrich event appears to be significant. This study has implications for the interpretation of proxy records, particularly from sites removed from the North Atlantic, such as the western equatorial Pacific, and with further investigation may shed light on the apparent differences in the strength and duration of Heinrich events recorded in this region (e.g., Partin et al. 2007; Carolin et al. 2013; Scroxton 2014).

2.10. References

- Ahn, J. and E. J. Brook (2007). Atmospheric CO₂ and climate from 65 to 30 ka B.P. *Geophysical Research Letters* 34: L10703.
- Ahn, J. and E. J. Brook (2008). Atmospheric CO₂ and climate on millennial time scales during the last glacial period. *Science* 322: 83–85.
- Ayliffe, L. K., M. K. Gagan, J.-x. Zhao, R. N. Drysdale, J. C. Hellstrom, W. S. Hantoro, M. L. Griffiths, H. Scott-Gagan, E. St Pierre, J. A. Cowley and B. W. Suwargadi (2013). Rapid interhemispheric climate links via the Australasian monsoon during the last deglaciation. *Nature Communications* 4: 2908.
- Barker, S., P. Diz, M. J. Vautravers, J. Pike, G. Knorr, I. R. Hall and W. S. Broecker (2009). Interhemispheric Atlantic seesaw response during the last deglaciation. *Nature* 457: 1097–1102.
- Bitz, C. M., J. C. H. Chiang, W. Cheng and J. J. Barsugli (2007). Rates of thermohaline recovery from freshwater pulses in modern, Last Glacial Maximum, and greenhouse warming climates. *Geophysical Research Letters* 34: L07708.

- Bond, G., W. Broecker, S. Johnsen, J. McManus, L. Labeyrie, J. Jouzel and G. Bonani (1993). Correlations between climate records from North Atlantic sediments and Greenland ice. *Nature* 365: 143–147.
- Bond, G., H. Heinrich, W. Broecker, L. Labeyrie, J. McManus, J. Andrews, S. Huon, R. Jantschik, S. Clasen, C. Simet, K. Tedesco, M. Klas, G. Bonani and S. Ivy (1992). Evidence for massive discharges of icebergs into the North Atlantic ocean during the last glacial period. *Nature* 360: 245–249.
- Borlace, S., W. Cai and A. Santos (2013). Multidecadal ENSO amplitude variability in a 1000-yr simulation of a coupled climate model: Implications for observed ENSO variability *Journal of Climate* 26: 9399–9407.
- Broecker, W., G. Bond, M. Klas, E. Clark and J. McManus (1992). Origin of the northern Atlantic's Heinrich events. *Climate Dynamics* 6: 265–273.
- Broecker, W. S. (1994). Massive iceberg discharges as triggers for global climate change. *Nature* 372: 421–424.
- Broecker, W. S. (1998). Paleocean circulation during the last deglaciation: A bipolar seesaw? *Paleoceanography* 13: 119–121.
- Broecker, W. S. (2006). Was the Younger Dryas triggered by a flood? *Science* 312: 1146–1148.
- Carlson, A. E., P. U. Clark, B. A. Haley, G. P. Klinkhammer, K. Simmons, E. J. Brook and K. J. Meissner (2007). Geochemical proxies of North American freshwater routing during the Younger Dryas cold event. *Proceedings of the National Academy of Sciences* 104: 6556–6561.
- Carolin, S. A., K. M. Cobb, J. F. Adkins, B. Clark, J. L. Conroy, S. Lejau, J. Malang and A. A. Tuen (2013). Varied response of Western Pacific hydrology to climate forcings over the Last Glacial period. *Science* 340: 1564–1566.
- Chen, J. L., C. R. Wilson and B. D. Tapley (2006). Satellite gravity measurements confirm accelerated melting of Greenland ice sheet. *Science* 313: 1958–1960.
- Cheng, W., J. C. H. Chiang and D. Zhang (2013). Atlantic Meridional Overturning Circulation (AMOC) in CMIP5 models: RCP and historical simulations. *Journal of Climate* 26: 7187–7197.
- Clarke, G. K. C. (2003). Hydraulics of subglacial outburst floods: new insights from the Spring-Hutter formulation. *Journal of Glaciology* 49: 299–313.

- Denniston, R. F., K.-H. Wyrwoll, Y. Asmerom, V. J. Polyak, W. F. Humphreys, J. Cugley, D. Woods, Z. LaPointe, J. Peota and E. Greaves (2013). North Atlantic forcing of millennial-scale Indo-Australian monsoon dynamics during the Last Glacial period. *Quaternary Science Reviews* 72: 159–168.
- Deschamps, P., N. Durand, E. Bard, B. Hamelin, G. Camoin, A. L. Thomas, G. M. Henderson, J. i. Okuno and Y. Yokoyama (2012). Ice-sheet collapse and sea-level rise at the Bølling warming 14,600 years ago. *Nature* 483: 559–564.
- Dong, B. and R. T. Sutton (2007). Enhancement of ENSO variability by a weakened Atlantic Thermohaline Circulation in a coupled GCM. *Journal of Climate* 20: 4920–4939.
- Dong, B.-W. and R. T. Sutton (2002). Adjustment of the coupled ocean-atmosphere system to a sudden change in the thermohaline circulation. *Geophysical Research Letters* 29: 1728.
- Driesschaert, E., T. Fichefet, H. Goosse, P. Huybrechts, I. Janssens, A. Mouchet, G. Munhoven, V. Brovkin and S. L. Weber (2007). Modeling the influence of Greenland ice sheet melting on the Atlantic meridional overturning circulation during the next millennia. *Geophysical Research Letters* 34: L10707.
- Fairbanks, R. G. (1989). A 17,000-year glacio-eustatic sea level record: influence of glacial melting rates on the Younger Dryas event and deep-ocean circulation. *Nature* 342: 637–642.
- Griffiths, M. L., R. N. Drysdale, M. K. Gagan, J.-x. Zhao, L. K. Ayliffe, J. C. Hellstrom, W. S. Hantoro, S. Frisia, Y. Feng, I. Cartwright, E. St Pierre, M. J. Fischer and B. W. Suwargadi (2009). Increasing Australian-Indonesian monsoon rainfall linked to early Holocene sea-level rise. *Nature Geoscience* 2: 636–639.
- Heinrich, H. (1988). Origin and consequences of cyclic ice rafting in the Northeast Atlantic Ocean during the past 130,000 years. *Quaternary Research* 29: 142–152.
- Hemming, S. R. (2004). Heinrich events: massive Late Pleistocene detritus layers of the North Atlantic and their global climate imprint. *Reviews of Geophysics* 42: RG1005.

- Hu, A., B. L. Otto-Bliesner, G. A. Meehl, W. Han, C. Morrill, E. C. Brady and B. Briegleb (2008). Response of thermohaline circulation to freshwater forcing under present-day and LGM conditions. *Journal of Climate* 21: 2239–2258.
- IPCC (2007). *Climate Change 2007: The Physical Science Basis. Contribution of Working Group I to the Fourth Assessment Report of the Intergovernmental Panel on Climate Change*. New York, Cambridge.
- IPCC (2013). *Climate change 2013: The physical science basis. Contribution of working group I to the fifth assessment report of the Intergovernmental Panel on Climate Change*. Cambridge, United Kingdom and New York, NY, USA.
- Jiang, D., X. Lang, Z. Tian and L. Ju (2013). Mid-Holocene East Asian summer monsoon strengthening: Insights from paleoclimate modeling intercomparison project (PMIP) simulations. *Palaeogeography, Palaeoclimatology, Palaeoecology* 369: 422–429.
- Johnsen, S. J., H. B. Clausen, W. Dansgaard, K. Fuhrer, N. Gundestrup, C. U. Hammer, P. Iversen, J. Jouzel, B. Stauffer and J. P. Steffensen (1992). Irregular glacial interstadials recorded in a new Greenland ice core. *Nature* 359: 311–313.
- Joussaume, S. and K. E. Taylor (2000). The Paleoclimate Modeling Intercomparison Project. *Proceedings of the third PMIP workshop, Canada, 4-8 October 1999, in WCRP-III WMO/TD-1007*: 9–24.
- Kageyama, M., U. Merkel, B. Otto-Bliesner, M. Prange, A. Abe-Ouchi, G. Lohmann, R. Ohgaito, D. M. Roche, J. Singarayer, D. Swingedouw and X. Zhang (2013). Climatic impacts of fresh water hosing under Last Glacial Maximum conditions: a multi-model study. *Climate of the Past* 9: 935–953.
- Kanner, L. C., S. J. Burns, H. Cheng and R. L. Edwards (2012). High-latitude forcing of the South American Summer Monsoon during the last glacial. *Science* 335: 570–573.
- Kriegler, E., J. W. Hall, H. Held, R. Dawson and H. Joachim Schellnhuber (2009). Imprecise probability assessment of tipping points in the climate system. *Proceedings of the National Academy of Sciences* 106: 5041–5046.
- Lamy, F., D. Hebbeln and G. Wefer (1998). Late Quaternary precessional cycles of terrigenous sediment input off the Norte Chico, Chile (27.5°S) and palaeoclimatic implications. *Palaeogeography, Palaeoclimatology, Palaeoecology* 141: 233–251.

- Ledru, M.-P. and J. Stevenson (2012). The rise and fall of the genus *Araucaria*: a southern hemisphere climate connection. *Peopled landscapes: archaeological and biogeographic approaches to landscapes*. S. Haberle and B. David. Canberra, Australia, ANU ePress. 34: 241–254.
- Legates, D. R. and C. J. Willmott (1990). Mean seasonal and spatial variability in gauge-corrected, global precipitation. *International Journal of Climatology* 10: 111–127.
- Lewis, S. C., A. N. LeGrande, M. Kelley and G. A. Schmidt (2010). Water vapour source impacts on oxygen isotope variability in tropical precipitation during Heinrich events. *Climate of the Past* 6: 325–343.
- Li, Y. and S. P. Harrison (2008). Simulations of the impact of orbital forcing and ocean on the Asian summer monsoon during the Holocene. *Global and Planetary Change* 60: 505–522.
- Li, Y., N. Wang, X. Zhou, C. Zhang and Y. Wang (2014). Synchronous or asynchronous Holocene Indian and East Asian summer monsoon evolution: A synthesis on Holocene Asian summer monsoon simulations, records and modern monsoon indices. *Global and Planetary Change* 116: 30–40.
- Liu, Z., E. Brady and J. Lynch-Stieglitz (2003). Global ocean response to orbital forcing in the Holocene. *Paleoceanography* 18: 1041.
- Lorenz, S. J., J.-H. Kim, N. Rimbu, R. R. Schneider and G. Lohmann (2006). Orbitally driven insolation forcing on Holocene climate trends: Evidence from alkenone data and climate modeling. *Paleoceanography* 21: PA1002.
- Lu, R., W. Chen and B. Dong (2008). How does a weakened Atlantic thermohaline circulation lead to an intensification of the ENSO-south Asian summer monsoon interaction? *Geophysical Research Letters* 35: L08706.
- Lu, R. and B. Dong (2008). Response of the Asian Summer Monsoon to weakening of Atlantic Thermohaline Circulation. *Advances in Atmospheric Sciences* 25: 723–736.
- Manabe, S. and K. Bryan (1969). Climate calculations with a combined ocean-atmosphere model. *Journal of the Atmospheric Sciences* 26: 786–789.
- Manabe, S. and R. J. Stouffer (2000). Study of abrupt climate change by a coupled ocean-atmosphere model. *Quaternary Science Reviews* 19: 285–299.

- Martínez-García, A., A. Rosell-Melé, S. L. Jaccard, W. Geibert, D. M. Sigman and G. H. Haug (2011). Southern Ocean dust-climate coupling over the past four million years. *Nature* 476: 312–316.
- McManus, J. F., R. Francois, J.-M. Gherardi, L. D. Keigwin and S. Brown-Leger (2004). Collapse and rapid resumption of Atlantic meridional circulation linked to deglacial climate changes. *Nature* 428: 834–837.
- Meese, D. A., A. J. Gow, R. B. Alley, G. A. Zielinski, P. M. Grootes, M. Ram, K. C. Taylor, P. A. Mayewski and J. F. Bolzan (1997). The Greenland Ice Sheet Project 2 depth-age scale: Methods and results. *Journal of Geophysical Research* 102: 26411–26423.
- Mohtadi, M., M. Prange, D. W. Oppo, R. De Pol-Holz, U. Merkel, X. Zhang, S. Steinke and A. Lückge (2014). North Atlantic forcing of tropical Indian Ocean climate. *Nature* 509: 76–80.
- Monnin, E., A. Indermühle, A. Dällenbach, J. Flückiger, B. Stauffer, T. F. Stocker, D. Raynaud and J.-M. Barnola (2001). Atmospheric CO₂ concentrations over the last glacial termination. *Science* 291: 112–114.
- Muller, J., J. F. McManus, D. W. Oppo and R. Francois (2012). Strengthening of the Northeast Monsoon over the Flores Sea, Indonesia, at the time of Heinrich event 1. *Geology* 40: 635–638.
- Partin, J. W., K. M. Cobb, J. F. Adkins, B. Clark and D. P. Fernandez (2007). Millennial-scale trends in west Pacific warm pool hydrology since the Last Glacial Maximum. *Nature* 449: 452–455.
- Pausata, F. S. R., D. S. Battisti, K. H. Nisancioglu and C. M. Bitz (2011). Chinese stalagmite $\delta^{18}\text{O}$ controlled by changes in the Indian monsoon during a simulated Heinrich event. *Nature Geoscience* 4: 474–480.
- Pedro, J. B., T. D. van Ommen, S. O. Rasmussen, V. I. Morgan, J. Chappellaz, A. D. Moy, V. Masson-Delmotte and M. Delmotte (2011). The last deglaciation: timing the bipolar seesaw. *Climate of the Past* 7: 671–683.
- Perez-Sanz, A., G. Li, P. González-Sampériz and S. P. Harrison (2014). Evaluation of modern and mid-Holocene seasonal precipitation of the Mediterranean and northern Africa in the CMIP5 simulations. *Climate of the Past* 10: 551–568.

- Phipps, S. J. (2010). *Technical report: The CSIRO Mk3L climate system model v1.2*. Sydney, The Antarctic Climate & Ecosystems Cooperative Research Centre, University of New South Wales.
- Phipps, S. J. and J. N. Brown (2010). Understanding ENSO dynamics through the exploration of past climates. *IOP Conference Series: Earth and Environmental Science* 9: 012010.
- Phipps, S. J., H. V. McGregor, J. Gergis, A. J. E. Gallant, R. Neukom, S. Stevenson, D. Ackerley, J. R. Brown, M. J. Fischer and T. D. van Ommen (2013). Paleoclimate data-model comparison and the role of climate forcings over the past 1500 years. *Journal of Climate* 26: 6915–6936.
- Phipps, S. J., L. D. Rotstayn, H. B. Gordon, J. L. Roberts, A. C. Hirst and W. F. Budd (2011). The CSIRO Mk3L climate system model version 1.0 - Part 1: Description and evaluation. *Geoscientific Model Development* 4: 483–509.
- Rahmstorf, S. (2006). Thermohaline Ocean Circulation. *Encyclopedia of Quaternary Sciences*. S. A. Elias. Amsterdam, Elsevier.
- Rahmstorf, S., J. E. Box, G. Feulner, M. E. Mann, A. Robinson, S. Rutherford and E. J. Schaffernicht (2015). Exceptional twentieth-century slowdown in Atlantic Ocean overturning circulation. *Nature Climate Change* 5: 475–480.
- Santoso, A., W. Cai, M. H. England and S. J. Phipps (2011). The role of the Indonesian Throughflow on ENSO dynamics in a coupled climate model. *Journal of Climate* 24: 585–601.
- Santoso, A., M. H. England and W. Cai (2012). Impact of Indo-Pacific feedback interactions on ENSO dynamics diagnosed using ensemble climate simulations. *Journal of Climate* 25: 7743–7763.
- Schmittner, A., M. Latif and B. Schneider (2005). Model projections of the North Atlantic thermohaline circulation for the 21st century assessed by observations. *Geophysical Research Letters* 32: L23710.
- Scroxton, N. G. (2014). *Late Pleistocene climate and environment from speleothems on Flores, Indonesia: vegetation, volcanoes and Homo floresiensis*, The Australian National University.
- Shulmeister, J., I. Goodwin, J. Renwick, K. Harle, L. Armand, M. S. McGlone, E. Cook, J. Dodson, P. P. Hesse, P. Mayewski and M. Curran (2004). The Southern

- Hemisphere westerlies in the Australasian sector over the last glacial cycle: a synthesis. *Quaternary International* 118–119: 23–53.
- Singarayer, J. S. and P. J. Valdes (2010). High-latitude climate sensitivity to ice-sheet forcing over the last 120 kyr. *Quaternary Science Reviews* 29: 43–55.
- Smith, R. S. and J. M. Gregory (2009). A study of the sensitivity of ocean overturning circulation and climate to freshwater input in different regions of the North Atlantic. *Geophysical Research Letters* 36: L15701.
- Srokosz, M., M. Baringer, H. Bryden, S. Cunningham, T. Delworth, S. Lozier, J. Marotzke and R. Sutton (2012). Past, present, and future changes in the Atlantic Meridional Overturning Circulation. *Bulletin of the American Meteorological Society* 93: 1663–1676.
- Stouffer, R. J., J. Yin, J. M. Gregory, K. W. Dixon, M. J. Spelman, W. Hurlin, A. J. Weaver, M. Eby, G. M. Flato, H. Hasumi, A. Hu, J. H. JungCLAUS, I. V. Kamenkovich, A. Levermann, M. Montoya, S. Murakami, S. Nawrath, A. Oka, W. R. Peltier, D. Y. Robitaille, A. Sokolov, G. Vettoretti and S. L. Weber (2006). Investigating the causes of the response of the thermohaline circulation to past and future climate changes. *Journal of Climate* 19: 1365–1387.
- Sun, Y., S. C. Clemens, C. Morrill, X. Lin, X. Wang and Z. An (2012). Influence of Atlantic meridional overturning circulation on the East Asian winter monsoon. *Nature Geoscience* 5: 46–49.
- Swingedouw, D., J. Mignot, P. Braconnot, E. Mosquet, M. Kageyama and R. Alkama (2009). Impact of freshwater release in the North Atlantic under different climate conditions in an OAGCM. *Journal of Climate* 22: 6377–6403.
- Swingedouw, D., C. B. Rodehacke, S. M. Olsen, M. Menary, Y. Gao, U. Mikolajewicz and J. Mignot (2015). On the reduced sensitivity of the Atlantic overturning to Greenland ice sheet melting in projections: a multi-model assessment. *Climate Dynamics* 44: 3261–3279.
- Tans, P. and R. Keeling. (2014). NOAA/ESRL and Scripps Institution of Oceanography. from <http://www.esrl.noaa.gov/gmd/ccgg/trends/>.
- Tao, W., W. Huijun and J. Dabang (2010). East Asian summer climate as simulation by the PMIP2 models. *Palaeogeography, Palaeoclimatology, Palaeoecology* 288: 93–102.

- Thorpe, R. B., J. M. Gregory, T. C. Johns, R. A. Wood and J. F. B. Mitchell (2001). Mechanisms determining the Atlantic Thermohaline Circulation response to greenhouse gas forcing in a non-flux adjusted coupled climate model. *Journal of Climate* 14: 3102–3116.
- Timmermann, A., S. J. Lorenz, S. I. An, A. Clement and S. P. Xie (2007a). The Effect of Orbital Forcing on the Mean Climate and Variability of the Tropical Pacific. *Journal of Climate* 20: 4147–4159.
- Timmermann, A., Y. Okumura, S.-I. An, A. Clement, B. Dong, E. Guilyardi, A. Hu, J. H. Jungclaus, M. Renold, T. F. Stocker, R. J. Stouffer, R. Sutton, S.-P. Xie and J. Yin (2007b). The influence of a weakening of the Atlantic meridional overturning circulation on ENSO. *Journal of Climate* 20: 4899–4919.
- U.S. Department of Commerce, National Oceanic and Atmospheric Administration and National Geophysical Data Center. (2006). 2-minute Gridded Global Relief Data (ETOPO2v2), 2006. from <http://www.ngdc.noaa.gov/mgg/fliers/06mgg01.html>.
- UCAR. (2011). Climate Modeling. Retrieved 6th March, 2015, from <http://scied.ucar.edu/longcontent/climate-modeling>.
- Wan, X., P. Chang, C. S. Jackson, L. Ji and M. Li (2011). Plausible effect of climate model bias on abrupt climate change simulations in Atlantic sector. *Deep-Sea Research II* 58: 1904–1913.
- Wang, Y. J., H. Cheng, R. L. Edwards, Z. S. An, J. Y. Wu, C.-C. Shen and J. A. Dorale (2001). A high-resolution absolute-dated Late Pleistocene monsoon record from Hulu Cave, China. *Science* 294: 2345–2348.
- Wu, L., C. Li, C. Yang and S.-P. Xie (2008). Global teleconnections in response to a shutdown of the Atlantic Meridional Overturning Circulation. *Journal of Climate* 21: 3002–3019.
- Yin, J. and R. J. Stouffer (2007). Comparison of the stability of the Atlantic Thermohaline Circulation in two coupled atmosphere-ocean general circulation models. *Journal of Climate* 20: 4293–4315.
- Zhang, R. and T. L. Delworth (2005). Simulated tropical response to a substantial weakening of the Atlantic Thermohaline Circulation. *Journal of Climate* 18: 1853–1860.

Zheng, W. and P. Braconnot (2013). Characterization of model spread in PMIP2 Mid-Holocene simulations of the African Monsoon. *Journal of Climate* 26: 1192–1210.

Zheng, W., B. Wu, J. He and Y. Yu (2013). The East Asian Summer Monsoon at the mid-Holocene: results from PMIP3 simulations. *Climate of the Past* 9: 453–466.

CHAPTER THREE

A 40,000-year speleothem $\delta^{13}\text{C}$ record of environmental change in southwest Sulawesi, Indonesia

3.1. Introduction

Speleothem $\delta^{18}\text{O}$ is a widely used proxy in palaeoclimate studies; however, $\delta^{13}\text{C}$, which is measured concurrently, is largely underutilised. Interpretation of $\delta^{13}\text{C}$ is difficult because of the large number of influences on the potential sources of carbon and modification of carbon isotope ratios during stalagmite formation.

To date, only three speleothem $\delta^{13}\text{C}$ records covering parts of the past 40 kyr have been published for the Indo-Pacific Warm Pool (IPWP) region (Griffiths et al. 2010; Partin et al. 2013; Scroxton 2014), whereas eight $\delta^{18}\text{O}$ records have been published for the region (Partin et al. 2007; Griffiths et al. 2009; Lewis et al. 2011; Ayliffe et al. 2013; Carolin et al. 2013; Denniston et al. 2013a; Denniston et al. 2013b; Scroxton 2014). The two $\delta^{13}\text{C}$ records for Flores, Indonesia, suggest that speleothem $\delta^{13}\text{C}$ records changes in vegetation productivity (Griffiths et al. 2010; Scroxton 2014). These records provide the foundation for a coherent interpretation for speleothem $\delta^{13}\text{C}$ within tropical and monsoonal Indonesia. A record of speleothem $\delta^{13}\text{C}$ for Borneo,

however, shows highly localised and likely insignificant $\delta^{13}\text{C}$ variations, which provide limited information on regional environmental signals (Partin et al. 2013). The apparent inconsistencies in speleothem $\delta^{13}\text{C}$ as a recorder of climate or vegetation shifts has led to scepticism of the robustness of interpretations developed using this proxy.

Interpretation of $\delta^{13}\text{C}$ in speleothems is particularly challenging because no definitive environmental controls have been agreed upon in the existing literature. To date, interpretations of speleothem $\delta^{13}\text{C}$ have been made on a case-by-case basis, with no clear consistency between regional or environmental settings. Although this approach is not completely unfounded, it is by no means the best way to understand the insights provided by $\delta^{13}\text{C}$. Previous studies have interpreted speleothem $\delta^{13}\text{C}$ as a proxy for $\text{C}_3:\text{C}_4$ vegetation shifts (e.g., Dorale et al. 1998; Denniston et al. 2000), vegetation/soil productivity and density (e.g., Hellstrom et al. 1998; Genty et al. 2003; Hou et al. 2003; Baldini et al. 2005; Cruz et al. 2006; Cosford et al. 2009; Jo et al. 2010; Blyth et al. 2013; Griffiths et al. 2013), inorganic karst processes (e.g., Cosford et al. 2009; Griffiths et al. 2010; Hartmann et al. 2013; Partin et al. 2013), soil temperature (e.g., Genty et al. 2003; Martín-Chivelet et al. 2011; Griffiths et al. 2013) and anthropogenic influences above the cave site (e.g., Hartmann et al. 2013). Replication of speleothem $\delta^{13}\text{C}$ records is also known to be problematic, making it even more difficult to interpret them with any certainty (e.g., Partin et al. 2013).

Here we present a stalagmite $\delta^{13}\text{C}$ record for southwest Sulawesi, which covers the period 40 kyr BP to present. This record is continuous, with an average resolution of 50 years, and provides a detailed history of changes in carbon input to the stalagmite over time. We interpret the Sulawesi record in terms of carbon isotope systematics in tropical karst systems, and then compare it with regional and global palaeoenvironmental records to place the result into a broad context.

3.2. Materials and methods

3.2.1. Stalagmite collection and ^{230}Th dating

Stalagmite GB09-3 was collected in 2009 from Gempa Bumi cave in southwest Sulawesi (5°S , 120°E , 140 m above sea level). GB09-3 has a length of ~ 700 mm and an

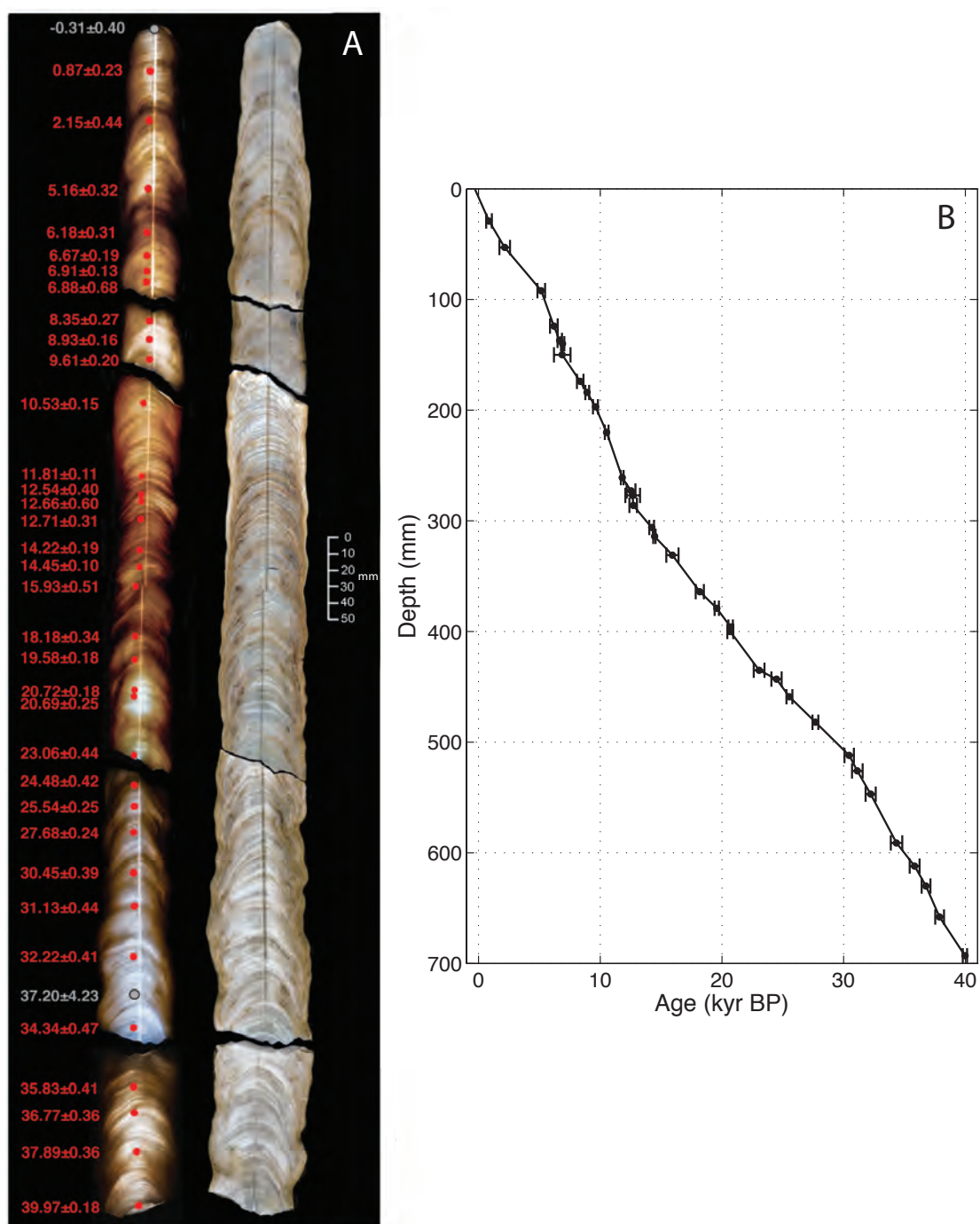


Figure 3.1: Stalagmite GS09-3 with age model. (A) Back-lit (left) and reflected light (right) photographs of stalagmite. Sampling track used for stable isotope analysis is visible down the centre of the stalagmite. Red dots show the locations of ^{230}Th dates, expressed as kyr BP (where present is defined as AD1950). Two dates shown in grey were not used in the final age model. Details of the ^{230}Th age data are given in Appendix Table A1. (B) ^{230}Th -corrected age-depth plot for GS09-3. All corrected ages are in stratigraphic sequence, within error. The mean growth rate for GS09-3 is 0.9 mm per 50 years, with no determinable hiatuses.

average diameter of ~50 mm (Figure 3.1). Stalagmite GB11-9 was collected in 2011 from Gempa Bumi Cave to demonstrate replication of the isotope record across its interval of overlap with the older glacial section of GB09-03. Stalagmite GB11-9 has a length of ~615 mm and an average diameter of ~80 mm (Figure 3.2). Both samples were not actively growing at the time of collection.

A total of 36 samples were analysed for uranium and thorium isotopes to develop the chronology for GB09-3 (Appendix Table A1). Six samples were analysed at the University of Minnesota (by Hai Cheng and R. Lawrence Edwards), with the remaining 30 samples analysed at the University of Melbourne (by John Hellstrom). Eight ^{230}Th dates for GB11-9 were analysed at the University of Melbourne (by John Hellstrom). Dates were taken adjacent to the stable isotope sampling track, with an

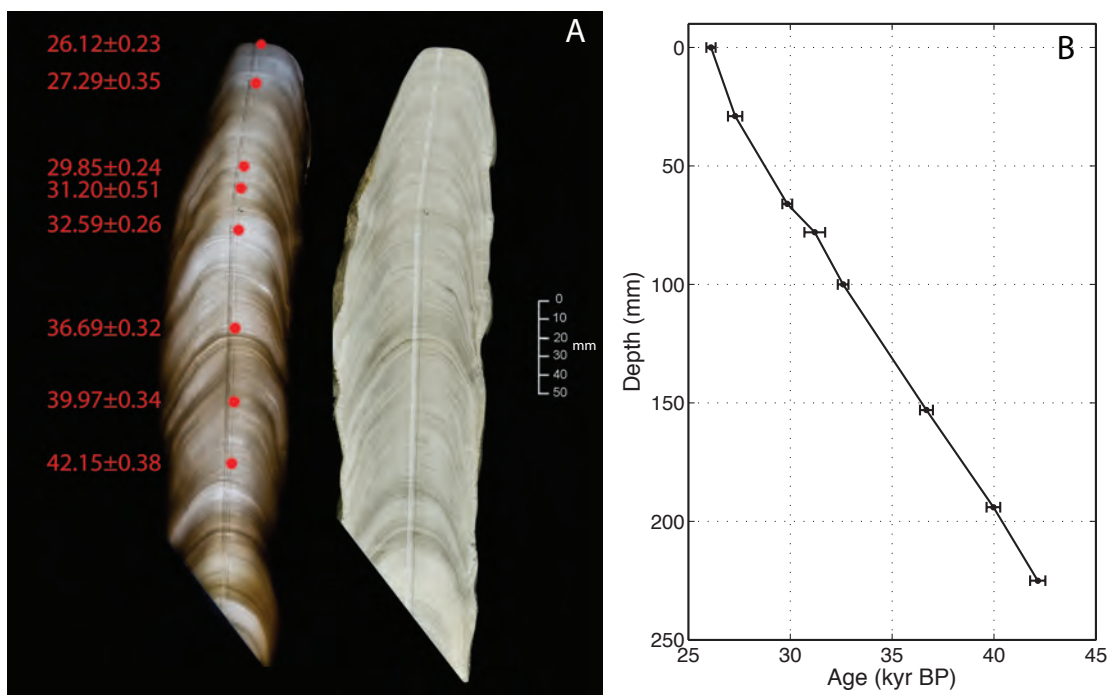


Figure 3.2: Stalagmite GS11-9 with age model. (A) Back-lit (left) and reflected light (right) photographs of stalagmite. Sampling track used for stable isotope analysis is visible down the centre of the stalagmite. Red dots show the locations of ^{230}Th dates, expressed as kyr BP (where present is defined as AD1950). Details of the ^{230}Th age data are given in Appendix Table A1. (B) ^{230}Th -corrected age-depth plot for GS11-9. All corrected ages are in stratigraphic sequence, within error. The mean growth rate for GS11-9 over the period 23–40 kyr BP is 0.7 mm per 50 years, with no determinable hiatuses. Data from the bottom of GS11-9 are not included in this study.

average sample size of 65 mg. Samples were analysed using multi-collector coupled plasma mass spectrometry (MC-ICP-MS), following the methods of Hellstrom et al. (2003). All samples were corrected for detrital thorium using an initial [$^{230}\text{Th}/^{232}\text{Th}$] ratio of 3.0 ± 0.75 . Age models were created using the Monte Carlo technique of Hellstrom (2006). Two ^{230}Th ages were excluded from the age model of GB09-3: GB09-3-2 and GB09-3-uD6. Both of these samples had very large relative errors due to high detrital thorium (130% and 11% respectively. N.B. GB09-3-2 was the stalagmite top date) and were inconsistent with surrounding dates. When these two ages were excluded, the remaining age model had all dates in stratigraphic sequence, with no determinable hiatuses (Figure 3.1). The mean growth rate for GB09-3 over the period 40–0 kyr BP was 0.9 mm per 50 years.

The age model for GB11-9 is comprised of eight ^{230}Th ages, all in stratigraphic order, within error. All eight dates were used in the final age model, which was produced using the same Monte Carlo method as for GB09-3. The mean growth rate for GB11-9 over the period 40–23 kyr BP was 0.7 mm per 50 years (Figure 3.2).

3.2.2. Stable isotope analysis and error reporting

GB09-3 was continuously sampled for stable isotope analysis at an average interval of 0.9 mm (~50-year resolution) along the central growth axis. Sampling was performed using a Sheridan GCM micromill and a 1 mm diameter mill bit. Stable isotope analysis was conducted on 755 samples (Appendix Table A1), with an average sample size of 200 μg . Measurements of $\delta^{18}\text{O}$ and $\delta^{13}\text{C}$ were made at The Australian National University using a Finnigan MAT-251 mass spectrometer coupled to an automated Kiel carbonate device. GB11-9 was slabbed about the central growth axis and micromilled along the central axis using a 1 mm diameter drill bit at an interval of 0.7 mm, equating at an average sampling interval of ~50 years. Analysis of $\delta^{18}\text{O}$ and $\delta^{13}\text{C}$ was conducted on a total of 323 samples (Appendix Table A1).

For the isotope analysis, one NBS-19 standard was analysed for every 5–8 samples to ensure consistency among runs. Results are reported relative to Vienna Pee Dee Belemnite (VPDB) following adjustment using the in-run measurements of NBS-19 ($\delta^{18}\text{O} = -2.20\text{‰}$, $\delta^{13}\text{C} = 1.95\text{‰}$) and less frequent measurements of NBS-18 ($\delta^{18}\text{O} = -23.0\text{‰}$, $\delta^{13}\text{C} = 5.0\text{‰}$). The analytical error for measurements of NBS-19 was

calculated by finding the standard deviation of NBS-19 across all runs. Using this method, the analytical error for NBS-19 $\delta^{13}\text{C}$ was 0.02‰ for GS09-3 ($n = 187$, 1σ), and 0.02‰ for GS11-9 ($n = 83$, 1σ).

The reproducibility of $\delta^{13}\text{C}$ for the stalagmite samples themselves was determined by running duplicate and triplicate measurements. Samples with a run standard deviation greater than 0.05‰ (in $\delta^{18}\text{O}$) were re-run, in order to minimise error related to analysis methods. Additionally, $\delta^{13}\text{C}$ values that deviated largely from adjacent values in the time series were duplicated to ensure that abrupt peaks and troughs in the data set reflect real changes in speleothem $\delta^{13}\text{C}$. Triplicates were run where duplicate measurements differed by more than 0.1‰ in $\delta^{18}\text{O}$. The mean standard error for duplicate/triplicate analyses of $\delta^{13}\text{C}$ was 0.02‰ for GS09-3 ($n = 126$), and 0.03‰ for GS11-9 ($n = 46$) (Figure 3.3).

Quantification of the sample errors for GB09-3 allows a comparison of the signal:error ratio. This relationship is important, as it clarifies whether observed variability is due to errors associated with the $\delta^{13}\text{C}$ measurements, or real $\delta^{13}\text{C}$ signal. Analysis of the standard error of the mean $\delta^{13}\text{C}$ values for individual samples suggests that small-scale variability within the $\delta^{13}\text{C}$ record is detectable (Figure 3.3A). The same technique was applied to GB11-9, which also shows good reproducibility of $\delta^{13}\text{C}$ (Figure 3.3B).

Signal replication of overlapping growth intervals in the two stalagmites provides a valuable test for calcite deposition in isotopic equilibrium because it is unlikely that different stalagmites could record similarly fractionated signals (Dorale and Liu 2009). Replication of $\delta^{13}\text{C}$ between records is reasonably good, with much of the high-frequency variability in GS09-3 reproduced in GS11-9 (Figure 3.4). There are periods, however, where the two records diverge: at 40–38 kyr BP, and again around 33 kyr BP. It has been noted that consistent replication of speleothem $\delta^{13}\text{C}$ records is difficult to achieve, even within the same cave (Partin et al. 2013), and some degree of variation between records is to be expected. Differences in the relative growth rates of the two speleothems may also account for the periods of divergence between the records. It has been suggested that faster growing stalagmites are less sensitive to positive isotope excursions than slower growing stalagmites, possibly accounting for the reduced magnitude of positive isotope excursions in GS11-9, compared to those in GS09-3 (Scropton 2014).

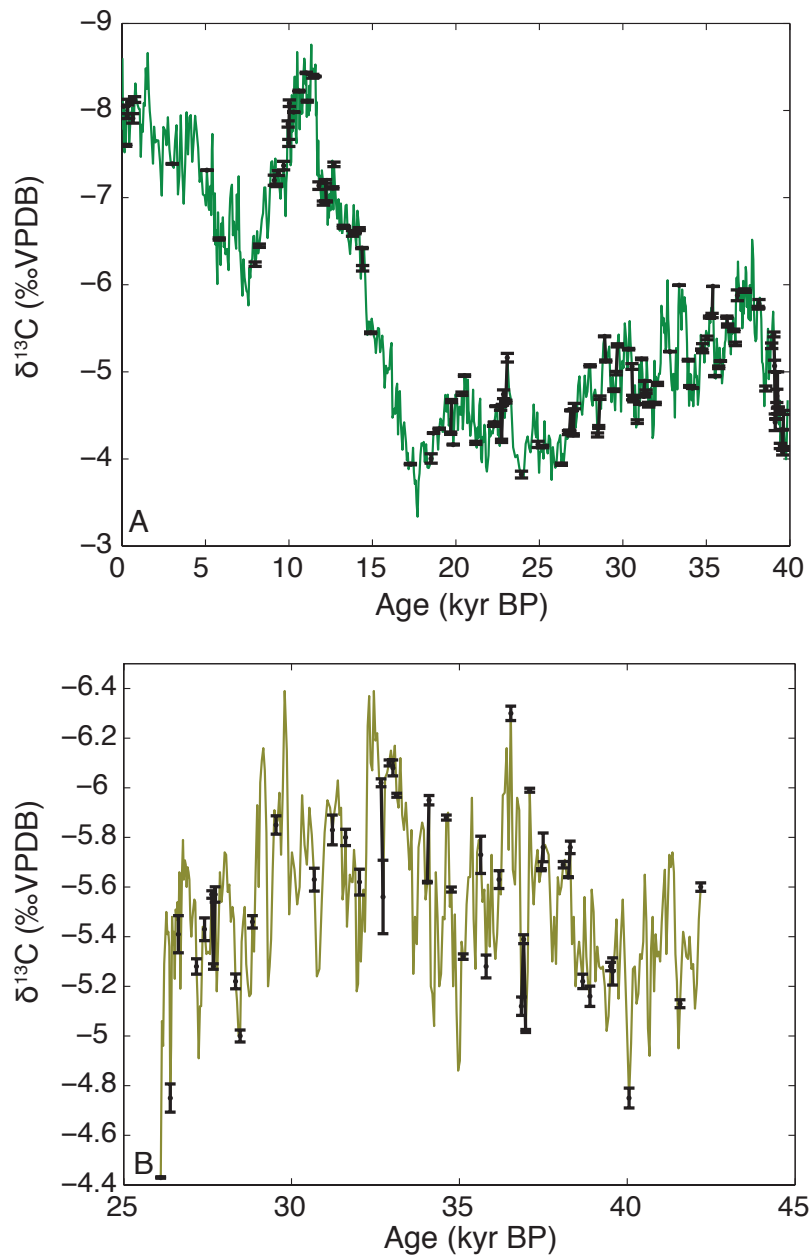


Figure 3.3: Reproducibility of $\delta^{13}\text{C}$ for stalagmites GS09-3 (A) and GS11-9 (B), as determined by duplicate or triplicate measurements. Error bars show the standard error of the mean $\delta^{13}\text{C}$ value for each sample where duplicate or triplicate measurements were performed. The standard errors of the $\delta^{13}\text{C}$ time series are small compared to the variability of both records.

3.2.3. Trace element analysis: Mg/Ca and Sr/Ca

Analysis of trace amounts of Mg/Ca and Sr/Ca in GS09-3 was conducted to supplement the stable isotope analyses. Mg/Ca and Sr/Ca were measured on aliquots of the sample

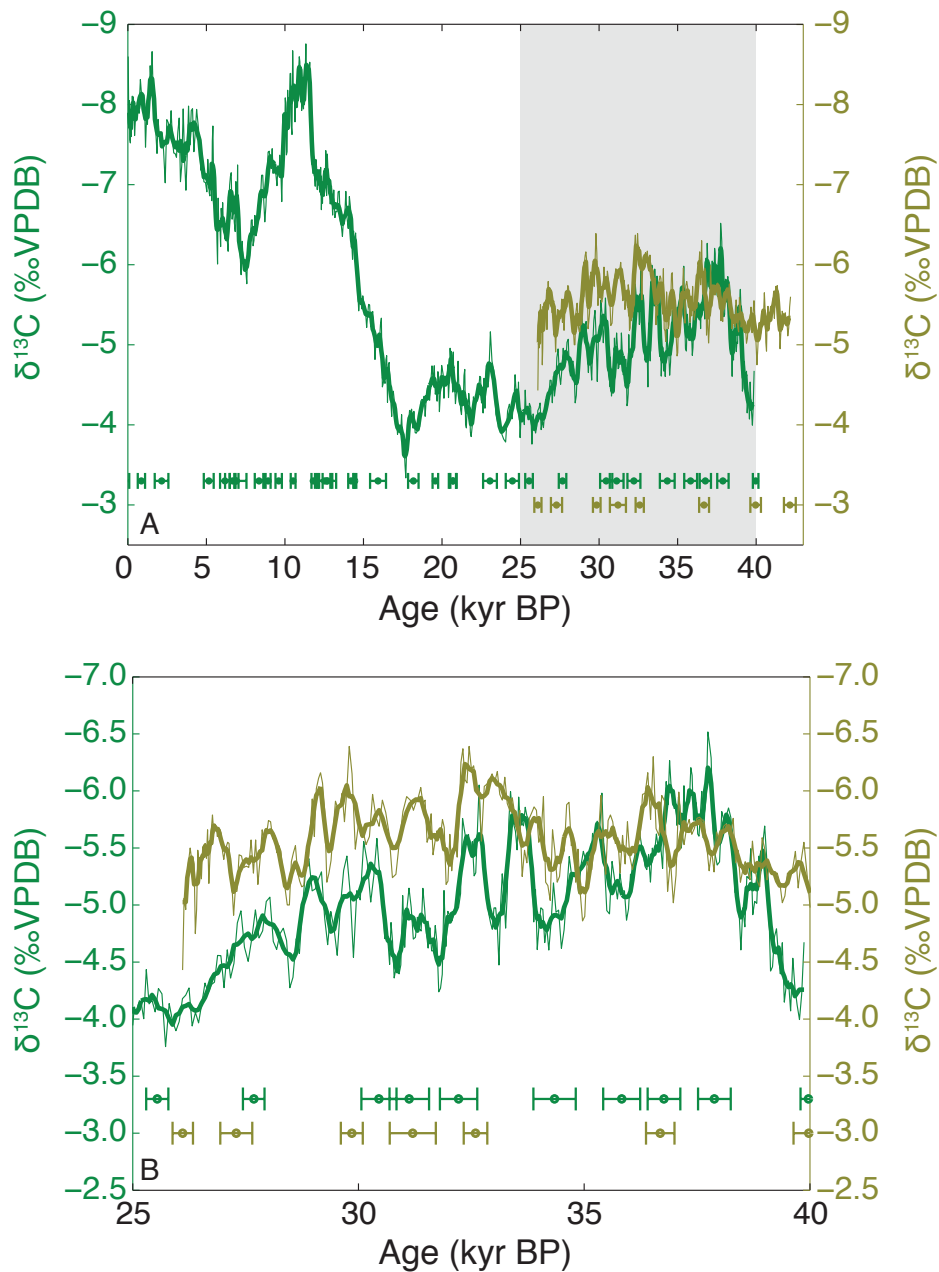


Figure 3.4: Reproducibility of the $\delta^{13}\text{C}$ record for Gempa Bumi Cave, Sulawesi. (A) Comparison of the $\delta^{13}\text{C}$ records for stalagmites GS09-3 (green) and GS11-9 (olive). Positions of ^{230}Th ages (with 2-sigma errors) are shown below the records for each stalagmite. Grey shading shows the section of the record highlighted in (B).

powders milled for stable isotope analysis, allowing direct comparison between stable isotope and trace element results. Low concentrations of Mg and Sr within the sample powders meant that analyses needed to be carried out on relatively large sample sizes (1.5–2 mg) to ensure signals within the detection limit of the instrument. This meant that replicate measurements could not be undertaken, as the analysis consumed the

remaining sample powders. Mg/Ca and Sr/Ca was measured in every second sample along the milled transect for a total of 375 measurements.

Samples were dissolved in 2% HNO_3 , before being analysed on a Vista AX ICP-AES using a Sturman-Masters spray chamber and V groove nebulizer at The Australian National University, based on the methods of Schrag (1999) and de Villiers (2002). Analytical precision was determined by 30 repeat analyses of a laboratory (coral) standard. The Mg/Ca and Sr/Ca values for the standard were determined via an internal standard prepared from Spec Pure CaCO_3 , SrCO_3 and MgCO_3 dissolved in 2% HNO_3 , and validated by TIMS (thermal ionisation mass spectrometry) against an accepted standard. Standards bracketed each unknown sample to monitor any drift occurring within and between runs. Each sample was measured 10 times within a single analysis, and results presented are the average of these measurements.

3.3. Results

3.3.1. Stable isotopes

The $\delta^{13}\text{C}$ time series for GS09-3 can be divided into three main sections: glacial (40–18 kyr BP), deglacial (18–11 kyr BP) and Holocene (11 kyr BP – present) (Figure 3.5). The glacial state includes data for Marine Isotope Stage 3 and the Last Glacial Maximum (LGM). The range of $\delta^{13}\text{C}$ values for this period is -6.5‰ to -3.3‰. The highest $\delta^{13}\text{C}$ value occurs at 17.7 kyr BP, just prior to the onset of global deglaciation (Pedro et al. 2011).

The deglacial interval contains the highest and lowest $\delta^{13}\text{C}$ in the time series, -3.3‰ at 17.7 kyr BP and -8.8‰ at 11.3 kyr BP (Figure 3.5). This period represents the isotopic response of the transition from the LGM to the Holocene. However, the transition is not smooth, and includes two abrupt negative excursions evident at 14.7–14.5 kyr BP (-1‰ change), and 11.7–11.6 kyr BP (-1.2‰ change). The magnitude of these events is relatively large, representing 18% and 22% of the total LGM/Holocene transition respectively.

The Holocene shows a surprisingly high degree of isotopic variability. During this time, $\delta^{13}\text{C}$ moves from the lowest value at ~11 kyr BP to -5.8‰ at 7.5 kyr BP,

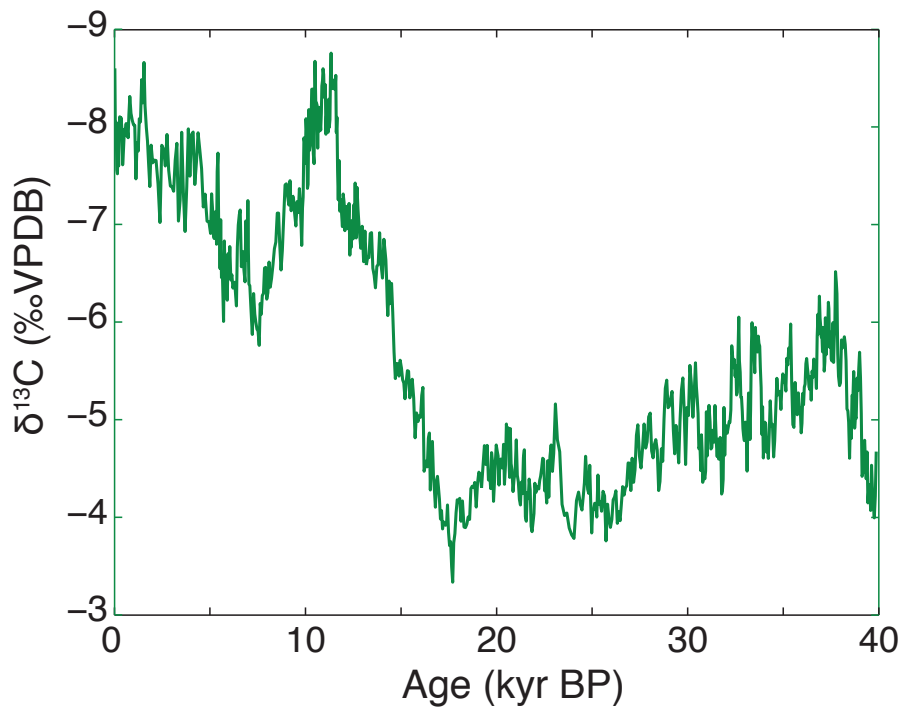


Figure 3.5: The 40-kyr $\delta^{13}\text{C}$ record for stalagmite GS09-3.

before returning to -8.6‰ in the late Holocene. This ‘v-like’ pattern of variability in the early to middle Holocene is relatively smooth, with high-frequency variability punctuating the gradual movement in and out of the relatively positive $\delta^{13}\text{C}$ excursion.

3.3.2. Trace elements: Mg/Ca and Sr/Ca

The Mg/Ca and Sr/Ca results appear to vary alongside speleothem $\delta^{13}\text{C}$, with a clear difference between the glacial (40–11 kyr BP) and Holocene (11 kyr BP–present) periods. Mg/Ca ratios vary between 0.4 mmol/mol in the Holocene and 2.7 mmol/mol during a number of peaks during the glacial (Figure 3.6). Variability in Mg/Ca during the glacial is relatively high, with an ~ 2 mmol/mol range in values. There is also an apparent ~ 10 -kyr cyclicity during the glacial period, with a change in mean values evident between 40–30 kyr BP, 30–20 kyr BP and 20–10 kyr BP. An abrupt step change in Mg/Ca from ~ 1.4 mmol/mol to ~ 0.7 mmol/mol occurs during the deglacial interval. Mg/Ca variability in the Holocene is relatively low, with a range of only ~ 0.4 mmol/mol. The high amplitude, rapid swings in Mg/Ca that occur during the glacial are not evident during the Holocene.

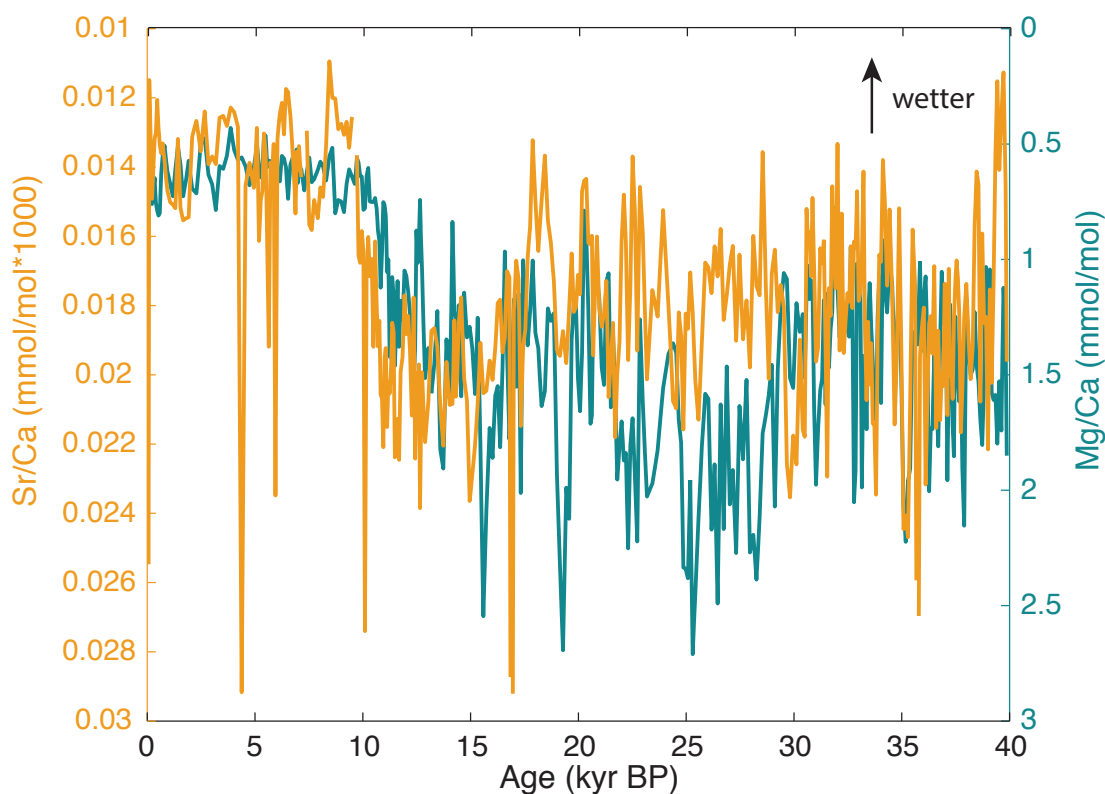


Figure 3.6: Mg/Ca and Sr/Ca data for stalagmite GS09-3. Sr/Ca (orange) and Mg/Ca (green) records for GS09-3. Note that the axes are reversed. Trace element analyses were conducted on every second stable isotope sample, resulting in a resolution of ~ 100 years.

The Sr/Ca data appear to be quite noisy; however, there is a glacial/interglacial differentiation evident, similar to Mg/Ca. Sr/Ca values range between $0.01 \text{ mmol/mol} \times 10^3$ and $0.03 \text{ mmol/mol} \times 10^3$ but the majority of the dataset ranges between 0.01 - $0.025 \text{ mmol/mol} \times 10^3$ (Figure 3.6). The average Sr/Ca value for the glacial ($\sim 0.018 \text{ mmol/mol} \times 10^3$) is higher than the average for the Holocene ($\sim 0.015 \text{ mmol/mol} \times 10^3$). In addition, the glacial Sr/Ca record shows relatively large variability, with some abrupt increases of as much as $0.01 \text{ mmol/mol} \times 10^3$, even when eight outliers were removed (large positive excursions occurring at a single data point, not shown). Replicate analysis of these data points was not possible because the sample powders were consumed in the initial analysis. It is likely these outliers resulted from analytical error associated with contamination of the sample by the standard.

3.4. Discussion

3.4.1. Tropical rainfall: $\delta^{18}\text{O}$ and $\delta^{13}\text{C}$

Comparison of $\delta^{13}\text{C}$ and $\delta^{18}\text{O}$ data from the same stalagmite provides information about the influence of precipitation on $\delta^{13}\text{C}$. Interpretation of $\delta^{18}\text{O}$ in tropical speleothems as a proxy for rainfall amount is well established in the literature (e.g., Partin et al. 2007; Wang et al. 2007; Griffiths et al. 2009; Lewis et al. 2011; Kanner et al. 2012; Ayliffe et al. 2013; Carolin et al. 2013). Examining the covariance of stalagmite $\delta^{18}\text{O}$ and $\delta^{13}\text{C}$ will therefore indicate whether $\delta^{13}\text{C}$ is responding to precipitation. The large-scale features of $\delta^{18}\text{O}$ and $\delta^{13}\text{C}$ in the GB09-3 record are different, showing little similarity in both the trends and the timing of low-frequency variability (Figure 3.7). Most notable is the large offset of approximately six thousand years between the initiation of the large

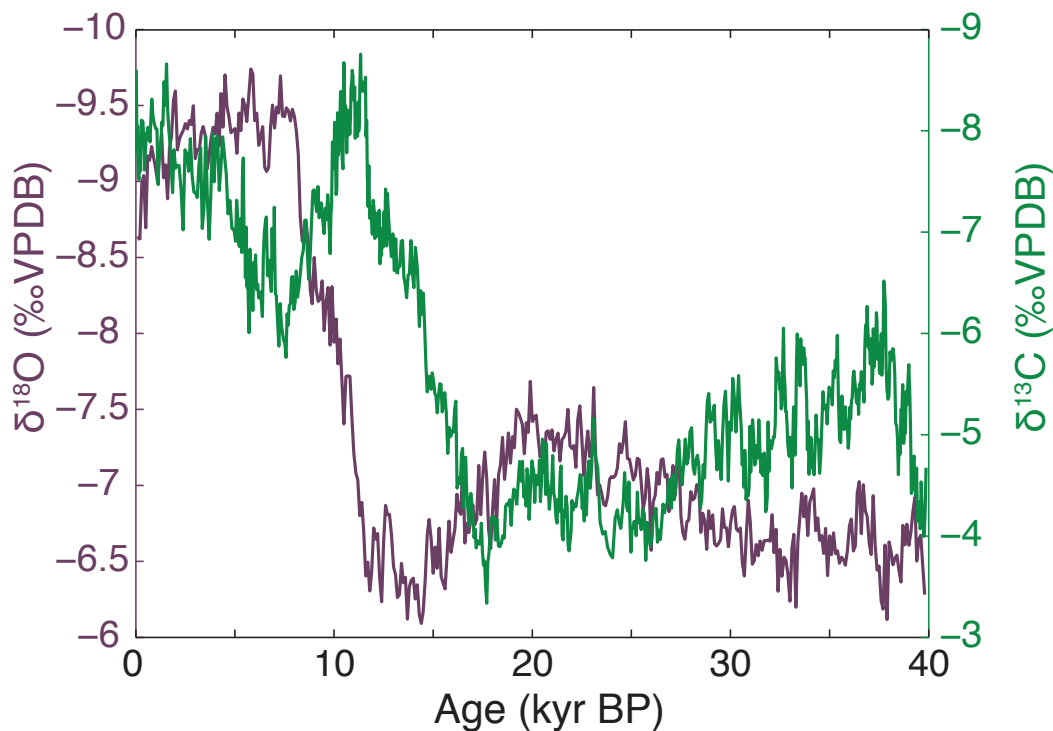


Figure 3.7: The 40-kyr $\delta^{13}\text{C}$ record for stalagmite GS09-3 (green; A) plotted with the $\delta^{18}\text{O}$ record (purple; B). There is a clear offset in the timing of the deglacial signal, suggesting these two proxies, within the same stalagmite, are responding to different environmental variables.

deglacial shifts in $\delta^{13}\text{C}$ (17.7 kyr BP) and $\delta^{18}\text{O}$ (11.8 kyr BP). The relative timing of these negative excursions provides us with information relating to the drivers of each signal. Changes in $\delta^{18}\text{O}$ from 11.8 kyr BP are related to an increase in deep atmospheric convection, associated with the inundation of exposed continental shelves within the western equatorial Pacific (see Chapter 2 for more information). The large excursion in $\delta^{13}\text{C}$ six thousand years prior to this suggests that precipitation is not a key driver of the $\delta^{13}\text{C}$ record. This means we can interpret $\delta^{13}\text{C}$ independently of $\delta^{18}\text{O}$, providing us with a second proxy for climatic and environmental change occurring at this site through time.

3.4.2. Interpreting speleothem $\delta^{13}\text{C}$

Here we use a process of elimination to establish the best interpretation of the Sulawesi speleothem $\delta^{13}\text{C}$ record, using our record and other palaeoenvironmental records from the region.

3.4.2.1. $\text{C}_3:\text{C}_4$ vegetation changes

Large-scale changes in vegetation types above a cave site can result in large changes in $\delta^{13}\text{C}$ in speleothems. Vegetation photosynthesises using one of two main chemical pathways: C_3 or C_4 , which are distinguished by the chemical reaction of carbon that takes place during photosynthesis. C_3 plants account for approximately 75% of terrestrial photosynthesis, and thrive under humid, warm and high CO_2 conditions (Edwards et al. 2010). C_4 plants are primarily found in more arid environments in savannah grasslands (Edwards et al. 2010), and largely constitute small grasses and shrubs (Still et al. 2003).

C_3 and C_4 plants fractionate carbon differently, with CO_2 respired in equilibrium with C_3 plants exhibiting a range in $\delta^{13}\text{C}$ values between -26‰ and -20‰, compared to C_4 plants of between -16‰ and -10‰ (McDermott 2004). Speleothems in caves overlain by C_3 vegetation record values between -14‰ and -6‰, and C_4 vegetation, -6‰ to +2‰ (McDermott 2004; Cosford et al. 2009). As a result, changes in the ratio of C_3 and C_4 vegetation types, driven by changes in climate or vegetation destruction, can result in a change in $\delta^{13}\text{C}$ in the underlying stalagmite. Vegetation shifts between forest and grassland were inferred from a stalagmite in Missouri, USA (Dorale et al. 1998),

where the $\delta^{13}\text{C}$ increased by up to 7‰ across the record, suggesting a change from C_3 to C_4 vegetation in the region. Denniston et al. (2000) found a similar signal in a stalagmite from Mississippi, USA, where an $\sim 8\%$ increase in $\delta^{13}\text{C}$ in the record marked a shift in vegetation from forest to savannah above the cave.

Sediment cores from around Sulawesi suggest that vegetation types were not dramatically different at the LGM, relative to modern times. The largest change in LGM vegetation occurred on the exposed Sunda Shelf during periods of low sea level. It has been suggested that grassland expanded onto the exposed shelf (Bird et al. 2005); however, other studies have suggested that rainforest continued to dominate this region during the LGM (Sun et al. 2000). Sulawesi remained disconnected from the Sunda Shelf during the LGM and therefore did not necessarily experience the same inferred shifts in vegetation. A sediment core from Lake Matano, north of the Gempa Bumi Cave study site, confirms the persistence of forest vegetation throughout the LGM; however, there was an increase in the amount of grassland (Hope 2001). It is important to note that the lake catchment includes areas up to 1400–1700 m elevation, which may make it more susceptible to grassland cover. A $\delta^{13}\text{C}$ leaf wax record from Lake Towuti in central Sulawesi suggests dramatic vegetation shifts during the LGM at this site, from forest to grassland (Russell et al. 2014) (Figure 3.8). However, the leaf wax $\delta^{13}\text{C}$ values of -40% to -25% recorded at this site suggest that vegetation may not be a direct driver of the $\delta^{13}\text{C}$ record, given that the values fall outside those traditionally associated with C_3 vegetation (Cosford et al. 2009). Additionally the topography of Sulawesi creates vastly different climate regimes across different parts of the island (Figure 3.8). Our site sits in a location strongly dominated by the summer monsoon, while Lake Towuti shows a less seasonal and weaker rainfall signal. It is therefore likely that this record does not reflect vegetation changes at our site, and we instead defer to the pollen records from closer to Makassar to make our assessment. Pollen from a sediment core from the Makassar Strait recorded no major vegetation changes during the LGM, suggesting there was not an expansion of grassland in this region (Visser et al. 2004) (Figure 3.8).

We find limited evidence of dramatic shifts in vegetation types in southern Sulawesi during the LGM and, therefore, do not interpret our speleothem $\delta^{13}\text{C}$ record in terms of vegetation change. We cannot discount the effects of vegetation shifts altogether, and concede that they may exert a minor influence on our record.

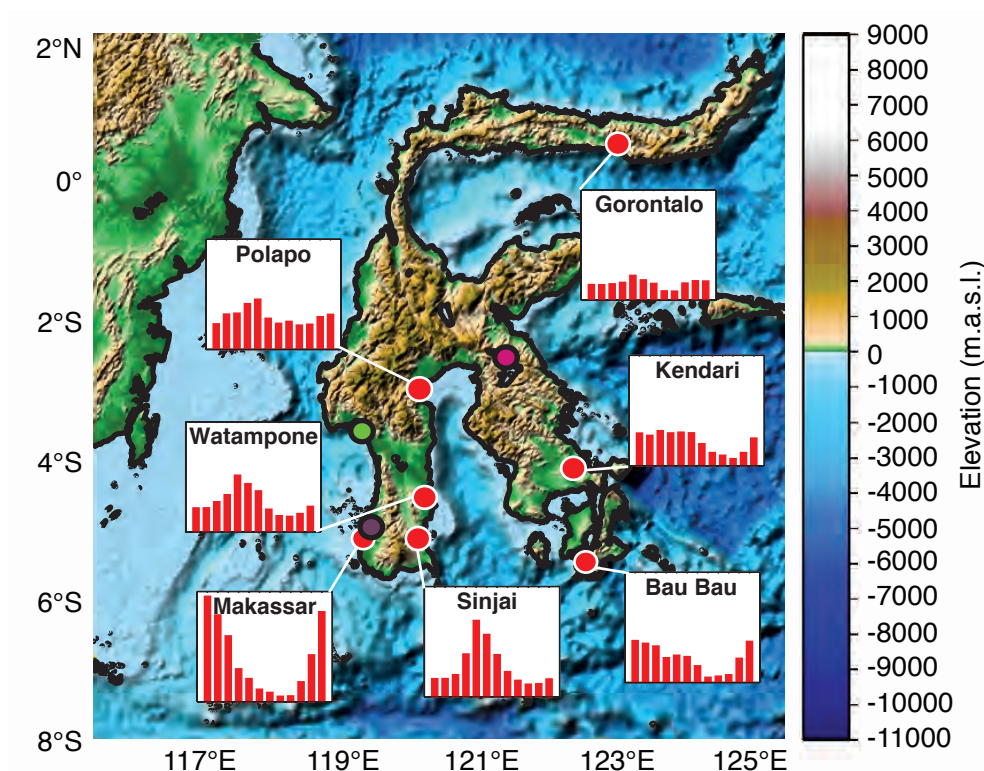


Figure 3.8: Topography of Sulawesi and its effect on annual rainfall. The locations of modern rainfall monitoring stations are shown with dark blue dots. The associated mean monthly rainfall climatology is shown for each site (Baker et al. 1994; Carolin et al. 2013). Note that all rainfall plots are shown on the same y-axis, from 0–700 mm. The location of our study site (near Makassar) is shown with a purple circle. The locations of two other key climate records: a sediment core from the Makassar Strait (green) and Lake Towuti (pink) are also shown.

3.4.2.2. Inorganic processes

Inorganic processes operating within the karst and in the cave itself may also contribute to the $\delta^{13}\text{C}$ value recorded in a stalagmite. Cave ventilation can influence Rayleigh fractionation of carbon isotopes in the cave itself, leading to higher $\delta^{13}\text{C}$ values in the speleothem. The partial pressure of CO_2 in the cave atmosphere influences the rate of CO_2 degassing from drip waters as they attempt to equilibrate with their surroundings (Hendy 1971). Ventilation of the cave atmosphere can lead to enhanced degassing of drip water, which will result in more enriched $\delta^{13}\text{C}$ values within the stalagmites (Fairchild et al. 2006). To minimise degassing within the cave system prior to

deposition on the stalagmite, cave ventilation needs to be minimised to allow the stabilisation of CO_2 within the cave.

The Gempa Bumi stalagmites were collected ~200m from the cave entrance, within an upper chamber accessed via a series of narrow passageways, to minimise ventilation effects. While the narrow passageways restrict airflow, the presence of a bat colony within the chamber indicates that it is not entirely isolated from the outside. Despite this, the stalagmites were deposited in near isotopic equilibrium cave conditions, therefore minimising the effects of inorganic processes on our speleothem $\delta^{13}\text{C}$.

Precipitation of calcite can sometimes occur prior to deposition on a stalagmite during a process known as prior calcite precipitation (PCP). PCP is enhanced during drier periods, when aeration of pockets within the karst promotes degassing of CO_2 from solution, and calcite precipitation, which leads to higher $\delta^{13}\text{C}$ values in the underlying stalagmite (Fairchild et al. 2006; Griffiths et al. 2010).

The signature of PCP is best identified by a positive correlation between the natural logarithm of Mg/Ca and Sr/Ca in the speleothem, where PCP leads to an increase in both ratios (Sinclair et al. 2012). PCP has been identified as a possible driver of speleothem $\delta^{13}\text{C}$ signals in monsoon regions (Griffiths et al. 2010; Sinclair et al. 2012), and needs to be considered in our interpretation.

3.4.2.3. Testing for prior calcite precipitation (PCP)

PCP is difficult to definitively identify using $\delta^{13}\text{C}$ and $\delta^{18}\text{O}$ alone. Analysis of stable isotope data together with trace element data provides additional information on PCP above the cave system. Sinclair et al. (2012) demonstrated that the slope of the relationship between the natural logarithm (\ln) of Mg/Ca and $\ln\text{Sr/Ca}$ is defined by the ratio of their distribution coefficients in calcite when PCP is present. This results in a slope between 0.7 and 1.0, with the best estimate between 0.88 and 0.97. The slope relationship between $\ln\text{Mg/Ca}$ and $\ln\text{Sr/Ca}$ for stalagmite GB09-3 is 0.20 ($R^2 = 0.18$), which is well below the minimum value of 0.71 calculated by Sinclair et al. (2012). This result suggests that PCP is not dominant above the Gempa Bumi cave system (Figure 3.9B).

The Mg/Ca and Sr/Ca results show a large step change to lower values around 10 kyr BP. Therefore, we break the trace element time series into three separate periods

to test for changes in the occurrence of PCP through time: the glacial period (15–40 kyr BP), deglacial period (where covariance between Mg/Ca and Sr/Ca is the strongest; 9.5–15 kyr BP), and the Holocene (9.5 kyr BP–present) (Figure 3.9A through C). The glacial and deglacial periods show no linear relationship between $\ln\text{Mg}/\text{Ca}$ and $\ln\text{Sr}/\text{Ca}$

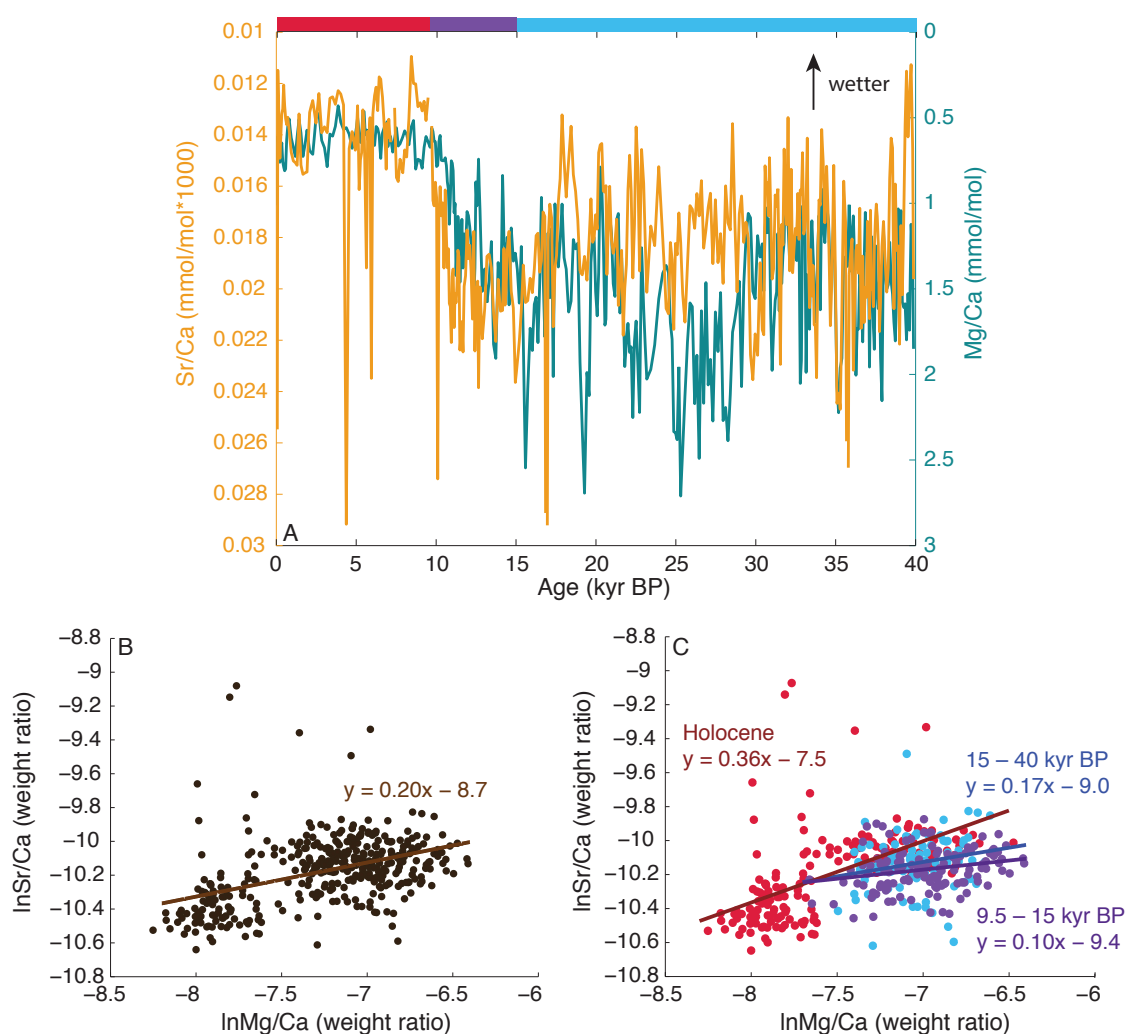


Figure 3.9: Mg/Ca and Sr/Ca data for stalagmite GS09-3. (A) Sr/Ca (orange) and Mg/Ca (green) records for GS09-3. Note that the axes are reversed. Trace element analyses were conducted on every second stable isotope sample, resulting in a resolution of ~ 100 years. (B) Comparison of the natural logs of Mg/Ca and Sr/Ca to test for PCP. Note that these values are shown as weight ratios, with the y-axis reversed. (C) As for (B) but with the data separated into Holocene, deglacial (9.5–15 kyr BP), and glacial (15–40 kyr BP) values. These periods are defined by changes in the variability and mean values of Mg/Ca, as shown by the coloured bar above plot (A). The shallow regression slopes calculated in plots (B) and (C) suggests that PCP is unlikely to be the dominant driver of the speleothem $\delta^{13}\text{C}$ record.

(slope = 0.17 and 0.10, $R^2 = 0.0$ and 0.1 respectively). Although Holocene values show a steeper linear regression slope of 0.34 for $\ln\text{Mg}/\text{Ca}$ and $\ln\text{Sr}/\text{Ca}$, this is still well below the minimum value of 0.71 calculated by Sinclair et al. (2012) and this line does not fit the data well ($R^2 = 0.3$).

Overall, the trace element results do not support the interpretation of Sulawesi speleothem $\delta^{13}\text{C}$ in terms of PCP. We therefore exclude it as a key driver of changes in speleothem $\delta^{13}\text{C}$ within the Sulawesi record, but note that it cannot be excluded as a minor driver.

3.4.2.4. Temperature and atmospheric CO_2 : vegetation productivity

The interactive effects of changes in temperature and atmospheric CO_2 on vegetation productivity (and stalagmite $\delta^{13}\text{C}$) are not easily separated. Temperature and CO_2 covary on glacial-interglacial timescales, with positive feedbacks on each other (e.g., Petit et al. 1999; NGRIP 2004; EPICA 2006). In the IPWP, sea surface temperatures (SSTs) rise concurrently with increases in atmospheric CO_2 during the last deglaciation, starting at approximately 18 kyr BP (Lea et al. 2000; Visser et al. 2003; Linsley et al. 2010).

Direct effects of temperature and atmospheric CO_2 on stalagmite $\delta^{13}\text{C}$ are negligible, however secondary effects via vegetation and soil processes help drive changes in stalagmite $\delta^{13}\text{C}$. Temperature-dependent fractionation of carbon isotopes in stalagmites is negligible, given that the atomic weight of ^{12}C and ^{13}C are similar, so phase changes during transport and deposition do not greatly favour one isotope over the other (Fairchild and Baker 2012). Changes in the atmospheric concentration of CO_2 also do not have a measurable direct effect on stalagmite $\delta^{13}\text{C}$, because the high partial pressure of CO_2 in tropical soils overwhelms any direct atmospheric inputs (Cosford et al. 2009).

Temperature and atmospheric CO_2 have secondary effects on stalagmite $\delta^{13}\text{C}$ through changes in vegetation and soil productivity. Changes in atmospheric CO_2 concentrations play a key role in driving vegetation changes in the tropics on glacial-interglacial scales (Levis et al. 1999; Bennett and Willis 2000; Harrison and Prentice 2003; Bragg et al. 2013). Model studies that look at the relative influence of temperature and CO_2 on tropical vegetation show a reduction in the net primary

productivity of tropical forests of 30% at the LGM, relative to modern, compared with a 10% reduction when only temperature was changed (Harrison and Prentice 2003). This suggests that the concentration of CO_2 in the atmosphere is a key determinant of vegetation productivity in the tropics (Bennett and Willis 2000; Bragg et al. 2013); however, the influence of CO_2 may be further amplified by changes in climate (Sinninghe Damsté et al. 2011; Claussen et al. 2013). This is due to carbon fertilisation of tropical vegetation, which promotes vegetation productivity, and can act to limit vegetation growth during periods of lower CO_2 , such as the LGM. Carbon fractionation in biological processes favours ^{12}C , so enhanced vegetation productivity and soil processes will lead to lower $\delta^{13}\text{C}$ values in seepage water (Cosford et al. 2009).

Changes in vegetation productivity have been used in the interpretation of tropical speleothem $\delta^{13}\text{C}$, and likely reflect a key component of our signal. Griffiths et al. (2013) suggest that a shift towards lower $\delta^{13}\text{C}$ values in Flores, Indonesia during D-O event 21 was likely triggered by increasing soil temperatures and soil biological productivity at this time. Similarly, Cruz et al. (2006) interpret changes in $\delta^{13}\text{C}$ in stalagmites from Botuverá Cave, Brazil to reflect changing soil CO_2 , driven by temperature and precipitation changes.

We show that the effects of changing $\text{C}_3:\text{C}_4$ vegetation, direct kinetic and CO_2 inputs as well as PCP on Sulawesi stalagmite $\delta^{13}\text{C}$ are likely to be small. Therefore, we interpret changes in $\delta^{13}\text{C}$ in the Sulawesi stalagmite record to primarily reflect changes in vegetation productivity above the cave.

3.4.3. Comparison with regional $\delta^{13}\text{C}$ records

Comparing the Gempa Bumi stalagmite $\delta^{13}\text{C}$ with regional palaeoclimate records suggests that the general pattern of variability in southwest Sulawesi is regionally reproducible. Comparison of the Sulawesi $\delta^{13}\text{C}$ record with the Borneo and Flores records allows us to test their combined value in providing a regional picture. Drip water studies and $\delta^{13}\text{C}$ analysis have demonstrated that stalagmites from Borneo do not record a regional climate signal (Partin et al. 2013). The Sulawesi and Borneo stalagmite $\delta^{13}\text{C}$ records show limited similarities, as would be expected (Figure 3.10).

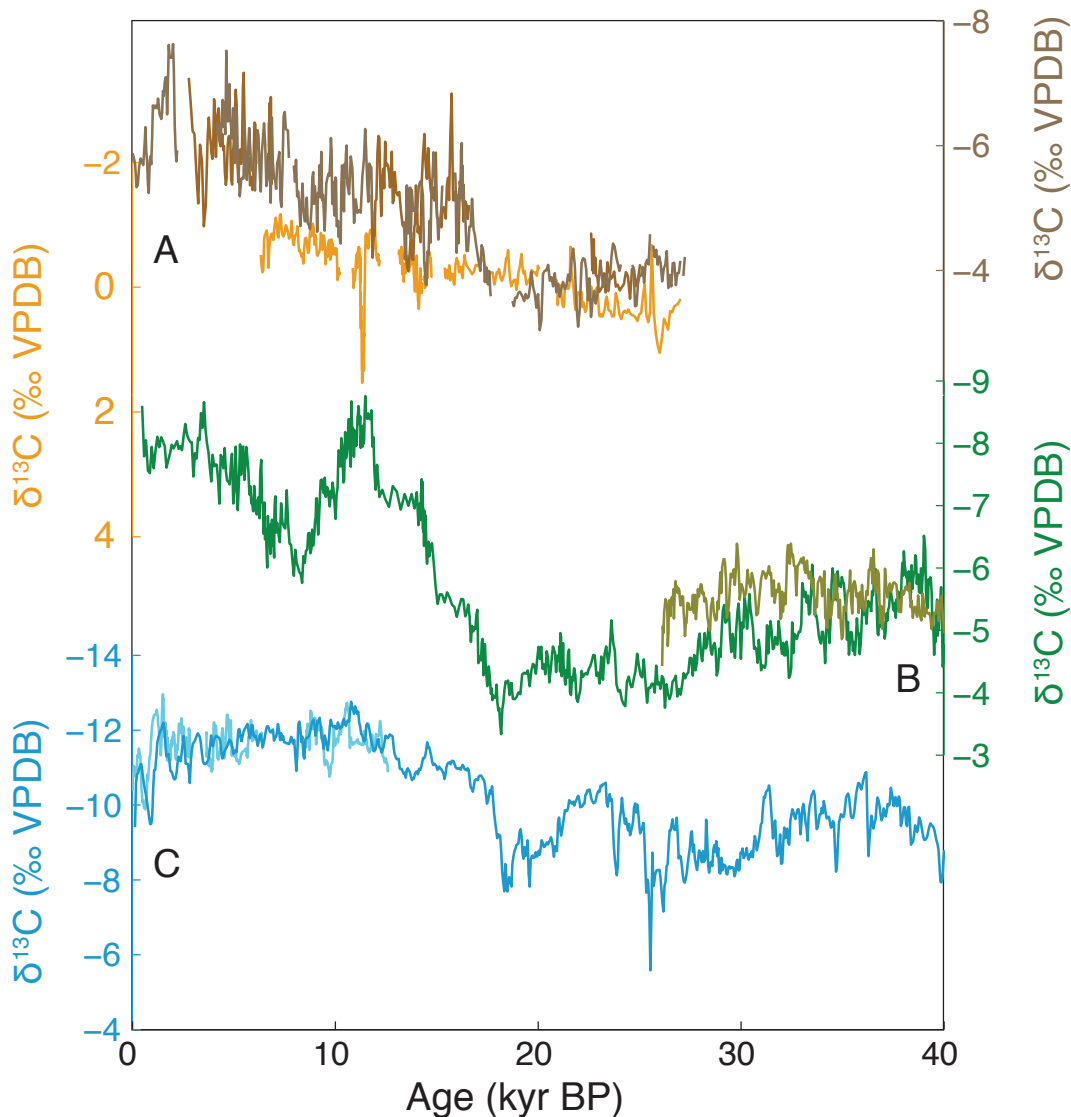


Figure 3.10: Speleothem $\delta^{13}\text{C}$ records for the IPWP region. (A) Borneo (orange/brown; Partin et al. 2013), (B) Sulawesi (green; GS09-3, olive; GS11-9; this study), and (C) Flores (light blue; Griffiths et al. 2010; dark blue; Scroxton 2014). Note that the Flores $\delta^{13}\text{C}$ scale is larger than the other records. Replication between Sulawesi and Flores $\delta^{13}\text{C}$ supports our assertion of Sulawesi $\delta^{13}\text{C}$ as a regional climate record.

The only other speleothem $\delta^{13}\text{C}$ records available for the equatorial Pacific come from Flores (Griffiths et al. 2010; Scroxton 2014). The large-scale features of the two records generally show good agreement, suggesting that they are both influenced by regional signals (Figure 3.10). The three separate states evident within the record from Sulawesi (glacial (40–18 kyr BP), deglacial (18–11 kyr BP) and Holocene (11 kyr BP–present)) are also evident in Flores. The glacial state appears to be quite similar at

Flores and Sulawesi, with both records showing similar patterns of variability until ~17 kyr BP.

The timing of the deglacial transition in stalagmite $\delta^{13}\text{C}$ is similar for Flores and Sulawesi, suggesting this is a regional signal. Flores shows a large negative excursion at 18.2 kyr BP, which is concurrent with the beginning of the transition to interglacial conditions in Sulawesi. The timing of this event matches the onset of deglacial warming in Antarctica (Pedro et al. 2011), suggesting that both Flores and Sulawesi $\delta^{13}\text{C}$ are sensitive to large-scale climate changes. While the exact nature of the transitional period differs between the two records, the general patterns of variability match well. The onset of full interglacial conditions occurs in both locations at ~11 kyr BP, again suggesting a regional driver at this time.

The Holocene epoch (11 kyr BP–present) sees little similarity between Sulawesi and Flores $\delta^{13}\text{C}$ records. Sulawesi shows a ‘v-shaped’ pattern of variability while Flores experiences a relatively stable Holocene. The climate of the Holocene is similar to modern, and the divergence of the records during this period likely represents localised differences in vegetation and environmental conditions.

3.4.4. Comparison with SST, CO₂ and CH₄

We have established that the Gempa Bumi speleothem $\delta^{13}\text{C}$ record is most likely an indicator of regional changes in environmental conditions. To further explore this idea, we now compare the Sulawesi record with regional SSTs, and atmospheric CO₂ and CH₄ records to examine possible climatic drivers.

3.4.4.1. IPWP SSTs and atmospheric CO₂

If stalagmite $\delta^{13}\text{C}$ does in fact reflect changes in vegetation and soil productivity and changes in rainfall do not play a significant role, the Sulawesi record would be expected to resemble reconstructions of regional SSTs and atmospheric CO₂. The Sulawesi speleothem $\delta^{13}\text{C}$ record appears to follow regional SST changes, particularly relating to the timing of deglaciation. SSTs calculated from *G. ruber* Mg/Ca ratios in a composite of cores from the western IPWP show a 3–4°C cooling during the LGM relative to the Holocene (Linsley et al. 2010) (Figure 3.11A). Deglacial warming begins at

approximately 18.5 kyr BP, with the majority of the warming completed by approximately 10 kyr BP.

The timing of deglaciation is mirrored in the Gempa Bumi stalagmite $\delta^{13}\text{C}$ record, which begins to transition to Holocene values at ~18 kyr BP. A slow-down in the rate of transition between 14.5–12 kyr BP is mirrored by a slowing in the rate of SST warming, before a continuation of the trend until ~11 kyr BP. The two records diverge during the Holocene, suggesting that temperature is not the dominant driver of Sulawesi $\delta^{13}\text{C}$ at this time.

Atmospheric CO_2 and temperature are known to co-vary over glacial-interglacial cycles (e.g., Petit et al. 1999), with positive feedbacks that drive climate change. Atmospheric CO_2 concentrations and temperature are important drivers of tropical vegetation productivity, both via CO_2 fertilisation of vegetation and increased vegetation productivity under warmer temperatures (Levis et al. 1999; Bennett and Willis 2000; Harrison and Prentice 2003; Claussen et al. 2013). The trends of CO_2 change over the last 40 kyr BP closely follows the Sulawesi $\delta^{13}\text{C}$ record, suggesting that CO_2 , alongside temperature, may be driving vegetation productivity. During the glacial period, the trend in CO_2 in the Byrd ice core record matches a similar trend in the $\delta^{13}\text{C}$ record (Figure 3.11B). The timing of the onset of deglaciation is similar in both records, occurring around 17.5 kyr BP, and ending at around 11 kyr BP. Two large negative isotope excursions during this transition also occur in the CO_2 record, surrounding a plateau in both $\delta^{13}\text{C}$ and CO_2 . During the Holocene, the pattern of variability is similar between records, with both records exhibiting a ‘trough’ during the middle Holocene. The good agreement between Sulawesi $\delta^{13}\text{C}$, regional SSTs and atmospheric CO_2 supports our conclusion that $\delta^{13}\text{C}$ is recording changes in vegetation and soil productivity, driven by changing temperature and CO_2 .

3.4.4.2. Atmospheric methane

Wetland vegetation has been shown to drive atmospheric methane concentrations on glacial/interglacial timescales (e.g., Chappellaz et al. 1997; Dällenbach et al. 2000; Valdes et al. 2005; Baumgartner et al. 2012). Quantification of the relative contributions of methane sources and sinks to the LGM atmospheric methane minimum remains an area of debate (e.g., Valdes et al. 2005; Fischer et al. 2008; Levine et al. 2011). However, it is thought that the tropics remained a source of atmospheric methane during

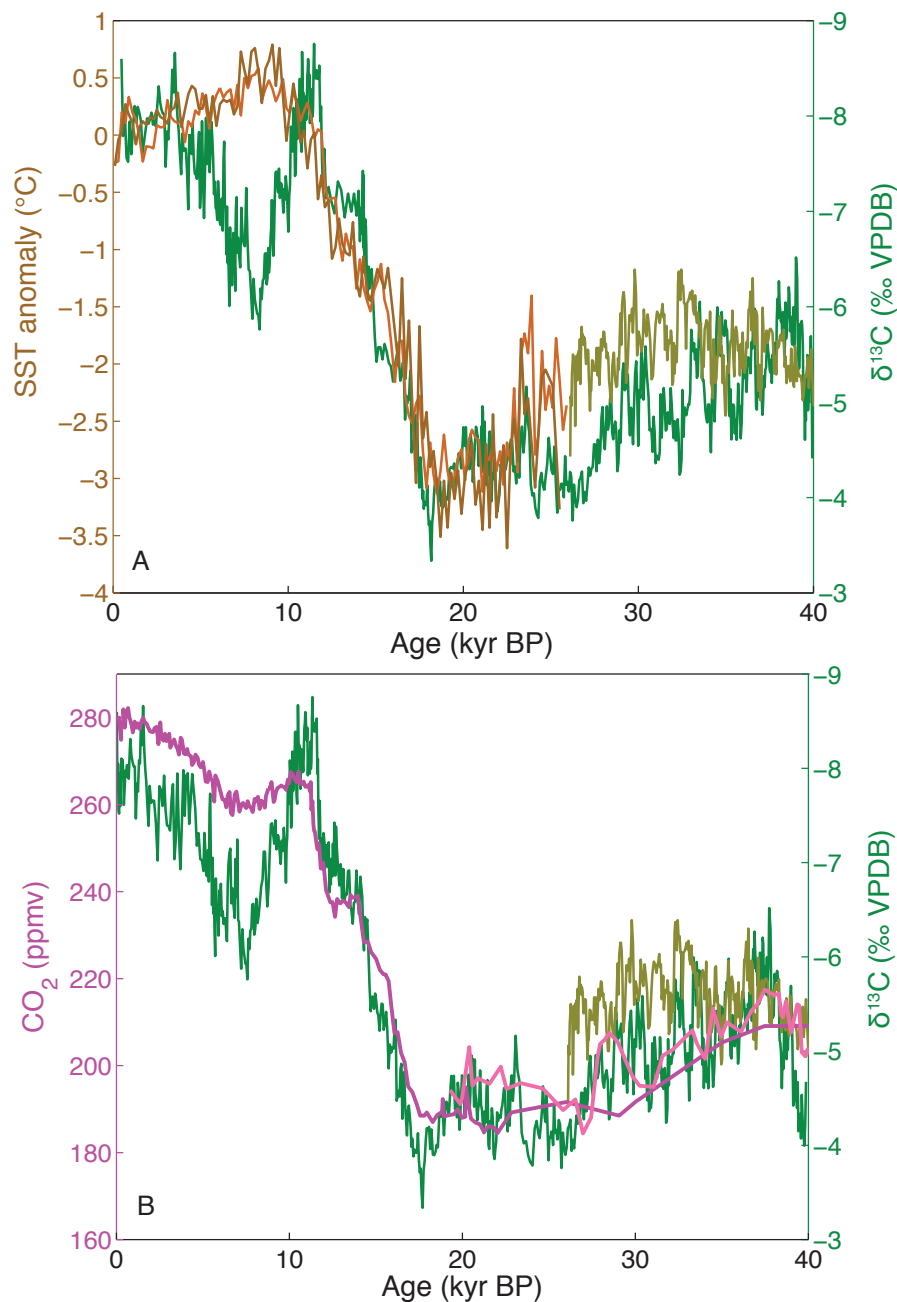


Figure 3.11: Relationship between Sulawesi $\delta^{13}\text{C}$, regional SSTs and atmospheric CO_2 over the last 40 kyr. (A) Sulawesi $\delta^{13}\text{C}$ compared with reconstructed SSTs for the western IPWP (Linsley et al. 2010). The SST anomaly curves are composites based on eight sediment cores from the western IPWP region (light brown), and four cores from Makassar Strait (dark brown). (B) Sulawesi $\delta^{13}\text{C}$ compared with ice core CO_2 concentrations. Purple is the composite CO_2 record of Luthi et al. (2008). Pink is the CO_2 record from the Byrd ice core (Ahn and Brook 2007; Ahn and Brook 2008). The close association between Sulawesi $\delta^{13}\text{C}$, regional SSTs and atmospheric CO_2 support our conclusion that Sulawesi $\delta^{13}\text{C}$ is recording changes in vegetation and soil productivity, driven by changing temperature and CO_2 .

the LGM, particularly on exposed continental shelves within the Indonesian archipelago (Kaplan 2002; Kaplan et al. 2006).

The Gempa Bumi stalagmite $\delta^{13}\text{C}$ record closely follows atmospheric methane concentrations, as recorded in polar ice cores (Figure 3.12). The agreement between the Sulawesi speleothem $\delta^{13}\text{C}$ and EPICA ice core methane is strongest during the glacial and deglacial periods, with the Holocene exhibiting a distinct mismatch in the timing of key features. Differences in the sampling resolution combined with small offsets in timing between records makes statistical quantification of this relationship difficult. However, when both records are detrended to remove the deglacial trend, and smoothed to remove high-frequency variability, there is a significant negative relationship evident between records ($R = -0.48$, $p \approx 0$).

During the glacial period (40–18 kyr BP), agreement between speleothem $\delta^{13}\text{C}$

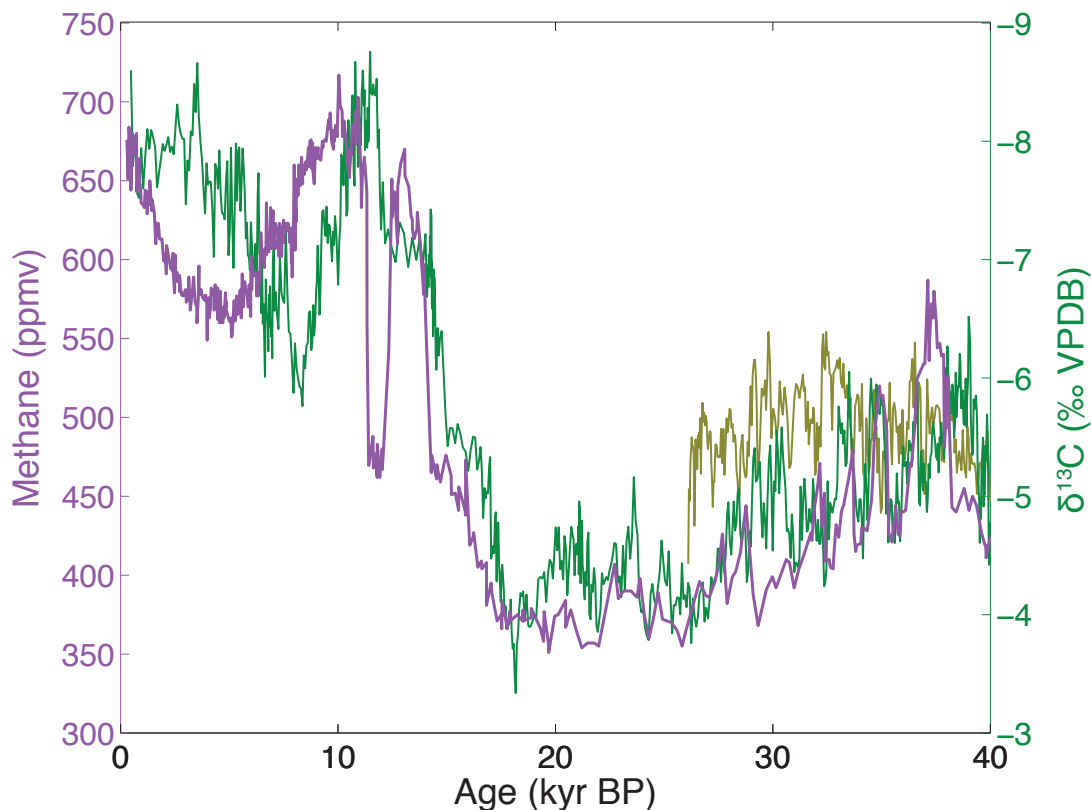


Figure 3.12: Comparison of Sulawesi $\delta^{13}\text{C}$ (green/olive) and methane concentrations in the EPICA ice core (purple; Louergue et al. 2008). The high degree of co-variance between records, particularly during abrupt climate events during the deglaciation suggest that Sulawesi $\delta^{13}\text{C}$ may be acting as a proxy for tropical methane emissions, via the demonstrated relationship with vegetation productivity (Figure 3.11).

and EPICA methane is good. The overall patterns of variability, as well as many of the smaller features are evident in both records, particularly prior to 30 kyr BP. During the glacial period, most of the boreal northern wetlands were covered by ice or permafrost, reducing their methane output (Kaplan et al. 2006). Wetland methane emissions during the LGM are therefore expected to be primarily from tropical sources. It is likely, therefore, that the correlation between atmospheric methane and Sulawesi speleothem $\delta^{13}\text{C}$ is related to vegetation productivity within the region.

The timing of rapid negative transitions in speleothem $\delta^{13}\text{C}$ at ~14 kyr BP and ~11 kyr BP correspond with times of rapid increases in the concentration of atmospheric methane (within dating error). These events occur at times of rapid global climate change during meltwater pulse 1A (Clark et al. 1996) and the end of Heinrich Event 1/beginning of Bølling-Allerød warming (Kienast et al. 2003; Weaver et al. 2003; Rosen et al. 2014) and during meltwater pulse 1B (Bard et al. 2010) and the end of the Younger Dryas (Fairbanks 1989; McManus et al. 2004) respectively. Previous studies have suggested that the rapid jumps in methane are driven by tropical wetlands (Schaefer et al. 2006; Rosen et al. 2014), and our results appear to observationally verify this hypothesis for the first time.

The Sulawesi stalagmite $\delta^{13}\text{C}$ record diverges from the record of atmospheric methane concentrations during the Holocene; however, the overall patterns of variability over this time do show some similarities. The decrease in methane concentrations during the mid-Holocene, and its gradual rise towards pre-industrial values remains an area of great debate, particularly as to whether this signal is natural or anthropogenic (e.g., Chappellaz et al. 1997; Ruddiman 2003; Ferretti et al. 2005; Burns 2011; Singarayer et al. 2011; Yu 2011). The Sulawesi $\delta^{13}\text{C}$ record shows a similar “trough” during the Holocene; however, the timing of the maximum occurs approximately 2.5 kyr earlier than the change in methane. Given the steep karst terrain from which the stalagmite was collected, it is unlikely to be recording an anthropogenic signal. During the Holocene, high latitude methane sources played a more dominant role in determining the global methane budget than during the LGM (Chappellaz et al. 1997). The increased importance of high latitude northern hemisphere methane emissions during this time could account for the apparent disconnect with tropical speleothem $\delta^{13}\text{C}$ and atmospheric methane concentration during the Holocene. Enhancement of the Australasian monsoon since the mid-Holocene, driven by increased

convection over the IPWP (DiNezio and Tierney 2013 and Chapter 2) (Figure 3.7) and an increasing northern summer insolation (Burns 2011; Singarayer et al. 2011), could help drive the rise in both speleothem $\delta^{13}\text{C}$ and methane at this time.

3.5. Conclusions

High-resolution, precisely dated speleothem $\delta^{13}\text{C}$ records for Sulawesi, Indonesia, appear to act as a proxy for vegetation productivity over the last 40 kyr. The good agreement between the Sulawesi $\delta^{13}\text{C}$ record and atmospheric methane suggests that $\delta^{13}\text{C}$ may be a proxy for changes in tropical methane emissions related to changes in vegetation productivity. While previous studies have suggested that tropical speleothem $\delta^{13}\text{C}$ may act as a proxy for tropical methane emissions (Burns 2011; Griffiths et al. 2013), the results of this study suggest that the Australasian tropics could be a contributor to the glacial atmospheric methane budget. Vegetation climate modelling is required to understand this dynamic link and explore the relationships between vegetation dynamics in Indonesia and the tropics as a whole. This concept will be explored in the following chapter.

3.6. References

- Ahn, J. and E. J. Brook (2007). Atmospheric CO_2 and climate from 65 to 30 ka B.P. *Geophysical Research Letters* 34: L10703.
- Ahn, J. and E. J. Brook (2008). Atmospheric CO_2 and climate on millennial time scales during the last glacial period. *Science* 322: 83–85.
- Ayliffe, L. K., M. K. Gagan, J.-x. Zhao, R. N. Drysdale, J. C. Hellstrom, W. S. Hantoro, M. L. Griffiths, H. Scott-Gagan, E. St Pierre, J. A. Cowley and B. W. Suwargadi (2013). Rapid interhemispheric climate links via the Australasian monsoon during the last deglaciation. *Nature Communications* 4: 2908.
- Baker, C. B., J. K. Eischeid, T. R. Karl and H. F. Diaz (1994). The quality control of long-term climatological data using objective data analysis. *Preprints of AMS Ninth Conference on Applied Climatology*, Dallas, TX.

- Baldini, J. U. L., F. McDermott, A. Baker, L. M. Baldini, D. P. Matthey and L. B. Railsback (2005). Biomass effects on stalagmite growth and isotope ratios: A 20th century analogue from Wiltshire, England. *Earth and Planetary Science Letters* 240: 486–494.
- Bard, E., B. Hamelin and D. Delanghe-Sabatier (2010). Deglacial Meltwater Pulse 1B and Younger Dryas sea levels revisited with boreholes at Tahiti. *Science* 327: 1235–1237.
- Baumgartner, M., A. Schilt, O. Eicher, J. Schmitt, J. Schwander, R. Spahni, H. Fischer and T. F. Stocker (2012). High-resolution inter-polar difference of atmospheric methane around the Last Glacial Maximum. *Biogeosciences* 9: 3961–3977.
- Bennett, K. D. and K. J. Willis (2000). Effect of global atmospheric carbon dioxide on glacial-interglacial vegetation change. *Global Ecology & Biogeography* 9: 355–361.
- Bird, M. I., D. Taylor and C. Hunt (2005). Palaeoenvironments of insular Southeast Asia during the Last Glacial Period: a savanna corridor in Sundaland? *Quaternary Science Reviews* 24: 2228–2242.
- Blyth, A. J., C. I. Smith and R. N. Drysdale (2013). A new perspective on the $\delta^{13}\text{C}$ signal preserved in speleothems using LC-IRMS analysis of bulk organic matter and compound specific stable isotope analysis. *Quaternary Science Reviews* 75: 143–149.
- Bragg, F. J., I. C. Prentice, S. P. Harrison, G. Eglinton, P. N. Foster, F. Rommerskirchen and J. Rullkötter (2013). Stable isotope and modelling evidence for CO_2 as a driver of glacial-interglacial vegetation shifts in southern Africa. *Biogeosciences* 10: 2001–2010.
- Burns, S. J. (2011). Speleothem records of changes in tropical hydrology over the Holocene and possible implications for atmospheric methane. *The Holocene* 21: 735–741.
- Carolin, S. A., K. M. Cobb, J. F. Adkins, B. Clark, J. L. Conroy, S. Lejau, J. Malang and A. A. Tuen (2013). Varied response of Western Pacific hydrology to climate forcings over the Last Glacial period. *Science* 340: 1564–1566.
- Chappellaz, J., T. Blunier, S. Kints, A. Dällenbach, J.-M. Barnola, J. Schwander, D. Raynaud and B. Stauffer (1997). Changes in the atmospheric CH_4 gradient

between Greenland and Antarctica during the Holocene. *Journal of Geophysical Research* 102: 15987–15997.

- Clark, P. U., R. B. Alley, L. D. Keigwin, J. M. Licciardi, S. J. Johnsen and H. Wang (1996). Origin of the first global meltwater pulse following the last glacial maximum. *Paleoceanography* 11: 563–577.
- Claussen, M., K. Selent, V. Brovkin, T. Raddatz and V. Gayler (2013). Impact of CO_2 and climate on Last Glacial maximum vegetation - a factor separation. *Biogeosciences* 10: 3593–3604.
- Cosford, J., H. Qing, D. Matthey, B. Eglington and M. Zhang (2009). Climatic and local effects on stalagmite $\delta^{13}\text{C}$ values at Lianhua Cave, China. *Palaeogeography, Palaeoclimatology, Palaeoecology* 280: 235–244.
- Cruz, F. W., S. J. Burns, I. Karmann, W. D. Sharp, M. Vuille and J. A. Ferrari (2006). A stalagmite record of changes in atmospheric circulation and soil processes in the Brazilian subtropics during the Late Pleistocene. *Quaternary Science Reviews* 25: 2749–2761.
- Dällenbach, A., T. Blunier, J. Flückiger, B. Stauffer, J. Chappellaz and D. Raynaud (2000). Changes in the atmospheric CH_4 gradient between Greenland and Antarctica during the Last Glacial and the transition to the Holocene. *Geophysical Research Letters* 27: 1005–1008.
- de Villiers, S., M. Greaves and H. Elderfield (2002). An intensity ratio calibration method for the accurate determination of Mg/Ca and Sr/Ca of marine carbonates by ICP-AES. *Geochemistry, Geophysics, Geosystems* 3: 2001GC000169.
- Denniston, R. F., L. A. González, Y. Asmerom, M. K. Reagan and H. Recelli-Snyder (2000). Speleothem carbon isotopic records of Holocene environments in the Ozark Highlands, USA. *Quaternary International* 67: 21–27.
- Denniston, R. F., K.-H. Wyrwoll, Y. Asmerom, V. J. Polyak, W. F. Humphreys, J. Cugley, D. Woods, Z. LaPointe, J. Peota and E. Greaves (2013a). North Atlantic forcing of millennial-scale Indo-Australian monsoon dynamics during the Last Glacial period. *Quaternary Science Reviews* 72: 159–168.
- Denniston, R. F., K.-H. Wyrwoll, V. J. Polyak, J. R. Brown, Y. Asmerom, A. D. Wanamaker Jr, Z. LaPointe, R. Ellerbroek, M. Barthelmes, D. Cleary, J. Cugley, D. Woods and W. F. Humphreys (2013b). A stalagmite record of Holocene

- Indonesia-Australian summer monsoon variability from the Australian tropics. *Quaternary Science Reviews* 78: 155–168.
- DiNezio, P. N. and J. E. Tierney (2013). The effect of sea level on glacial Indo-Pacific climate. *Nature Geoscience* 6: 485–491.
- Dorale, J. A., R. L. Edwards, E. Ito and L. A. González (1998). Climate and vegetation history of the midcontinent from 75 to 25 ka: A speleothem record from Crevice Cave, Missouri, USA. *Science* 282: 1871–1874.
- Dorale, J. A. and Z. Liu (2009). Limitations of Hندی Test criteria in judging the paleoclimate suitability of speleothems and the need for replication. *Journal of Cave and Karst Studies* 71: 73–80.
- Edwards, E. J., C. P. Osborne, C. A. E. Strömberg, S. A. Smith and C. G. Consortium (2010). The origins of C_4 grasslands: Integrating evolutionary and ecosystem science. *Science* 328: 587–591.
- EPICA (2006). One-to-one coupling of glacial climate variability in Greenland and Antarctica. *Nature* 444: 195–198.
- Fairbanks, R. G. (1989). A 17,000-year glacio-eustatic sea level record: influence of glacial melting rates on the Younger Dryas event and deep-ocean circulation. *Nature* 342: 637–642.
- Fairchild, I., C. Smith, A. Baker, L. Fuller, C. Spötl, D. Matthey, F. McDermott and E.I.M.F. (2006). Modification and preservation of environmental signals in speleothems. *Earth-Science Reviews* 75: 105–153.
- Fairchild, I. J. and A. Baker (2012). *Speleothem science: From process to past environments*. West Sussex, UK, John Wiley & Sons Ltd.
- Ferretti, D. F., J. B. Miller, J. W. C. White, D. M. Etheridge, K. R. Lassey, D. C. Lowe, C. M. MacFarling Meure, M. F. Dreier, C. M. Trudinger, T. D. van Ommen and R. L. Langenfelds (2005). Unexpected changes to the global methane budget over the past 2000 years. *Science* 309: 1714–1717.
- Fischer, H., M. Behrens, M. Bock, U. Richter, J. Schmitt, L. Loulergue, J. Chappellaz, R. Spahni, T. Blunier, M. Leuenberger and T. F. Stocker (2008). Changing boreal methane sources and constant biomass burning during the last termination. *Nature* 452: 864–867.

- Genty, D., D. Blamart, R. Ouahdi, M. Gilmour, A. Baker, J. Jouzel and S. Van-Exter (2003). Precise dating of Dansgaard-Oeschger climate oscillations in western Europe from stalagmite data. *Nature* 421: 833–837.
- Griffiths, M. L., R. N. Drysdale, M. K. Gagan, S. Frisia, J.-x. Zhao, L. K. Ayliffe, W. S. Hantoro, J. C. Hellstrom, M. J. Fischer, Y. Feng and B. W. Suwargadi (2010). Evidence for Holocene changes in Australian-Indonesian monsoon rainfall from stalagmite trace element and stable isotope ratios. *Earth and Planetary Science Letters* 292: 27–38.
- Griffiths, M. L., R. N. Drysdale, M. K. Gagan, J. C. Hellstrom, I. Couchoud, L. K. Ayliffe, H. B. Vonhof and W. S. Hantoro (2013). Australasian monsoon response to Dansgaard-Oeschger event 21 and teleconnections to higher latitudes *Earth and Planetary Science Letters* 369–370: 294–304.
- Griffiths, M. L., R. N. Drysdale, M. K. Gagan, J.-x. Zhao, L. K. Ayliffe, J. C. Hellstrom, W. S. Hantoro, S. Frisia, Y. Feng, I. Cartwright, E. St Pierre, M. J. Fischer and B. W. Suwargadi (2009). Increasing Australian-Indonesian monsoon rainfall linked to early Holocene sea-level rise. *Nature Geoscience* 2: 636–639.
- Harrison, S. P. and C. I. Prentice (2003). Climate and CO_2 controls on global vegetation distribution at the last glacial maximum: analysis based on palaeovegetation data, biome modelling and palaeoclimate simulations. *Global Change Biology* 9: 983–1004.
- Hartmann, A., E. Eiche, T. Neumann, J. Fohlmeister, A. Schröder-Ritzrau, A. Mangini and E. Haryono (2013). Multi-proxy evidence for human-induced deforestation and cultivation from a late Holocene stalagmite from middle Java, Indonesia. *Chemical Geology* 357: 8–17.
- Hellstrom, J., M. T. McCulloch and J. Stone (1998). A detailed 31,000-year record of climate and vegetation change, from the isotope geochemistry of two New Zealand speleothems. *Quaternary Research* 50: 167–178.
- Hellstrom, J. C. (2003). Rapid and accurate U/Th dating using parallel ion-counting multi-collector ICP-MS. *Journal of Analytical Atomic Spectrometry* 18: 1346–1351.
- Hellstrom, J. C. (2006). U-Th dating of speleothems with high initial ^{230}Th using stratigraphical constraint. *Quaternary Geochronology* 1: 289–295.

- Hendy, C. H. (1971). The isotopic geochemistry of speleothems-I. The calculation of the effects of different modes of formation on the isotopic composition of speleothems and their applicability as palaeoclimatic indicators. *Geochimica et Cosmochimica Acta* 35: 801–824.
- Hope, G. (2001). Environmental change in the Late Pleistocene and later Holocene at Wanda site, Soroako, South Sulawesi, Indonesia. *Palaeogeography, Palaeoclimatology, Palaeoecology* 171: 129–145.
- Hou, J. Z., M. Tan, H. Cheng and T. S. Liu (2003). Stable isotope records of plant cover change and monsoon variation in the past 2200 years: evidence from laminated stalagmites in Beijing, China. *Boreas* 32: 304–313.
- Jo, K.-n., K. Sik Woo, H. Cheng, R. L. Edwards, Y. Wang, R. Kim and X. Jiang (2010). Textural and carbon isotopic evidence of monsoonal changes recorded in a composite-type speleothem from Korea since MIS 5a. *Quaternary Research* 74: 100–112.
- Kanner, L. C., S. J. Burns, H. Cheng and R. L. Edwards (2012). High-latitude forcing of the South American Summer Monsoon during the last glacial. *Science* 335: 570–573.
- Kaplan, J. O. (2002). Wetlands at the Last Glacial Maximum: Distribution and methane emissions. *Geophysical Research Letters* 29: 1079.
- Kaplan, J. O., G. Folberth and D. A. Hauglustaine (2006). Role of methane and biogenic volatile organic compound sources in late glacial and Holocene fluctuations of atmospheric methane concentrations. *Global Biogeochemical Cycles* 20: GB2016.
- Kienast, M., T. J. J. Hanebuth, C. Pelejero and S. Steinke (2003). Synchronicity of meltwater pulse 1a and the Bølling warming: New evidence from the South China Sea. *Geology* 31: 67–70.
- Lea, D. W., D. K. Pak and H. J. Spero (2000). Climate impact of Late Quaternary equatorial Pacific sea surface temperature variations. *Science* 289: 1719–1724.
- Levine, J. G., E. W. Wolff, A. E. Jones, M. A. Hutterli, O. Wild, G. D. Carver and J. A. Pyle (2011). In search of an ice core signal to differentiate between source-driven and sink-driven changes in atmospheric methane. *Journal of Geophysical Research* 116: D05305.

- Levis, S., J. A. Foley and D. Pollard (1999). CO_2 , climate, and vegetation feedbacks at the Last Glacial Maximum. *Journal of Geophysical Research* 104: 31191–31198.
- Lewis, S. C., M. K. Gagan, L. K. Ayliffe, J.-x. Zhao, W. S. Hantoro, P. C. Treble, J. C. Hellstrom, A. N. LeGrande, M. Kelley, G. A. Schmidt and B. W. Suwargadi (2011). High-resolution stalagmite reconstructions of Australian-Indonesian monsoon rainfall variability during Heinrich stadial 3 and Greenland interstadial 4. *Earth and Planetary Science Letters* 303: 133–142.
- Linsley, B. K., Y. Rosenthal and D. W. Oppo (2010). Holocene evolution of the Indonesian throughflow and the western Pacific warm pool. *Nature Geoscience* 3: 578–583.
- Louergue, L., A. Schilt, R. Spahni, V. Masson-Delmotte, T. Blunier, B. Lemieux, J.-M. Barnola, D. Raynaud, T. F. Stocker and J. Chappellaz (2008). Orbital and millennial-scale features of atmospheric CH_4 over the past 800,000 years. *Nature* 453: 383–386.
- Lüthi, D., M. Le Floch, B. Bereiter, T. Blunier, J.-M. Barnola, U. Siegenthaler, D. Raynaud, J. Jouzel, H. Fischer, K. Kawamura and T. F. Stocker (2008). High-resolution carbon dioxide concentration record 650,000 - 800,000 years before present. *Nature* 453: 379–382.
- Martín-Chivelet, J., M. B. Muñoz-García, R. L. Edwards, M. J. Turrero and A. I. Ortega (2011). Land surface temperature changes in Northern Iberia since 4000 yr BP, based on $\delta^{13}\text{C}$ of speleothems. *Global and Planetary Change* 77: 1–12.
- McDermott, F. (2004). Palaeo-climate reconstruction from stable isotope variations in speleothems: a review. *Quaternary Science Reviews* 23: 901–918.
- McManus, J. F., R. Francois, J.-M. Gherardi, L. D. Keigwin and S. Brown-Leger (2004). Collapse and rapid resumption of Atlantic meridional circulation linked to deglacial climate changes. *Nature* 428: 834–837.
- NGRIP (2004). High-resolution record of Northern Hemisphere climate extending into the last interglacial period. *Nature* 431: 147–151.
- Partin, J. W., K. M. Cobb, J. F. Adkins, B. Clark and D. P. Fernandez (2007). Millennial-scale trends in west Pacific warm pool hydrology since the Last Glacial Maximum. *Nature* 449: 452–455.

- Partin, J. W., K. M. Cobb, J. F. Adkins, A. A. Tuen and B. Clark (2013). Trace metal and carbon isotopic variations in cave dripwater and stalagmite geochemistry from Northern Borneo. *Geochemistry, Geophysics, Geosystems* 14: 3567–3585.
- Pedro, J. B., T. D. van Ommen, S. O. Rasmussen, V. I. Morgan, J. Chappellaz, A. D. Moy, V. Masson-Delmotte and M. Delmotte (2011). The last deglaciation: timing the bipolar seesaw. *Climate of the Past* 7: 671–683.
- Petit, J. R., J. Jouzel, D. Raynaud, N. I. Barkov, J. M. Barnola, I. Basile, M. Bender, J. Chappellaz, M. Davis, G. Delaygue, M. Delmotte, V. M. Kotlyakov, M. Legrand, V. Y. Lipenkov, C. Lorius, L. Pépin, C. Ritz, E. Saltzman and M. Stievenard (1999). Climate and atmospheric history of the past 420,000 years from the Vostok ice core, Antarctica. *Nature* 399: 429–436.
- Rosen, J. L., E. J. Brook, J. P. Severinghaus, T. Blunier, L. E. Mitchell, J. E. Lee, J. S. Edwards and V. Gkinis (2014). An ice core record of near-synchronous global climate changes at the Bølling transition. *Nature Geoscience* 7: 459–463.
- Ruddiman, W. F. (2003). The anthropogenic greenhouse era began thousands of years ago. *Climatic Change* 61: 261–293.
- Russell, J. M., H. Vogel, B. L. Konecky, S. Bijaksana, Y. Huang, M. Melles, N. Wattrus, K. Costa and J. W. King (2014). Glacial forcing of central Indonesian hydroclimate since 60,000 y B.P. *Proceedings of the National Academy of Sciences* 111: 5100.
- Schaefer, H., M. J. Whiticar, E. J. Brook, V. V. Petrenko, D. F. Ferretti and J. P. Severinghaus (2006). Ice record of $\delta^{13}\text{C}$ for atmospheric CH_4 across the Younger Dryas-Preboreal transition. *Science* 313: 1109–1112.
- Schrag, D. P. (1999). Rapid analysis of high-precision Sr/Ca ratios in corals and other marine carbonates. *Paleoceanography* 14: 97–102.
- Scropton, N. G. (2014). *Late Pleistocene climate and environment from speleothems on Flores, Indonesia: vegetation, volcanoes and Homo floresiensis*, The Australian National University.
- Sinclair, D. J., J. L. Banner, F. W. Taylor, J. Partin, J. Jenson, J. Mylroie, E. Goddard, T. Quinn, J. Jocson and M. Blaž (2012). Magnesium and strontium systematics in tropical speleothems from the Western Pacific. *Chemical Geology* 294–295: 1–17.

- Singarayer, J. S., P. J. Valdes, P. Friedlingstein, S. Nelson and D. J. Beerling (2011). Late Holocene methane rise caused by orbitally controlled increase in tropical sources. *Nature* 470: 82–86.
- Sinninghe Damsté, J. S., D. Verschuren, J. Ossebaar, J. Blokker, R. van Houten, M. T. J. van der Meer, B. Plessen and S. Schouten (2011). A 25,000-year record of climate-induced changes in lowland vegetation of eastern equatorial Africa revealed by the stable carbon-isotopic composition of fossil plant leaf waxes. *Earth and Planetary Science Letters* 302: 236–246.
- Still, C. J., J. A. Berry, G. J. Collatz and R. S. DeFries (2003). Global distribution of C_3 and C_4 vegetation: Carbon cycle implications. *Global Biogeochemical Cycles* 17: 1006.
- Sun, X., X. Li, Y. Luo and X. Chen (2000). The vegetation and climate at the last deglaciation on the emerged continental shelf of the South China Sea. *Palaeogeography, Palaeoclimatology, Palaeoecology* 160: 301–316.
- Valdes, P. J., D. J. Beerling and C. E. Johnson (2005). The ice age methane budget. *Geophysical Research Letters* 32: L02704.
- Visser, K., R. Thunell and M. A. Goñi (2004). Glacial-interglacial organic carbon record from the Makassar Strait, Indonesia: implications for regional changes in continental vegetation. *Quaternary Science Reviews* 23: 17–27.
- Visser, K., R. Thunell and L. Stott (2003). Magnitude and timing of temperature change in the Indo-Pacific warm pool during deglaciation. *Nature* 421: 152–155.
- Wang, X., A. S. Auler, R. L. Edwards, H. Cheng, E. Ito, Y. Wang, X. Kong and M. Solheid (2007). Millennial-scale precipitation changes in southern Brazil over the past 90,000 years. *Geophysical Research Letters* 34: L23701.
- Weaver, A. J., O. A. Saenko, P. U. Clark and J. X. Mitrovica (2003). Meltwater Pulse 1A from Antarctica as a trigger of the Bølling-Allerød warm interval. *Science* 299: 1709–1713.
- Yu, Z. (2011). Holocene carbon flux histories of the world's peatlands: Global carbon-cycle implications. *The Holocene* 21: 761–774.

CHAPTER FOUR

Speleothem $\delta^{13}\text{C}$, vegetation modelling and the glacial methane budget

4.1. Introduction

4.1.1. A tropical driver of glacial atmospheric methane concentrations?

In chapter three of this thesis, it was suggested that tropical vegetation productivity appears to be the primary driver of the glacial methane budget (e.g., Valdes et al. 2005; Kaplan et al. 2006; Fischer et al. 2008). The strong relationship between ice core methane concentrations and speleothem $\delta^{13}\text{C}$ from Sulawesi provides evidence for this relationship, via the common influence of changes in tropical vegetation productivity on speleothem $\delta^{13}\text{C}$ and tropical methane production (Figure 4.1). It has previously been suggested that speleothem $\delta^{13}\text{C}$ could provide a proxy for atmospheric methane (Griffiths et al. 2013); however, this study is the first to explore this relationship explicitly. The Sulawesi $\delta^{13}\text{C}$ record likely provides the first tropical proxy evidence for the contribution of tropical wetlands and vegetation productivity to the atmospheric methane budget over the last 40 kyr.

In this chapter, we will attempt to quantify and explore this relationship through the use of the Sheffield Dynamic Global Vegetation Model (SDGVM), in order to further validate our interpretation of Sulawesi speleothem $\delta^{13}\text{C}$ (see chapter 3). The addition of vegetation modelling to our proxy-based study allows us to explore the nature and drivers of tropical methane emissions, and determine if Sulawesi $\delta^{13}\text{C}$ is acting as a proxy for tropical vegetation production, and glacial methane concentrations.

4.1.2. The global methane budget

The modern global methane cycle is dominated by methane from natural wetlands, which account for ~60-80% of methane emissions (excluding anthropogenic sources; Kirschke et al. 2013). The remaining atmospheric methane is from geological sources including oceans (~15%), freshwater lakes and rivers (~11%), animals (~4%), termites (~3%), hydrates (~2%), biomass burning (~1%) and permafrost (<1%) (Kirschke et al. 2013). Natural wetlands are primarily located in the tropics and northern hemisphere mid-high latitudes. About 60% of modern methane emissions from wetlands are from tropical sources, and ~40% from boreal (Aselmann and Crutzen 1989; Cao et al. 1996; Guo et al. 2012). This ratio is not consistent through time, with swings between glacial and interglacial climates having a huge impact on both the absolute and relative tropical:boreal strength of wetland emissions (e.g., Chappellaz et al. 1997; Dällenbach et al. 2000).

4.1.3. Palaeo-records of atmospheric methane concentration

Ice cores from the high latitudes provide a direct proxy of past atmospheric methane concentrations in air trapped within layers of ice. Analysis of atmospheric methane concentrations in ice cores has provided a high quality record of methane variability over the last 800 kyr (e.g., Loulergue et al. 2008) (Figure 4.1). While the concentration of atmospheric methane is well constrained, identifying the changing sources of methane through time remains an area of debate, because of the limited spatial availability of methane proxies (e.g., Brook et al. 2000; Fischer et al. 2008; Levine et al. 2011).

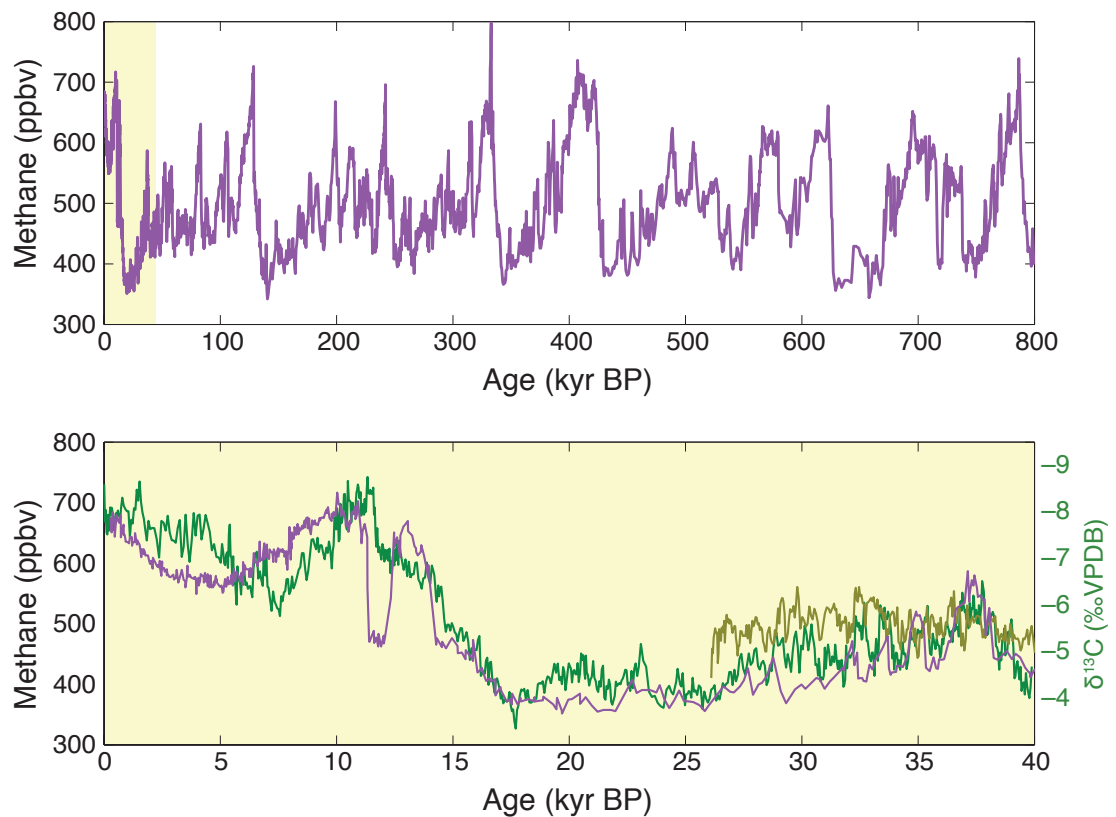


Figure 4.1: EPICA Dome C methane concentration (top) over the last 800 kyr BP. (bottom) Methane concentrations for the last 40 kyr BP. Sulawesi speleothem $\delta^{13}\text{C}$ data are overlain on the right-hand axis. Methane data from Louergue et al. (2008).

The difference in methane concentrations between Greenland and Antarctica (referred to as the methane “gradient”) has been used to infer methane sources through time. Methane is relatively well mixed within the atmosphere, however a methane gradient exists because of the dominance of methane sources in the northern hemisphere, compared to the southern hemisphere. Greater concentrations of methane recorded in Greenland ice cores, relative to Antarctic ice cores, imply a dominant northern hemisphere source (Baumgartner et al. 2012). A reduction in the strength of this gradient suggests an increase in the relative importance of southern hemisphere methane sources. Chappellaz et al. (1997) and Dällenbach et al. (2000) used this method, and a simple three-box model, to argue for a dominant tropical source of methane during the last glacial period. Fischer et al. (2008) similarly argue for enhanced boreal wetland emissions during the Bølling-Allerød, and the early Holocene because of the relatively higher methane concentrations seen in Greenland, relative to Antarctica.

Examining the methane gradient provides valuable information on the changing contribution of northern boreal methane sources to the global atmospheric budget. This method is less useful for studying the tropics however, since the tropics straddle the equator, contributing to both the northern and southern hemisphere budgets as the Intertropical Convergence Zone moves north/south on both seasonal and orbital timescales.

The other key proxy evidence of past atmospheric methane sources is related to the isotopic composition of the methane preserved in ice cores. Isotopes of carbon and hydrogen are incorporated into the methane molecule and are fractionated according to the sink (Fischer et al. 2008). These isotopic differences between methane reservoirs can be used to infer the likely source of methane. Methane emitted by marine clathrates for example, is enriched in both ^{13}C and deuterium (D), making it isotopically distinct from living methane sources, which are depleted in D (Figure 4.2) (Fischer et al. 2008).

While this method is useful for examining the contribution of some sources, including marine clathrates and biomass burning, the isotopic signature of methane emitted from living plants and wetlands is very similar between sources. This method, therefore, cannot be used to distinguish the relative influence of tropical or boreal wetlands on the atmospheric methane budget.

4.2. Possible contributors to the past atmospheric methane signal

While tropical and boreal wetlands produce the vast majority of natural methane emissions at present, the sources and magnitude of methane emissions have not remained constant through time. By combining ice core records of the concentration and isotopic composition of methane in both the northern and southern high latitudes with climate models, a number of hypotheses of the changing sources of methane over the last glacial period and through to the Holocene have emerged (e.g., Chappellaz et al. 1997; Dällenbach et al. 2000; Kaplan 2002; Baumgartner et al. 2012). We explore the main theories below.

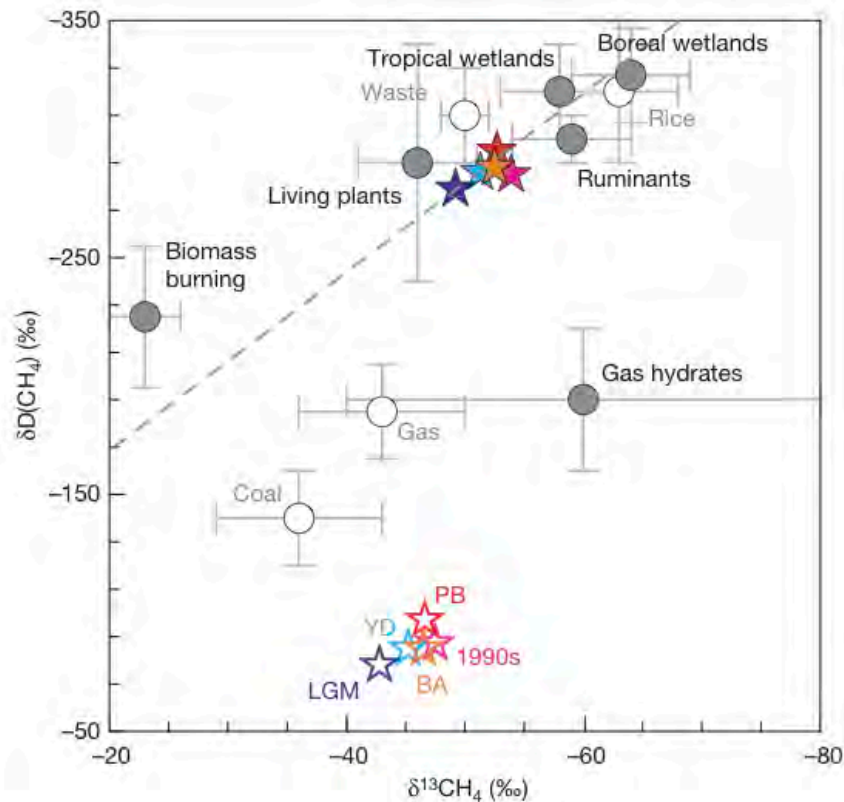


Figure 4.2: Carbon and hydrogen isotope signatures in methane as an indicator of source (from Fischer et al. 2008). Mainly anthropogenic sources are indicated by open circles, mainly natural sources by dark grey dots. The error bars indicate the spread of reported values. No δD values for plant emissions are available so far. Open stars indicate the modelled average atmospheric $\delta^{13}\text{CH}_4$ and $\delta\text{D}(\text{CH}_4)$ for the 1990s, preboreal Holocene (PB), Younger Dryas (YD), Bølling/Allerød (BA) and LGM (Fischer et al. 2008). Filled stars represent best-guess model estimates for average $\delta^{13}\text{CH}_4$ and $\delta\text{D}(\text{CH}_4)$ emitted. The dashed line represents a linear fit through these isotopic emission averages. See Fischer et al. (2008) for a full description of the methods used to produce this figure.

4.2.1. Wetlands

Natural wetland emissions of methane are split between two main sources: tropical wetlands (~60% of wetland emissions) and boreal wetlands (~40%) (Aselmann and Crutzen 1989; Cao et al. 1996; Guo et al. 2012). Methane production is the result of microbiological processes, where organic material is degraded anaerobically (Segers

1998). In freshwater environments, methanogens primarily produce methane through the decomposition of plant material (Reddy and DeLaune 2004):



The amount of methane produced within wetlands is controlled by a number of factors, including the organic matter content and nutrient composition of soil, as well as climatological factors such as regional hydrology and temperature (Reddy and DeLaune 2004). Regional hydrology is an important contributor to methane emissions. Since methanogens require anoxic conditions to produce methane, the height of the water table is an important factor in determining methane production (Moore and Roulet 1993). In regions where water table height is relatively constant, soil temperature becomes the primary determinant of methane emissions. Soil temperature influences the metabolic activity of microorganisms, directly affecting methane emission rates (Reddy and DeLaune 2004). Field studies on northern peat-land sites suggest that mean seasonal soil temperature can account for as much as 84% of the observed variance in methane emissions (Christensen et al. 2003). However, the relative importance of hydrology and temperature are not universally agreed upon, with studies often disagreeing as to the primary control on methane emissions. Ecosystem productivity acts as an excellent proxy for wetland methane emissions, encompassing the effects of both hydrology and temperature, among other factors (Whiting and Chanton 1993).

It is generally agreed that wetland methane emissions were an important contributor to the atmospheric methane budget in the past (e.g., Valdes et al. 2005; Kaplan et al. 2006; Baumgartner et al. 2012; Guo et al. 2012). Estimates of the relative influence of wetlands on the past atmospheric methane budget have relied upon secondary proxy evidence and modelling studies. Examination of the atmospheric methane gradient between Greenland and Antarctica suggests that it is greatest during warmer periods, when northern hemisphere boreal sources play a stronger role (Baumgartner et al. 2012).

Model studies of methane emissions since the Last Glacial Maximum (LGM; ~21 kyr BP) similarly suggest the continued importance of wetlands in the global methane budget, but do not necessarily agree as to the changes in tropical versus boreal contributions. Simple box models have been used in a number of studies to examine the changing methane source regions since the LGM. The relative influence of the tropics versus boreal wetlands varies between models, from a relatively stable tropics and

variable boreal source (Dällenbach et al. 2000) to co-varying tropics and boreal sources (Chappellaz et al. 1997; Baumgartner et al. 2012). Coupled general circulation models (GCMs) have also been used to examine this question, and tend to suggest a more dominant role for the tropics, because of the freezing of northern boreal wetlands (Valdes et al. 2005; Kaplan et al. 2006; Fischer et al. 2008).

4.2.2. Shelf flooding hypothesis

Global sea level and atmospheric methane show good agreement in the timing of rapid events (Ridgwell et al. 2012). Ridgwell et al. (2012) proposed that flooding of shallow continental shelves during sea-level rises leads to an abrupt release of methane as the vegetation cover decomposes. The rising water table favours anoxic conditions, promoting decomposition of organic material by methanogens. This mechanism has been observed in the modern day following flooding caused by the creation of a dam (e.g., Galy-Lacaux et al. 1999; Kemenes et al. 2007), and is particularly pronounced in the tropics, where warm temperatures reduce oxygen solubility and enhance metabolic processes.

The possible influence of shelf flooding on atmospheric methane concentrations can be best demonstrated during meltwater pulse 1A and 1B at 14.6–14.3 kyr BP and 11.4–11.1 kyr BP respectively. During these events, large shelf areas were inundated, particularly within the Indonesian archipelago, resulting in methane ‘bursts’ amounting to rises in atmospheric methane of ~24–50 ppbv (Ridgwell et al. 2012). While such a change is significant, it only accounts for ~15–30% of the total methane change observed at these times, suggesting this mechanism acts alongside other processes.

4.2.3. Marine gas clathrates

Catastrophic release of marine gas clathrates has been suggested as a source of large methane excursions recorded by ice cores during the deglaciation. The “methane-led hypothesis” suggests that large releases of methane from clathrates destabilised during large underwater landslides triggered the last deglaciation, which subsequently led to increases in atmospheric CO_2 and global temperature (e.g., Kennett et al. 2000; Nisbet 2002). Studies of the $\delta^{13}\text{C}$ of foraminifera preserved in a sediment core off the west

coast of the USA provide key proxy evidence for methane hydrate instability during the last deglaciation, with foraminifera recording large and abrupt carbon isotopic excursions during the inferred methane events (Kennett et al. 2000). This work has been discussed in subsequent studies, which suggest that the “methane” signal observed in this study was highly localised, and not an indicator of a larger clathrate destabilisation (Sowers 2006; Etiope et al. 2008).

The distinct isotopic signature of methane derived from marine clathrates acts as a fingerprint for this reservoir. Marine methane reservoirs are relatively enriched in deuterium ($\delta\text{D}(\text{CH}_4)$), but have $\delta^{13}\text{CH}_4$ values similar to wetlands (Sowers 2006; Fischer et al. 2008) (Figure 4.2). Comparison with ice core $\delta^{13}\text{CH}_4$ records allows it to be ruled out as a major contributor to the glacial/interglacial change in atmospheric methane, which was derived from a source depleted in deuterium (Schaefer et al. 2006; Fischer et al. 2008).

4.3. Models and methods

In this study, we use model outputs from the Sheffield Dynamic Global Vegetation Model (SDGVM), a vegetation model that is coupled to the HadCM3 climate model to simulate changes in vegetation dynamics over the last 40 kyr. These simulations were run by Dr Joy Singarayer and Dr Paul Valdes at Bristol University, and provided to this author for analysis. All analyses presented in this chapter are original work, unless stated otherwise.

4.3.1. HadCM3 general circulation model

The HadCM3 model (short for the Hadley Centre Coupled Model, version 3) is a coupled ocean-atmosphere-sea ice GCM, used to simulate global climate change. The resolution of the atmospheric model is 2.5° latitude by 3.25° longitude, with 19 unequally spaced vertical levels (Gordon et al. 2000). The ocean model resolution is 1.25° latitude by 1.25° longitude with 20 unequally spaced layers extending to a depth of 5200 m. The sea-ice model uses a simple thermodynamic scheme, and a parameterisation of ice drift and leads (Cattle et al. 1995). Coupling between the model components occurs daily, with fields passed between the models at this time, prior to

continuing the simulation (Gordon et al. 2000). The third version of the HadCM model does not require flux adjustments (see Gordon et al., 2000 for a detailed discussion of the model parameters).

Climate simulations from the HadCM3 model have been validated against both proxy records, and other GCMs. The HadCM3 model has been shown to represent modern climate conditions well, through comparison with observational datasets (Gordon et al. 2000; Pope et al. 2000) (Figure 4.3). The spatial distribution of temperature gradients is well represented within HadCM3, as are the broad meridional structures, and absolute temperatures. The spatial pattern of precipitation is also well captured by HadCM3, particularly across the tropics, where the location and strength of the Inter-tropical Convergence Zone compares well with observations (Figure 4.3). Validation of HadCM3 palaeoclimate simulations has also been undertaken, namely through the palaeoclimate intercomparison projects (PMIP) (Braconnot et al. 2007a; Braconnot et al. 2007b), and a proxy-model study by DiNezio and Tierney (2013). HadCM3 represents LGM climate conditions relatively well when compared to other PMIP models (Braconnot et al. 2007a; Braconnot et al. 2007b); however, when compared with LGM proxy data from the Indo-Pacific Warm Pool, HadCM3 becomes the only model to successfully capture the climate conditions recorded by both terrestrial and marine proxies (DiNezio and Tierney 2013) (Figure 4.4). For the purposes of this study, the HadCM3 climate model has been coupled to the SDGVM vegetation model to produce high resolution simulations of global vegetation.

4.3.2. SDGVM vegetation and wetland model

The SDGVM is a global primary productivity and phytogeography model (Woodward et al. 1995). The model uses climatic inputs from HadCM3 to simulate dynamic changes in vegetation properties, in response to changing climate variables. Several key processes simulated within the SDGVM include: net biome production, net primary productivity (NPP), gross primary productivity (GPP), intercellular CO_2 concentration, nitrogen uptake into plant, leaf area index (LAI), maximum canopy height, above ground tree mass, plant density and vegetation functional type composition (Woodward and Lomas 2004).

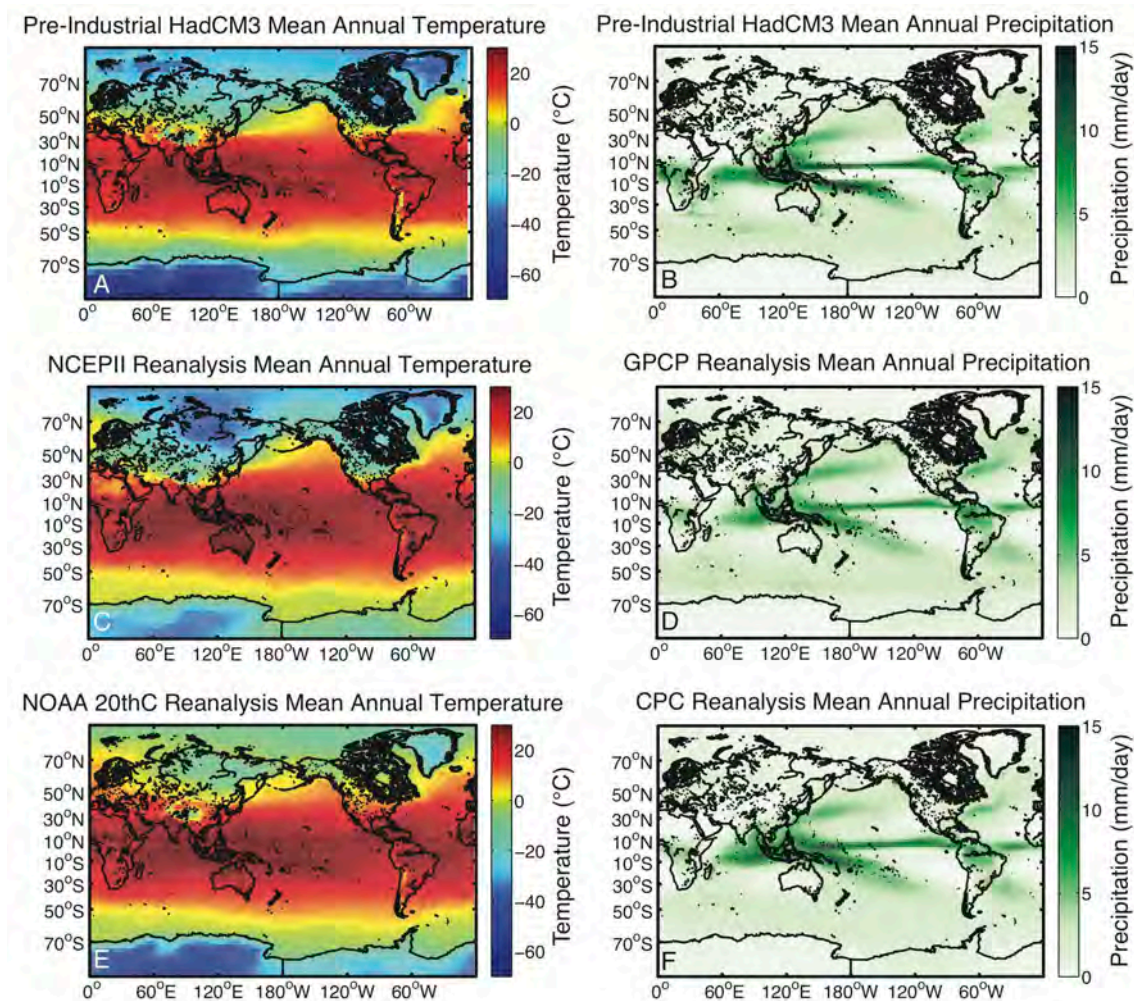


Figure 4.3: Temperature and precipitation as represented by HadCM3, compared against modern observations. Mean annual temperature (A) and precipitation (B) for HadCM3. (C) Observational temperature data from the NCEP-II reanalysis (Kanamitsu et al. 2002) and (E) NOAA’s 20th Century Reanalysis Project (Compo et al. 2011). (D) Observational precipitation data from the Global Precipitation Climatology Project (Adler et al. 2003) and (F) the CPC Merged Analysis of Precipitation (Xie and Arkin 1997). N.B. Reanalysis datasets (which combine observations and model outputs), while not strictly observations, are global in extent, making them suitable for comparison with global HadCM3 output.

Vegetation characteristics are diagnosed from the model by simulating the processes that affect vegetation (Woodward and Lomas 2004). The main processes driving vegetation are climate, atmospheric CO_2 concentration, the soil nitrogen budget and soil characteristics. Vegetation types are categorised into “plant functional types” (PFTs), which allows plant species to be broadly categorised, thus simplifying model

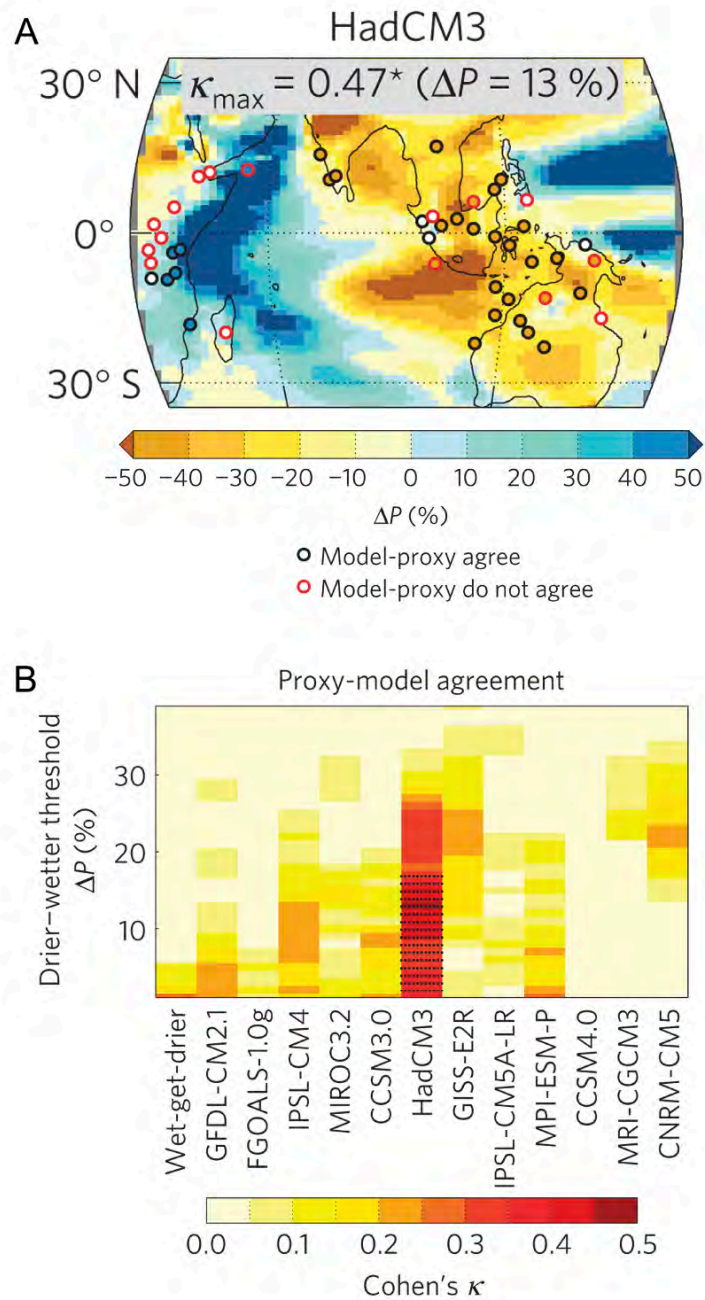


Figure 4.4: Proxy-model comparison demonstrating the skill of HadCM3 at simulating LGM climate across the Indo-Pacific Warm Pool. (A) Rainfall changes between LGM and pre-industrial (PI) climate simulations expressed as a percentage of PI annual mean precipitation. The maximum Cohen's κ and optimal threshold for defining drier or wetter conditions is shown for each model. (B) Cohen's κ for each model as a function of wetter/drier threshold. Stippling indicates statistically significant ($p < 0.05$) κ values. Figure adapted after DiNezio et al. (2013). See DiNezio et al. (2013) for a full description of the methods and models used to produce this figure.

calculations, and facilitating their dynamic response to other model variables. The response of PFTs is driven by sensitivities to temperature, net precipitation (precipitation minus evapotranspiration) and net primary productivity. This means that vegetation is able to respond to changes in the environment and provides a dynamic feedback to both small-scale vegetation processes, and large-scale climate changes. Vegetation response to changing climate and environment is not instantaneous, but is dependent on the cycle of mortality and establishment of PFTs. Fire is simulated in the model when leaf litter reaches a critical dryness (Singarayer et al. 2011), with grassland re-establishing the burnt region, followed by larger trees, if climate conditions permit (Woodward and Lomas 2004).

Validation of this model has been undertaken on a variety of scales, from leaf processes to global scale fluxes, and it has been shown to compare well with observational datasets (Woodward and Lomas 2004). The ability of SDGVM to accurately simulate observed vegetation lends confidence to its ability to reasonably simulate past changes in vegetation (Figure 4.5).

4.3.2.1. Wetland module

The SDGVM does not model methane emissions in its standard configuration, and an additional methane module is used to simulate wetland extent and methane emissions (Note that the name SDGVM will now include reference to the methane module). The methane module uses temperature, precipitation, relative humidity, soil type and atmospheric CO_2 concentration outputs from HadCM3 and the SDGVM to calculate methane emissions (see Singarayer et al. 2011; Wania et al. 2013 for a detailed discussion of the methods used to calculate methane emissions.)

4.3.2.2. Wetland module validation

The SDGVM participated in the Wetland and Wetland CH_4 Inter-comparison of Models Project (WETCHIMP) project in 2013, which aimed to compare and validate available methane models (Melton et al. 2013; Wania et al. 2013). This project provides a multi-model comparison of the skill of the SDGVM in simulating global methane emissions, and a means of validating it for use within this study. SDGVM over-represents total wetland area when compared against modern observations, with large areas of the

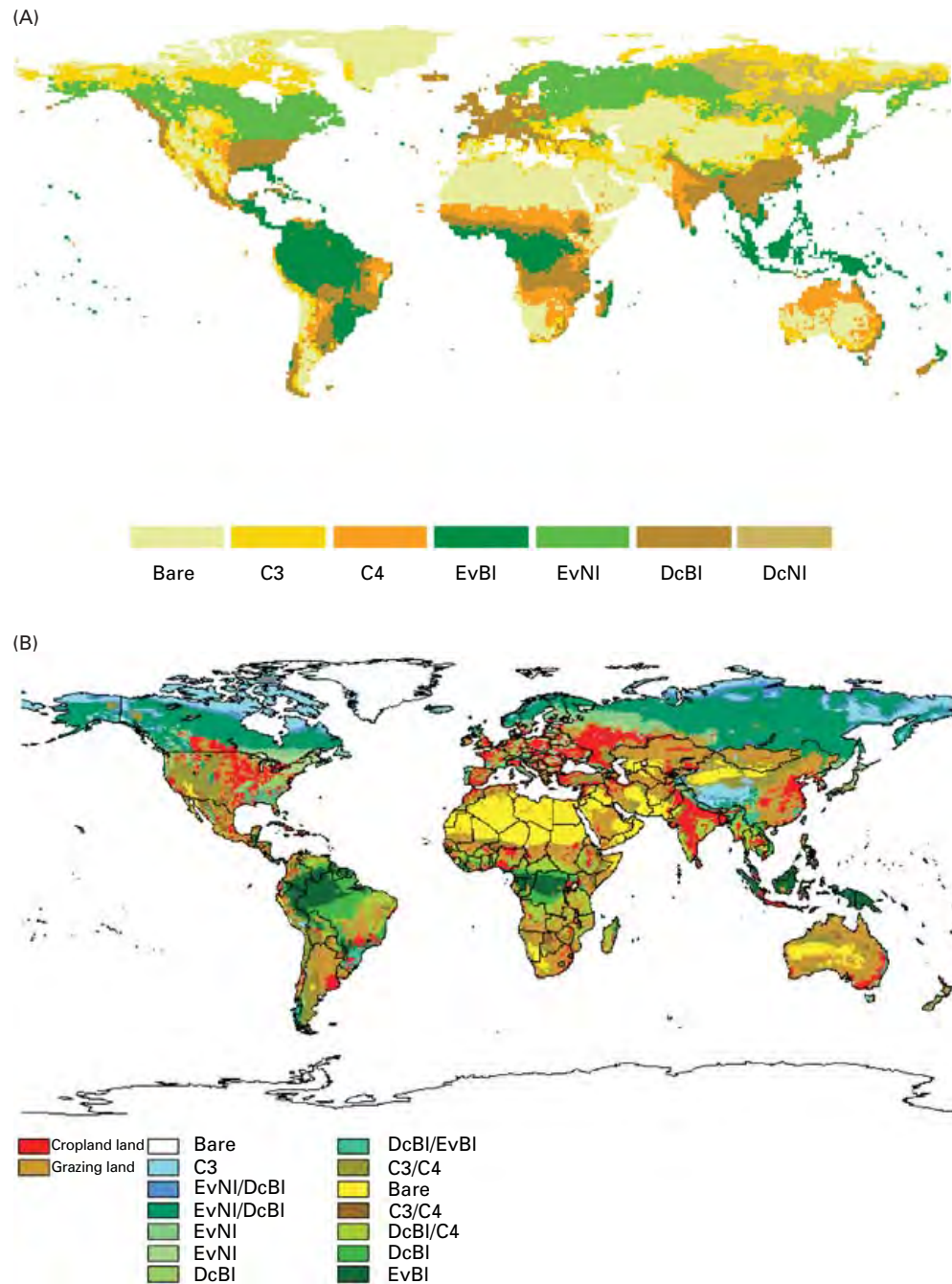


Figure 4.5: SDGVM modelled and observational modern vegetation cover (figure from Woodward and Lomas 2004) (A) Simulated distribution of dominant plant functional types. Bare, bare ground (desert); C3, C3 grasses and shrubs; C4, C4 grassland; EvBI, evergreen broadleaf trees; EvNI, evergreen needleleaf trees; DcBI, deciduous broadleaf trees; DcNI, deciduous needleleaf trees (boreal). (B) Actual global land cover for 1990 (from Goldewijk 2001), with vegetation classes simplified to functional types, for comparison with A.

tropics and boreal regions represented by near-100% wetland cover, however the spatial distribution of wetlands is relatively well represented. Despite this, the spatial distribution and absolute amount of methane emissions compare well with other models, showing a maximum in emissions across the tropics, driven largely by emissions from the Amazon (Figure 4.6).

Methane emissions are dependent on temperature, water table depth and the organic load within the soil. Sensitivity experiments undertaken within the SDGVM for WETCHIMP demonstrate the SDGVM's sensitivity to changing CO_2 concentrations, air temperature and precipitation (Melton et al. 2013). Wetland sensitivity varied by location in SDGVM, with the tropics and extratropics responding differently to the various forcings (Melton et al. 2013). The tropics proved most sensitive to an increase in CO_2 concentrations via fertilisation of tropical vegetation, while the extratropics were most sensitive to an increase in temperature, because of the seasonal sub-zero temperature experienced across the northern mid to high-latitudes.

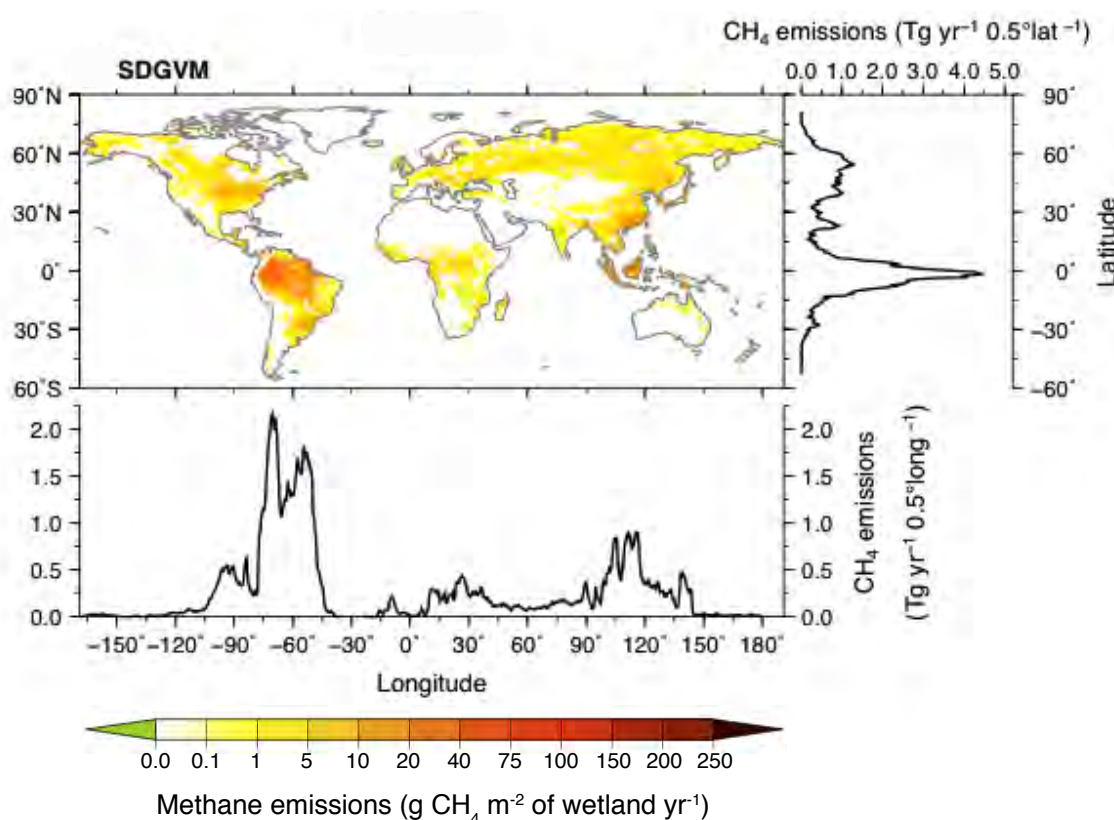


Figure 4.6: Magnitude and distribution of methane emissions as simulated by the SDGVM. Figure after Melton et al. (2013).

4.3.3. Model simulations

HadCM3 and SDGVM were run at 1–2 kyr time slices over the last 40 kyr to produce a time-series of global vegetation and methane change. Time slices were run in HadCM3 every 1 kyr for the period 22 kyr–0 kyr BP, and every 2 kyr for the period 40 kyr–22 kyr BP. This resulted in a total of 32 time slice simulations for the period 40 kyr BP to present. The model simulations were produced and published in Singarayer et al. (2010) and Singarayer et al. (2011).

HadCM3 was forced with time slice accurate changes to orbital configuration, ice sheet volume (and sea level) and greenhouse gases for each time slice, following the methods of Singarayer et al. (2010), and Singarayer et al. (2011). All time slices were run from an equilibrated pre-industrial control run, and forced with boundary conditions appropriate to the time slice being run. The model was then allowed to re-equilibrate under these new conditions for 500 model years. The results presented here represent the climatology of the last 30 years of each model run.

SDGVM was forced by the climate outputs derived from HadCM3, to produce a dynamic vegetation response to the modelled climate time slices. It is important to note that abrupt millennial-scale events were not simulated in this experiment. The model simulations were run using 1–2 kyr “snap shots” of climate, which were subsequently combined to provide a time-evolving picture of climate change since 40 kyr BP. This is not a “transient” experiment, in that a continually evolving climate was not simulated, but rather the time evolution of climate was simulated through the use of 1–2 kyr snap shots. For this reason, we do not see key millennial-scale events within our output, including Heinrich events, Dansgaard-Oeschger events, the Bølling-Allerød and the Younger Dryas.

4.4. Results

4.4.1. Methane sources

The sources of methane over the last 40 kyr BP can be examined within the SDGVM. Methane sources are broken up into three categories: tropics ($\pm 30^\circ$), boreal ($\geq 35^\circ\text{N}$) and other ($\geq 30^\circ\text{S}$ and $30\text{--}35^\circ\text{N}$). These definitions have been used to follow the convention

established by the WETCHIMP project, to allow comparisons between models (Melton et al. 2013).

Throughout the last 40 kyr, the tropics remain the dominant source of methane emissions, with the boreal region playing a more variable role (Figure 4.7). Methane emissions from the tropics remain relatively high throughout the last 40 kyr, with only a small reduction in total emissions during the LGM. The small reduction is due to the relatively warm temperatures that remained in the tropics during the last glacial period.

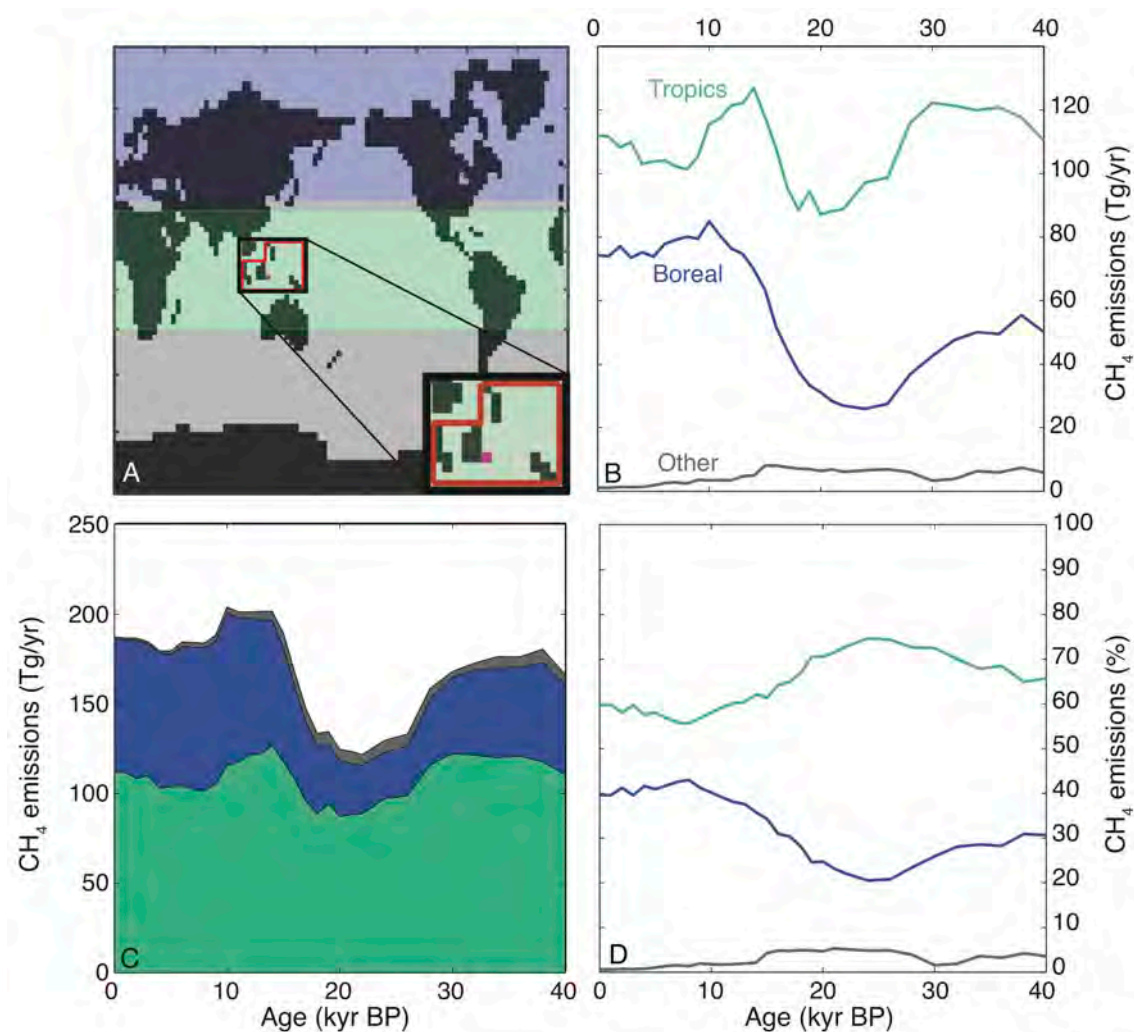


Figure 4.7: Methane sources from the SDGVM. (A) Map showing the spatial distribution of regions using in this study. Inset map shows Indonesia (red box) and Sulawesi (pink grid cell) as represented for the present day in the SDGVM. (B) Methane emissions by region. (C) Stacked regional emissions showing the relative contribution to the global total. (D) Regional emissions as a percentage of the total emissions. Regions are identified by the same colour in each panel: tropics (green), boreal (blue) and other (grey).

However, methane emissions from boreal sources decrease dramatically during the LGM, because of the presence of sub-zero temperatures throughout most of the year. During boreal summer, temperatures move above zero, facilitating the emission of methane from the northern high latitudes at this time (Figure 4.8). The relative contributions of tropical and boreal sources to glacial methane emissions highlight the importance of the tropics in the glacial methane budget (~75%), relative to the boreal (~20%). During the Holocene, however, their relative contributions converge, with the tropics contributing ~60% of methane emissions, compared to ~40% from boreal sources, in line with modern observations (Aselmann and Crutzen 1989; Cao et al.

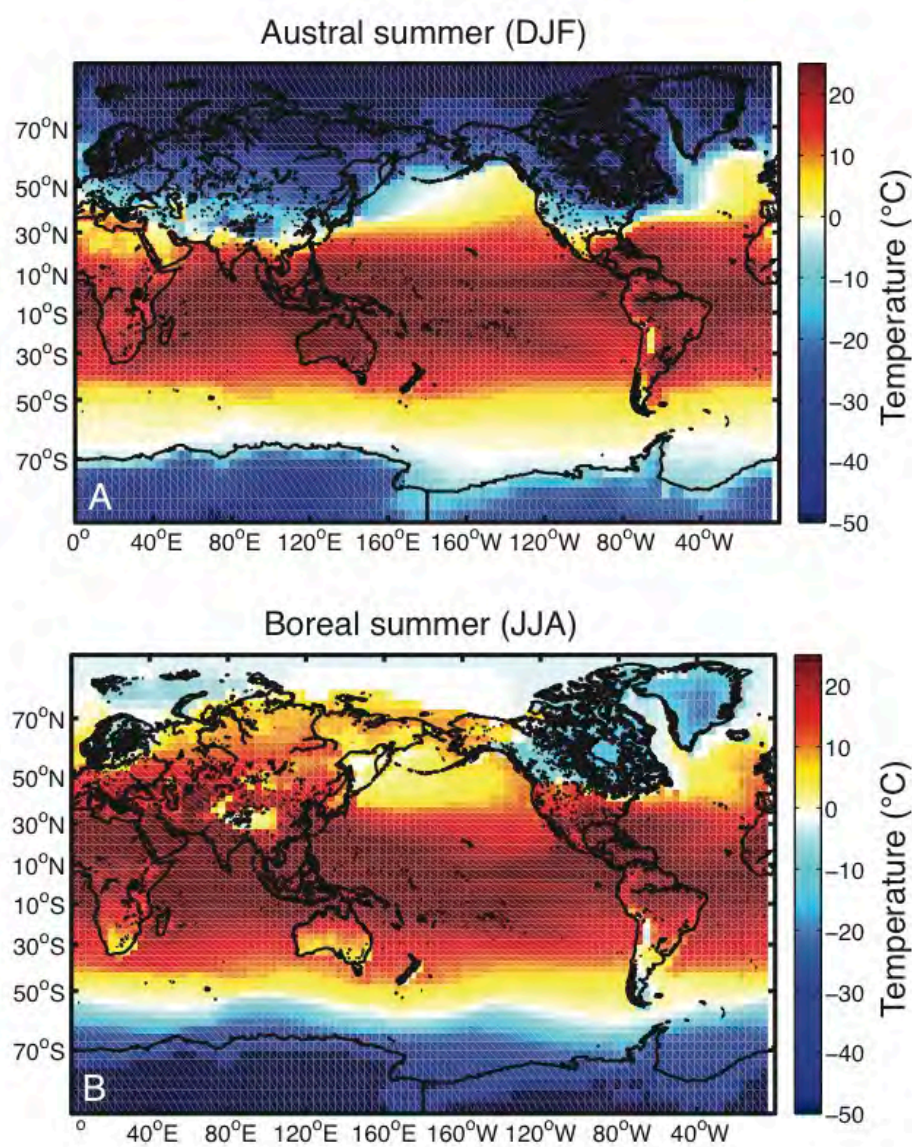


Figure 4.8: Surface air temperature during the glacial period (32–15 kyr BP) in HadCM3 (used to drive the SDGVM). (A) Austral summer air temperature (DJF). (B) Boreal summer air temperature (JJA).

1996; Guo et al. 2012). This result agrees well with previous studies (Chappellaz et al. 1997; Dällenbach et al. 2000; Valdes et al. 2005; Kaplan et al. 2006; Fischer et al. 2008), and validates our use of this model for further investigation of methane emissions.

4.4.2. Methane emissions from exposed Indonesian shelves

Vegetation on exposed shallow continental shelves during the LGM, when sea level was ~120 m lower than modern, present a challenge and a source of uncertainty within the SDGVM. Changes in sea level over the last 40 kyr result in an increase in land area across Indonesia of ~42% (~7% for the tropics) between 40 kyr BP and the present in the SDGVM. This new land area within the Indonesian archipelago is treated as a continuation of the surrounding vegetation on permanently exposed island areas within the SDGVM, and is designated as tropical rainforest. Changes in sea level, therefore, have a large impact on the total methane emissions, particularly across Indonesia, which increase dramatically when sea level is lower than at present (Figure 4.9). Methane emissions from exposed shelf grid cells have a smaller influence on emissions from Sulawesi and the tropics as a whole, where the total amount of methane emitted increases, but the general trends and patterns of emissions over the last 40 kyr remain relatively constant.

Vegetation of newly exposed continental shelves across Indonesia remains controversial, with palaeoenvironmental studies suggesting a range in vegetation conditions could have existed across the Sunda Shelf during low sea levels. A synthesis of palaeoenvironmental records by Bird et al. (2005) suggested the existence of a savannah grassland across the exposed Sunda Shelf during the last glacial period, supported by a range of palynological, geomorphological and biogeographical studies. This result is not conclusive however, with a number of studies suggesting the existence of tropical rainforest across the same area, or a combination of the two vegetation types (e.g., Sun et al. 2000; Hope 2001; Taylor et al. 2001; Meijaard 2003). Population of tropical rainforest on the exposed shelf area, as simulated by the SDGVM, can therefore be considered an upper estimate of the likely methane emissions from this region during the glacial period. Methane emissions for Indonesia are dominated by this signal when

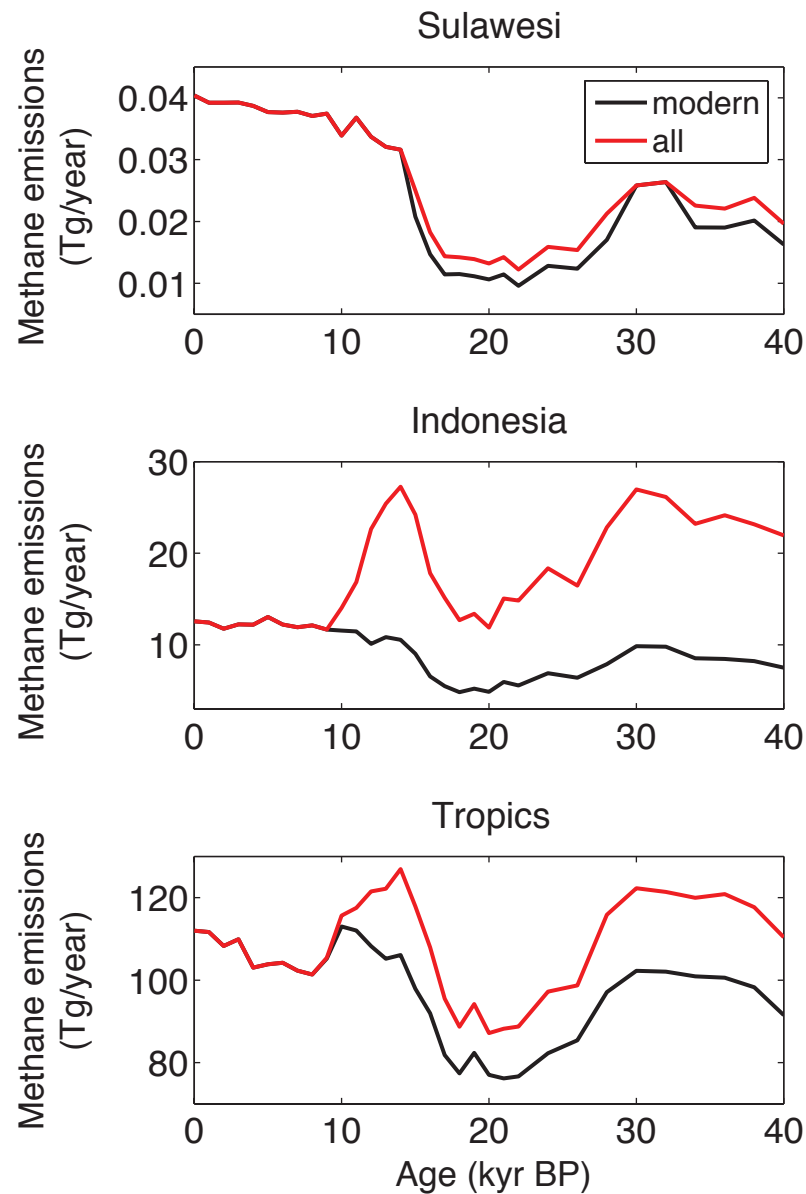


Figure 4.9: Influence of exposed land area across Indonesia on total methane emissions in the SDGVM. Only modern land areas are included in the black totals. Changing ocean/land grid cells resulting from changes in sea level are included in red. Top: methane emissions from Sulawesi. Middle: methane emissions summed over Indonesia. Bottom: methane emissions summed over the tropics ($\pm 30^\circ$). Regions are defined in Figure 4.7A.

exposed land area is considered (Figure 4.9), introducing a large source of uncertainty into results from this region. We therefore choose to only consider emissions from land areas exposed in the present-day to reduce the uncertainties associated with the

treatment of vegetation on the Sunda Shelf, but note that our subsequent analyses present a minimum estimate of Indonesian and tropical methane emissions.

4.4.3. Seasonality of methane signal

The seasonally uniform methane emissions from Sulawesi lend confidence that the speleothem is recording the mean annual vegetation signal and methane emissions. A seasonally skewed signal that may be recorded if karst processes and residence time biased speleothem growth towards a particular season. The lack of seasonality in methane production simulated by the model suggests that the Sulawesi speleothem $\delta^{13}\text{C}$ is recording the annual mean in local methane production. Results are given for Sulawesi, the whole of Indonesia, and the whole of the tropics (Figure 4.7A). We chose to look at all three regions to ensure that we are comparing both the local and regional signals of methane emissions. The model simulation of monthly methane production in Sulawesi shows a relatively uniform methane emission rate throughout the year, with a slight reduction in emissions during the winter monsoon months (Figure 4.10).

4.4.4. Tropical drivers of glacial methane emissions

The dominance of tropical methane emissions during the last glacial period (prior to deglaciation beginning at ~ 18 kyr BP) provides a mechanism by which the Sulawesi speleothem $\delta^{13}\text{C}$ and ice core atmospheric methane concentrations co-vary so closely over this period (Figure 4.1). The relationship between ice core methane and speleothem $\delta^{13}\text{C}$ is strongest during the glacial period, when tropical methane sources dominated the total wetland emissions (Figure 4.7). The Sulawesi speleothem $\delta^{13}\text{C}$, which we suggest is indicative of a wider regional signal, is recording the key changes in tropical vegetation productivity and methane emissions, and therefore the general pattern of change in glacial atmospheric methane concentrations.

During the Holocene, boreal methane sources play a much stronger role in the overall budget, contributing $\sim 40\%$ of the total emissions. This results in a disconnect between Sulawesi speleothem $\delta^{13}\text{C}$ and the ice core methane record, which now reflects a more equal mix of methane from both tropical and boreal sources.

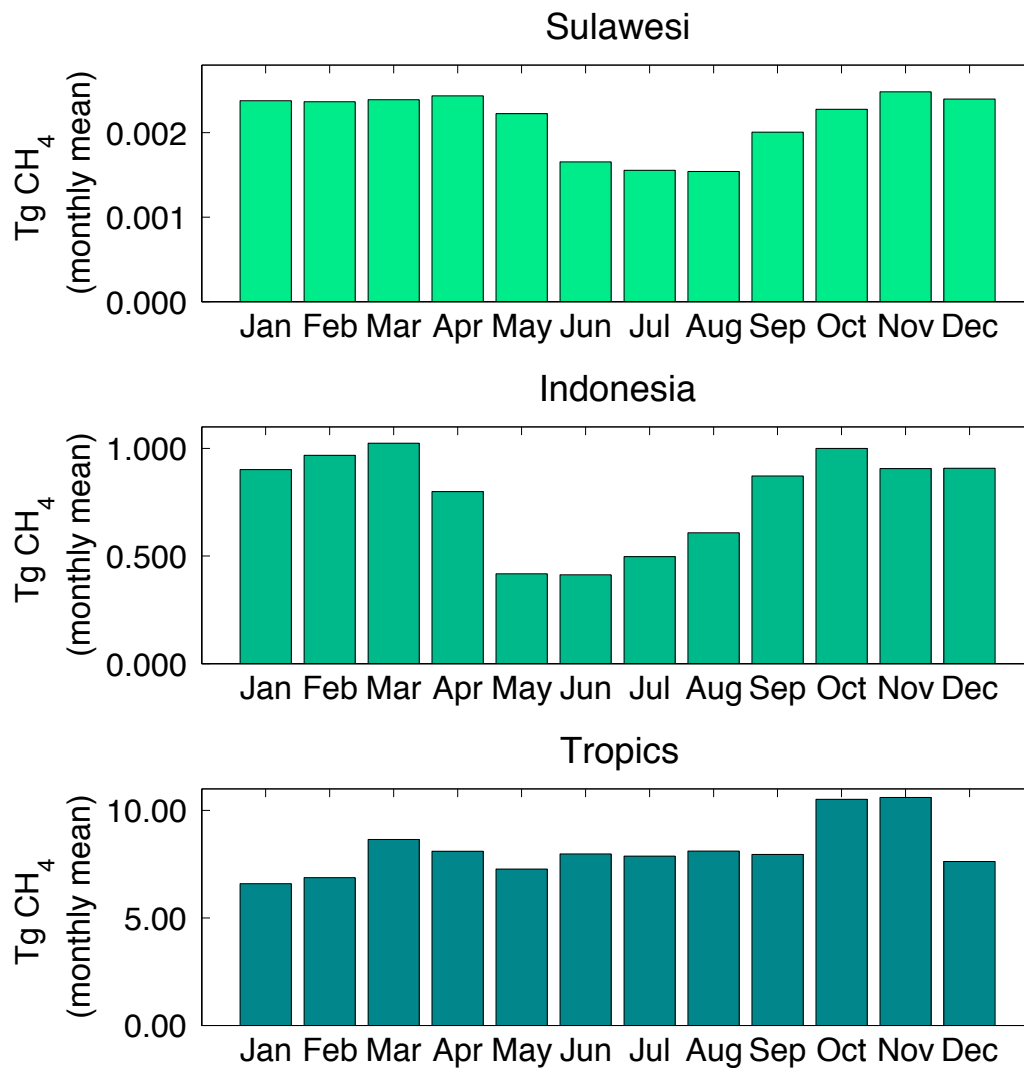


Figure 4.10: Mean monthly methane emissions in the SDGVM. Top: monthly methane emissions from Sulawesi. Middle: monthly methane emissions summed over Indonesia. Bottom: monthly methane emissions summed over the tropics ($\pm 30^\circ$). Regions are defined in Figure 4.7A.

4.5. Discussion

4.5.1. Speleothem $\delta^{13}\text{C}$ and the SDGVM

In order to compare the Sulawesi speleothem $\delta^{13}\text{C}$ record with the SDGVM model output, we identify soil respiration as the model parameter closest to speleothem $\delta^{13}\text{C}$ and use this parameter as a proxy for our record within the model environment. Soil

respiration refers to the emission of CO_2 from the soil surface (Schlesinger and Andrews 2000), that is produced within the soil profile by roots and soil organisms (Raich and Schlesinger 1992). It is sustained by organic matter contribution to the soil from above ground, and from roots (Raich and Schlesinger 1992). Temperature is the biggest predictor of soil respiration rates, particularly in regions of low temperature; however, the addition of precipitation improves this relationship (Raich and Schlesinger 1992).

Soil respiration acts as an indicator of vegetation productivity, as increased vegetation growth leads to an increase in organic material available to decomposers (Schlesinger and Andrews 2000), and within the SDGVM, correlates very strongly with net primary productivity ($r = 0.98$). The rate of soil respiration is influenced by the rate of CO_2 production in the soil by roots and organisms, the gradient between the partial pressures of CO_2 in the soil and atmosphere, as well as other factors including soil porosity, air temperature and wind speed (Raich and Schlesinger 1992). The rate of soil respiration reflects the concentration of CO_2 within the soil profile, which is the most likely primary source for carbon in the Sulawesi speleothem. We therefore use soil respiration as a qualitative proxy for speleothem $\delta^{13}\text{C}$ within the SDGVM.

4.5.2. Drivers of speleothem $\delta^{13}\text{C}$

The close agreement between soil respiration and speleothem $\delta^{13}\text{C}$ supports our conclusion that Sulawesi speleothem carbon isotopes are being driven by changes in vegetation productivity (Figure 4.11). Speleothem $\delta^{13}\text{C}$ correlates strongly with soil respiration across all three regions of the tropics. The Sulawesi grid box shows a strong correlation with Sulawesi speleothem $\delta^{13}\text{C}$ ($r = -0.71$, $p \approx 0.01$), which is mirrored in results from Indonesia ($r = -0.66$, $p \approx 0$) and the tropics as a whole ($r = -0.66$, $p \approx 0$). The strongest relationship exists for the Sulawesi grid box, suggesting the model is able to replicate changes in local vegetation productivity across the last 40 kyr in this area, supporting our use of the SDGVM model to evaluate the drivers and signals recorded within our speleothem results.

The strong agreement in soil respiration rates across both the local, regional and latitudinal scales suggests that tropical vegetation across the whole of the tropics behaved in a similar way to changing boundary conditions over the last 40 kyr. This

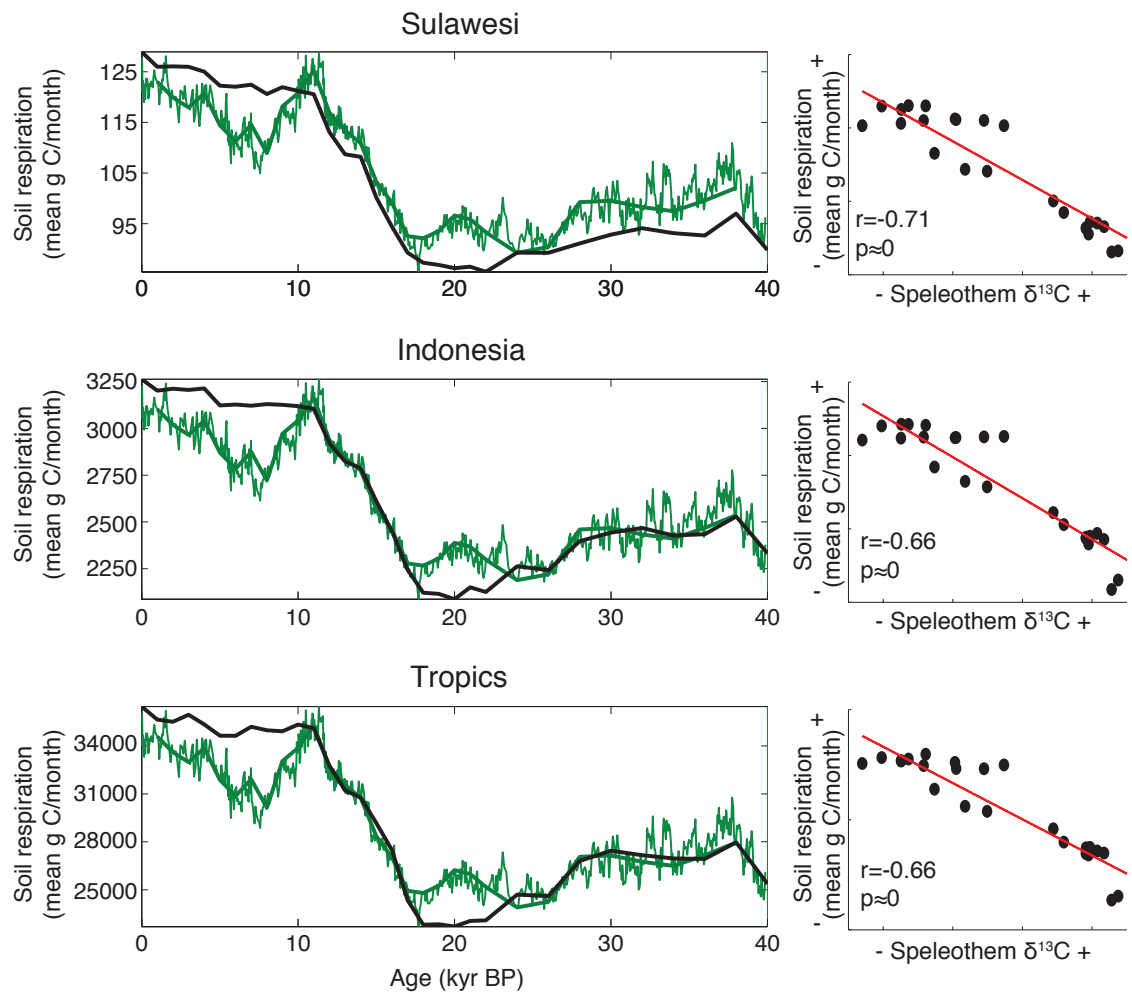


Figure 4.11: Modelled soil respiration compared with Sulawesi speleothem $\delta^{13}\text{C}$. Top: mean soil respiration for Sulawesi. Middle: mean soil respiration for Indonesia. Bottom: mean soil respiration for the tropics ($\pm 30^\circ$). Sulawesi speleothem $\delta^{13}\text{C}$ is plotted on each graph for reference (green). Correlation statistics are given for each relationship in the scatter plots. Note that the correlation was performed on records filtered with a 10 kyr high pass filter to remove the strong deglacial trend.

supports our assumption that the Sulawesi record represents large-scale changes in vegetation productivity across the tropics, which would be enough to have a significant influence on the global methane budget.

4.5.3. Is Indonesia representative of the tropics?

The basis for this study relies on the assumption that the “point-source” speleothem $\delta^{13}\text{C}$ record for Sulawesi is indicative of a regional methane signal. Comparing the

Sulawesi record with the speleothem $\delta^{13}\text{C}$ record for the nearby island of Flores supports this assumption (see Section 3.4.3 for discussion); however, the global scale of the SDGVM results allow us to more rigorously test this assumption.

We tested the correlation between Sulawesi and the rest of the globe by calculating the correlation of methane emissions from each grid box in the model against methane emissions at Sulawesi over the last 40 kyr. Time-series of methane emissions were created for each grid box and correlated against the methane emissions time-series from the Sulawesi grid box. All time-series were detrended using a 10-kyr high-pass filter to remove the dominant influence of deglaciation on the correlations (Figure 4.12B).

Methane emissions from Sulawesi show a positive correlation with those from large regions of the tropics, the Asian landmass and Alaska during the glacial period (Figure 4.12). Sulawesi also shows strong correlations across the Indo-Pacific Warm Pool, central Africa and tropical South America. Positive correlations are particularly strong for parts of boreal North America and Eurasia. This relationship is likely due to the influence of deglaciation, particularly an LGM minimum in methane emissions that remains despite the use of a filter to minimise this signal, highlighting the dominant global extent of the LGM on regional methane emissions. The spatial extent of the positive correlation decreases during the Holocene, when boreal sources play a more dominant role in the total methane emissions.

Interestingly, Sulawesi shows some strong anti-correlations with parts of North America and southern Africa during the glacial period. The negative relationship observed with North America occurs at the margins of the Laurentide ice sheet, which retreats from its maximum extent following the LGM, and disappears completely during the Holocene. This results in a reduction in moisture in this region following the LGM, causing a gradual decline in methane emissions. The negative relationship with southern Africa results from a peak in methane emissions in this region during the LGM. Similar relationships can be seen in northern Australia and southern tropical South America. Orbital forcing led to a gradual drying in these southern sub-tropical regions as the summer insolation maximum and Intertropical Convergence Zone moved north during deglaciation, resulting in a gradual decrease in southern methane emissions.

Modelled methane emissions from Sulawesi correlate strongly with large parts of the tropics and eastern Asia during the glacial, suggesting that the speleothem $\delta^{13}\text{C}$

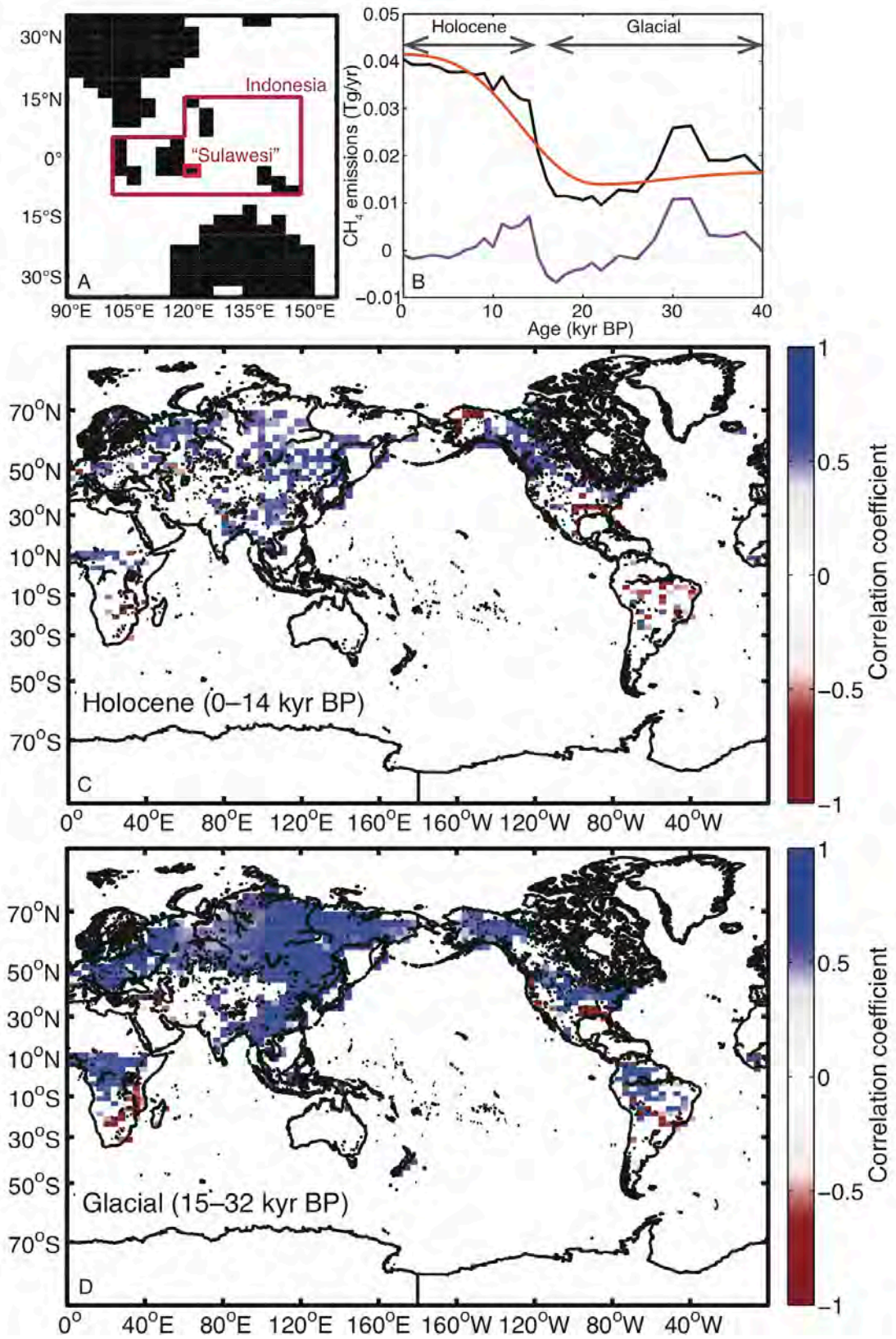


Figure 4.12

Figure 4.12: Correlation between modelled methane emissions from Sulawesi and global methane emissions within the SDGVM. (A) Representation of Sulawesi and Indonesia in the modern day in the SDGVM. (B) Time-series of methane emissions from Sulawesi (black), with low-pass filter removed from the time-series (orange), and high-pass filtered time-series used to calculate correlation coefficients (purple). (C) Map of correlation coefficients during the Holocene – taken as the stable period following deglaciation in (B). Filtered methane emissions time-series for each grid box were regressed against the filtered Sulawesi methane emissions time-series (B) and the resulting correlation coefficients (r) were plotted. Only statistically significant correlations are shown ($p < 0.1$). (D) as in (C), but for the glacial period (32–15 kyr BP).

record is likely to be representative of a wider regional signal. This relationship breaks down during the Holocene, when there is a disconnection between Sulawesi methane emissions and the wider tropics, supporting our conclusion that Sulawesi speleothem $\delta^{13}\text{C}$ is not a faithful recorder of tropical methane emissions during this period.

4.5.4. Does modelled methane match speleothem $\delta^{13}\text{C}$?

The SDGVM modelled methane compares well with the Sulawesi speleothem $\delta^{13}\text{C}$ record over the last 40 kyr, supporting our interpretation that the record reflects changes in tropical vegetation methanogenesis. Modelled methane emissions for Sulawesi, Indonesia and the tropics are all negatively correlated with speleothem $\delta^{13}\text{C}$ for Sulawesi (Figure 4.13). The timing of the glacial minimum in methane emissions modelled in the SDGVM is relatively late compared to that in ice core records, which show a gradual decrease in atmospheric methane concentrations into the LGM (Figure 4.1). The difference between the records is due to methane and precipitation maxima at ~30 kyr BP in the model, which drives anomalously high-modelled methane emissions across the tropics (Figure 4.13).

Model methane emissions from Sulawesi, Indonesia and the whole tropics match speleothem $\delta^{13}\text{C}$ closely during the deglaciation (Figure 4.13). The timing of the initiation of the increase in emissions associated with deglaciation is the same in both the model and speleothem time-series, as well as in ice core methane records. The plateau in speleothem $\delta^{13}\text{C}$ at ~14–12 kyr BP is mirrored in the model. The SDGVM is

only forced by climate changes every 1 kyr and so does not include a representation of abrupt climate events. Despite this, the model reproduces the slow-down in methane emissions across the Younger Dryas, although not to the same extent as in the speleothem and ice core records.

Model methane emissions from Sulawesi and Indonesia diverge from the speleothem time-series during the Holocene; however, the speleothem record agrees well with model methane emissions from the tropics as a whole. The mid-Holocene

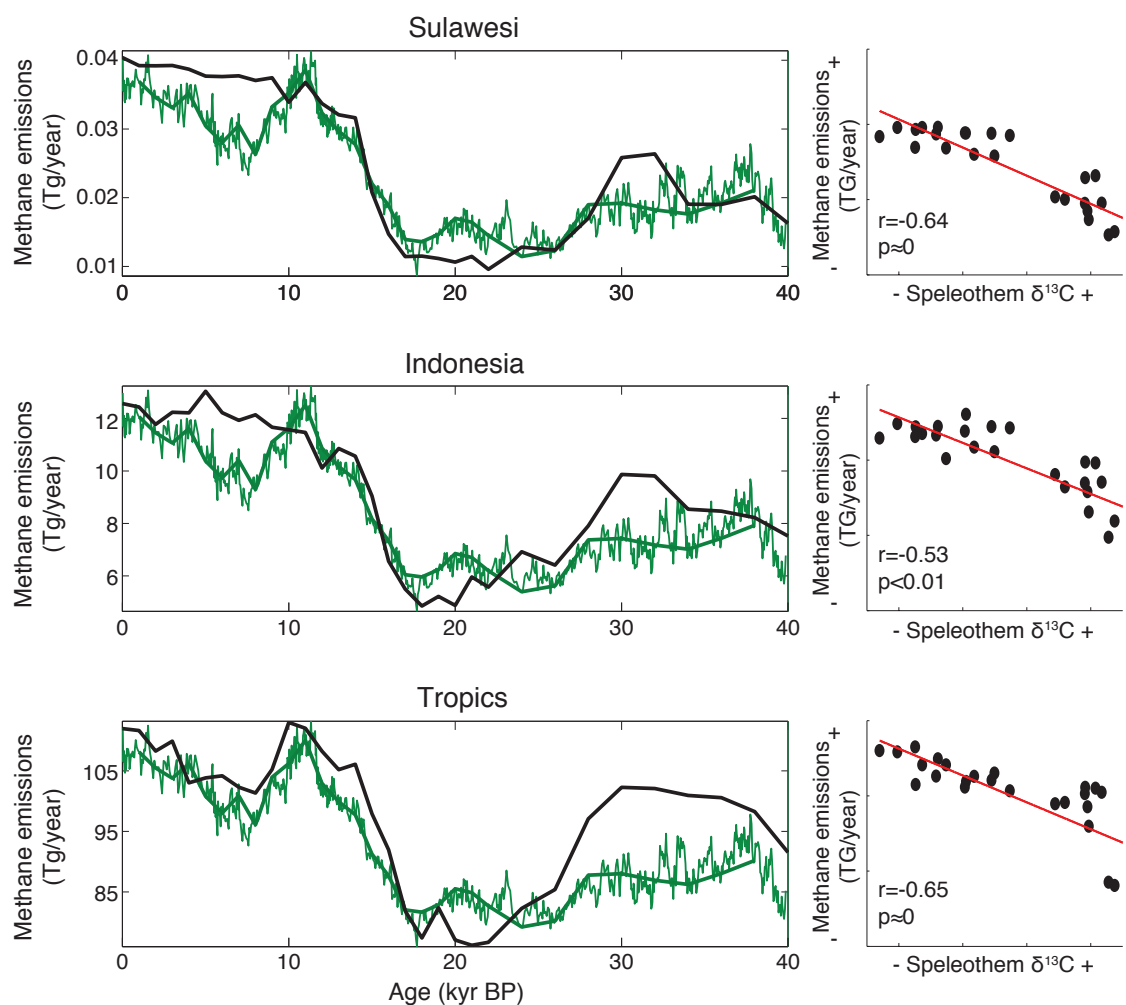


Figure 4.13: Comparison of methane emissions from the SDGVM and Sulawesi speleothem $\delta^{13}\text{C}$. Top: mean methane emissions for Sulawesi. Middle: mean methane emissions for Indonesia. Bottom: mean methane emissions for the tropics ($\pm 30^\circ$). Sulawesi speleothem $\delta^{13}\text{C}$ is plotted on each graph for reference (green). Correlation statistics are given for each relationship in the scatter plots. Note that the correlation was performed on records filtered with a 10-kyr high pass filter to remove the strong deglacial trend.

decrease in methane emissions modelled across the tropics is likely driven by orbital forcing, which brought about a decline in the strength of northern hemisphere summer insolation and the East Asian summer monsoon until ~ 5 kyr BP, after which time southern summer insolation and monsoons began to strengthen. This results in a gradual decrease, then increase in tropical methane emissions. This mechanism for driving the observed mid-Holocene decrease in atmospheric methane has been proposed from records of speleothem $\delta^{18}\text{O}$ from China and Brazil (Burns 2011).

However, the abrupt nature of the Holocene decrease in methane emissions in the SDGVM does not mirror the smooth insolation driver. This suggests either a non-linear response in methane emissions to orbital forcing across the tropics or the presence of an alternative, or complementary, driver of this signal. Examination of the origins of this abrupt signal point to a source between the equator and 10°S , and suggest it is likely a combination of gradual orbital forcing, and a sharp increase in atmospheric CO_2 concentrations since ~ 5 kyr BP.

4.6. A tropical driver of glacial atmospheric methane

The Sulawesi speleothem $\delta^{13}\text{C}$ record and results from the SDGVM support the idea of a strong tropical driver of glacial atmospheric methane concentrations. The good agreement between Sulawesi $\delta^{13}\text{C}$ and ice core methane, as well as Sulawesi $\delta^{13}\text{C}$ and modelled methane emissions from both local and regional sources, supports our conclusion (Figure 4.14). Tropical sources of methane emissions dominated during the glacial period when boreal sources were largely dormant. Tropical vegetation productivity was maintained during the glacial period despite moderate decreases in temperature and precipitation, facilitating the continuation of decomposition and methanogenesis. The relationship between Sulawesi $\delta^{13}\text{C}$ and ice core is masked during the Holocene, when boreal wetland methane emissions become more influential and tropical sources no longer dominate the atmospheric methane budget.

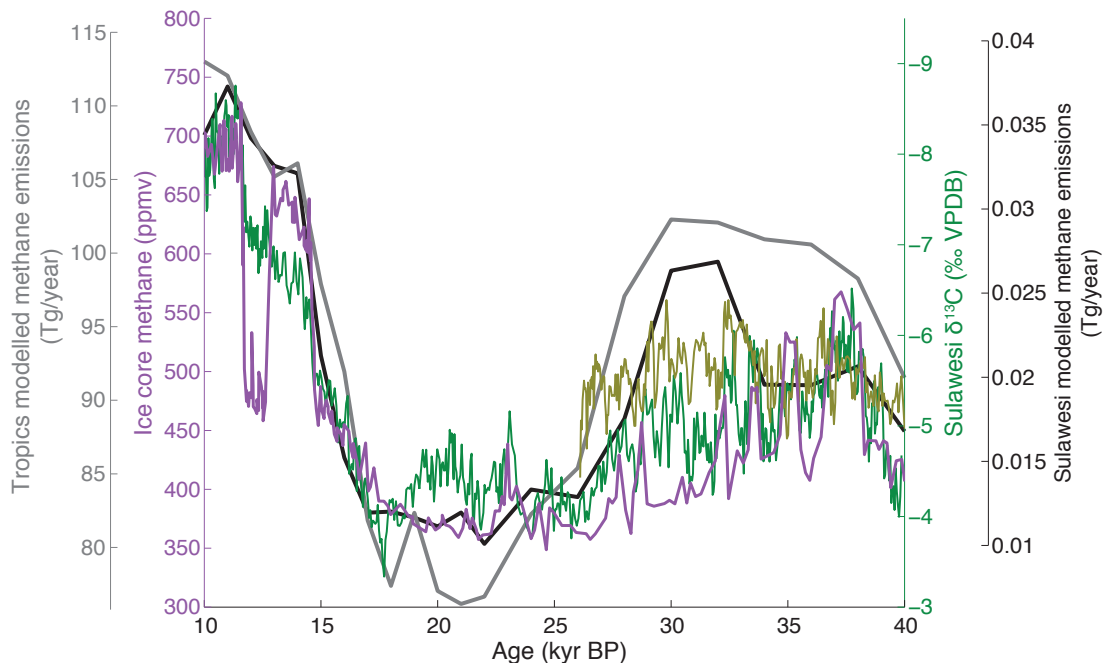


Figure 4.14: A tropical driver of glacial methane. Sulawesi speleothem $\delta^{13}\text{C}$ (green), ice core methane (purple) and the SDGVM modelled methane emissions for Sulawesi (black) and the tropics (grey).

Previous work has identified the tropics as a likely source of methane emissions during the last glacial period but, until now, a proxy for tropical vegetation productivity has not been available to verify this possibility. The combination of the Sulawesi speleothem $\delta^{13}\text{C}$ record and the SDGVM allows us to test our hypothesis and demonstrate a dynamical mechanism between tropical vegetation productivity and methane emissions. We therefore conclude that Sulawesi speleothem $\delta^{13}\text{C}$ is a proxy for changes in vegetation productivity, which in turn is recording changes in tropical methane production, which appears to have made a substantial contribution to the glacial atmospheric methane budget. Sulawesi speleothem $\delta^{13}\text{C}$ therefore acts as a tropical proxy of glacial methane emissions, providing the first non-polar constraint on the likely sources of past atmospheric methane.

4.7. Acknowledgements

HadCM3 and SDGVM simulations were run by Dr Joy Singarayer and Dr Paul Valdes at Bristol University, and originally published by these authors in Singarayer et al.

(2010) and Singarayer et al. (2011). Technical collaboration for this project was with Dr Peter Hopcroft at Bristol University. All model analyses presented in this chapter were carried out by this author, and represent new and original work, unless stated otherwise.

4.8. References

- Adler, R. F., G. J. Huffman, A. Chang, R. Ferraro, P.-P. Xie, J. Janowiak, B. Rudolf, U. Schneider, S. Curtis, D. Bolvin, A. Gruber, J. Susskind, P. Arkin and E. Nelkin (2003). The version-2 Global Precipitation Climatology Project (GPCP) monthly precipitation analysis (1979–present). *Journal of Hydrometeorology* 4: 1147–1167.
- Aselmann, I. and P. J. Crutzen (1989). Global distribution of natural freshwater wetlands and rice paddies, their net primary productivity, seasonality and possible methane emissions. *Journal of Atmospheric Chemistry* 8: 307–358.
- Baumgartner, M., A. Schilt, O. Eicher, J. Schmitt, J. Schwander, R. Spahni, H. Fischer and T. F. Stocker (2012). High-resolution interglacial difference of atmospheric methane around the Last Glacial Maximum. *Biogeosciences* 9: 3961–3977.
- Bird, M. I., D. Taylor and C. Hunt (2005). Palaeoenvironments of insular Southeast Asia during the Last Glacial Period: a savanna corridor in Sundaland? *Quaternary Science Reviews* 24: 2228–2242.
- Braconnot, P., B. Otto-Bliesner, S. Harrison, S. Joussaume, J.-Y. Peterchmitt, A. Abe-Ouchi, M. Crucifix, E. Driesschaert, T. Fichefet, C. D. Hewitt, M. Kageyama, A. Kitoh, A. Laîne, M.-F. Loutre, O. Marti, U. Merkel, G. Ramstein, P. Valdes, S. L. Weber, Y. Yu and Y. Zhao (2007a). Results of PMIP2 coupled simulations of the Mid-Holocene and Last Glacial Maximum - Part 1: experiments and large-scale features. *Climate of the Past* 3: 261–277.
- Braconnot, P., B. Otto-Bliesner, S. Harrison, S. Joussaume, J.-Y. Peterchmitt, A. Abe-Ouchi, M. Crucifix, E. Driesschaert, T. Fichefet, C. D. Hewitt, M. Kageyama, A. Kitoh, M.-F. Loutre, O. Marti, U. Merkel, G. Ramstein, P. Valdes, L. Weber, Y. Yu and Y. Zhao (2007b). Results of PMIP2 coupled simulations of the Mid-Holocene and Last Glacial Maximum - Part 2: feedbacks with emphasis on the location of the ITCZ and mid- and high latitudes heat budget. *Climate of the Past* 3: 279–296.

- Brook, E. J., S. Harder, J. Severinghaus, E. J. Steig and C. M. Sucher (2000). On the origin and timing of rapid changes in atmospheric methane during the last glacial period. *Global Biogeochemical Cycles* 14: 559–572.
- Burns, S. J. (2011). Speleothem records of changes in tropical hydrology over the Holocene and possible implications for atmospheric methane. *The Holocene* 21: 735–741.
- Cao, M., S. Marshall and K. Gregson (1996). Global carbon exchange and methane emissions from natural wetlands: Application of a process-based model. *Journal of Geophysical Research* 101: 14399–14414.
- Cattle, H., J. Crossley and D. J. Drewry (1995). Modelling Arctic climate change. *Philosophical Transactions of the Royal Society A* 352: 201–213.
- Chappellaz, J., T. Blunier, S. Kints, A. Dällenbach, J.-M. Barnola, J. Schwander, D. Raynaud and B. Stauffer (1997). Changes in the atmospheric CH_4 gradient between Greenland and Antarctica during the Holocene. *Journal of Geophysical Research* 102: 15987–15997.
- Christensen, T. R., A. Ekberg, L. Ström, M. Mastepanov, N. Panikov, M. Öquist, B. H. Svensson, H. Nykänen, P. J. Martikainen and H. Oskarsson (2003). Factors controlling large scale variations in methane emissions from wetlands. *Geophysical Research Letters* 30: 1414.
- Compo, G. P., J. S. Whitaker, P. D. Sardeshmukh, N. Matsui, R. J. Allan, X. Yin, B. E. Gleason, R. S. Vose, G. Rutledge, P. Bessemoulin, S. Brönnimann, M. Brunet, R. I. Crouthamel, A. N. Grant, P. Y. Groisman, P. D. Jones, M. C. Kruk, A. C. Kruger, G. J. Marshall, M. Maugeri, H. Y. Mok, Ø. Nordil, T. F. Ross, R. M. Trigo, X. L. Wang, S. D. Woodruff and S. J. Worley (2011). The twentieth century reanalysis project. *Quarterly Journal of the Royal Meteorological Society* 137: 1–28.
- Dällenbach, A., T. Blunier, J. Flückiger, B. Stauffer, J. Chappellaz and D. Raynaud (2000). Changes in the atmospheric CH_4 gradient between Greenland and Antarctica during the Last Glacial and the transition to the Holocene. *Geophysical Research Letters* 27: 1005–1008.
- DiNezio, P. N. and J. E. Tierney (2013). The effect of sea level on glacial Indo-Pacific climate. *Nature Geoscience* 6: 485–491.

- Etioppe, G., A. V. Milkov and E. Derbyshire (2008). Did geologic emissions of methane play any role in Quaternary climate change? *Global and Planetary Change* 61: 79–88.
- Fischer, H., M. Behrens, M. Bock, U. Richter, J. Schmitt, L. Loulergue, J. Chappellaz, R. Spahni, T. Blunier, M. Leuenberger and T. F. Stocker (2008). Changing boreal methane sources and constant biomass burning during the last termination. *Nature* 452: 864–867.
- Galy-Lacaux, C., R. Delmas, G. Kouadio, S. Richard and P. Gosse (1999). Long-term greenhouse gas emissions from hydroelectric reservoirs in tropical forest regions. *Global Biogeochemical Cycles* 13: 503–517.
- Goldewijk, K. K. (2001). Estimating global land use change over the past 300 years: the HYDE database. *Global Biogeochemical Cycles* 15: 417–433.
- Gordon, C., C. Cooper, C. A. Senior, H. Banks, J. M. Gregory, T. C. Johns, J. F. B. Mitchell and R. A. Wood (2000). The simulation of SST, sea ice extents and ocean heat transports in a version of the Hadley Centre coupled model without flux adjustments. *Climate Dynamics* 16: 147–168.
- Griffiths, M. L., R. N. Drysdale, M. K. Gagan, J. C. Hellstrom, I. Couchoud, L. K. Ayliffe, H. B. Vonhof and W. S. Hantoro (2013). Australasian monsoon response to Dansgaard-Oeschger event 21 and teleconnections to higher latitudes *Earth and Planetary Science Letters* 369–370: 294–304.
- Guo, Z., X. Zhou and H. Wu (2012). Glacial-interglacial water cycle, global monsoon and atmospheric methane changes. *Climate Dynamics* 39: 1073–1092.
- Hope, G. (2001). Environmental change in the Late Pleistocene and later Holocene at Wanda site, Soroako, South Sulawesi, Indonesia. *Palaeogeography, Palaeoclimatology, Palaeoecology* 171: 129–145.
- Kanamitsu, M., W. Ebisuzaki, J. Woollen, S.-K. Yang, J. J. Hnilo, M. Fiorino and G. L. Potter (2002). NCEP-DOE AMIP-II Reanalysis (R-2). *Bulletin of the American Meteorological Society* 83: 1631–1643.
- Kaplan, J. O. (2002). Wetlands at the Last Glacial Maximum: Distribution and methane emissions. *Geophysical Research Letters* 29: 1079.
- Kaplan, J. O., G. Folberth and D. A. Hauglustaine (2006). Role of methane and biogenic volatile organic compound sources in late glacial and Holocene

fluctuations of atmospheric methane concentrations. *Global Biogeochemical Cycles* 20: GB2016.

Kemenes, A., B. R. Forsberg and J. M. Melack (2007). Methane release below a tropical hydroelectric dam. *Geophysical Research Letters* 34: L12809.

Kennett, J. P., K. G. Cannariato, I. L. Hendy and R. J. Behl (2000). Carbon isotopic evidence for methane hydrate instability during Quaternary interstadials. *Science* 288: 128–133.

Kirschke, S., P. Bousquet, P. Ciais, M. Saunois, J. Canadell, E. Dlugokencky, P. Bergamaschi, D. Bergmann, D. Blake, L. Bruhwiler, P. Cameron-Smith, S. Castaldi, F. Chevallier, L. Feng, A. Fraser, M. Heimann, E. Hodson, S. Houweling, B. Josse, P. Fraser, P. Krummel, J.-F. Lamarque, R. Langenfelds, C. Le Quéré, V. Naik, S. O'Doherty, P. Palmer, I. Pison, D. Plummer, B. Poulter, R. Prinn, M. Rigby, B. Ringeval, M. Santini, M. Schmidt, D. Shindell, I. Simpson, R. Spahni, P. Steele, S. Strode, K. Sudo, S. Szopa, G. van der Werf, A. Voulgarakis, M. van Weele, R. Weiss, J. Williams and G. Zeng (2013). Three decades of global methane sources and sinks. *Nature Geoscience* 6: 813–823.

Levine, J. G., E. W. Wolff, A. E. Jones, M. A. Hutterli, O. Wild, G. D. Carver and J. A. Pyle (2011). In search of an ice core signal to differentiate between source-driven and sink-driven changes in atmospheric methane. *Journal of Geophysical Research* 116: D05305.

Loulergue, L., A. Schilt, R. Spahni, V. Masson-Delmotte, T. Blunier, B. Lemieux, J.-M. Barnola, D. Raynaud, T. F. Stocker and J. Chappellaz (2008). Orbital and millennial-scale features of atmospheric CH_4 over the past 800,000 years. *Nature* 453: 383–386.

Meijaard, E. (2003). Mammals of south-east Asian islands and their Late Pleistocene environments. *Journal of Biogeography* 30: 1245–1257.

Melton, J. R., R. Wania, E. L. Hodson, B. Poulter, B. Ringeval, R. Spahni, T. Bohn, C. A. Avis, D. J. Beerling, G. Chen, A. V. Eliseev, S. N. Denisov, P. O. Hopcroft, D. P. Lettenmaier, W. J. Riley, J. S. Singarayer, Z. M. Subin, H. Tian, S. Zürcher, V. Brovkin, P. M. van Bodegom, T. Kleinen, Z. C. Yu and J. O. Kaplan (2013). Present state of global wetland extent and wetland methane modelling: conclusions from a model inter-comparison project (WETCHIMP). *Biogeosciences* 10: 753–788.

- Moore, T. R. and N. T. Roulet (1993). Methane flux: Water table relations in northern wetlands. *Geophysical Research Letters* 20: 587–590.
- Nisbet, E. G. (2002). Have sudden large releases of methane from geological reservoirs occurred since the Last Glacial Maximum, and could such releases occur again? *Philosophical Transactions of the Royal Society B* 360: 581–607.
- Pope, V. D., M. L. Gallani, P. R. Rowntree and R. A. Stratton (2000). The impact of new physical parametrizations in the Hadley Centre climate model: HadAM3. *Climate Dynamics* 16: 123–146.
- Raich, J. W. and W. H. Schlesinger (1992). The global carbon dioxide flux in soil respiration and its relationship to vegetation and climate. *Tellus B* 44: 81–99.
- Reddy, K. R. and R. D. DeLaune (2004). *Biogeochemistry of Wetlands: Science and Applications*. Florida, CRC Press.
- Ridgwell, A., M. Maslin and J. O. Kaplan (2012). Flooding of the continental shelves as a contributor to deglacial CH_4 rise. *Journal of Quaternary Science* 27: 800–806.
- Schaefer, H., M. J. Whiticar, E. J. Brook, V. V. Petrenko, D. F. Ferretti and J. P. Severinghaus (2006). Ice record of $\delta^{13}\text{C}$ for atmospheric CH_4 across the Younger Dryas-Preboreal transition. *Science* 313: 1109–1112.
- Schlesinger, W. H. and J. A. Andrews (2000). Soil respiration and the global carbon cycle. *Biogeochemistry* 48: 7–20.
- Segers, R. (1998). Methane production and methane consumption: a review of processes underlying wetland methane fluxes. *Biogeochemistry* 41: 23–51.
- Singarayer, J. S. and P. J. Valdes (2010). High-latitude climate sensitivity to ice-sheet forcing over the last 120 kyr. *Quaternary Science Reviews* 29: 43–55.
- Singarayer, J. S., P. J. Valdes, P. Friedlingstein, S. Nelson and D. J. Beerling (2011). Late Holocene methane rise caused by orbitally controlled increase in tropical sources. *Nature* 470: 82–86.
- Sowers, T. (2006). Late Quaternary atmospheric CH_4 isotope record suggests marine clathrates are stable. *Science* 311: 838–840.
- Sun, X., X. Li, Y. Luo and X. Chen (2000). The vegetation and climate at the last deglaciation on the emerged continental shelf of the South China Sea. *Palaeogeography, Palaeoclimatology, Palaeoecology* 160: 301–316.

- Taylor, D., O. H. Yen, P. G. Sanderson and J. Dodson (2001). Late Quaternary peat formation and vegetation dynamics in a lowland tropical swamp: Nee Soon, Singapore. *Palaeogeography, Palaeoclimatology, Palaeoecology* 171: 269–287.
- Valdes, P. J., D. J. Beerling and C. E. Johnson (2005). The ice age methane budget. *Geophysical Research Letters* 32: L02704.
- Wania, R., J. R. Melton, E. L. Hodson, B. Poulter, B. Ringeval, R. Spahni, T. Bohn, C. A. Avis, G. Chen, A. V. Eliseev, P. O. Hopcroft, W. J. Riley, Z. M. Subin, H. Tian, P. M. van Bodegom, T. Kleinen, Z. C. Yu, J. S. Singarayer, S. Zürcher, D. P. Lettenmaier, D. J. Beerling, S. N. Denisov, C. Prigent, F. Papa and J. O. Kaplan (2013). Present state of global wetland extent and wetland methane modelling: methodology of a model inter-comparison project (WETCHIMP). *Geoscientific Model Development* 6: 617–641.
- Whiting, G. J. and J. P. Chanton (1993). Primary production control of methane emission from wetlands. *Nature* 364: 794–795.
- Woodward, F. I. and M. R. Lomas (2004). Vegetation dynamics - simulating responses to climatic change. *Biological Reviews* 79: 643–670.
- Woodward, F. I., T. M. Smith and W. R. Emanuel (1995). A global land primary productivity and phytogeography model. *Global Biogeochemical Cycles* 9: 471–490.
- Xie, P. and P. A. Arkin (1997). Global precipitation: a 17-year monthly analysis based on gauge observations, satellite estimates, and numerical model outputs. *Bulletin of the American Meteorological Society* 78: 2539–2558.

CONCLUSIONS

In this thesis, we have used speleothems from Sulawesi, Indonesia, together with palaeoclimate modelling, to explore the hydroclimate dynamics of the western equatorial Pacific and Indo-Australian Summer Monsoon over the last 40,000 years. We combined published speleothem $\delta^{18}\text{O}$ records from across the Australasian monsoon domain to develop a spatio-temporal understanding of the relative roles of deep atmospheric convection and the Intertropical Convergence Zone in driving regional hydroclimate. The variable sensitivity of the western equatorial Pacific to Heinrich events was further explored using the HadCM3 and CSIRO Mk3L general circulation models. We also combined the palaeoenvironmental records produced for this thesis with the SDGVM palaeovegetation model to explore the role of the tropics in driving the late-glacial atmospheric methane budget.

Revisiting the key research questions

1. What are the key drivers of western equatorial Pacific hydroclimate, and how do they interact?

In chapter one, we combined new speleothem $\delta^{18}\text{O}$ records from Gempa Bumi cave in Sulawesi, Indonesia, with published speleothem records from across the Australasian monsoon domain to examine regional spatial and temporal rainfall variability. In Australasia, glacial-interglacial changes in continental shelf exposure influence the intensity of deep atmospheric convection over the centre of the western equatorial Pacific, driving low-frequency changes in the $\delta^{18}\text{O}$ of precipitation at Sulawesi. In

contrast, precession-dominated modulation of rainfall $\delta^{18}\text{O}$ is largely restricted to the northern and southern peripheries of the Australasian monsoon domain and has relatively little influence over the equatorial core of the monsoon system.

On millennial scales, the latitudinal response of the Australasian monsoon decreases toward the equatorial core of the system, culminating in a lack of expression in the Sulawesi speleothem $\delta^{18}\text{O}$ record. This finding was further explored using the HadCM3 general circulation model whereby Heinrich events were simulated by adding a surface freshwater flux to the North Atlantic Ocean. We show that the largest change in rainfall over Sulawesi during simulated Heinrich events occurred during the austral winter, in the local dry season. The dominance of the local summer monsoon at our site possibly overprinted any signal experienced during the winter months, resulting in no discernable signal in the speleothem record.

Taken together, our findings demonstrate that glacial-interglacial changes in northern ice sheets drive the intensity of deep atmospheric convection over the western equatorial Pacific via changes in sea level and continental shelf exposure in the region. Conversely, North Atlantic millennial-scale climate change serves to redistribute monsoon rainfall latitudinally across Australasia, via the Intertropical Convergence Zone, with only a relatively small accompanying change in the overall strength of deep atmospheric convection.

2. How did Heinrich events affect western equatorial Pacific hydroclimate?

In chapter two we further explored the sensitivity of the western equatorial Pacific to Heinrich events using the CSIRO Mk3L general circulation model. Three experiments were performed, which aimed to explore the sensitivity of the model itself to freshwater fluxes into the North Atlantic, as well as the modelled climate response to freshwater hosing under different boundary conditions. The experiments demonstrate that it is the volume of freshwater, rather than the rate of application, that drives the amplitude of the CSIRO Mk3L model response and its recovery from a simulated Heinrich. We validate the use of the standard PMIP protocol for a hosing experiment (1 Sv of freshwater applied for 100 model years from 50–70°N across the North Atlantic Ocean) with the CSIRO Mk3L model and demonstrate that a more conservative hosing procedure (0.1

Sv of freshwater for 100 model years) is insufficient to induce a climate response outside of the Atlantic Ocean basin.

The response of modelled climate to freshwater hosing of the North Atlantic under different boundary conditions was tested and shown to affect the model response to a simulated Heinrich event. The influence of precessional forcing was examined by setting the CSIRO Mk3L model precession parameter to 0 kyr (a southern hemisphere summer insolation maximum – experiment OSH) and 10 kyr (a northern hemisphere summer insolation maximum – experiment ONH). Despite the relatively subtle nature of the change in boundary conditions, a difference in the model response to freshwater hosing of the North Atlantic was observed between experiments. While both experiments saw a weak El-Niño-like state across the tropical Pacific, the experiments differed in the response of the southern high latitudes. A strong annular response was evident in the ONH experiment, particularly over the Southern Ocean, with a southward shift of the Intertropical Convergence Zone occurring alongside an increase in the strength of the Southern Ocean westerly winds. In contrast, experiment OSH produced a more asymmetrical response to the freshwater perturbation, with a negative SAM-like state across the southern mid-high latitudes. Both of these responses to simulated Heinrich events have been reported in the literature; however, this study is the first to reveal both responses within the same model.

The third freshwater hosing experiment was carried out under different atmospheric CO₂ concentrations: 280 ppmv CO₂ (CO2-280) and 400 ppmv CO₂ (CO2-400). The relatively strong climate response to the boundary condition forcing was evident in the control runs of both experiments. Interestingly, the atmospheric CO₂ concentration did not influence the nature of the model Atlantic meridional overturning circulation (AMOC) response to surface freshwater hosing of the North Atlantic as much as the duration of the anomaly. Anomalies lasted ~100 years longer in the CO2-400 experiment compared to CO2-280; a result that agrees with a previously published study. The mechanism for the different lengths of climate perturbations in the experiments was due to different buoyancy forcing of the North Atlantic, with warmer North Atlantic sea surface temperatures in the CO2-400 experiment acting as an additional barrier to the resumption of the AMOC following the cessation of hosing.

3. What role does the tropics play in driving global climate change?

In chapters three and four, we combined the Sulawesi speleothem $\delta^{13}\text{C}$ record with palaeovegetation modelling to explore the role of tropical vegetation in driving the glacial atmospheric methane budget in order to answer this question.

3.a. How did Sulawesi vegetation respond to glacial-interglacial climate change?

In chapter three, we explored the Sulawesi speleothem $\delta^{13}\text{C}$ record to develop a robust interpretation for this underutilised proxy. Comparison of the Sulawesi speleothem $\delta^{13}\text{C}$ and $\delta^{18}\text{O}$ records revealed a difference in the timing of the transition from the glacial state into the Holocene of ~ 6 kyr, with $\delta^{13}\text{C}$ leading $\delta^{18}\text{O}$. Based on this finding, we concluded that precipitation was not the dominant driver of $\delta^{13}\text{C}$ within the record, and used other proxies and records from the western equatorial Pacific to develop an interpretation for Sulawesi $\delta^{13}\text{C}$. It was determined that Sulawesi $\delta^{13}\text{C}$ was most likely a record of vegetation productivity, driven by changes in atmospheric CO_2 concentration and regional temperature.

This analysis was taken a step further by exploring the role of tropical vegetation in driving the glacial atmospheric methane budget. A strong covariance between Sulawesi $\delta^{13}\text{C}$ and atmospheric methane concentrations as recorded in high-latitude ice cores was evident, particularly during the glacial period. It was therefore hypothesised that the tropics was a key source of atmospheric methane during this period.

3.b. Did the tropics play a role in driving the glacial atmospheric methane budget?

In chapter four, we built upon the conclusions of chapter three to test the hypothesis of a tropical driver of the glacial methane budget using the Sheffield Dynamic Global Vegetation Model (SDGVM), coupled to HadCM3. The use of a global climate model allowed us to show that the Sulawesi speleothem $\delta^{13}\text{C}$ record is likely representative of the wider tropics. We show that local, regional and tropical methane emissions, as modelled by the SDGVM, correlate well with the Sulawesi speleothem $\delta^{13}\text{C}$ supporting the interpretation of this record as a proxy for the tropical contribution to the atmospheric methane budget. During the glacial period, when boreal methane sources

were largely dormant, tropical vegetation likely became the dominant driver of the atmospheric methane budget.

Future work

The conclusions presented in this thesis have been tested and explored within the limits of available data, but would benefit from further investigation. We have here identified three questions arising from this thesis that particularly warrant further investigation:

1. What is the response of the Indo-Australian winter monsoon to North Atlantic Heinrich events?

Modelling of simulated Heinrich events carried out in chapter one has identified the potential for their climatic impacts to penetrate into the equatorial core of the Australasian monsoon region during the boreal summer months. The Sulawesi speleothem records produced for this thesis record changes in western equatorial Pacific hydroclimate during the austral summer, but the strong seasonality at the study site excludes extensive exploration of hydroclimate changes occurring during the local dry season. Future work that targets speleothems from southeast Sulawesi that are sensitive to the winter monsoon would assist in the understanding of the seasonality of Heinrich events across this region.

2. What is the influence of low atmospheric CO₂ concentrations on model sensitivity to a simulated Heinrich event?

In this thesis, we tested the influence of high atmospheric CO₂ (400 ppm) and pre-industrial CO₂ (280 ppm) on the modelled climate sensitivity to a simulated Heinrich event. Given that Heinrich events occurred predominantly during the low atmospheric CO₂ conditions of the glacial period (~180 ppm) it would be useful to test the influence of low atmospheric CO₂ conditions on the modelled climate response to a Heinrich event. This experiment was originally intended for inclusion within this thesis, however model runs proved to be highly unstable and were not able to be completed within the timeframe of this work. Further work on these climate experiments would provide further insight into the climate response to Heinrich events recorded by multiple proxies.

3. What are the above-cave and karst processes that result in a vegetation productivity signal within speleothems?

Although we identify vegetation productivity as the key driver of Sulawesi speleothem $\delta^{13}\text{C}$, exploration of the processes that transmit this signal into the stalagmite is outside the scope of this thesis. Karst hydrology and/or soil geochemistry modelling could be used to investigate the processes by which infiltrating surface waters develop and maintain a vegetation signal that is then transmitted into the cave. Monitoring of soil chemistry and CO_2 concentrations may also help to improve our understanding of the processes involved above the cave system and help to constrain future karst modelling.

APPENDIX

This appendix contains:

Table A1: Summary of ^{230}Th data for stalagmites GB09-3 and GB11-9	212
Table A2: Summary of stalagmite GB09-3 isotope data	215
Table A3: Summary of stalagmite GB11-9 isotope data	236
Table A4: Summary of stalagmite GB09-3 trace element data	245

Table A1

Summary of ^{230}Th data for stalagmites GB09-3 and GB11-9

Acknowledgements: Stalagmite dates and age models were produced collaboratively with John Hellstrom, Hai Cheng and R. Lawrence Edwards

Sample I.D.	Depth (mm)	U (ppb)	$^{230}\text{Th}/^{238}\text{U}^*$	± 2 se	$^{234}\text{U}/^{238}\text{U}^*$	± 2 se	$^{232}\text{Th}/^{238}\text{U}^*$	± 2 se	$^{230}\text{Th}/^{232}\text{Th}^*$	Age (kyr BP) uncorr.	Age (kyr BP) corr. [†]	± 2 se	Corr. initial $^{234}\text{U}/^{238}\text{U}^*$	± 2 se
GB09-3-2 ³³	0	149	0.0121	0.0008	1.0688	0.0034	0.005017	0.000193	2.4	1.24	-0.31	0.40	1.0687	0.0033
GB09-3-uA1	29	220	0.0169	0.0006	1.0552	0.0032	0.002882	0.000017	5.9	1.76	0.87	0.23	1.0554	0.0032
GB09-3-uA2	53	161	0.0309	0.0031	1.0499	0.0037	0.003540	0.000030	8.7	3.25	2.15	0.44	1.0502	0.0037
GB09-3-uA3	92	189	0.0582	0.0012	1.0383	0.0023	0.003603	0.000054	16.1	6.27	5.16	0.32	1.0389	0.0023
GB09-3-uA4	124	217	0.0671	0.0013	1.0392	0.0027	0.003475	0.000053	19.3	7.25	6.18	0.31	1.0399	0.0028
GB09-3-uA1 [‡]	137	81	0.0685	0.0007	1.0541	0.0020	0.002118	0.000053	32.3	7.32	6.67	0.19	1.0551	0.0021
GB09-3-uA5	140	210	0.0682	0.0006	1.0441	0.0021	0.001464	0.000017	46.6	7.34	6.91	0.13	1.0450	0.0022
GB09-3-uA6	150	162	0.0711	0.0058	1.0375	0.0036	0.002748	0.000053	25.9	7.71	6.88	0.68	1.0383	0.0037
GB09-3-uB1	174	168	0.0841	0.0014	1.0370	0.0029	0.002766	0.000031	30.4	9.19	8.35	0.27	1.0379	0.0030
GB09-3-uB2	184	179	0.0854	0.0011	1.0448	0.0026	0.001201	0.000010	71.1	9.27	8.93	0.16	1.0459	0.0027
GB09-3-uB3	197	194	0.0891	0.0017	1.0417	0.0023	0.000485	0.000010	183.8	9.72	9.61	0.20	1.0428	0.0024
GB09-3-uC1	220	154	0.0989	0.0010	1.0396	0.0028	0.001208	0.000012	81.9	10.86	10.53	0.15	1.0408	0.0029

Sample I.D.	Depth (mm)	U (ppb)	$^{230}\text{Th}/^{238}\text{U}^*$	± 2 se	$^{234}\text{U}/^{238}\text{U}^*$	± 2 se	$^{232}\text{Th}/^{238}\text{U}^*$	± 2 se	$^{230}\text{Th}/^{232}\text{Th}^*$	Age (kyr BP) uncorr.	Age (kyr BP) corr. [†]	± 2 se	Corr. initial $^{234}\text{U}/^{238}\text{U}^*$	± 2 se
GB09-3-uC1 [‡]	261	105	0.1128	0.0006	1.0687	0.0014	0.001179	0.000025	95.6	12.14	11.81	0.11	1.0710	0.0014
GB09-3-uC1b	273	158	0.1247	0.0022	1.0691	0.0041	0.003221	0.000010	38.7	13.47	12.54	0.36	1.0716	0.0042
GB09-3-uC2	277	161	0.1351	0.0010	1.0527	0.0026	0.007376	0.000103	18.3	14.92	12.66	0.60	1.0546	0.0027
GB09-3-uC3	286	147	0.1244	0.0019	1.0662	0.0044	0.002667	0.000038	46.6	13.48	12.71	0.31	1.0686	0.0046
GB09-3-uC4	306	168	0.1343	0.0014	1.0719	0.0026	0.001229	0.000016	109.3	14.54	14.22	0.19	1.0749	0.0027
GB09-3-uC2 [‡]	314	89	0.1363	0.0005	1.0773	0.0013	0.000975	0.000020	139.8	14.73	14.45	0.10	1.0805	0.0013
GB09-3-uC5	331	153	0.1526	0.0038	1.0665	0.0034	0.002946	0.000033	51.8	16.77	15.93	0.51	1.0696	0.0035
GB09-3-uC6	364	196	0.1673	0.0026	1.0688	0.0036	0.001231	0.000016	135.9	18.48	18.18	0.34	1.0724	0.0038
GB09-3-uC7	379	174	0.1793	0.0011	1.0697	0.0025	0.001350	0.000016	132.8	19.92	19.58	0.18	1.0737	0.0026
GB09-3-uC3 [‡]	396	84	0.1933	0.0006	1.0854	0.0013	0.002141	0.000044	90.3	21.33	20.72	0.18	1.0906	0.0014
GB09-3-uC8	400	167	0.1912	0.0015	1.0783	0.0030	0.001903	0.000046	100.5	21.18	20.69	0.25	1.0830	0.0032
GB09-3-uC9	435	229	0.2084	0.0034	1.0745	0.0023	0.001418	0.000022	147.0	23.38	23.06	0.44	1.0795	0.0025
GB09-3-uD0	443	177	0.2279	0.0024	1.0878	0.0040	0.003676	0.000006	62.0	25.48	24.48	0.42	1.0941	0.0043
GB09-3-uD1	459	160	0.2290	0.0015	1.0751	0.0025	0.001771	0.000016	129.3	25.98	25.54	0.25	1.0807	0.0027
GB09-3-uD2	482	169	0.2444	0.0014	1.0713	0.0026	0.001675	0.000014	145.8	28.07	27.68	0.24	1.0771	0.0028
GB09-3-uD3	512	133	0.2647	0.0026	1.0764	0.0047	0.000845	0.000002	313.3	30.59	30.45	0.39	1.0832	0.0051
GB09-3-uD4	526	160	0.2743	0.0025	1.0752	0.0046	0.003029	0.000007	90.6	31.92	31.13	0.44	1.0821	0.0050
GB09-3-uD5	547	136	0.2790	0.0027	1.0765	0.0043	0.001375	0.000005	202.8	32.50	32.22	0.41	1.0838	0.0046
<i>GB09-3-uD6[§]</i>	<i>569</i>	<i>492</i>	<i>0.4131</i>	<i>0.0038</i>	<i>1.0732</i>	<i>0.0052</i>	<i>0.047817</i>	<i>0.000175</i>	<i>8.6</i>	<i>52.53</i>	<i>37.20</i>	<i>4.23</i>	<i>1.0813</i>	<i>0.0058</i>
GB09-3-uD7	591	187	0.2945	0.0030	1.0756	0.0046	0.001493	0.000004	197.2	34.65	34.34	0.47	1.0833	0.0051

Sample I.D.	Depth (mm)	U (ppb)	$^{230}\text{Th}/^{238}\text{U}^*$	± 2 se	$^{234}\text{U}/^{238}\text{U}^*$	± 2 se	$^{232}\text{Th}/^{238}\text{U}^*$	± 2 se	$^{230}\text{Th}/^{232}\text{Th}^*$	Age (kyr BP) uncorr.	Age (kyr BP) corr. [†]	± 2 se	Corr. initial $^{234}\text{U}/^{238}\text{U}^*$	± 2 se
GB09-3-uE1	612	150	0.3042	0.0025	1.0738	0.0046	0.001307	0.000003	232.8	36.07	35.83	0.41	1.0817	0.0050
GB09-3-uE2	630	136	0.3095	0.0021	1.0760	0.0046	0.000377	0.000003	819.9	36.73	36.77	0.36	1.0843	0.0051
GB09-3-uE3	658	171	0.3183	0.0021	1.0783	0.0045	0.000462	0.000003	689.1	37.87	37.89	0.36	1.0872	0.0049
GB09-3-1 [‡]	693	190	0.3340	0.0008	1.0745	0.0010	0.001632	0.000005	204.6	40.46	39.97	0.18	1.0834	0.0011
GB11-9-2	0	147	0.2140	0.0013	1.0018	0.0043	0.000398	0.000004	100.2	26.24	26.11	0.23	1.0019	0.0047
GB11-9-uA-1	29	157	0.2213	0.0024	0.9998	0.0033	0.000082	0.000003	2686.7	27.21	27.29	0.35	0.9998	0.0036
GB11-9-uA-2	66	173	0.2400	0.0015	1.0025	0.0031	0.000070	0.000005	3407.0	29.76	29.85	0.24	1.0027	0.0034
GB11-9-uA-3	78	155	0.2494	0.0034	1.0024	0.0037	0.000088	0.000007	2846.3	31.11	31.20	0.51	1.0026	0.0040
GB11-9-uA-4	100	172	0.2577	0.0016	0.9983	0.0031	0.000050	0.000002	5189.6	32.48	32.59	0.26	0.9981	0.0033
GB11-9-uA-5	153	181	0.2848	0.0019	0.9977	0.0028	0.000064	0.000004	4474.3	36.56	36.69	0.32	0.9975	0.0031
GB11-9-uA-6	194	149	0.3066	0.0020	0.9993	0.0025	0.000138	0.000003	2221.0	39.86	39.97	0.34	0.9992	0.0028
GB11-9-uA-7	225	162	0.3193	0.0018	0.9972	0.0045	0.000016	0.000003	3822.6	42.16	42.15	0.38	0.9968	0.0051

“Depth (mm)” refers to the distance (from the top of the stalagmite), along the sampling track

“Age (kyr BP)” gives ages in thousands of years before the present, with present defined as the year 1950 CE

* Values are activity ratios

† Corrected ^{230}Th ages, assuming an initial $^{230}\text{Th}/^{232}\text{Th}$ ratio of 3.0 ± 0.75

‡ Dates measured at the University of Minnesota (Cheng, Edwards). All other dates were measured at the University of Melbourne (Hellstrom)

§ Dates not included in the final age model

Table A2

Summary of stalagmite GB09-3 isotope data

Note that “ $\delta^{18}\text{O}$ corr” refers to the ice volume corrected $\delta^{18}\text{O}$ values. Where applicable, isotope values shown equal the mean of replicate measurements.

Sample ID	Depth (mm)	Age (kyr BP)	$\delta^{18}\text{O}$ (‰VPDB)	$\delta^{18}\text{O}$ corr (‰)	$\delta^{13}\text{C}$ (‰VPDB)
GB09-3-A1	0.00	0.03	-8.79	-8.80	-8.60
GB09-3-A2	1.20	0.06	-8.81	-8.83	-7.79
GB09-3-A3	2.40	0.09	-8.60	-8.61	-8.05
GB09-3-A4	3.60	0.13	-8.75	-8.76	-7.56
GB09-3-A5	4.80	0.16	-8.65	-8.67	-7.52
GB09-3-A6	6.00	0.19	-8.47	-8.49	-7.94
GB09-3-A7	7.20	0.22	-8.94	-8.96	-7.60
GB09-3-A8	8.40	0.25	-8.78	-8.79	-7.89
GB09-3-A9	9.60	0.28	-9.00	-9.01	-8.10
GB09-3-A10	10.80	0.31	-8.95	-8.96	-7.94
GB09-3-A11	12.00	0.34	-8.62	-8.63	-8.10
GB09-3-A12	13.20	0.37	-8.88	-8.90	-8.03
GB09-3-A13	14.40	0.40	-9.04	-9.06	-7.95
GB09-3-A14	15.60	0.43	-8.97	-8.98	-7.61
GB09-3-A15	16.80	0.46	-9.06	-9.07	-7.73
GB09-3-A16	18.00	0.49	-8.67	-8.69	-7.84
GB09-3-A17	19.20	0.52	-8.71	-8.73	-7.98
GB09-3-A18	20.40	0.55	-8.98	-8.99	-7.92
GB09-3-A19	21.60	0.58	-9.11	-9.12	-7.97
GB09-3-A20	22.80	0.61	-9.20	-9.21	-8.04
GB09-3-A21	24.00	0.65	-8.72	-8.74	-7.91
GB09-3-A22	25.20	0.68	-9.17	-9.18	-7.95
GB09-3-A23	26.40	0.72	-9.09	-9.10	-7.89
GB09-3-A24	27.60	0.76	-9.32	-9.34	-8.13
GB09-3-A25	28.80	0.80	-9.20	-9.22	-8.31
GB09-3-A26	30.00	0.87	-9.23	-9.25	-8.14
GB09-3-A27	31.20	0.94	-9.04	-9.05	-8.07
GB09-3-A28	32.40	1.00	-9.07	-9.09	-8.02
GB09-3-A29	33.60	1.07	-8.90	-8.91	-8.02
GB09-3-A30	34.80	1.13	-9.05	-9.07	-7.47
GB09-3-A31	36.00	1.19	-9.14	-9.16	-7.84
GB09-3-A32	37.20	1.25	-9.28	-9.30	-7.75
GB09-3-A33	38.40	1.31	-9.30	-9.31	-8.09

Sample ID	Depth (mm)	Age (kyr BP)	$\delta^{18}\text{O}$ (‰VPDB)	$\delta^{18}\text{O}$ corr (‰)	$\delta^{13}\text{C}$ (‰VPDB)
GB09-3-A34	39.60	1.36	-9.05	-9.07	-8.05
GB09-3-A35	40.80	1.43	-8.97	-8.99	-8.49
GB09-3-A36	42.00	1.49	-9.11	-9.13	-8.25
GB09-3-A37	43.20	1.55	-9.03	-9.05	-8.66
GB09-3-A38	44.40	1.61	-8.85	-8.87	-8.22
GB09-3-A39	45.60	1.67	-9.27	-9.29	-8.00
GB09-3-A40	46.80	1.73	-9.13	-9.15	-7.86
GB09-3-A41	48.00	1.79	-9.24	-9.26	-7.61
GB09-3-A42	49.20	1.86	-9.60	-9.63	-7.39
GB09-3-A43	50.40	1.93	-9.46	-9.48	-7.81
GB09-3-A44	51.60	2.00	-9.58	-9.60	-7.63
GB09-3-A45	52.80	2.08	-9.17	-9.19	-7.66
GB09-3-A46	54.00	2.18	-9.25	-9.27	-7.66
GB09-3-A47	55.20	2.28	-9.28	-9.31	-7.42
GB09-3-A48	56.40	2.38	-9.30	-9.33	-7.02
GB09-3-A49	57.60	2.48	-9.37	-9.40	-7.81
GB09-3-A50	58.80	2.58	-9.28	-9.31	-7.77
GB09-3-A51	60.00	2.67	-9.42	-9.45	-7.60
GB09-3-A52	61.20	2.75	-9.29	-9.32	-7.92
GB09-3-A53	62.40	2.84	-9.40	-9.42	-7.56
GB09-3-A54	63.60	2.93	-9.50	-9.53	-7.40
GB09-3-A55	64.80	3.01	-9.06	-9.08	-7.39
GB09-3-A56	66.00	3.10	-9.18	-9.21	-7.34
GB09-3-A57	67.20	3.18	-9.16	-9.19	-7.66
GB09-3-A58	68.40	3.27	-9.24	-9.27	-7.83
GB09-3-A59	69.60	3.35	-9.36	-9.39	-7.04
GB09-3-A60	70.80	3.44	-9.30	-9.34	-7.25
GB09-3-A61	72.00	3.52	-9.26	-9.29	-7.95
GB09-3-A62	73.20	3.61	-9.02	-9.06	-7.32
GB09-3-A63	74.40	3.70	-9.14	-9.17	-6.93
GB09-3-A64	75.60	3.78	-9.21	-9.25	-7.39
GB09-3-A65	76.80	3.87	-9.42	-9.46	-7.98
GB09-3-A66	78.00	3.95	-9.15	-9.19	-7.50
GB09-3-A67	79.20	4.04	-9.37	-9.41	-7.92
GB09-3-A68	80.40	4.12	-9.43	-9.46	-7.95
GB09-3-A69	81.60	4.21	-9.17	-9.21	-7.41
GB09-3-A70	82.80	4.29	-9.56	-9.60	-7.65

Sample ID	Depth (mm)	Age (kyr BP)	$\delta^{18}\text{O}$ (‰VPDB)	$\delta^{18}\text{O}$ corr (‰)	$\delta^{13}\text{C}$ (‰VPDB)
GB09-3-A71	84.00	4.38	-9.20	-9.24	-7.94
GB09-3-A72	85.20	4.47	-9.75	-9.79	-7.77
GB09-3-A73	86.40	4.56	-9.49	-9.53	-7.57
GB09-3-A74	87.60	4.65	-9.40	-9.44	-7.18
GB09-3-A75	88.80	4.75	-9.36	-9.40	-7.31
GB09-3-A76	90.00	4.85	-9.20	-9.25	-7.04
GB09-3-A77	91.20	4.95	-9.37	-9.42	-7.03
GB09-3-A78	108.00	5.57	-9.25	-9.31	-7.05
GB09-3-A79	92.40	5.03	-9.26	-9.31	-6.91
GB09-3-A80	93.60	5.09	-9.12	-9.17	-7.32
GB09-3-A81	94.80	5.14	-9.21	-9.26	-7.14
GB09-3-A82	96.00	5.18	-9.35	-9.40	-6.90
GB09-3-A83	97.20	5.23	-9.47	-9.52	-6.86
GB09-3-A84	98.40	5.27	-9.45	-9.50	-7.09
GB09-3-A85	99.60	5.30	-9.26	-9.31	-7.14
GB09-3-A86	100.80	5.34	-9.18	-9.23	-6.80
GB09-3-A87	102.00	5.38	-9.50	-9.55	-7.55
GB09-3-A88	103.20	5.42	-9.48	-9.53	-7.73
GB09-3-A89	104.40	5.46	-9.49	-9.55	-7.05
GB09-3-A90	105.60	5.49	-9.42	-9.47	-7.03
GB09-3-A91	106.80	5.53	-9.58	-9.64	-6.55
GB09-3-A78	108.00	5.57	-9.25	-9.31	-7.05
GB09-3-A92	109.20	5.60	-9.34	-9.40	-6.46
GB09-3-A93	110.40	5.64	-9.73	-9.79	-6.63
GB09-3-A94	111.60	5.68	-9.61	-9.67	-6.28
GB09-3-A95	112.80	5.71	-9.44	-9.50	-6.01
GB09-3-A96	114.00	5.75	-9.82	-9.89	-6.83
GB09-3-A97	115.20	5.79	-9.69	-9.75	-6.55
GB09-3-A98	116.40	5.83	-9.64	-9.70	-6.53
GB09-3-A99	117.60	5.87	-9.69	-9.75	-6.47
GB09-3-A100	118.80	5.91	-9.63	-9.70	-6.23
GB09-3-A101	120.00	5.95	-9.48	-9.55	-6.70
GB09-3-A102	121.20	5.99	-9.32	-9.39	-6.51
GB09-3-A103	122.40	6.04	-9.41	-9.48	-6.78
GB09-3-A104	123.60	6.09	-9.39	-9.46	-6.43
GB09-3-A105	124.80	6.15	-9.31	-9.38	-6.49
GB09-3-A106	126.00	6.20	-9.16	-9.24	-6.35

Sample ID	Depth (mm)	Age (kyr BP)	$\delta^{18}\text{O}$ (‰VPDB)	$\delta^{18}\text{O}$ corr (‰)	$\delta^{13}\text{C}$ (‰VPDB)
GB09-3-A107	127.20	6.25	-9.16	-9.23	-6.40
GB09-3-A108	128.40	6.30	-9.22	-9.29	-6.41
GB09-3-A109	129.60	6.34	-9.22	-9.29	-6.27
GB09-3-A110	130.80	6.39	-9.32	-9.39	-6.17
GB09-3-A111	132.00	6.44	-9.18	-9.26	-6.77
GB09-3-A112	133.20	6.48	-9.03	-9.11	-6.99
GB09-3-A113	134.40	6.53	-8.98	-9.06	-7.10
GB09-3-A114	135.60	6.59	-9.02	-9.10	-7.15
GB09-3-A115	136.80	6.64	-8.88	-8.96	-6.57
GB09-3-A116	138.00	6.71	-9.04	-9.12	-6.73
GB09-3-A117	139.20	6.78	-9.36	-9.44	-6.53
GB09-3-A118	140.40	6.84	-9.13	-9.21	-6.41
GB09-3-A119	141.60	6.88	-9.16	-9.25	-7.04
GB09-3-A120	142.80	6.91	-9.50	-9.59	-6.73
GB09-3-A121	144.00	6.93	-9.42	-9.50	-6.66
GB09-3-A122	145.20	6.96	-9.17	-9.26	-6.64
GB09-3-A123	146.40	6.99	-9.34	-9.42	-7.25
GB09-3-A124	147.60	7.01	-9.20	-9.29	-6.72
GB09-3-A125	148.80	7.04	-9.26	-9.35	-6.39
GB09-3-A126	150.00	7.09	-9.42	-9.50	-6.37
GB09-3-A127	151.20	7.15	-9.34	-9.43	-6.13
GB09-3-A128	152.40	7.22	-9.37	-9.46	-5.87
GB09-3-A129	153.60	7.28	-9.67	-9.76	-6.29
GB09-3-A130	154.80	7.34	-9.44	-9.54	-6.08
GB09-3-A131	156.00	7.40	-9.33	-9.42	-6.00
GB09-3-A132	157.20	7.46	-9.22	-9.32	-5.93
GB09-3-A133	158.40	7.52	-9.37	-9.47	-5.91
GB09-3-A134	159.60	7.57	-9.37	-9.47	-5.76
GB09-3-A135	160.80	7.63	-9.40	-9.50	-6.19
GB09-3-A136	162.00	7.69	-9.36	-9.47	-6.08
GB09-3-A137	163.20	7.74	-9.35	-9.45	-6.27
GB09-3-A138	164.40	7.80	-9.29	-9.40	-6.30
GB09-3-B1	165.60	7.86	-9.32	-9.43	-6.56
GB09-3-B2	166.80	7.91	-9.38	-9.49	-6.56
GB09-3-B3	168.00	7.97	-9.26	-9.37	-6.24
GB09-3-B4	169.20	8.03	-9.39	-9.50	-6.30
GB09-3-B5	170.40	8.09	-9.22	-9.33	-6.62

Sample ID	Depth (mm)	Age (kyr BP)	$\delta^{18}\text{O}$ (‰VPDB)	$\delta^{18}\text{O}$ corr (‰)	$\delta^{13}\text{C}$ (‰VPDB)
GB09-3-B6	171.60	8.16	-9.21	-9.33	-6.36
GB09-3-B7	172.80	8.23	-8.97	-9.09	-6.45
GB09-3-B8	174.00	8.30	-8.64	-8.76	-6.59
GB09-3-B9	175.20	8.38	-8.54	-8.67	-6.75
GB09-3-B10	176.40	8.45	-8.35	-8.48	-6.82
GB09-3-B11	177.60	8.52	-8.57	-8.70	-7.12
GB09-3-B12	178.80	8.59	-8.62	-8.75	-7.12
GB09-3-B13	180.00	8.66	-8.47	-8.60	-6.80
GB09-3-B14	181.20	8.72	-8.44	-8.58	-6.54
GB09-3-B15	182.40	8.79	-8.14	-8.28	-6.73
GB09-3-B16	183.60	8.87	-8.16	-8.30	-7.09
GB09-3-B17	184.80	8.93	-7.94	-8.09	-7.41
GB09-3-B18	186.00	9.00	-8.36	-8.51	-7.42
GB09-3-B19	187.20	9.07	-8.33	-8.48	-7.29
GB09-3-B20	188.40	9.13	-7.97	-8.13	-7.20
GB09-3-B21	189.60	9.19	-8.02	-8.18	-7.45
GB09-3-B22	190.80	9.25	-8.19	-8.36	-7.14
GB09-3-B23	192.00	9.31	-8.04	-8.20	-7.30
GB09-3-B24	193.20	9.37	-8.30	-8.47	-7.28
GB09-3-B25	194.40	9.43	-8.05	-8.22	-7.12
GB09-3-B26	195.60	9.50	-7.83	-8.01	-6.99
GB09-3-B27	196.80	9.56	-8.06	-8.24	-7.24
GB09-3-B28	198.00	9.63	-7.99	-8.18	-7.12
GB09-3-B29	199.20	9.68	-8.29	-8.48	-7.37
GB09-3-B30	200.20	9.72	-7.90	-8.09	-7.25
GB09-3-B31	201.20	9.76	-7.81	-8.01	-7.03
GB09-3-B32	202.20	9.80	-7.71	-7.91	-6.79
GB09-3-C1	203.20	9.84	-8.29	-8.49	-7.17
GB09-3-C2	204.20	9.88	-8.14	-8.35	-7.28
GB09-3-C3	205.20	9.92	-8.07	-8.27	-7.89
GB09-3-C4	206.20	9.95	-7.96	-8.17	-7.85
GB09-3-C5	207.20	9.99	-7.65	-7.86	-7.63
GB09-3-C6	208.20	10.03	-7.96	-8.18	-8.08
GB09-3-C7	209.20	10.06	-7.86	-8.08	-7.95
GB09-3-C8	210.20	10.10	-7.88	-8.10	-7.37
GB09-3-C9	211.20	10.14	-7.54	-7.77	-7.41
GB09-3-C10	212.20	10.18	-7.56	-7.79	-8.18

Sample ID	Depth (mm)	Age (kyr BP)	$\delta^{18}\text{O}$ (‰VPDB)	$\delta^{18}\text{O}$ corr (‰)	$\delta^{13}\text{C}$ (‰VPDB)
GB09-3-C11	213.20	10.21	-7.58	-7.81	-7.76
GB09-3-C12	214.20	10.25	-7.26	-7.48	-7.82
GB09-3-C13	215.20	10.29	-7.86	-8.09	-7.98
GB09-3-C14	216.20	10.33	-7.43	-7.66	-8.39
GB09-3-C15	217.20	10.37	-7.41	-7.64	-8.39
GB09-3-C16	218.20	10.41	-7.44	-7.68	-7.73
GB09-3-C17	219.20	10.45	-7.44	-7.69	-7.63
GB09-3-C18	220.20	10.49	-7.13	-7.38	-8.67
GB09-3-C19	221.20	10.53	-7.30	-7.55	-8.25
GB09-3-C20	222.20	10.57	-7.21	-7.46	-8.25
GB09-3-C21	223.20	10.61	-7.52	-7.78	-8.22
GB09-3-C22	224.20	10.64	-7.40	-7.66	-7.78
GB09-3-C23	225.20	10.67	-7.34	-7.60	-8.19
GB09-3-C24	226.20	10.71	-7.48	-7.74	-8.20
GB09-3-C25	227.20	10.74	-7.39	-7.66	-7.96
GB09-3-C26	228.20	10.77	-7.27	-7.54	-8.06
GB09-3-C27	229.20	10.80	-7.45	-7.72	-7.97
GB09-3-C28	230.20	10.83	-7.32	-7.59	-8.14
GB09-3-C29	231.20	10.86	-7.32	-7.61	-8.42
GB09-3-C30	232.20	10.89	-7.28	-7.56	-8.48
GB09-3-C31	233.20	10.92	-6.93	-7.22	-8.60
GB09-3-C32	234.20	10.95	-6.93	-7.22	-8.54
GB09-3-C33	235.20	10.98	-6.87	-7.16	-8.31
GB09-3-C34	236.20	11.01	-6.93	-7.23	-8.30
GB09-3-C35	237.20	11.04	-6.64	-6.94	-8.43
GB09-3-C36	238.20	11.07	-7.11	-7.41	-7.93
GB09-3-C37	239.20	11.10	-6.74	-7.05	-8.11
GB09-3-C38	240.20	11.13	-7.10	-7.41	-8.18
GB09-3-C39	241.20	11.16	-6.84	-7.15	-8.00
GB09-3-C40	242.20	11.19	-6.60	-6.92	-7.95
GB09-3-C41	243.20	11.22	-6.86	-7.18	-8.28
GB09-3-C42	244.20	11.25	-6.96	-7.28	-8.00
GB09-3-C43	245.20	11.28	-6.67	-7.00	-8.08
GB09-3-C44	246.20	11.31	-6.41	-6.74	-8.51
GB09-3-C45	247.20	11.34	-6.34	-6.67	-8.76
GB09-3-C46	248.20	11.37	-6.47	-6.81	-8.41
GB09-3-C47	249.20	11.40	-6.56	-6.90	-8.41

Sample ID	Depth (mm)	Age (kyr BP)	$\delta^{18}\text{O}$ (‰VPDB)	$\delta^{18}\text{O}$ corr (‰)	$\delta^{13}\text{C}$ (‰VPDB)
GB09-3-C48	250.20	11.43	-6.47	-6.81	-8.39
GB09-3-C49	251.20	11.46	-6.46	-6.80	-8.48
GB09-3-C50	252.20	11.49	-6.25	-6.61	-8.43
GB09-3-C51	253.20	11.52	-6.50	-6.86	-8.39
GB09-3-C52	254.20	11.55	-6.09	-6.45	-8.39
GB09-3-C53	255.20	11.58	-6.05	-6.41	-8.53
GB09-3-C54	256.20	11.62	-6.03	-6.40	-7.95
GB09-3-C55	257.20	11.65	-6.22	-6.59	-8.10
GB09-3-C56	258.20	11.68	-6.11	-6.48	-7.55
GB09-3-C57	259.20	11.72	-6.13	-6.51	-7.25
GB09-3-C58	260.20	11.75	-6.28	-6.67	-7.66
GB09-3-C59	261.20	11.80	-5.90	-6.29	-7.14
GB09-3-C60	262.20	11.84	-6.17	-6.57	-7.26
GB09-3-C61	263.20	11.89	-6.04	-6.45	-7.11
GB09-3-C62	264.20	11.93	-5.98	-6.39	-6.98
GB09-3-C63	265.20	11.98	-6.22	-6.64	-7.31
GB09-3-C64	266.20	12.02	-6.36	-6.78	-7.22
GB09-3-C65	267.20	12.06	-5.98	-6.41	-6.94
GB09-3-C66	268.20	12.10	-6.23	-6.67	-7.19
GB09-3-C67	269.20	12.15	-6.13	-6.57	-7.00
GB09-3-C68	270.20	12.19	-6.32	-6.76	-7.19
GB09-3-C69	271.20	12.23	-6.00	-6.44	-6.96
GB09-3-C70	272.20	12.28	-6.20	-6.65	-7.22
GB09-3-C71	273.20	12.32	-5.69	-6.15	-6.69
GB09-3-C72	274.20	12.36	-5.79	-6.26	-6.95
GB09-3-C73	275.20	12.39	-5.63	-6.10	-6.77
GB09-3-C74	276.20	12.43	-6.31	-6.78	-7.04
GB09-3-C75	277.20	12.46	-6.26	-6.74	-6.92
GB09-3-C76	278.20	12.49	-6.10	-6.59	-6.85
GB09-3-C77	279.20	12.52	-6.20	-6.68	-7.20
GB09-3-C78	280.20	12.55	-6.34	-6.83	-6.96
GB09-3-C79	281.20	12.58	-6.34	-6.83	-7.12
GB09-3-C80	282.20	12.60	-6.37	-6.87	-7.43
GB09-3-C81	283.20	12.63	-6.02	-6.52	-7.11
GB09-3-C82	284.20	12.66	-6.46	-6.97	-6.86
GB09-3-C83	285.20	12.70	-6.30	-6.81	-7.38
GB09-3-C84	286.20	12.75	-6.25	-6.77	-7.15

Sample ID	Depth (mm)	Age (kyr BP)	$\delta^{18}\text{O}$ (‰VPDB)	$\delta^{18}\text{O}$ corr (‰)	$\delta^{13}\text{C}$ (‰VPDB)
GB09-3-C85	287.20	12.81	-6.29	-6.82	-6.96
GB09-3-C86	288.20	12.89	-6.15	-6.69	-6.76
GB09-3-C87	289.20	12.97	-6.03	-6.58	-6.98
GB09-3-C88	290.20	13.04	-5.75	-6.32	-6.62
GB09-3-C89	291.20	13.11	-5.86	-6.43	-6.93
GB09-3-C90	292.20	13.18	-5.71	-6.29	-6.59
GB09-3-C91	293.20	13.25	-5.59	-6.18	-6.67
GB09-3-C92	294.20	13.32	-5.73	-6.33	-6.66
GB09-3-C93	295.20	13.39	-5.88	-6.49	-6.91
GB09-3-C94	296.20	13.46	-5.87	-6.49	-6.92
GB09-3-C95	297.20	13.53	-5.66	-6.28	-6.55
GB09-3-C96	298.20	13.59	-5.77	-6.40	-6.48
GB09-3-C97	299.20	13.66	-5.65	-6.30	-6.35
GB09-3-C98	300.20	13.73	-5.30	-5.95	-6.57
GB09-3-C99	301.20	13.81	-5.71	-6.37	-6.59
GB09-3-C100	302.20	13.88	-5.61	-6.28	-6.92
GB09-3-C101	303.20	13.95	-5.96	-6.65	-6.59
GB09-3-C102	304.20	14.03	-5.53	-6.22	-6.45
GB09-3-C103	305.20	14.10	-5.55	-6.25	-6.85
GB09-3-C104	306.20	14.16	-5.48	-6.19	-6.74
GB09-3-C105	307.20	14.21	-5.67	-6.38	-6.64
GB09-3-C106	308.20	14.25	-5.54	-6.26	-6.43
GB09-3-C107	309.20	14.28	-5.52	-6.24	-6.18
GB09-3-C108	310.20	14.31	-5.39	-6.11	-6.07
GB09-3-C109	311.20	14.34	-5.57	-6.30	-6.24
GB09-3-C110	312.20	14.37	-5.49	-6.22	-6.42
GB09-3-C111	313.20	14.41	-5.30	-6.04	-6.19
GB09-3-C112	314.00	14.45	-5.28	-6.03	-6.34
GB09-3-C113	314.80	14.50	-5.43	-6.18	-6.40
GB09-3-C114	315.60	14.57	-5.62	-6.38	-6.10
GB09-3-C115	316.40	14.63	-5.62	-6.39	-5.70
GB09-3-C116	317.20	14.70	-5.90	-6.67	-5.42
GB09-3-C117	318.00	14.77	-6.15	-6.93	-5.58
GB09-3-C118	318.80	14.83	-5.85	-6.64	-5.58
GB09-3-C119	319.60	14.89	-5.88	-6.68	-5.45
GB09-3-C120	320.40	14.96	-5.49	-6.29	-5.61
GB09-3-C121	321.20	15.02	-5.67	-6.48	-5.53

Sample ID	Depth (mm)	Age (kyr BP)	$\delta^{18}\text{O}$ (‰VPDB)	$\delta^{18}\text{O}$ corr (‰)	$\delta^{13}\text{C}$ (‰VPDB)
GB09-3-C122	322.00	15.08	-5.76	-6.58	-5.41
GB09-3-C123	322.80	15.15	-5.82	-6.64	-5.38
GB09-3-C124	323.60	15.21	-5.60	-6.43	-5.22
GB09-3-C125	324.40	15.27	-5.82	-6.65	-5.38
GB09-3-C126	325.20	15.33	-5.95	-6.79	-5.50
GB09-3-C127	326.00	15.39	-5.56	-6.41	-5.50
GB09-3-C128	326.80	15.46	-5.49	-6.34	-5.23
GB09-3-C129	327.60	15.52	-5.51	-6.37	-5.30
GB09-3-C130	328.40	15.59	-5.44	-6.31	-5.42
GB09-3-C131	329.20	15.66	-5.47	-6.34	-5.22
GB09-3-C132	330.00	15.73	-5.82	-6.71	-4.82
GB09-3-C133	330.80	15.81	-5.88	-6.77	-5.07
GB09-3-C134	331.60	15.88	-5.71	-6.60	-4.98
GB09-3-C135	332.40	15.95	-5.51	-6.41	-5.04
GB09-3-C136	333.20	16.02	-5.82	-6.73	-5.03
GB09-3-C137	334.00	16.08	-5.74	-6.66	-5.25
GB09-3-C138	334.80	16.14	-5.93	-6.85	-5.33
GB09-3-C139	335.60	16.20	-6.02	-6.95	-4.47
GB09-3-C140	336.40	16.26	-5.90	-6.83	-4.52
GB09-3-C141	337.20	16.32	-5.90	-6.84	-4.58
GB09-3-C142	338.00	16.37	-5.83	-6.77	-4.52
GB09-3-C143	338.80	16.43	-5.91	-6.86	-4.81
GB09-3-C144	339.60	16.48	-6.24	-7.19	-4.87
GB09-3-C145	340.40	16.54	-6.18	-7.13	-4.28
GB09-3-C146	341.20	16.59	-5.69	-6.64	-4.76
GB09-3-C147	342.00	16.64	-5.59	-6.55	-4.78
GB09-3-C148	342.80	16.69	-5.80	-6.76	-4.42
GB09-3-C149	343.60	16.75	-5.72	-6.69	-4.27
GB09-3-C150	344.40	16.80	-5.72	-6.69	-4.11
GB09-3-C151	345.20	16.85	-5.96	-6.93	-4.37
GB09-3-C152	346.00	16.90	-5.79	-6.76	-4.42
GB09-3-C153	346.80	16.96	-5.94	-6.91	-4.32
GB09-3-C154	347.60	17.01	-5.88	-6.86	-4.19
GB09-3-C155	348.40	17.06	-5.70	-6.68	-3.98
GB09-3-C156	349.20	17.12	-5.78	-6.76	-4.07
GB09-3-C157	350.00	17.17	-5.70	-6.68	-3.88
GB09-3-C158	350.80	17.22	-5.86	-6.85	-3.96

Sample ID	Depth (mm)	Age (kyr BP)	$\delta^{18}\text{O}$ (‰VPDB)	$\delta^{18}\text{O}$ corr (‰)	$\delta^{13}\text{C}$ (‰VPDB)
GB09-3-C159	351.60	17.28	-6.16	-7.15	-3.94
GB09-3-C160	352.40	17.33	-6.11	-7.11	-3.92
GB09-3-C161	353.20	17.38	-5.79	-6.79	-3.94
GB09-3-C162	354.00	17.43	-5.84	-6.84	-4.13
GB09-3-C163	354.80	17.49	-5.99	-6.99	-3.85
GB09-3-C164	355.60	17.54	-6.26	-7.27	-3.71
GB09-3-C165	356.40	17.59	-6.26	-7.27	-3.75
GB09-3-C166	357.20	17.65	-5.86	-6.87	-3.49
GB09-3-C167	358.00	17.70	-6.04	-7.05	-3.34
GB09-3-C168	358.80	17.76	-5.75	-6.76	-3.74
GB09-3-C169	359.60	17.82	-5.66	-6.68	-3.83
GB09-3-C170	360.40	17.88	-5.55	-6.57	-4.05
GB09-3-C171	361.20	17.94	-5.60	-6.62	-4.18
GB09-3-C172	362.00	18.01	-5.85	-6.87	-4.16
GB09-3-C173	362.80	18.07	-6.14	-7.17	-4.20
GB09-3-C174	363.60	18.14	-5.83	-6.86	-3.96
GB09-3-C175	364.40	18.21	-5.69	-6.72	-4.17
GB09-3-C176	365.20	18.29	-6.03	-7.06	-3.90
GB09-3-C177	366.00	18.37	-6.17	-7.20	-3.90
GB09-3-C178	366.80	18.44	-6.02	-7.05	-3.93
GB09-3-C179	367.60	18.52	-6.36	-7.39	-4.01
GB09-3-C180	368.40	18.59	-6.03	-7.06	-3.98
GB09-3-C181	369.20	18.66	-5.92	-6.95	-4.30
GB09-3-C182	370.00	18.73	-6.27	-7.30	-4.32
GB09-3-C183	370.80	18.79	-6.32	-7.35	-4.31
GB09-3-C184	371.60	18.86	-6.20	-7.24	-4.36
GB09-3-C185	372.40	18.93	-6.03	-7.06	-4.11
GB09-3-C186	373.20	19.00	-6.30	-7.34	-4.35
GB09-3-C187	374.00	19.07	-6.19	-7.22	-4.46
GB09-3-C188	374.80	19.14	-6.26	-7.29	-4.44
GB09-3-C189	375.60	19.22	-6.53	-7.56	-4.31
GB09-3-C190	376.40	19.29	-6.47	-7.51	-4.53
GB09-3-C191	377.20	19.36	-6.29	-7.33	-4.74
GB09-3-C192	378.00	19.44	-6.53	-7.57	-4.54
GB09-3-C193	378.80	19.51	-6.35	-7.38	-4.74
GB09-3-C194	379.60	19.58	-6.12	-7.15	-4.38
GB09-3-C195	380.40	19.63	-6.26	-7.29	-4.45

Sample ID	Depth (mm)	Age (kyr BP)	$\delta^{18}\text{O}$ (‰VPDB)	$\delta^{18}\text{O}$ corr (‰)	$\delta^{13}\text{C}$ (‰VPDB)
GB09-3-C196	381.20	19.69	-6.43	-7.46	-4.30
GB09-3-C197	382.00	19.74	-6.20	-7.24	-4.66
GB09-3-C198	382.80	19.79	-6.37	-7.40	-4.56
GB09-3-C199	383.60	19.84	-6.13	-7.16	-4.17
GB09-3-C200	384.40	19.89	-6.61	-7.64	-4.36
GB09-3-C201	385.20	19.94	-6.79	-7.82	-4.56
GB09-3-C202	386.00	19.98	-6.48	-7.51	-4.74
GB09-3-C203	386.80	20.03	-6.22	-7.25	-4.68
GB09-3-C204	387.60	20.08	-6.39	-7.41	-4.63
GB09-3-C205	388.40	20.12	-6.46	-7.49	-4.33
GB09-3-C206	389.20	20.17	-6.37	-7.40	-4.57
GB09-3-C207	390.00	20.22	-6.48	-7.51	-4.60
GB09-3-C208	390.80	20.27	-6.31	-7.34	-4.51
GB09-3-C209	391.60	20.32	-6.27	-7.29	-4.51
GB09-3-C210	392.40	20.36	-6.07	-7.09	-4.75
GB09-3-C211	393.20	20.41	-6.20	-7.23	-4.34
GB09-3-C212	394.00	20.46	-6.14	-7.16	-4.54
GB09-3-C213	394.80	20.52	-6.26	-7.28	-4.96
GB09-3-C214	395.60	20.56	-6.09	-7.11	-4.82
GB09-3-C215	396.40	20.60	-6.06	-7.09	-4.92
GB09-3-C216	397.20	20.63	-6.13	-7.15	-4.87
GB09-3-C217	398.00	20.66	-6.36	-7.38	-4.54
GB09-3-C218	398.80	20.68	-6.20	-7.22	-4.41
GB09-3-C219	399.60	20.72	-6.49	-7.51	-4.91
GB09-3-C220	400.40	20.76	-6.58	-7.60	-4.55
GB09-3-C221	401.20	20.81	-6.30	-7.32	-4.49
GB09-3-C222	402.00	20.86	-6.35	-7.37	-4.27
GB09-3-C223	402.80	20.92	-6.26	-7.28	-4.40
GB09-3-C224	403.60	20.97	-6.29	-7.31	-4.46
GB09-3-C225	404.40	21.03	-6.40	-7.42	-4.80
GB09-3-C226	405.20	21.08	-6.17	-7.18	-4.43
GB09-3-C227	406.00	21.14	-6.30	-7.32	-4.36
GB09-3-C228	406.80	21.19	-6.29	-7.31	-4.19
GB09-3-C229	407.60	21.25	-6.27	-7.29	-4.13
GB09-3-C230	408.40	21.30	-6.33	-7.35	-4.36
GB09-3-C231	409.20	21.35	-6.12	-7.14	-4.24
GB09-3-C232	410.00	21.40	-6.15	-7.16	-4.62

Sample ID	Depth (mm)	Age (kyr BP)	$\delta^{18}\text{O}$ (‰VPDB)	$\delta^{18}\text{O}$ corr (‰)	$\delta^{13}\text{C}$ (‰VPDB)
GB09-3-C233	410.80	21.45	-6.20	-7.21	-4.69
GB09-3-C234	411.60	21.51	-6.30	-7.31	-4.01
GB09-3-C235	412.40	21.56	-6.48	-7.50	-3.96
GB09-3-C236	413.20	21.61	-6.28	-7.29	-4.25
GB09-3-C237	414.00	21.66	-6.12	-7.13	-4.19
GB09-3-C238	414.80	21.71	-6.38	-7.39	-4.39
GB09-3-C239	415.60	21.76	-6.44	-7.45	-4.28
GB09-3-C240	416.40	21.81	-6.50	-7.51	-3.91
GB09-3-C241	417.20	21.86	-6.30	-7.31	-3.85
GB09-3-C242	418.00	21.91	-6.25	-7.25	-3.95
GB09-3-C243	418.80	21.96	-6.15	-7.15	-4.04
GB09-3-C244	419.60	22.01	-6.25	-7.26	-4.35
GB09-3-C245	420.40	22.06	-6.17	-7.18	-4.26
GB09-3-C246	421.20	22.11	-6.27	-7.27	-4.29
GB09-3-C247	422.00	22.16	-6.41	-7.42	-4.32
GB09-3-C248	422.80	22.21	-6.06	-7.07	-4.29
GB09-3-C249	423.60	22.26	-5.85	-6.85	-4.38
GB09-3-C250	424.40	22.31	-6.52	-7.52	-4.42
GB09-3-C251	425.20	22.36	-6.69	-7.70	-4.50
GB09-3-C252	426.00	22.41	-6.48	-7.48	-4.61
GB09-3-C253	426.80	22.46	-6.61	-7.61	-4.60
GB09-3-C254	427.60	22.52	-6.18	-7.18	-4.27
GB09-3-C255	428.40	22.57	-6.14	-7.14	-4.32
GB09-3-C256	429.20	22.62	-6.02	-7.01	-4.15
GB09-3-C257	430.00	22.68	-6.31	-7.31	-4.58
GB09-3-C258	430.80	22.73	-6.10	-7.10	-4.21
GB09-3-C259	431.60	22.79	-6.39	-7.39	-4.62
GB09-3-C260	432.40	22.86	-6.15	-7.15	-4.74
GB09-3-C261	433.20	22.92	-6.21	-7.21	-4.47
GB09-3-C262	434.00	22.99	-6.15	-7.14	-4.66
GB09-3-D1	434.80	23.08	-6.75	-7.74	-5.16
GB09-3-D2	435.60	23.18	-6.23	-7.22	-4.80
GB09-3-D3	436.40	23.31	-5.94	-6.93	-4.67
GB09-3-D4	437.20	23.43	-6.04	-7.03	-4.13
GB09-3-D5	438.00	23.55	-5.91	-6.89	-4.02
GB09-3-D6	438.80	23.68	-5.87	-6.85	-4.05
GB09-3-D7	439.60	23.80	-5.95	-6.93	-3.89

Sample ID	Depth (mm)	Age (kyr BP)	$\delta^{18}\text{O}$ (‰VPDB)	$\delta^{18}\text{O}$ corr (‰)	$\delta^{13}\text{C}$ (‰VPDB)
GB09-3-D8	440.40	23.93	-6.10	-7.07	-3.82
GB09-3-D9	441.20	24.05	-6.07	-7.05	-3.79
GB09-3-D10	442.00	24.18	-6.09	-7.06	-4.17
GB09-3-D11	442.80	24.29	-6.14	-7.10	-4.26
GB09-3-D12	443.60	24.39	-6.32	-7.28	-4.13
GB09-3-D13	444.40	24.47	-6.25	-7.22	-4.08
GB09-3-D14	445.20	24.54	-6.25	-7.21	-4.23
GB09-3-D15	446.00	24.60	-6.33	-7.29	-4.36
GB09-3-D16	446.80	24.66	-6.59	-7.55	-4.63
GB09-3-D17	447.60	24.71	-6.42	-7.38	-4.44
GB09-3-D18	448.40	24.77	-6.25	-7.21	-4.29
GB09-3-D19	449.20	24.82	-6.20	-7.16	-4.25
GB09-3-D20	450.00	24.87	-6.35	-7.30	-4.53
GB09-3-D21	450.80	24.92	-6.10	-7.06	-4.17
GB09-3-D22	451.60	24.98	-6.29	-7.24	-3.84
GB09-3-D23	452.40	25.03	-5.98	-6.94	-4.08
GB09-3-D24	453.20	25.08	-6.02	-6.98	-4.08
GB09-3-D25	454.00	25.14	-6.20	-7.16	-4.15
GB09-3-D26	454.80	25.19	-6.09	-7.04	-4.14
GB09-3-D27	455.60	25.24	-6.23	-7.18	-4.00
GB09-3-D28	456.40	25.30	-6.23	-7.18	-4.43
GB09-3-D29	457.20	25.36	-6.18	-7.13	-4.13
GB09-3-D30	458.00	25.43	-6.25	-7.20	-4.16
GB09-3-D31	458.80	25.50	-6.07	-7.02	-4.06
GB09-3-D32	459.60	25.57	-5.92	-6.86	-4.27
GB09-3-D33	460.40	25.65	-5.88	-6.82	-4.22
GB09-3-D34	461.20	25.73	-6.02	-6.96	-3.76
GB09-3-D35	462.00	25.81	-6.19	-7.12	-4.14
GB09-3-D36	462.80	25.88	-6.16	-7.10	-3.98
GB09-3-D37	463.60	25.96	-5.65	-6.58	-3.90
GB09-3-D38	464.40	26.03	-5.63	-6.57	-3.98
GB09-3-D39	465.20	26.10	-5.97	-6.91	-4.18
GB09-3-D40	466.00	26.18	-6.00	-6.93	-4.21
GB09-3-D41	466.80	26.25	-6.02	-6.95	-4.27
GB09-3-D42	467.60	26.32	-6.20	-7.13	-3.94
GB09-3-D43	468.40	26.39	-6.06	-6.99	-4.06
GB09-3-D44	469.20	26.46	-6.17	-7.10	-3.97

Sample ID	Depth (mm)	Age (kyr BP)	$\delta^{18}\text{O}$ (‰VPDB)	$\delta^{18}\text{O}$ corr (‰)	$\delta^{13}\text{C}$ (‰VPDB)
GB09-3-D45	470.00	26.53	-6.30	-7.22	-4.13
GB09-3-D46	470.80	26.60	-6.25	-7.17	-4.32
GB09-3-D47	471.60	26.67	-6.20	-7.12	-4.23
GB09-3-D48	472.40	26.74	-6.05	-6.97	-4.30
GB09-3-D49	473.20	26.81	-6.18	-7.09	-4.32
GB09-3-D50	474.00	26.88	-5.84	-6.75	-4.56
GB09-3-D51	474.80	26.95	-6.13	-7.04	-4.56
GB09-3-D52	475.60	27.02	-6.07	-6.98	-4.28
GB09-3-D53	476.40	27.09	-6.24	-7.15	-4.61
GB09-3-D54	477.20	27.17	-6.02	-6.92	-4.36
GB09-3-D55	478.00	27.24	-6.04	-6.95	-4.49
GB09-3-D56	478.80	27.32	-6.23	-7.13	-4.84
GB09-3-D57	479.60	27.40	-6.31	-7.21	-4.95
GB09-3-D58	480.40	27.48	-5.94	-6.83	-4.63
GB09-3-D59	481.20	27.56	-5.81	-6.71	-4.51
GB09-3-D60	482.00	27.64	-5.78	-6.67	-4.71
GB09-3-D61	482.80	27.72	-5.75	-6.64	-4.96
GB09-3-D62	483.60	27.80	-5.87	-6.76	-4.71
GB09-3-D63	484.40	27.88	-5.89	-6.78	-4.77
GB09-3-D64	485.20	27.96	-5.88	-6.76	-5.03
GB09-3-D65	486.00	28.04	-6.26	-7.14	-5.07
GB09-3-D66	486.80	28.11	-5.97	-6.85	-4.68
GB09-3-D67	487.60	28.19	-6.04	-6.92	-4.61
GB09-3-D68	488.40	28.26	-6.02	-6.90	-4.75
GB09-3-D69	489.20	28.33	-6.22	-7.10	-4.80
GB09-3-D70	490.00	28.41	-6.12	-6.99	-4.69
GB09-3-D71	490.80	28.48	-5.89	-6.77	-4.28
GB09-3-D72	491.60	28.55	-5.64	-6.51	-4.37
GB09-3-D73	492.40	28.62	-6.09	-6.96	-4.70
GB09-3-D74	493.20	28.69	-5.92	-6.79	-4.58
GB09-3-D75	494.00	28.76	-5.70	-6.57	-5.00
GB09-3-D76	494.80	28.83	-5.73	-6.59	-5.32
GB09-3-D77	495.60	28.90	-5.98	-6.84	-5.41
GB09-3-D78	496.40	28.97	-5.82	-6.67	-5.12
GB09-3-D79	497.20	29.04	-5.93	-6.78	-5.14
GB09-3-D80	498.00	29.11	-5.96	-6.81	-5.22
GB09-3-D81	498.80	29.18	-5.81	-6.66	-5.29

Sample ID	Depth (mm)	Age (kyr BP)	$\delta^{18}\text{O}$ (‰VPDB)	$\delta^{18}\text{O}$ corr (‰)	$\delta^{13}\text{C}$ (‰VPDB)
GB09-3-D82	499.60	29.25	-5.66	-6.51	-4.89
GB09-3-D83	500.40	29.32	-5.79	-6.64	-4.65
GB09-3-D84	501.20	29.39	-5.80	-6.65	-4.94
GB09-3-D85	502.00	29.46	-5.61	-6.46	-4.79
GB09-3-D86	502.80	29.53	-5.94	-6.78	-4.56
GB09-3-D87	503.60	29.60	-6.01	-6.85	-4.99
GB09-3-D88	504.40	29.67	-5.79	-6.63	-5.30
GB09-3-D89	505.20	29.74	-6.05	-6.88	-5.43
GB09-3-D90	506.00	29.82	-5.84	-6.67	-5.11
GB09-3-D91	506.80	29.89	-5.74	-6.58	-4.54
GB09-3-D92	507.60	29.96	-5.87	-6.70	-5.13
GB09-3-D93	508.40	30.04	-5.97	-6.79	-5.04
GB09-3-D94	509.20	30.12	-6.02	-6.85	-5.56
GB09-3-D95	510.00	30.19	-6.04	-6.87	-5.38
GB09-3-D96	510.80	30.27	-5.97	-6.80	-5.03
GB09-3-D97	511.60	30.34	-5.78	-6.59	-5.26
GB09-3-D98	512.40	30.41	-5.89	-6.71	-5.58
GB09-3-D99	513.20	30.46	-5.84	-6.66	-5.34
GB09-3-D100	514.00	30.50	-5.91	-6.72	-5.21
GB09-3-D101	514.80	30.54	-5.62	-6.43	-5.06
GB09-3-D102	515.60	30.58	-5.63	-6.45	-4.71
GB09-3-D103	516.40	30.62	-5.73	-6.54	-4.73
GB09-3-D104	517.20	30.65	-5.90	-6.71	-4.68
GB09-3-D105	518.00	30.69	-5.60	-6.41	-4.48
GB09-3-D106	518.80	30.72	-5.59	-6.40	-4.85
GB09-3-D107	519.60	30.76	-5.67	-6.48	-4.68
GB09-3-D108	520.40	30.79	-5.87	-6.68	-4.36
GB09-3-D109	521.20	30.83	-5.87	-6.68	-4.44
GB09-3-D110	522.00	30.86	-5.71	-6.51	-4.43
GB09-3-D111	522.80	30.90	-6.10	-6.90	-4.40
GB09-3-D112	523.60	30.94	-6.04	-6.85	-4.48
GB09-3-D113	524.40	30.98	-6.16	-6.97	-5.08
GB09-3-D114	525.20	31.02	-5.72	-6.52	-4.63
GB09-3-D115	526.00	31.07	-5.83	-6.63	-4.96
GB09-3-D116	526.80	31.12	-5.58	-6.38	-5.15
GB09-3-D117	527.60	31.17	-5.75	-6.55	-4.98
GB09-3-D118	528.40	31.22	-5.68	-6.48	-4.70

Sample ID	Depth (mm)	Age (kyr BP)	$\delta^{18}\text{O}$ (‰VPDB)	$\delta^{18}\text{O}$ corr (‰)	$\delta^{13}\text{C}$ (‰VPDB)
GB09-3-D119	529.20	31.26	-5.95	-6.75	-4.72
GB09-3-D120	530.00	31.31	-5.79	-6.59	-4.89
GB09-3-D121	530.80	31.35	-5.93	-6.72	-4.79
GB09-3-D122	531.60	31.39	-5.67	-6.47	-4.77
GB09-3-D123	532.40	31.43	-5.89	-6.69	-5.15
GB09-3-D124	533.20	31.47	-5.81	-6.60	-4.97
GB09-3-D125	534.00	31.50	-5.84	-6.64	-4.75
GB09-3-D126	534.80	31.54	-6.03	-6.83	-4.62
GB09-3-D127	535.60	31.58	-5.70	-6.50	-4.80
GB09-3-D128	536.40	31.62	-5.88	-6.67	-4.60
GB09-3-D129	537.20	31.66	-5.66	-6.46	-4.60
GB09-3-D130	538.00	31.70	-5.85	-6.64	-4.82
GB09-3-D131	538.80	31.74	-5.96	-6.75	-4.67
GB09-3-D132	539.60	31.78	-5.85	-6.64	-4.24
GB09-3-D133	540.40	31.82	-5.84	-6.63	-4.27
GB09-3-D134	541.20	31.86	-5.88	-6.67	-4.39
GB09-3-D135	542.00	31.90	-5.87	-6.66	-5.13
GB09-3-D136	542.80	31.94	-5.69	-6.48	-4.64
GB09-3-D137	543.60	31.98	-5.86	-6.65	-4.95
GB09-3-D138	544.40	32.02	-5.83	-6.62	-4.91
GB09-3-D139	545.20	32.07	-6.02	-6.81	-4.86
GB09-3-D140	546.00	32.12	-6.02	-6.81	-4.92
GB09-3-D141	546.80	32.17	-5.79	-6.58	-4.98
GB09-3-D142	547.60	32.21	-5.76	-6.55	-4.98
GB09-3-D143	548.40	32.26	-5.95	-6.73	-5.10
GB09-3-D144	549.20	32.31	-5.92	-6.71	-5.76
GB09-3-D145	550.00	32.35	-5.84	-6.62	-5.64
GB09-3-D146	550.80	32.40	-5.51	-6.29	-5.53
GB09-3-D147	551.60	32.44	-5.64	-6.42	-5.62
GB09-3-D148	552.40	32.48	-5.71	-6.50	-5.45
GB09-3-D149	553.20	32.52	-5.89	-6.68	-5.56
GB09-3-D150	554.00	32.56	-5.74	-6.52	-5.26
GB09-3-D151	554.80	32.60	-5.62	-6.41	-5.28
GB09-3-D152	555.60	32.64	-5.35	-6.13	-5.68
GB09-3-D153	556.40	32.67	-5.50	-6.28	-6.05
GB09-3-D154	557.20	32.71	-5.86	-6.64	-5.60
GB09-3-D155	558.00	32.75	-5.78	-6.56	-5.49

Sample ID	Depth (mm)	Age (kyr BP)	$\delta^{18}\text{O}$ (‰VPDB)	$\delta^{18}\text{O}$ corr (‰)	$\delta^{13}\text{C}$ (‰VPDB)
GB09-3-D156	558.80	32.78	-5.82	-6.60	-5.23
GB09-3-D157	559.60	32.82	-5.61	-6.39	-5.23
GB09-3-D158	560.40	32.86	-5.83	-6.61	-5.09
GB09-3-D159	561.20	32.89	-5.64	-6.41	-4.91
GB09-3-D160	562.00	32.93	-5.64	-6.42	-4.84
GB09-3-D161	562.80	32.96	-5.37	-6.14	-4.79
GB09-3-D162	563.60	33.00	-5.47	-6.24	-4.98
GB09-3-D163	564.40	33.04	-5.76	-6.54	-4.98
GB09-3-D164	565.20	33.08	-5.80	-6.57	-4.80
GB09-3-D165	566.00	33.11	-5.82	-6.59	-4.47
GB09-3-D166	566.80	33.15	-5.85	-6.62	-5.00
GB09-3-D167	567.60	33.19	-5.96	-6.73	-5.27
GB09-3-D168	568.40	33.22	-5.81	-6.59	-5.09
GB09-3-D169	569.20	33.26	-5.73	-6.50	-4.80
GB09-3-D170	570.00	33.30	-5.41	-6.18	-5.10
GB09-3-D171	570.80	33.33	-5.55	-6.32	-5.75
GB09-3-D172	571.60	33.37	-5.49	-6.26	-5.99
GB09-3-D173	572.40	33.40	-5.91	-6.68	-5.83
GB09-3-D174	573.20	33.44	-5.93	-6.70	-5.71
GB09-3-D175	574.00	33.48	-6.03	-6.80	-5.65
GB09-3-D176	574.80	33.51	-6.01	-6.78	-5.48
GB09-3-D177	575.60	33.55	-5.89	-6.66	-5.95
GB09-3-D178	576.40	33.58	-6.17	-6.94	-5.72
GB09-3-D179	577.20	33.62	-6.19	-6.96	-5.72
GB09-3-D180	578.00	33.66	-6.22	-6.99	-5.69
GB09-3-D181	578.80	33.69	-6.02	-6.79	-5.86
GB09-3-D182	579.60	33.73	-6.05	-6.82	-5.78
GB09-3-D183	580.40	33.77	-6.06	-6.83	-5.76
GB09-3-D184	581.20	33.80	-6.18	-6.94	-5.53
GB09-3-D185	582.00	33.84	-5.82	-6.59	-5.33
GB09-3-D186	582.80	33.88	-5.75	-6.51	-4.85
GB09-3-D187	583.60	33.92	-6.09	-6.85	-5.13
GB09-3-D188	584.40	33.96	-5.97	-6.74	-4.61
GB09-3-D189	585.20	34.00	-6.13	-6.89	-4.83
GB09-3-D190	586.00	34.04	-6.16	-6.92	-4.98
GB09-3-D191	586.80	34.08	-6.23	-6.99	-4.96
GB09-3-D192	587.60	34.13	-6.07	-6.83	-4.67

Sample ID	Depth (mm)	Age (kyr BP)	$\delta^{18}\text{O}$ (‰VPDB)	$\delta^{18}\text{O}$ corr (‰)	$\delta^{13}\text{C}$ (‰VPDB)
GB09-3-D193	588.40	34.17	-6.33	-7.09	-4.81
GB09-3-D194	589.20	34.22	-6.16	-6.92	-4.61
GB09-3-D195	590.00	34.27	-5.88	-6.64	-4.86
GB09-3-D196	590.80	34.32	-5.98	-6.74	-5.19
GB09-3-D197	591.60	34.38	-6.02	-6.78	-4.94
GB09-3-D198	592.40	34.43	-6.04	-6.79	-4.96
GB09-3-D199	593.20	34.50	-5.89	-6.65	-4.62
GB09-3-D200	594.00	34.55	-5.80	-6.55	-4.78
GB09-3-D201	594.80	34.61	-5.95	-6.70	-5.12
GB09-3-D202	595.60	34.67	-5.96	-6.72	-5.43
GB09-3-D203	596.40	34.72	-5.69	-6.44	-5.25
GB09-3-D204	597.20	34.77	-5.98	-6.73	-5.27
GB09-3-E1	598.00	34.83	-5.95	-6.70	-5.29
GB09-3-E2	598.80	34.88	-5.67	-6.42	-5.11
GB09-3-E3	599.60	34.93	-5.64	-6.39	-5.36
GB09-3-E4	600.40	34.98	-5.99	-6.74	-5.47
GB09-3-E5	601.20	35.03	-5.79	-6.54	-5.39
GB09-3-E6	602.00	35.08	-5.77	-6.51	-5.44
GB09-3-E7	602.80	35.14	-5.87	-6.61	-5.29
GB09-3-E8	603.60	35.19	-5.95	-6.70	-5.63
GB09-3-E9	604.40	35.24	-5.92	-6.67	-5.56
GB09-3-E10	605.20	35.29	-5.86	-6.60	-5.74
GB09-3-E11	606.00	35.34	-5.61	-6.35	-5.65
GB09-3-E12	606.80	35.39	-5.85	-6.59	-5.98
GB09-3-E13	607.60	35.45	-5.70	-6.44	-5.38
GB09-3-E14	608.40	35.50	-5.75	-6.49	-4.95
GB09-3-E15	609.20	35.56	-5.74	-6.48	-4.92
GB09-3-E16	610.00	35.62	-5.82	-6.55	-5.38
GB09-3-E17	610.80	35.68	-5.68	-6.42	-5.22
GB09-3-E18	611.60	35.74	-5.94	-6.67	-5.05
GB09-3-E19	612.40	35.79	-5.71	-6.44	-5.28
GB09-3-E20	613.20	35.84	-5.91	-6.64	-5.12
GB09-3-E21	614.00	35.89	-5.82	-6.55	-5.12
GB09-3-E22	614.80	35.94	-5.96	-6.69	-4.87
GB09-3-E23	615.60	35.98	-6.11	-6.84	-4.97
GB09-3-E24	616.40	36.02	-5.86	-6.59	-5.27
GB09-3-E25	617.20	36.07	-6.05	-6.77	-5.16

Sample ID	Depth (mm)	Age (kyr BP)	$\delta^{18}\text{O}$ (‰VPDB)	$\delta^{18}\text{O}$ corr (‰)	$\delta^{13}\text{C}$ (‰VPDB)
GB09-3-E26	618.00	36.11	-6.05	-6.78	-5.34
GB09-3-E27	618.80	36.15	-5.95	-6.67	-5.37
GB09-3-E28	619.60	36.19	-5.80	-6.52	-5.57
GB09-3-E29	620.40	36.23	-5.96	-6.68	-5.63
GB09-3-E30	621.20	36.27	-5.61	-6.33	-5.53
GB09-3-E31	622.00	36.31	-5.96	-6.68	-5.46
GB09-3-E32	622.80	36.35	-5.97	-6.69	-5.34
GB09-3-E33	623.60	36.39	-6.22	-6.94	-5.31
GB09-3-E34	624.40	36.43	-6.26	-6.98	-5.44
GB09-3-E35	625.20	36.47	-6.21	-6.93	-5.20
GB09-3-E36	626.00	36.51	-6.33	-7.05	-5.50
GB09-3-E37	626.80	36.55	-6.03	-6.75	-5.44
GB09-3-E38	627.60	36.60	-5.96	-6.68	-5.62
GB09-3-E39	628.40	36.65	-5.90	-6.62	-5.48
GB09-3-E40	629.20	36.69	-6.27	-6.99	-5.53
GB09-3-E41	630.00	36.74	-6.33	-7.05	-5.32
GB09-3-E42	630.80	36.78	-6.24	-6.95	-5.86
GB09-3-E43	631.60	36.82	-6.03	-6.75	-6.08
GB09-3-E44	632.40	36.85	-6.00	-6.71	-5.88
GB09-3-E45	633.20	36.89	-6.14	-6.86	-6.27
GB09-3-E46	634.00	36.93	-5.88	-6.59	-6.04
GB09-3-E47	634.80	36.96	-5.91	-6.63	-5.96
GB09-3-E48	635.60	36.99	-5.96	-6.68	-5.85
GB09-3-E49	636.40	37.03	-5.65	-6.37	-5.88
GB09-3-E50	637.20	37.06	-5.65	-6.37	-5.70
GB09-3-E51	638.00	37.09	-5.83	-6.54	-5.95
GB09-3-E52	638.80	37.12	-5.84	-6.55	-5.87
GB09-3-E53	639.60	37.15	-5.98	-6.70	-5.50
GB09-3-E54	640.40	37.18	-6.13	-6.84	-5.60
GB09-3-E55	641.20	37.21	-6.26	-6.97	-6.05
GB09-3-E56	642.00	37.24	-5.89	-6.61	-5.67
GB09-3-E57	642.80	37.27	-5.80	-6.51	-5.82
GB09-3-E58	643.60	37.30	-5.90	-6.61	-5.93
GB09-3-E59	644.40	37.33	-5.75	-6.46	-5.92
GB09-3-E60	645.20	37.36	-5.93	-6.64	-6.20
GB09-3-E61	646.00	37.39	-5.74	-6.45	-6.14
GB09-3-E62	646.80	37.42	-5.72	-6.43	-5.74

Sample ID	Depth (mm)	Age (kyr BP)	$\delta^{18}\text{O}$ (‰VPDB)	$\delta^{18}\text{O}$ corr (‰)	$\delta^{13}\text{C}$ (‰VPDB)
GB09-3-E63	647.60	37.45	-5.80	-6.51	-5.88
GB09-3-E64	648.40	37.48	-5.71	-6.42	-5.90
GB09-3-E65	649.20	37.51	-5.80	-6.51	-5.62
GB09-3-E66	650.00	37.54	-5.61	-6.31	-5.60
GB09-3-E67	650.80	37.57	-5.47	-6.18	-5.80
GB09-3-E68	651.60	37.61	-5.55	-6.25	-6.00
GB09-3-E69	652.40	37.64	-5.61	-6.31	-5.59
GB09-3-E70	653.20	37.67	-5.43	-6.13	-5.83
GB09-3-E71	654.00	37.71	-5.49	-6.19	-5.98
GB09-3-E72	654.80	37.74	-5.83	-6.54	-6.52
GB09-3-E73	655.60	37.78	-6.07	-6.78	-6.41
GB09-3-E74	656.40	37.81	-5.81	-6.51	-6.29
GB09-3-E75	657.20	37.85	-5.82	-6.53	-5.67
GB09-3-E76	658.00	37.90	-5.40	-6.11	-5.45
GB09-3-E77	658.80	37.95	-5.51	-6.22	-5.35
GB09-3-E78	659.60	38.00	-5.91	-6.62	-5.38
GB09-3-E79	660.40	38.05	-6.13	-6.83	-5.82
GB09-3-E80	661.20	38.10	-5.86	-6.57	-5.74
GB09-3-E81	662.00	38.15	-5.89	-6.59	-5.78
GB09-3-E82	662.80	38.20	-5.77	-6.48	-5.85
GB09-3-E83	663.60	38.25	-5.75	-6.46	-5.77
GB09-3-E84	664.40	38.29	-5.86	-6.56	-5.61
GB09-3-E85	665.20	38.34	-5.64	-6.34	-5.11
GB09-3-E86	666.00	38.38	-5.77	-6.48	-5.09
GB09-3-E87	666.80	38.43	-5.94	-6.64	-4.98
GB09-3-E88	667.60	38.47	-5.71	-6.41	-4.61
GB09-3-E89	668.40	38.52	-5.76	-6.46	-4.98
GB09-3-E90	669.20	38.56	-5.75	-6.45	-4.81
GB09-3-E91	670.00	38.60	-5.66	-6.36	-5.25
GB09-3-E92	670.80	38.65	-5.88	-6.58	-5.23
GB09-3-E93	671.60	38.69	-6.01	-6.72	-5.49
GB09-3-E94	672.40	38.73	-6.12	-6.82	-4.92
GB09-3-E95	673.20	38.78	-5.93	-6.63	-5.03
GB09-3-E96	674.00	38.82	-5.89	-6.59	-5.02
GB09-3-E97	674.80	38.87	-5.96	-6.66	-5.43
GB09-3-E98	675.60	38.91	-6.07	-6.77	-5.30
GB09-3-E99	676.40	38.95	-5.82	-6.52	-5.53

Sample ID	Depth (mm)	Age (kyr BP)	$\delta^{18}\text{O}$ (‰VPDB)	$\delta^{18}\text{O}$ corr (‰)	$\delta^{13}\text{C}$ (‰VPDB)
GB09-3-E100	677.20	39.00	-5.90	-6.60	-5.69
GB09-3-E101	678.00	39.04	-5.98	-6.68	-5.43
GB09-3-E102	678.80	39.08	-5.96	-6.65	-5.07
GB09-3-E103	679.60	39.13	-6.04	-6.74	-4.42
GB09-3-E104	680.40	39.17	-6.05	-6.75	-4.46
GB09-3-E105	681.20	39.22	-6.16	-6.86	-4.72
GB09-3-E106	682.00	39.26	-6.37	-7.07	-4.79
GB09-3-E107	682.80	39.30	-6.22	-6.91	-4.56
GB09-3-E108	683.60	39.35	-5.65	-6.35	-4.40
GB09-3-E109	684.40	39.39	-5.76	-6.46	-4.67
GB09-3-E110	685.20	39.43	-5.94	-6.63	-4.15
GB09-3-E111	686.00	39.48	-6.06	-6.75	-4.31
GB09-3-E112	686.80	39.53	-5.81	-6.50	-4.34
GB09-3-E113	687.60	39.57	-6.09	-6.79	-4.07
GB09-3-E114	688.40	39.62	-5.89	-6.58	-4.53
GB09-3-E115	689.20	39.67	-5.81	-6.51	-4.28
GB09-3-E116	690.00	39.72	-5.76	-6.46	-4.12
GB09-3-E117	690.80	39.77	-5.69	-6.38	-4.00
GB09-3-E118	691.60	39.82	-5.53	-6.23	-4.22
GB09-3-E119	692.40	39.87	-5.32	-4.67	-4.67

Table A3

Summary of stalagmite GB11-9 isotope data

Note that “ $\delta^{18}\text{O}$ corr” refers to the ice volume corrected $\delta^{18}\text{O}$ values. Where applicable, isotope values shown equal the mean of replicate measurements.

Acknowledgements: Daniel Becker milled samples 193 to 323 of GB11-9 (i.e., 131 of 323 samples). Joan Cowley weighed all GB11-9 samples for analysis. Joan Cowley, Heather Scott-Gagan and Joe Cali analysed all GB11-9 samples on the MAT251.

Sample ID	Depth (mm)	Age (kyr BP)	$\delta^{18}\text{O}$ (‰VPDB)	$\delta^{18}\text{O}$ corr (‰)	$\delta^{13}\text{C}$ (‰VPDB)
GB11-9-A-1	0.00	26.10	-5.64	-6.57	-4.43
GB11-9-A-2	0.70	26.14	-5.68	-6.61	-5.06
GB11-9-A-3	1.40	26.17	-5.81	-6.74	-4.96
GB11-9-A-4	2.10	26.21	-5.76	-6.69	-5.29
GB11-9-A-5	2.80	26.24	-5.80	-6.73	-5.39
GB11-9-A-6	3.50	26.27	-5.53	-6.46	-5.50
GB11-9-A-7	4.20	26.30	-5.50	-6.43	-5.41
GB11-9-A-8	4.90	26.33	-5.70	-6.63	-5.42
GB11-9-A-9	5.60	26.36	-5.68	-6.61	-5.36
GB11-9-A-10	6.30	26.39	-5.49	-6.42	-4.75
GB11-9-A-11	7.00	26.41	-5.68	-6.61	-4.96
GB11-9-A-12	7.70	26.44	-5.69	-6.61	-5.48
GB11-9-A-13	8.40	26.47	-5.63	-6.55	-5.37
GB11-9-A-14	9.10	26.50	-5.58	-6.50	-5.42
GB11-9-A-15	9.80	26.52	-5.59	-6.51	-5.23
GB11-9-A-16	10.50	26.55	-5.75	-6.67	-5.51
GB11-9-A-17	11.20	26.58	-5.84	-6.76	-5.47
GB11-9-A-18	11.90	26.60	-5.67	-6.59	-5.54
GB11-9-A-19	12.60	26.63	-5.44	-6.36	-5.41
GB11-9-A-20	13.30	26.66	-5.76	-6.68	-5.66
GB11-9-A-21	14.00	26.69	-5.71	-6.63	-5.19
GB11-9-A-22	14.70	26.71	-5.80	-6.72	-5.44
GB11-9-A-23	15.40	26.74	-5.84	-6.76	-5.66
GB11-9-A-24	16.10	26.77	-5.64	-6.56	-5.79
GB11-9-A-25	16.80	26.79	-5.54	-6.46	-5.63
GB11-9-A-26	17.50	26.82	-5.84	-6.75	-5.71

Sample ID	Depth (mm)	Age (kyr BP)	$\delta^{18}\text{O}$ (‰VPDB)	$\delta^{18}\text{O}$ corr (‰)	$\delta^{13}\text{C}$ (‰VPDB)
GB11-9-A-27	18.20	26.85	-5.94	-6.85	-5.69
GB11-9-A-28	18.90	26.88	-5.76	-6.67	-5.60
GB11-9-A-29	19.60	26.90	-5.63	-6.54	-5.68
GB11-9-A-30	20.30	26.93	-5.61	-6.52	-5.66
GB11-9-A-31	21.00	26.96	-5.45	-6.36	-5.63
GB11-9-A-32	21.70	26.99	-5.32	-6.23	-5.47
GB11-9-A-33	22.40	27.02	-5.57	-6.48	-5.40
GB11-9-A-34	23.10	27.04	-5.59	-6.50	-5.47
GB11-9-A-35	23.80	27.07	-5.60	-6.51	-5.51
GB11-9-A-36	24.50	27.10	-5.85	-6.76	-5.55
GB11-9-A-37	25.20	27.13	-5.95	-6.86	-5.54
GB11-9-A-38	25.90	27.17	-5.63	-6.53	-5.28
GB11-9-A-39	26.60	27.20	-5.69	-6.59	-5.15
GB11-9-A-40	27.30	27.24	-5.83	-6.73	-4.91
GB11-9-A-41	28.00	27.27	-5.63	-6.53	-5.12
GB11-9-A-42	28.70	27.31	-5.67	-6.57	-5.12
GB11-9-A-43	29.40	27.36	-5.78	-6.68	-5.44
GB11-9-A-44	30.10	27.41	-5.48	-6.38	-5.43
GB11-9-A-45	30.80	27.46	-5.74	-6.64	-5.33
GB11-9-A-46	31.50	27.52	-5.82	-6.72	-5.34
GB11-9-A-47	32.20	27.57	-5.87	-6.76	-5.33
GB11-9-A-48	32.90	27.62	-5.84	-6.73	-5.57
GB11-9-A-49	33.60	27.67	-5.79	-6.68	-5.28
GB11-9-A-50	34.30	27.72	-5.87	-6.76	-5.57
GB11-9-A-51	35.00	27.77	-5.77	-6.66	-5.18
GB11-9-A-52	35.70	27.82	-5.72	-6.61	-5.40
GB11-9-A-53	36.40	27.87	-5.45	-6.34	-5.66
GB11-9-A-54	37.10	27.91	-5.38	-6.27	-5.54
GB11-9-A-55	37.80	27.96	-5.32	-6.20	-5.61
GB11-9-A-56	38.50	28.01	-5.53	-6.41	-5.74
GB11-9-A-57	39.20	28.05	-5.66	-6.54	-5.73
GB11-9-A-58	39.90	28.10	-5.82	-6.70	-5.58
GB11-9-A-59	40.60	28.15	-5.82	-6.70	-5.61
GB11-9-A-60	41.30	28.19	-5.68	-6.56	-5.46
GB11-9-A-61	42.00	28.24	-5.89	-6.77	-5.52
GB11-9-A-62	42.70	28.29	-5.90	-6.78	-5.47
GB11-9-A-63	43.40	28.33	-5.63	-6.51	-5.22

Sample ID	Depth (mm)	Age (kyr BP)	$\delta^{18}\text{O}$ (‰VPDB)	$\delta^{18}\text{O}$ corr (‰)	$\delta^{13}\text{C}$ (‰VPDB)
GB11-9-A-64	44.10	28.38	-5.80	-6.67	-5.14
GB11-9-A-65	44.80	28.42	-5.59	-6.46	-5.00
GB11-9-A-66	45.50	28.47	-5.38	-6.25	-5.00
GB11-9-A-67	46.20	28.51	-5.61	-6.48	-5.38
GB11-9-A-68	46.90	28.56	-5.65	-6.52	-5.46
GB11-9-A-69	47.60	28.61	-5.79	-6.66	-5.52
GB11-9-A-70	48.30	28.65	-5.64	-6.51	-5.29
GB11-9-A-71	49.00	28.70	-5.56	-6.43	-5.21
GB11-9-A-72	49.70	28.74	-5.60	-6.46	-5.16
GB11-9-A-73	50.40	28.79	-5.53	-6.39	-5.17
GB11-9-A-74	51.10	28.84	-5.96	-6.82	-5.46
GB11-9-A-75	51.80	28.88	-5.50	-6.36	-5.34
GB11-9-A-76	52.50	28.93	-5.33	-6.19	-5.66
GB11-9-A-77	53.20	28.98	-5.35	-6.21	-5.93
GB11-9-A-78	53.90	29.02	-5.26	-6.12	-5.60
GB11-9-A-79	54.60	29.07	-5.55	-6.41	-6.02
GB11-9-A-80	55.30	29.12	-5.53	-6.38	-6.11
GB11-9-A-81	56.00	29.16	-5.62	-6.47	-6.16
GB11-9-A-82	56.70	29.21	-5.52	-6.37	-6.07
GB11-9-A-83	57.40	29.25	-5.41	-6.26	-5.82
GB11-9-A-84	58.10	29.30	-5.51	-6.36	-5.20
GB11-9-A-85	58.80	29.35	-5.38	-6.23	-5.28
GB11-9-A-86	59.50	29.39	-5.36	-6.21	-5.39
GB11-9-A-87	60.20	29.44	-5.44	-6.28	-5.67
GB11-9-A-88	60.90	29.49	-5.53	-6.37	-5.91
GB11-9-A-89	61.60	29.54	-5.71	-6.55	-5.85
GB11-9-A-90	62.30	29.59	-5.59	-6.43	-5.87
GB11-9-A-91	63.00	29.64	-5.47	-6.31	-5.98
GB11-9-A-92	63.70	29.69	-5.65	-6.49	-5.73
GB11-9-A-93	64.40	29.74	-5.76	-6.60	-6.00
GB11-9-A-94	65.10	29.80	-5.98	-6.81	-6.39
GB11-9-A-95	65.80	29.86	-5.76	-6.59	-6.15
GB11-9-A-96	66.50	29.93	-5.61	-6.44	-5.49
GB11-9-A-97	67.20	30.01	-5.35	-6.18	-5.74
GB11-9-A-98	67.90	30.09	-5.38	-6.21	-5.67
GB11-9-A-99	68.60	30.17	-5.31	-6.13	-5.53
GB11-9-A-100	69.30	30.24	-5.36	-6.18	-5.60

Sample ID	Depth (mm)	Age (kyr BP)	$\delta^{18}\text{O}$ (‰VPDB)	$\delta^{18}\text{O}$ corr (‰)	$\delta^{13}\text{C}$ (‰VPDB)
GB11-9-A-101	70.00	30.31	-5.30	-6.12	-5.97
GB11-9-A-102	70.70	30.39	-5.29	-6.11	-5.77
GB11-9-A-103	71.40	30.46	-5.32	-6.14	-5.69
GB11-9-A-104	72.10	30.53	-5.43	-6.24	-5.92
GB11-9-A-105	72.80	30.60	-5.44	-6.25	-5.81
GB11-9-A-106	73.50	30.68	-5.66	-6.47	-5.63
GB11-9-A-107	74.20	30.75	-5.56	-6.37	-5.24
GB11-9-A-108	74.90	30.83	-5.74	-6.55	-5.27
GB11-9-A-109	75.60	30.90	-5.66	-6.47	-5.55
GB11-9-A-110	76.30	30.98	-5.93	-6.73	-5.82
GB11-9-A-111	77.00	31.07	-5.84	-6.64	-5.95
GB11-9-A-112	77.70	31.15	-5.77	-6.57	-5.92
GB11-9-A-113	78.40	31.22	-5.60	-6.40	-5.83
GB11-9-A-114	79.10	31.28	-5.86	-6.66	-5.90
GB11-9-A-115	79.80	31.33	-5.85	-6.65	-5.95
GB11-9-A-116	80.50	31.38	-5.75	-6.55	-6.03
GB11-9-A-117	81.20	31.43	-5.77	-6.57	-5.89
GB11-9-A-118	81.90	31.48	-5.61	-6.41	-5.92
GB11-9-A-119	82.60	31.52	-5.53	-6.33	-5.55
GB11-9-A-120	83.30	31.57	-5.68	-6.48	-5.61
GB11-9-A-121	84.00	31.61	-5.65	-6.44	-5.80
GB11-9-A-122	84.70	31.65	-5.47	-6.26	-5.44
GB11-9-A-123	85.40	31.69	-5.30	-6.09	-5.55
GB11-9-A-124	86.10	31.74	-5.48	-6.27	-5.65
GB11-9-A-125	86.80	31.78	-5.71	-6.50	-5.62
GB11-9-A-126	87.50	31.82	-5.72	-6.51	-5.62
GB11-9-A-127	88.20	31.86	-5.55	-6.34	-5.75
GB11-9-A-128	88.90	31.90	-5.47	-6.26	-5.68
GB11-9-A-129	89.60	31.94	-5.64	-6.43	-5.18
GB11-9-A-130	90.30	31.98	-5.67	-6.46	-5.21
GB11-9-A-131	91.00	32.02	-5.77	-6.56	-5.62
GB11-9-A-132	91.70	32.06	-5.85	-6.64	-5.30
GB11-9-A-133	92.40	32.11	-5.61	-6.40	-5.46
GB11-9-A-134	93.10	32.15	-5.47	-6.26	-5.59
GB11-9-A-135	93.80	32.19	-5.49	-6.28	-5.42
GB11-9-A-136	94.50	32.23	-5.39	-6.18	-5.74
GB11-9-A-137	95.20	32.27	-5.33	-6.12	-6.25

Sample ID	Depth (mm)	Age (kyr BP)	$\delta^{18}\text{O}$ (‰VPDB)	$\delta^{18}\text{O}$ corr (‰)	$\delta^{13}\text{C}$ (‰VPDB)
GB11-9-A-138	95.90	32.31	-5.28	-6.07	-6.37
GB11-9-A-139	96.60	32.36	-5.33	-6.12	-6.10
GB11-9-A-140	97.30	32.40	-5.40	-6.18	-6.07
GB11-9-A-141	98.00	32.45	-5.61	-6.39	-6.39
GB11-9-A-142	98.70	32.50	-5.49	-6.27	-6.19
GB11-9-A-143	99.40	32.55	-5.23	-6.01	-6.22
GB11-9-A-144	100.10	32.61	-5.14	-5.92	-6.04
GB11-9-A-145	100.80	32.67	-5.44	-6.22	-6.02
GB11-9-A-146	101.50	32.73	-5.38	-6.16	-5.56
GB11-9-A-147	102.20	32.79	-5.38	-6.16	-6.04
GB11-9-A-148	102.90	32.85	-5.43	-6.21	-6.06
GB11-9-A-149	103.60	32.90	-5.24	-6.02	-6.10
GB11-9-A-150	104.30	32.96	-5.39	-6.17	-6.15
GB11-9-A-151	105.00	33.02	-5.44	-6.22	-6.08
GB11-9-A-152	105.70	33.08	-5.14	-5.92	-6.17
GB11-9-A-153	106.40	33.13	-5.01	-5.79	-5.97
GB11-9-A-154	107.10	33.19	-5.32	-6.09	-5.92
GB11-9-A-155	107.80	33.24	-5.42	-6.19	-6.12
GB11-9-A-156	108.50	33.30	-5.41	-6.18	-5.89
GB11-9-A-157	109.20	33.35	-5.32	-6.09	-5.83
GB11-9-A-158	109.90	33.41	-5.70	-6.47	-5.94
GB11-9-A-159	110.60	33.46	-5.63	-6.40	-5.80
GB11-9-A-160	111.30	33.52	-5.54	-6.31	-5.67
GB11-9-A-161	112.00	33.57	-5.48	-6.25	-5.83
GB11-9-A-162	112.70	33.63	-5.60	-6.37	-5.25
GB11-9-A-163	113.40	33.68	-5.36	-6.13	-5.48
GB11-9-A-164	114.10	33.73	-5.18	-5.95	-5.37
GB11-9-A-165	114.80	33.78	-5.05	-5.82	-5.76
GB11-9-A-166	115.50	33.84	-5.24	-6.01	-5.81
GB11-9-A-167	116.20	33.89	-5.36	-6.12	-5.86
GB11-9-A-168	116.90	33.94	-5.49	-6.25	-5.83
GB11-9-A-169	117.60	33.99	-5.62	-6.38	-5.55
GB11-9-A-170	118.30	34.05	-5.21	-5.97	-5.62
GB11-9-A-171	119.00	34.10	-5.56	-6.32	-5.95
GB11-9-A-172	119.70	34.15	-5.32	-6.08	-5.20
GB11-9-A-173	120.40	34.20	-5.23	-5.99	-5.17
GB11-9-A-174	121.10	34.25	-5.19	-5.95	-5.04

Sample ID	Depth (mm)	Age (kyr BP)	$\delta^{18}\text{O}$ (‰VPDB)	$\delta^{18}\text{O}$ corr (‰)	$\delta^{13}\text{C}$ (‰VPDB)
GB11-9-A-175	121.80	34.30	-5.22	-5.98	-5.66
GB11-9-A-176	122.50	34.35	-5.45	-6.21	-5.48
GB11-9-A-177	123.20	34.40	-5.39	-6.15	-5.20
GB11-9-A-178	123.90	34.45	-5.35	-6.11	-5.25
GB11-9-A-179	124.60	34.51	-5.35	-6.11	-5.48
GB11-9-A-180	125.30	34.56	-5.66	-6.41	-5.47
GB11-9-A-181	126.00	34.61	-5.86	-6.61	-5.88
GB11-9-A-182	126.70	34.66	-5.51	-6.26	-5.90
GB11-9-A-183	127.40	34.72	-5.40	-6.15	-5.52
GB11-9-A-184	128.10	34.76	-5.64	-6.39	-5.59
GB11-9-A-185	128.80	34.81	-5.53	-6.28	-5.20
GB11-9-A-186	129.50	34.86	-5.49	-6.19	-5.44
GB11-9-A-187	130.20	34.91	-5.20	-5.95	-5.10
GB11-9-A-188	130.90	34.96	-5.28	-6.03	-4.86
GB11-9-A-189	131.60	35.01	-5.32	-6.07	-4.90
GB11-9-A-190	132.30	35.06	-5.35	-6.10	-5.38
GB11-9-A-191	133.00	35.12	-5.22	-5.97	-5.32
GB11-9-A-192	133.70	35.17	-5.44	-6.18	-5.31
GB11-9-A-193	134.40	35.22	-5.33	-6.07	-5.53
GB11-9-A-194	135.10	35.27	-5.53	-6.27	-5.64
GB11-9-A-195	135.80	35.32	-5.56	-6.30	-5.64
GB11-9-A-196	136.50	35.37	-5.45	-6.19	-5.96
GB11-9-A-197	137.20	35.42	-5.27	-6.01	-5.47
GB11-9-A-198	137.90	35.48	-5.43	-6.17	-5.27
GB11-9-A-199	138.60	35.53	-5.43	-6.17	-5.74
GB11-9-A-200	139.30	35.58	-5.39	-6.13	-5.79
GB11-9-A-201	140.00	35.63	-5.07	-5.80	-5.73
GB11-9-A-202	140.70	35.69	-5.28	-6.01	-5.54
GB11-9-A-203	141.40	35.74	-5.36	-6.09	-5.59
GB11-9-A-204	142.10	35.80	-5.42	-6.15	-5.28
GB11-9-A-205	142.80	35.85	-5.57	-6.30	-5.61
GB11-9-A-206	143.50	35.91	-5.64	-6.37	-5.36
GB11-9-A-207	144.20	35.96	-5.58	-6.31	-5.73
GB11-9-A-208	144.90	36.01	-5.46	-6.19	-5.42
GB11-9-A-209	145.60	36.07	-5.62	-6.35	-5.31
GB11-9-A-210	146.30	36.13	-5.77	-6.50	-5.41
GB11-9-A-211	147.00	36.18	-5.47	-6.19	-5.63

Sample ID	Depth (mm)	Age (kyr BP)	$\delta^{18}\text{O}$ (‰VPDB)	$\delta^{18}\text{O}$ corr (‰)	$\delta^{13}\text{C}$ (‰VPDB)
GB11-9-A-212	147.70	36.24	-5.73	-6.45	-5.57
GB11-9-A-213	148.40	36.29	-5.65	-6.37	-5.97
GB11-9-A-214	149.10	36.35	-5.60	-6.32	-5.98
GB11-9-A-215	149.80	36.41	-5.67	-6.39	-6.16
GB11-9-A-216	150.50	36.47	-5.64	-6.36	-5.75
GB11-9-A-217	151.20	36.53	-5.76	-6.48	-6.30
GB11-9-A-218	151.90	36.59	-5.78	-6.50	-5.67
GB11-9-A-219	152.60	36.66	-5.66	-6.38	-5.61
GB11-9-A-220	153.30	36.72	-5.71	-6.43	-5.96
GB11-9-A-221	154.00	36.78	-5.82	-6.54	-5.91
GB11-9-A-222	154.70	36.85	-5.65	-6.37	-5.12
GB11-9-A-223	155.40	36.91	-5.81	-6.53	-5.39
GB11-9-A-224	156.10	36.97	-5.72	-6.44	-5.02
GB11-9-A-225	156.80	37.04	-5.68	-6.40	-5.26
GB11-9-A-226	157.50	37.10	-5.69	-6.40	-5.99
GB11-9-A-227	158.20	37.16	-5.46	-6.17	-5.68
GB11-9-A-228	158.90	37.21	-5.33	-6.04	-5.53
GB11-9-A-229	159.60	37.27	-5.28	-5.99	-5.68
GB11-9-A-230	160.30	37.33	-5.38	-6.09	-5.75
GB11-9-A-231	161.00	37.38	-5.27	-5.98	-5.62
GB11-9-A-232	161.70	37.44	-5.35	-6.06	-5.67
GB11-9-A-233	162.40	37.50	-5.11	-5.82	-5.76
GB11-9-A-234	163.10	37.55	-5.38	-6.09	-5.77
GB11-9-A-235	163.80	37.61	-5.48	-6.19	-5.75
GB11-9-A-236	164.50	37.66	-5.42	-6.13	-5.73
GB11-9-A-237	165.20	37.71	-5.55	-6.26	-5.52
GB11-9-A-238	165.90	37.77	-5.66	-6.37	-5.30
GB11-9-A-239	166.60	37.82	-5.49	-6.20	-5.48
GB11-9-A-240	167.30	37.88	-5.44	-6.15	-5.29
GB11-9-A-241	168.00	37.93	-5.49	-6.20	-5.64
GB11-9-A-242	168.70	37.99	-5.54	-6.25	-5.57
GB11-9-A-243	169.40	38.04	-5.60	-6.31	-5.60
GB11-9-A-244	170.10	38.09	-5.72	-6.43	-5.69
GB11-9-A-245	170.80	38.14	-5.57	-6.28	-5.71
GB11-9-A-246	171.50	38.20	-5.60	-6.30	-5.65
GB11-9-A-247	172.20	38.25	-5.35	-6.05	-5.64
GB11-9-A-248	172.90	38.30	-5.54	-6.24	-5.76

Sample ID	Depth (mm)	Age (kyr BP)	$\delta^{18}\text{O}$ (‰VPDB)	$\delta^{18}\text{O}$ corr (‰)	$\delta^{13}\text{C}$ (‰VPDB)
GB11-9-A-249	173.60	38.35	-5.41	-6.11	-5.37
GB11-9-A-250	174.30	38.41	-5.52	-6.22	-5.48
GB11-9-A-251	175.00	38.46	-5.68	-6.38	-5.20
GB11-9-A-252	175.70	38.51	-5.67	-6.37	-5.31
GB11-9-A-253	176.40	38.57	-5.72	-6.42	-5.38
GB11-9-A-254	177.10	38.62	-5.75	-6.45	-5.30
GB11-9-A-255	177.80	38.67	-5.60	-6.30	-5.22
GB11-9-A-256	178.50	38.73	-5.83	-6.53	-5.56
GB11-9-A-257	179.20	38.78	-5.83	-6.53	-5.32
GB11-9-A-258	179.90	38.83	-5.65	-6.35	-5.21
GB11-9-A-259	180.60	38.89	-5.51	-6.21	-5.16
GB11-9-A-260	181.30	38.94	-5.77	-6.47	-5.59
GB11-9-A-261	182.00	39.00	-5.75	-6.45	-5.50
GB11-9-A-262	182.70	39.05	-5.75	-6.45	-5.22
GB11-9-A-263	183.40	39.11	-5.66	-6.36	-5.36
GB11-9-A-264	184.10	39.16	-5.78	-6.48	-5.28
GB11-9-A-265	184.80	39.22	-5.72	-6.42	-5.27
GB11-9-A-266	185.50	39.27	-5.78	-6.48	-5.28
GB11-9-A-267	186.20	39.33	-5.73	-6.43	-5.20
GB11-9-A-268	186.90	39.39	-5.83	-6.53	-5.02
GB11-9-A-269	187.60	39.44	-5.84	-6.54	-5.08
GB11-9-A-270	188.30	39.50	-6.16	-6.86	-5.28
GB11-9-A-271	189.00	39.56	-5.67	-6.37	-5.26
GB11-9-A-272	189.70	39.62	-5.89	-6.59	-5.33
GB11-9-A-273	190.40	39.68	-5.93	-6.63	-5.47
GB11-9-A-274	191.10	39.74	-5.84	-6.54	-5.15
GB11-9-A-275	191.80	39.80	-5.91	-6.61	-5.38
GB11-9-A-276	192.50	39.87	-5.95	-6.64	-5.55
GB11-9-A-277	193.20	39.93	-5.83	-6.52	-5.29
GB11-9-A-278	193.90	39.99	-5.78	-6.47	-5.02
GB11-9-A-279	194.60	40.05	-5.98	-6.67	-4.75
GB11-9-A-280	195.30	40.11	-5.95	-6.64	-4.97
GB11-9-A-281	196.00	40.17	-5.66	-6.35	-5.27
GB11-9-A-282	196.70	40.22	-5.73	-6.42	-5.28
GB11-9-A-283	197.40	40.28	-5.69	-6.38	-5.13
GB11-9-A-284	198.10	40.33	-5.69	-6.38	-5.17
GB11-9-A-285	198.80	40.38	-5.39	-6.08	-5.33

Sample ID	Depth (mm)	Age (kyr BP)	$\delta^{18}\text{O}$ (‰VPDB)	$\delta^{18}\text{O}$ corr (‰)	$\delta^{13}\text{C}$ (‰VPDB)
GB11-9-A-286	199.50	40.43	-5.46	-6.15	-5.31
GB11-9-A-287	200.20	40.48	-5.39	-6.08	-5.38
GB11-9-A-288	200.90	40.52	-5.47	-6.16	-5.65
GB11-9-A-289	201.60	40.57	-5.37	-6.06	-5.46
GB11-9-A-290	202.30	40.62	-5.64	-6.33	-5.03
GB11-9-A-291	203.00	40.66	-5.72	-6.41	-4.92
GB11-9-A-292	203.70	40.71	-5.84	-6.53	-5.35
GB11-9-A-293	204.40	40.76	-5.85	-6.54	-5.48
GB11-9-A-294	205.10	40.80	-5.65	-6.33	-5.18
GB11-9-A-295	205.80	40.85	-5.62	-6.30	-5.41
GB11-9-A-296	206.50	40.89	-5.69	-6.37	-5.32
GB11-9-A-297	207.20	40.93	-5.82	-6.50	-5.34
GB11-9-A-298	207.90	40.98	-5.80	-6.48	-5.30
GB11-9-A-299	208.60	41.03	-5.78	-6.46	-5.46
GB11-9-A-300	209.30	41.07	-5.80	-6.48	-5.57
GB11-9-A-301	210.00	41.12	-5.97	-6.65	-5.67
GB11-9-A-302	210.70	41.16	-6.11	-6.79	-5.33
GB11-9-A-303	211.40	41.21	-6.06	-6.74	-5.53
GB11-9-A-304	212.10	41.25	-5.91	-6.59	-5.73
GB11-9-A-305	212.80	41.30	-5.86	-6.54	-5.68
GB11-9-A-306	213.50	41.34	-5.75	-6.43	-5.74
GB11-9-A-307	214.20	41.39	-5.69	-6.37	-5.66
GB11-9-A-308	214.90	41.44	-5.86	-6.54	-5.33
GB11-9-A-309	215.60	41.48	-5.87	-6.55	-5.22
GB11-9-A-310	216.30	41.53	-5.81	-6.48	-4.95
GB11-9-A-311	217.00	41.57	-5.56	-6.23	-5.13
GB11-9-A-312	217.70	41.62	-5.78	-6.45	-5.29
GB11-9-A-313	218.40	41.66	-5.84	-6.51	-5.42
GB11-9-A-314	219.10	41.71	-5.64	-6.31	-5.38
GB11-9-A-315	219.80	41.76	-5.65	-6.32	-5.32
GB11-9-A-316	220.50	41.81	-5.74	-6.41	-5.31
GB11-9-A-317	221.20	41.86	-5.70	-6.37	-5.40
GB11-9-A-318	221.90	41.91	-5.77	-6.44	-5.27
GB11-9-A-319	222.60	41.96	-5.72	-6.39	-5.29
GB11-9-A-320	223.30	42.02	-5.55	-6.22	-5.11
GB11-9-A-321	224.00	42.07	-5.55	-6.22	-5.21
GB11-9-A-322	224.70	42.13	-5.52	-6.19	-5.47

Table A4

Summary of stalagmite GB09-3 trace element data

Sample ID	Depth (mm)	Age (kyr BP)	Mg/Ca (mmol/mol)	Sr/Ca (mmol/mol*1000)
GB09-3-A1	0.00	0.03	1.0120	0.0395
GB09-3-A3	2.40	0.09	0.6091	0.0115
GB09-3-A7	7.20	0.22	0.7604	0.0149
GB09-3-A11	12.00	0.34	0.6473	0.0132
GB09-3-A13	14.40	0.40	0.7554	0.0130
GB09-3-A15	16.80	0.46	0.7881	0.0121
GB09-3-A17	19.20	0.52	0.8097	0.0129
GB09-3-A19	21.60	0.58	0.7993	0.0134
GB09-3-A21	24.00	0.65	0.6299	0.0136
GB09-3-A23	26.40	0.72	0.5511	0.0133
GB09-3-A25	28.80	0.80	0.5071	0.0138
GB09-3-A27	31.20	0.94	0.6181	0.0147
GB09-3-A29	33.60	1.07	0.6720	0.0150
GB09-3-A31	36.00	1.19	0.7265	0.0151
GB09-3-A33	38.40	1.31	0.6114	0.0152
GB09-3-A35	40.80	1.43	0.5094	0.0132
GB09-3-A37	43.20	1.55	0.5900	0.0152
GB09-3-A39	45.60	1.67	0.7261	0.0155
GB09-3-A41	48.00	1.79	0.6606	0.0155
GB09-3-A43	50.40	1.93	0.5727	0.0154
GB09-3-A45	52.80	2.08	0.6922	0.0131
GB09-3-A47	55.20	2.28	0.7137	0.0127
GB09-3-A49	57.60	2.48	0.5021	0.0135
GB09-3-A51	60.00	2.67	0.4751	0.0124
GB09-3-A53	62.40	2.84	0.6324	0.0139
GB09-3-A55	64.80	3.01	0.6752	0.0137
GB09-3-A57	67.20	3.18	0.7862	0.0139
GB09-3-A59	69.60	3.35	0.5954	0.0126
GB09-3-A61	72.00	3.52	0.6078	0.0125
GB09-3-A63	74.40	3.70	0.5506	0.0128
GB09-3-A65	76.80	3.87	0.4303	0.0123
GB09-3-A67	79.20	4.04	0.5258	0.0124
GB09-3-A69	81.60	4.21	0.5688	0.0128

Sample ID	Depth (mm)	Age (kyr BP)	Mg/Ca (mmol/mol)	Sr/Ca (mmol/mol*1000)
GB09-3-A71	84.00	4.38	0.5577	0.0292
GB09-3-A73	86.40	4.56	0.5961	0.0145
GB09-3-A75	88.80	4.75	0.6787	0.0139
GB09-3-A77	91.20	4.95	0.6007	0.0146
GB09-3-A78	108.00	5.57	0.6001	0.0162
GB09-3-A80	93.60	5.09	0.4969	0.0129
GB09-3-A82	96.00	5.18	0.6023	0.0161
GB09-3-A84	98.40	5.27	0.6449	0.0150
GB09-3-A86	100.80	5.34	0.6103	0.0147
GB09-3-A88	103.20	5.42	0.4648	0.0130
GB09-3-A90	105.60	5.49	0.4634	0.0136
GB09-3-A93	110.40	5.64	0.5721	0.0192
GB09-3-A95	112.80	5.71	0.5741	0.0139
GB09-3-A97	115.20	5.79	0.5893	0.0144
GB09-3-A99	117.60	5.87	0.5691	0.0133
GB09-3-A101	120.00	5.95	0.5623	0.0235
GB09-3-A103	122.40	6.04	0.6442	0.0132
GB09-3-A105	124.80	6.15	0.6621	0.0125
GB09-3-A107	127.20	6.25	0.5514	0.0121
GB09-3-A109	129.60	6.34	0.5632	0.0131
GB09-3-A111	132.00	6.44	0.6006	0.0117
GB09-3-A113	134.40	6.53	0.7377	0.0118
GB09-3-A115	136.80	6.64	0.5890	0.0125
GB09-3-A117	139.20	6.78	0.5492	0.0140
GB09-3-A119	141.60	6.88	0.5828	0.0153
GB09-3-A121	144.00	6.93	0.5236	0.0136
GB09-3-A123	146.40	6.99	0.6683	0.0141
GB09-3-A125	148.80	7.04	0.6171	0.0134
GB09-3-A127	151.20	7.15	0.6090	0.0143
GB09-3-A129	153.60	7.28	0.7008	0.0521
GB09-3-A131	156.00	7.40	0.6211	0.0129
GB09-3-A133	158.40	7.52	0.5592	0.0157
GB09-3-A135	160.80	7.63	0.6657	0.0158
GB09-3-A137	163.20	7.74	0.6520	0.0150
GB09-3-B2	166.80	7.91	0.6119	0.0155
GB09-3-B4	169.20	8.03	0.5766	0.0146
GB09-3-B6	171.60	8.16	0.5973	0.0149

Sample ID	Depth (mm)	Age (kyr BP)	Mg/Ca (mmol/mol)	Sr/Ca (mmol/mol*1000)
GB09-3-B8	174.00	8.30	0.6578	0.0134
GB09-3-B10	176.40	8.45	0.5531	0.0109
GB09-3-B12	178.80	8.59	0.5162	0.0120
GB09-3-B14	181.20	8.72	0.8003	0.0120
GB09-3-B16	183.60	8.87	0.7426	0.0129
GB09-3-B18	186.00	9.00	0.7497	0.0127
GB09-3-B20	188.40	9.13	0.7955	0.0131
GB09-3-B22	190.80	9.25	0.6730	0.0127
GB09-3-B24	193.20	9.37	0.6096	0.0134
GB09-3-B26	195.60	9.50	0.6408	0.0125
GB09-3-B28	198.00	9.63	0.6733	0.0487
GB09-3-B30	200.20	9.72	0.5599	0.0137
GB09-3-B32	202.20	9.80	0.5801	0.0166
GB09-3-C2	204.20	9.88	0.6383	0.0168
GB09-3-C4	206.20	9.95	0.6407	0.0158
GB09-3-C6	208.20	10.03	0.7849	0.0164
GB09-3-C8	210.20	10.10	0.7792	0.0274
GB09-3-C10	212.20	10.18	0.6395	0.0172
GB09-3-C12	214.20	10.25	0.6034	0.0160
GB09-3-C14	216.20	10.33	0.7488	0.0172
GB09-3-C16	218.20	10.41	0.7510	0.0167
GB09-3-C18	220.20	10.49	0.7512	0.0192
GB09-3-C20	222.20	10.57	0.7340	0.0161
GB09-3-C22	224.20	10.64	0.7793	0.0179
GB09-3-C24	226.20	10.71	0.8737	0.0192
GB09-3-C26	228.20	10.77	0.9195	0.0184
GB09-3-C28	230.20	10.83	1.1225	0.0206
GB09-3-C30	232.20	10.89	0.9674	0.0207
GB09-3-C32	234.20	10.95	0.7518	0.0221
GB09-3-C34	236.20	11.01	0.7655	0.0195
GB09-3-C36	238.20	11.07	0.8093	0.0192
GB09-3-C38	240.20	11.13	1.0545	0.0215
GB09-3-C40	242.20	11.19	1.0008	0.0202
GB09-3-C42	244.20	11.25	1.4220	0.0205
GB09-3-C44	246.20	11.31	1.2101	0.0199
GB09-3-C46	248.20	11.37	1.0765	0.0185
GB09-3-C48	250.20	11.43	1.1532	0.0188

Sample ID	Depth (mm)	Age (kyr BP)	Mg/Ca (mmol/mol)	Sr/Ca (mmol/mol*1000)
GB09-3-C50	252.20	11.49	1.4615	0.0224
GB09-3-C52	254.20	11.55	1.2803	0.0218
GB09-3-C54	256.20	11.62	1.0937	0.0213
GB09-3-C56	258.20	11.68	1.3785	0.0225
GB09-3-C58	260.20	11.75	1.1790	0.0199
GB09-3-C60	262.20	11.84	1.2645	0.0195
GB09-3-C62	264.20	11.93	1.0482	0.0177
GB09-3-C64	266.20	12.02	1.0718	0.0188
GB09-3-C66	268.20	12.10	1.1361	0.0183
GB09-3-C68	270.20	12.19	1.2346	0.0193
GB09-3-C70	272.20	12.28	1.3804	0.0212
GB09-3-C72	274.20	12.36	1.5608	0.0178
GB09-3-C74	276.20	12.43	1.3775	0.0224
GB09-3-C76	278.20	12.49	0.8749	0.0199
GB09-3-C78	280.20	12.55	1.0155	0.0207
GB09-3-C80	282.20	12.60	0.9164	0.0197
GB09-3-C82	284.20	12.66	0.7420	0.0239
GB09-3-C84	286.20	12.75	1.0433	0.0199
GB09-3-C86	288.20	12.89	1.5140	0.0219
GB09-3-C88	290.20	13.04	1.3841	0.0208
GB09-3-C90	292.20	13.18	1.5796	0.0187
GB09-3-C92	294.20	13.32	1.4515	0.0187
GB09-3-C94	296.20	13.46	1.2238	0.0192
GB09-3-C96	298.20	13.59	1.8233	0.0209
GB09-3-C98	300.20	13.73	1.9062	0.0220
GB09-3-C100	302.20	13.88	1.3466	0.0196
GB09-3-C102	304.20	14.03	1.6030	0.0209
GB09-3-C104	306.20	14.16	0.8374	0.0208
GB09-3-C106	308.20	14.25	1.2234	0.0184
GB09-3-C108	310.20	14.31	1.2649	0.0206
GB09-3-C110	312.20	14.37	1.3853	0.0202
GB09-3-C112	314.00	14.45	1.1981	0.0185
GB09-3-C114	315.60	14.57	1.5931	0.0178
GB09-3-C116	317.20	14.70	1.1441	0.0201
GB09-3-C118	318.80	14.83	1.3377	0.0207
GB09-3-C120	320.40	14.96	1.2918	0.0236
GB09-3-C122	322.00	15.08	1.3869	0.0229

Sample ID	Depth (mm)	Age (kyr BP)	Mg/Ca (mmol/mol)	Sr/Ca (mmol/mol*1000)
GB09-3-C124	323.60	15.21	1.5829	0.0220
GB09-3-C126	325.20	15.33	1.2528	0.0208
GB09-3-C128	326.80	15.46	1.8021	0.0191
GB09-3-C130	328.40	15.59	2.5458	0.0205
GB09-3-C132	330.00	15.73	2.0885	0.0205
GB09-3-C134	331.60	15.88	1.7301	0.0196
GB09-3-C136	333.20	16.02	1.8597	0.0201
GB09-3-C138	334.80	16.14	1.5897	0.0192
GB09-3-C140	336.40	16.26	1.5487	0.0179
GB09-3-C142	338.00	16.37	1.8139	0.0178
GB09-3-C144	339.60	16.48	1.4693	0.0194
GB09-3-C146	341.20	16.59	0.9657	0.0189
GB09-3-C148	342.80	16.69	1.4062	0.0170
GB09-3-C150	344.40	16.80	1.7794	0.0172
GB09-3-C152	346.00	16.90	1.5316	0.0403
GB09-3-C154	347.60	17.01	1.1737	0.0181
GB09-3-C156	349.20	17.12	1.5518	0.0167
GB09-3-C158	350.80	17.22	1.1484	0.0172
GB09-3-C160	352.40	17.33	2.0118	0.0215
GB09-3-C162	354.00	17.43	1.0037	0.0192
GB09-3-C164	355.60	17.54	1.1541	0.0187
GB09-3-C166	357.20	17.65	1.3722	0.0166
GB09-3-C168	358.80	17.76	1.2230	0.0157
GB09-3-C170	360.40	17.88	1.0045	0.0132
GB09-3-C172	362.00	18.01	1.3173	0.0150
GB09-3-C174	363.60	18.14	1.3847	0.0164
GB09-3-C176	365.20	18.29	1.6354	0.0150
GB09-3-C178	366.80	18.44	1.5713	0.0137
GB09-3-C180	368.40	18.59	1.2121	0.0155
GB09-3-C182	370.00	18.73	1.2661	0.0162
GB09-3-C184	371.60	18.86	1.2332	0.0173
GB09-3-C186	373.20	19.00	1.9283	0.0193
GB09-3-C188	374.80	19.14	2.3256	0.0195
GB09-3-C190	376.40	19.29	2.6938	0.0187
GB09-3-C192	378.00	19.44	1.9886	0.0197
GB09-3-C194	379.60	19.58	2.1234	0.0181
GB09-3-C196	381.20	19.69	1.3471	0.0165

Sample ID	Depth (mm)	Age (kyr BP)	Mg/Ca (mmol/mol)	Sr/Ca (mmol/mol*1000)
GB09-3-C198	382.80	19.79	1.1845	0.0182
GB09-3-C200	384.40	19.89	1.2011	0.0180
GB09-3-C202	386.00	19.98	1.5159	0.0171
GB09-3-C204	387.60	20.08	1.6574	0.0177
GB09-3-C206	389.20	20.17	1.4048	0.0147
GB09-3-C208	390.80	20.27	0.7883	0.0144
GB09-3-C210	392.40	20.36	0.8948	0.0143
GB09-3-C212	394.00	20.46	1.2250	0.0162
GB09-3-C214	395.60	20.56	1.7121	0.0162
GB09-3-C216	397.20	20.63	1.6763	0.0160
GB09-3-C218	398.80	20.68	1.2034	0.0194
GB09-3-C220	400.40	20.76	1.1068	0.0180
GB09-3-C222	402.00	20.86	1.0639	0.0160
GB09-3-C224	403.60	20.97	1.1757	0.0181
GB09-3-C226	405.20	21.08	1.4697	0.0186
GB09-3-C228	406.80	21.19	1.5443	0.0182
GB09-3-C230	408.40	21.30	1.0934	0.0173
GB09-3-C232	410.00	21.40	1.0598	0.0206
GB09-3-C234	411.60	21.51	1.6411	0.0196
GB09-3-C236	413.20	21.61	1.3184	0.0185
GB09-3-C238	414.80	21.71	1.5785	0.0218
GB09-3-C240	416.40	21.81	1.9538	0.0200
GB09-3-C242	418.00	21.91	1.8102	0.0190
GB09-3-C244	419.60	22.01	1.7016	0.0161
GB09-3-C246	421.20	22.11	1.8709	0.0148
GB09-3-C248	422.80	22.21	1.8387	0.0162
GB09-3-C250	424.40	22.31	2.2519	0.0196
GB09-3-C252	426.00	22.41	1.8047	0.0175
GB09-3-C254	427.60	22.52	1.6883	0.0137
GB09-3-C256	429.20	22.62	1.9403	0.0153
GB09-3-C258	430.80	22.73	2.2221	0.0193
GB09-3-C260	432.40	22.86	1.2598	0.0146
GB09-3-C262	434.00	22.99	1.6157	0.0159
GB09-3-D2	435.60	23.18	2.0273	0.0201
GB09-3-D4	437.20	23.43	1.9708	0.0176
GB09-3-D6	438.80	23.68	1.8271	0.0183
GB09-3-D8	440.40	23.93	1.5583	0.0152

Sample ID	Depth (mm)	Age (kyr BP)	Mg/Ca (mmol/mol)	Sr/Ca (mmol/mol*1000)
GB09-3-D10	442.00	24.18	1.4086	0.0180
GB09-3-D12	443.60	24.39	1.3630	0.0208
GB09-3-D14	445.20	24.54	1.4045	0.0210
GB09-3-D16	446.80	24.66	1.6967	0.0182
GB09-3-D18	448.40	24.77	1.7947	0.0189
GB09-3-D20	450.00	24.87	2.3345	0.0216
GB09-3-D22	451.60	24.98	2.3402	0.0182
GB09-3-D24	453.20	25.08	2.3812	0.0187
GB09-3-D26	454.80	25.19	1.9559	0.0170
GB09-3-D28	456.40	25.30	2.7104	0.0182
GB09-3-D30	458.00	25.43	2.4404	0.0202
GB09-3-D32	459.60	25.57	2.1264	0.0213
GB09-3-D34	461.20	25.73	1.8119	0.0191
GB09-3-D36	462.80	25.88	1.5819	0.0168
GB09-3-D38	464.40	26.03	1.6040	0.0169
GB09-3-D40	466.00	26.18	2.1709	0.0176
GB09-3-D42	467.60	26.32	1.8881	0.0163
GB09-3-D44	469.20	26.46	2.4907	0.0172
GB09-3-D46	470.80	26.60	1.6281	0.0158
GB09-3-D48	472.40	26.74	2.1685	0.0184
GB09-3-D50	474.00	26.88	1.4635	0.0177
GB09-3-D52	475.60	27.02	2.0613	0.0168
GB09-3-D54	477.20	27.17	1.9122	0.0163
GB09-3-D56	478.80	27.32	2.2719	0.0190
GB09-3-D58	480.40	27.48	1.6348	0.0165
GB09-3-D60	482.00	27.64	1.8661	0.0190
GB09-3-D62	483.60	27.80	1.5217	0.0179
GB09-3-D64	485.20	27.96	2.2696	0.0198
GB09-3-D66	486.80	28.11	2.1932	0.0160
GB09-3-D68	488.40	28.26	2.3871	0.0174
GB09-3-D70	490.00	28.41	2.1170	0.0177
GB09-3-D72	491.60	28.55	1.7530	0.0136
GB09-3-D74	493.20	28.69	1.6755	0.0174
GB09-3-D76	494.80	28.83	1.5872	0.0201
GB09-3-D78	496.40	28.97	1.4566	0.0171
GB09-3-D80	498.00	29.11	2.0708	0.0164
GB09-3-D82	499.60	29.25	1.4785	0.0182

Sample ID	Depth (mm)	Age (kyr BP)	Mg/Ca (mmol/mol)	Sr/Ca (mmol/mol*1000)
GB09-3-D84	501.20	29.39	1.2023	0.0174
GB09-3-D86	502.80	29.53	1.0590	0.0180
GB09-3-D88	504.40	29.67	1.0850	0.0226
GB09-3-D90	506.00	29.82	1.5135	0.0235
GB09-3-D92	507.60	29.96	1.5568	0.0218
GB09-3-D94	509.20	30.12	1.1890	0.0226
GB09-3-D96	510.80	30.27	1.3138	0.0190
GB09-3-D98	512.40	30.41	1.2370	0.0216
GB09-3-D100	514.00	30.50	1.5129	0.0218
GB09-3-D102	515.60	30.58	1.1451	0.0152
GB09-3-D104	517.20	30.65	1.0276	0.0162
GB09-3-D106	518.80	30.72	1.1718	0.0159
GB09-3-D108	520.40	30.79	1.0899	0.0172
GB09-3-D110	522.00	30.86	1.1153	0.0149
GB09-3-D112	523.60	30.94	1.6476	0.0169
GB09-3-D114	525.20	31.02	1.9763	0.0196
GB09-3-D116	526.80	31.12	1.7347	0.0192
GB09-3-D118	528.40	31.22	1.5669	0.0163
GB09-3-D120	530.00	31.31	1.5186	0.0168
GB09-3-D122	531.60	31.39	1.1765	0.0161
GB09-3-D124	533.20	31.47	1.6286	0.0192
GB09-3-D126	534.80	31.54	1.1478	0.0229
GB09-3-D128	536.40	31.62	1.4683	0.0175
GB09-3-D130	538.00	31.70	1.3011	0.0183
GB09-3-D132	539.60	31.78	1.2285	0.0146
GB09-3-D134	541.20	31.86	0.7772	0.0166
GB09-3-D136	542.80	31.94	0.9871	0.0175
GB09-3-D138	544.40	32.02	1.1263	0.0133
GB09-3-D140	546.00	32.12	1.3375	0.0193
GB09-3-D142	547.60	32.21	1.1246	0.0153
GB09-3-D144	549.20	32.31	1.3228	0.0194
GB09-3-D146	550.80	32.40	1.2188	0.0184
GB09-3-D148	552.40	32.48	1.3026	0.0176
GB09-3-D150	554.00	32.56	1.3349	0.0179
GB09-3-D152	555.60	32.64	0.9466	0.0163
GB09-3-D154	557.20	32.71	1.2084	0.0181
GB09-3-D156	558.80	32.78	2.0524	0.0162

Sample ID	Depth (mm)	Age (kyr BP)	Mg/Ca (mmol/mol)	Sr/Ca (mmol/mol*1000)
GB09-3-D158	560.40	32.86	1.9194	0.0163
GB09-3-D160	562.00	32.93	1.0170	0.0147
GB09-3-D162	563.60	33.00	1.1215	0.0179
GB09-3-D164	565.20	33.08	1.0463	0.0176
GB09-3-D166	566.80	33.15	1.9876	0.0166
GB09-3-D168	568.40	33.22	1.4176	0.0141
GB09-3-D170	570.00	33.30	1.4280	0.0188
GB09-3-D172	571.60	33.37	1.7358	0.0207
GB09-3-D174	573.20	33.44	1.2544	0.0185
GB09-3-D176	574.80	33.51	1.1026	0.0203
GB09-3-D178	576.40	33.58	1.2937	0.0191
GB09-3-D180	578.00	33.66	1.4364	0.0214
GB09-3-D182	579.60	33.73	1.6678	0.0214
GB09-3-D184	581.20	33.80	1.6962	0.0235
GB09-3-D186	582.80	33.88	1.2528	0.0190
GB09-3-D188	584.40	33.96	1.0718	0.0165
GB09-3-D190	586.00	34.04	1.6222	0.0167
GB09-3-D192	587.60	34.13	0.9172	0.0138
GB09-3-D194	589.20	34.22	1.1231	0.0150
GB09-3-D196	590.80	34.32	1.2298	0.0174
GB09-3-D198	592.40	34.43	1.0085	0.0152
GB09-3-D200	594.00	34.55	1.1066	0.0176
GB09-3-D202	595.60	34.67	1.4442	0.0214
GB09-3-D204	597.20	34.77	1.3169	0.0195
GB09-3-E2	598.80	34.88	1.0923	0.0152
GB09-3-E4	600.40	34.98	1.5389	0.0194
GB09-3-E6	602.00	35.08	2.0687	0.0245
GB09-3-E8	603.60	35.19	2.2235	0.0241
GB09-3-E10	605.20	35.29	1.9609	0.0247
GB09-3-E12	606.80	35.39	1.9057	0.0208
GB09-3-E14	608.40	35.50	1.3136	0.0158
GB09-3-E16	610.00	35.62	1.3389	0.0174
GB09-3-E18	611.60	35.74	1.3687	0.0345
GB09-3-E20	613.20	35.84	1.0087	0.0195
GB09-3-E22	614.80	35.94	1.3954	0.0186
GB09-3-E24	616.40	36.02	1.1621	0.0181
GB09-3-E26	618.00	36.11	1.0734	0.0232

Sample ID	Depth (mm)	Age (kyr BP)	Mg/Ca (mmol/mol)	Sr/Ca (mmol/mol*1000)
GB09-3-E28	619.60	36.19	1.3679	0.0207
GB09-3-E30	621.20	36.27	2.0046	0.0185
GB09-3-E32	622.80	36.35	1.7324	0.0183
GB09-3-E34	624.40	36.43	1.7354	0.0194
GB09-3-E36	626.00	36.51	1.4108	0.0169
GB09-3-E38	627.60	36.60	1.5491	0.0215
GB09-3-E40	629.20	36.69	1.8096	0.0187
GB09-3-E42	630.80	36.78	1.3631	0.0213
GB09-3-E44	632.40	36.85	1.0531	0.0199
GB09-3-E46	634.00	36.93	1.2773	0.0203
GB09-3-E48	635.60	36.99	1.2132	0.0174
GB09-3-E50	637.20	37.06	1.3729	0.0178
GB09-3-E52	638.80	37.12	1.9568	0.0212
GB09-3-E54	640.40	37.18	1.5017	0.0169
GB09-3-E56	642.00	37.24	1.1946	0.0200
GB09-3-E58	643.60	37.30	1.4113	0.0196
GB09-3-E60	645.20	37.36	1.7198	0.0207
GB09-3-E62	646.80	37.42	1.8527	0.0184
GB09-3-E64	648.40	37.48	1.2475	0.0173
GB09-3-E66	650.00	37.54	1.4487	0.0167
GB09-3-E68	651.60	37.61	1.5209	0.0172
GB09-3-E70	653.20	37.67	1.6155	0.0183
GB09-3-E72	654.80	37.74	1.4494	0.0217
GB09-3-E74	656.40	37.81	1.9025	0.0204
GB09-3-E76	658.00	37.90	2.1537	0.0183
GB09-3-E78	659.60	38.00	1.1687	0.0174
GB09-3-E80	661.20	38.10	1.3964	0.0189
GB09-3-E82	662.80	38.20	1.5015	0.0201
GB09-3-E84	664.40	38.29	1.4754	0.0192
GB09-3-E86	666.00	38.38	1.2278	0.0157
GB09-3-E88	667.60	38.47	1.4572	0.0141
GB09-3-E90	669.20	38.56	1.5293	0.0145
GB09-3-E92	670.80	38.65	1.6947	0.0208
GB09-3-E94	672.40	38.73	1.8042	0.0159
GB09-3-E96	674.00	38.82	1.5214	0.0185
GB09-3-E98	675.60	38.91	1.0327	0.0183
GB09-3-E100	677.20	39.00	1.2947	0.0222

Sample ID	Depth (mm)	Age (kyr BP)	Mg/Ca (mmol/mol)	Sr/Ca (mmol/mol*1000)
GB09-3-E102	678.80	39.08	1.0430	0.0175
GB09-3-E104	680.40	39.17	1.5773	0.0202
GB09-3-E106	682.00	39.26	1.6083	0.0173
GB09-3-E108	683.60	39.35	1.5874	0.0136
GB09-3-E110	685.20	39.43	1.7981	0.0115
GB09-3-E112	686.80	39.53	1.5277	0.0141
GB09-3-E114	688.40	39.62	1.7416	0.0126
GB09-3-E116	690.00	39.72	1.1230	0.0113
GB09-3-E118	691.60	39.82	1.3398	0.0145
GB09-3-E119	692.40	39.87	1.8505	0.0196
